

# Carbon Nanomaterials for Bioanalytical Sensing and Multicolor Cell Imaging

DISSERTATION

zur Erlangung des

DOKTORGRADES DER NATURWISSENSCHAFTEN

(Dr. rer. nat.)

der Fakultät Chemie und Pharmazie

der Universität Regensburg



vorgelegt von

**Michael-Maximilian Lemberger**

aus Pilsting

(Landkreis Dingolfing-Landau)

im Oktober 2015



# Carbon Nanomaterials for Bioanalytical Sensing and Multicolor Cell Imaging

DISSERTATION

zur Erlangung des

DOKTORGRADES DER NATURWISSENSCHAFTEN

(Dr. rer. nat.)

der Fakultät Chemie und Pharmazie

der Universität Regensburg



vorgelegt von

**Michael-Maximilian Lemberger**

aus Pilsting

(Landkreis Dingolfing-Landau)

im Oktober 2015

Diese Doktorarbeit entstand in der Zeit von Oktober 2012 bis September 2015 am Institut für Analytische Chemie, Chemo- und Biosensorik der Fakultät Chemie und Pharmazie der Universität Regensburg.

Die Arbeit wurde angeleitet von Prof. Dr. Joachim Wegener.

Promotionsgesuch eingereicht am: 02.11.2015

Kolloquiumstermin: 21.12.2015

**Prüfungsausschuss:**

Vorsitzender: Prof. Dr. Oliver Tepner

Erstgutachter: Prof. Dr. Joachim Wegener

Zweitgutachter: PD Dr. Miriam Breunig

Drittprüfer: Prof. Dr. Ralph Witzgall





*Meiner Familie*





## Danksagung

Ich möchte mich zuallererst bei **Prof. Dr. Joachim Wegener** und **Dr. Thomas Hirsch** herzlichst bedanken, die Möglichkeit bekommen zu haben an beiden Arbeitsgruppen beteiligt zu sein und dieses Promotionsthema behandeln zu dürfen. Außerdem möchte mich für die immer verfügbare Betreuung, Hilfe und v.a. die grandiose Arbeitsatmosphäre bedanken.

Bei **PD Dr. Miriam Breunig** möchte ich mich für die Übernahme des Zweitgutachtens bedanken. Auch gilt mein Dank **Prof. Dr. Ralph Witzgall** für die Ausübung der Funktion des Drittprüfers und **Prof. Dr. Oliver Tepner** für die Übernahme des Prüfungsvorsitzes.

**Dr. Daniel Wastl** möchte ich danken für die Aufnahme der AFM Bilder meiner Partikel, sowie der ausschweifenden Unterhaltungen und Diskussionen. Desweiteren danke ich **Dr. Stefan Nagl** für die Messung der Fluoreszenz-Abklingzeiten der C-dots, sowie **Dr. Andreas Schäfer** für deren Charakterisierung mittels XPS.

Für die Möglichkeit der Zell-Analyse mittels FACS möchte ich **PD Dr. Miriam Breunig**, sowie **Renate Liebl** für deren Durchführung danken.

Bei **Christina Hupf** möchte ich mich bedanken für die Präparation der Zell-Sphäroide und die jederzeit verfügbare Unterstützung bei deren Untersuchung.

**Christoph Fenzl** möchte ich für die Herstellung der Liposomen, den Diskussionen und die gemeinsame Zeit im „4. Stock“ danken.

Außerdem gilt mein Dank **Romy Freund**, dafür dass immer ein paar Wells in ihren ITO Arrays für mich frei waren für die Phototoxizitäts-Messungen.

Ich möchte mich bei **Pierre Pütz, Raphael Urban, Melanie Bähz** und **Daniel Robin** bedanken, die im Rahmen ihrer Bachelorarbeiten und Forschungspraktika an einigen Studien dieser Arbeit beteiligt waren.

Bei **Dr. Alexander Zöpfl, Kathrin Hajek** und **Markus Buchner** möchte ich mich ganz besonders bedanken für die immer verfügbare Hilfe und Geduld bei arbeitsrelevanten Angelegenheiten, aber besonders für Alles was nichts damit zu tun hatte.

Und natürlich Danke **allen weiteren Mitarbeitern der Arbeitsgruppen Wegener und Hirsch** für die gemeinsame Zeit und die Unterstützung.

Bei **Steffi**, die immer für mich da war.

Mein größter Dank aber gilt **meiner Familie**, die mir nicht nur mein Studium ermöglicht hat, sondern mir auch immer den nötigen Rückhalt geboten hat.

***Dankeschön!***



# Table of Content

<b>1</b>	<b>INTRODUCTION</b> .....	<b>1</b>
<b>2</b>	<b>OBJECTIVES</b> .....	<b>25</b>
<b>3</b>	<b>MATERIALS AND METHODS</b> .....	<b>27</b>
<b>3.1</b>	<b>Preparation of Photoluminescent Carbon Nanomaterials</b> .....	<b>27</b>
3.1.1	Hydrothermal Carbonization of Molecular Precursors .....	27
3.1.2	Graphene Oxide via Hummers Method .....	34
3.1.3	Graphene Quantum Dots via Hydrothermal Treatment of Graphene Oxide .....	36
<b>3.2</b>	<b>Modification of Carbon Dots and Embedding in other Nanomaterials</b> .....	<b>37</b>
3.2.1	Modification of Carbon Dots with Oleic Acid .....	37
3.2.2	Preparation of Agarose Nanoparticles doped with Carbon Dots .....	39
3.2.3	Encapsulation of Carbon Dots in Liposomes .....	40
<b>3.3</b>	<b>Material Characterization Techniques</b> .....	<b>41</b>
<b>3.4</b>	<b>Optical Spectroscopy and Microscopy</b> .....	<b>44</b>
3.4.1	Optical Spectroscopy and Fluorescence Lifetime Determination .....	44
3.4.2	Imaging via Confocal Laser Scanning Microscopy .....	45
3.4.3	Reagents for Fluorescence Imaging Experiments .....	46
<b>3.5</b>	<b>Cell Culture Techniques</b> .....	<b>49</b>
3.5.1	Cultivation of Adherent Cell Lines .....	49
3.5.2	Cultivation of Three Dimensional Multicellular Spheroids .....	52
3.5.3	Cultivation of Beating Cardiomyocytes .....	54
<b>3.6</b>	<b>Electric Cell-Substrate Impedance Sensing</b> .....	<b>55</b>
3.6.1	Cell-based Assays using Commercially Available ECIS Arrays .....	56
3.6.2	Monitoring the Impact of Carbon Dots on Cardiomyocyte Beating .....	59
3.6.3	Monitoring the Phototoxicity of Carbon Dots by ECIS .....	60
<b>3.7</b>	<b>Permeation Studies across Barrier-forming Cell Monolayers</b> .....	<b>62</b>
<b>3.8</b>	<b>Protocols for <i>Loading</i> and Imaging of Mammalian Cells with Carbon Dots</b> .....	<b>63</b>
<b>4</b>	<b>CHARACTERIZATION OF THE CARBON NANOMATERIALS</b> .....	<b>67</b>
<b>4.1</b>	<b>Characterization of Carbon Dots</b> .....	<b>67</b>
4.1.1	Size Determination of Carbon Dots .....	67
4.1.2	Functionalization of Carbon Dots .....	70
4.1.3	Spectroscopic Properties of Carbon Dots .....	74

4.2	Characterization of Graphene Quantum Dots .....	85
4.3	Characterization of the Modified and Embedded Carbon Dots .....	90
<b>5</b>	<b>INTERACTION OF CARBON DOTS WITH MAMMALIAN CELLS.....</b>	<b>97</b>
5.1	Cytotoxicity Profile in Normal Rat Kidney Cells .....	97
5.2	Uptake and Localization in Normal Rat Kidney Cells .....	101
5.3	Influence on Cell Adhesion, Proliferation and Migration .....	106
5.4	Permeation across Mammalian Cell Monolayers.....	112
5.5	Impact of Carbon Dots on Beating Cardiomyocytes .....	116
<b>6</b>	<b>MULTICOLOR CELL IMAGING USING CARBON NANOMATERIALS AS LUMINESCENT PROBES .....</b>	<b>119</b>
6.1	Carbon Nanomaterials for Multicolor Imaging of Normal Rat Kidney Cells.....	119
6.2	Distinguishing Between Living and Dead Mammalian Cells Using Carbon Dots.....	127
6.3	Imaging of MCF-7 Spheroids as Tissue Models using Carbon Dots .....	141
<b>7</b>	<b>CARBON DOTS AS “THERANOSTIC” PARTICLES IN PHOTODYNAMIC TREATMENT .....</b>	<b>145</b>
7.1	Photogeneration of Reactive Oxygen Species through Irradiation of Carbon Dots .....	145
7.2	Phototoxicity of Carbon Dots under Long-term Irradiation .....	150
7.3	“Theranostic” Approach Based on the Photodynamic Treatment and Imaging of Mammalian Cells .....	156
<b>8</b>	<b>SUMMARY AND OUTLOOK .....</b>	<b>165</b>
8.1	Summary.....	165
8.2	Zusammenfassung auf Deutsch.....	169
8.3	Conclusion and Outlook .....	174
<b>9</b>	<b>REFERENCES.....</b>	<b>177</b>
<b>10</b>	<b>APPENDIX .....</b>	<b>193</b>

<b>10.1</b>	<b>List of Abbreviations .....</b>	<b>193</b>
<b>10.2</b>	<b>Publications and Presentations .....</b>	<b>196</b>
<b>10.3</b>	<b>Curriculum Vitae .....</b>	<b>198</b>
<b>10.4</b>	<b>Eidesstattliche Erklärung .....</b>	<b>201</b>



# 1 Introduction

The following chapter was adapted from:

**“Carbon Nanodots: Synthesis, Characterization and Bioanalytical Applications”.**

Michael-M. Lemberger, Thomas Hirsch, Joachim Wegener, *Bioanalytical Reviews*, 2014.

DOI: 10.1007/11663\_2014\_11.

Nanobiotechnology has emerged as a major area of fundamental and applied research due to the enormous potential and unprecedented performance of nanoscale tools in analytics, diagnostics, therapy (Fortina *et al.* 2005). Nanostructures are by definition between 1 and 100 nm in size, which is one of the reasons for their ability to manipulate and study biological objects on-site as well as to measure compounds with biomedical relevance *in situ* (Whitesides 2003). Nanoscale particles have been modified in many different ways so that they can accommodate multiple functionalities needed for their site-specific targeting within a biological system, e.g. by binding to cell-surface receptors, and providing local functionality like measuring the concentration of an analyte of interest or releasing a cargo compound. In contrast to organic molecules nanoparticles are commonly very stable and they are rather resistant to oxidation or degradation processes in living organisms. Accordingly, targeted interactions between the nanoparticles with their inherent functionalities and biological structures open up a new avenue of applications in biomedical research. Throughout the last decade several types of nanoparticles have been developed and studied in detail. Their most important classes are metal oxide particles (such as  $\text{TiO}_2$  or  $\text{Fe}_3\text{O}_4$ ), polymer particles like latex beads, silica particles, colloidal gold and *quantum dots* (Q-dots) (Thurn *et al.* 2007).

Among them, Q-dots are particularly interesting, since they exhibit intrinsic fluorescence which makes them attractive candidates for imaging applications. The particles themselves are nanocrystals of semiconducting material, such as ZnSe, CdSe or CdTe, typically in a size range between 1 and 10 nm (Warnement *et al.* 2007). A special feature of Q-dots is that their optical properties can be tuned by varying the particle diameter (Brus 1991). Furthermore, they show high brilliancy, photostability and rather broad excitation spectra that allow for simultaneous excitation of several different Q-dots and thus, multicolor fluorescence colors with a single excitation source (Gao *et al.* 2005). However, these particles also have certain disadvantages such as their hydrophobicity, making it impossible to use them without further surface modification in a physiological environment. Therefore, Q-dots have to be encapsulated in silica or decorated by polymers, such as polyethylene glycol (PEG), rendering them water-dispersible (Gerion *et al.* 2001). This, in turn, leads to increasing particle sizes, and limits their application *in vitro* and *in vivo*. Additionally, it was found that certain Q-dots exhibit a significant cytotoxicity, which can be

## Introduction

caused by very different mechanisms (Medintz *et al.* 2005): (i) Q-dots often contain toxic elements (with the exception of ZnSe, for example), such as cadmium or other heavy metals, which may leach out of the particle and enter the cells during particle degradation (Derfus *et al.* 2004); (ii) Q-dots can catalyze the formation of harmful free radicals, particularly reactive oxygen species, upon incubation with living cells (Clarke *et al.* 2006).

Dealing with those disadvantages drives the search for alternative nano-materials with similar luminescence properties but lower toxicity and better stability in aqueous dispersions. The search for new materials brought carbon nano-allotropes into the focus of researchers. After the discovery of fullerenes (Kroto *et al.* 1985), other carbon-based materials like nanodiamonds (Greiner *et al.* 1988), carbon nanotubes (Iijima 1991), carbon nanofibers (De Jong *et al.* 2000) and graphene (Novoselov *et al.* 2004) have been described and characterized. Most recently, a new allotrope with strong intrinsic luminescence has been named *carbon nanodot* or *carbon dot* (C-dot). C-dots were first described in the year 2004 as “fluorescent carbon” in a fraction of electrophoretically purified carbon nanotubes derived from arc discharge soot (Xu *et al.* 2004). Nomenclature of these new particles was not uniform in the very first years after their discovery, calling them “fluorescent carbon nanoparticles” or “carbon nanocrystals”. In the meantime the term *carbon (nano)dots* became most common, emphasizing their similarity to Q-dots.

Since C-dots have been first mentioned in the literature, several different preparation methods have been developed and the full characterization of the material has made considerable progress. Typically, C-dots are in a size range of just a few nanometers. They are mostly described to have a graphitic core with a surface passivated by oxidation processes or by a polymer layer (Baker *et al.* 2010; Nandi *et al.* 2014). However, there are several descriptions in literature of amorphous carbon cores (Zhu *et al.* 2013b) or amorphous structures with only small areas of regular lattice-like order (Tian *et al.* 2009).

Carbon dots may even contain other elements such as hydrogen, oxygen, nitrogen or sulfur (Dong *et al.* 2013a). The presence of these elements, especially oxygen, increases hydrophilicity, leading to very good water dispersibility and is furthermore the chemical basis for the particles’ luminescence properties. C-dots show high photostability, do not contain toxic elements, such as heavy metals, and they can be synthesized at low cost (da Silva *et al.* 2011). These unique properties make C-dots interesting for various scientific applications in (bio)analytics or optoelectronics to mention just two (Song *et al.* 2012). Fig. 1.1 supports this notion strongly by presenting the number of publications per year that deal with carbon dots and their use in various fields of science. The number of publications increased drastically over the last years, indicating the high potential of C-dots in bioanalytical applications.



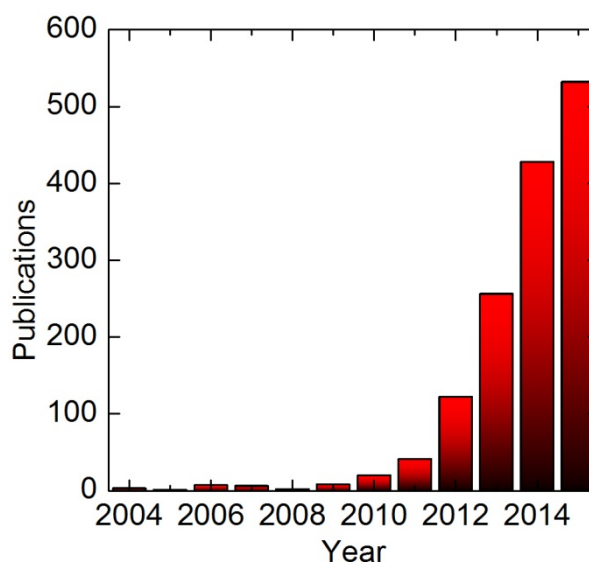


**Fig. 1.1:** The number of publications per year according to SciFinder®, when the terms “carbon dots” and “carbon nanodots” are used for searching the database from 2004 – 2015. State: Sep 8<sup>th</sup> 2015.

Among all possible applications it has been predicted that C-dots have their highest potential as a contrast agent in fluorescence imaging of biological systems, like cells or even living organisms (Luo *et al.* 2013).

### Synthesis and Particle Preparation

Starting from the first identification of C-dots (Xu *et al.* 2004) in the year 2004 as luminescent fraction (“fluorescent carbon”) in an electrophoretic purification of carbon nanotube fragments that had been exposed to arc discharge, a lot of methods were developed to produce this material. In the first publication describing the preparation of C-dots only two years later, Sun *et al.* used laser ablation of carbon targets, which is similar to the fabrication of carbon nanotubes (Sun *et al.* 2006). The nanometer-sized carbon particles, characterized by electron microscopy, had to be passivated by a polymer layer (such as PEG) to obtain stable aqueous suspensions of C-dots with bright luminescence. Polymer coating is one out of several techniques for the preparation of C-dots from raw carbon nanoparticles through passivation, as indicated in the schematic in Fig. 1.2. C-dots are also obtained by oxidative passivation of raw carbon nanoparticles. As such, ordinary (candle) soot oxidized with nitric acid or hydrogen peroxide yields luminescent C-dots that are stable in aqueous suspensions (Liu *et al.* 2007). According to these studies surface passivation is a major requirement for photoluminescence (PL) of C-dots as it provides emissive surface states, described in detail in the luminescence properties chapter.

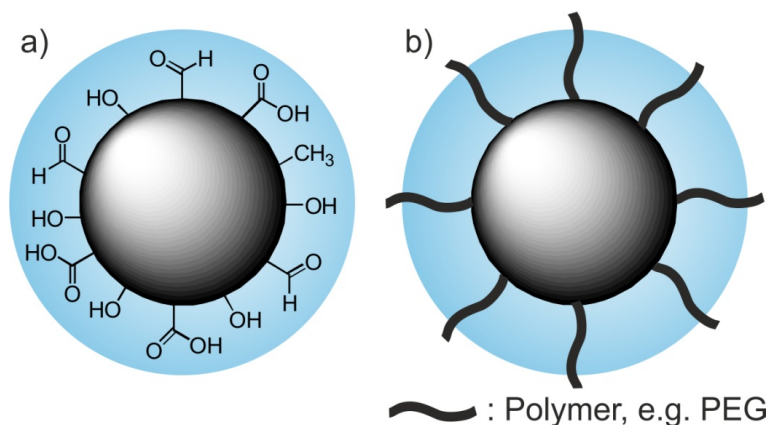


**Fig. 1.2:** Passivation of C-dots (a) by surface oxidation or (b) by decoration with polymers.

A lot of other, very different techniques to prepare C-dots have been described. The reason for this great variety of preparation techniques is the lack of a precise definition of the C-dots' molecular composition and structure. In general, C-dots can be prepared like many other nanomaterials in *top-down* or *bottom-up* approaches (Fig. 1.3). The *top-down* approaches apply methods like arc discharge, laser ablation and electrochemical exfoliation to break down macroscopic carbon materials and obtain nanometer sized C-dots. In contrast, the *bottom-up* approaches make use of molecular precursors or complex mixtures of precursors that are exposed to microwave radiation, heat, ultrasound or harsh chemicals to form C-dots (Baker *et al.* 2010). The various methods are discussed in detail below.

### Top-Down Preparation of C-dots

Top-down approaches apply physical methods to prepare C-dots from carbon macro materials. Laser ablation has been the first technique applied for C-dot preparation as mentioned before. Sun *et al.* used a Nd:YAG laser (1064 nm) for the ablation of a carbon target under a flow of argon and water vapor at 900 °C (Sun *et al.* 2006). These raw carbon nanoparticles showed no photoluminescence (PL) and had to be oxidized with nitric acid under reflux in a second preparation step. Afterwards they were passivated with PEG or poly propionylethylene-imine-co-ethyleneimine (PPEI-EI), respectively, before they showed PL in aqueous suspensions. The estimated size of the C-dots obtained from this protocol was about 5 nm with a quantum yield in the range of 4%. A similar approach was described by Li *et al.* (Li *et al.* 2011b). Here commercially available carbon nanoparticles were dispersed in solvent and irradiated by an unfocussed Nd:YAG laser (532 nm) under stirring. The laser irradiation passivated the surface of the carbon nanoparticles and decorated it with oxygen containing groups which renders the C-dots photoluminescent. This method was a simplification to the one of Sun *et al.*, since C-dots were prepared in liquid medium by laser irradiation without an additional complex set-up.

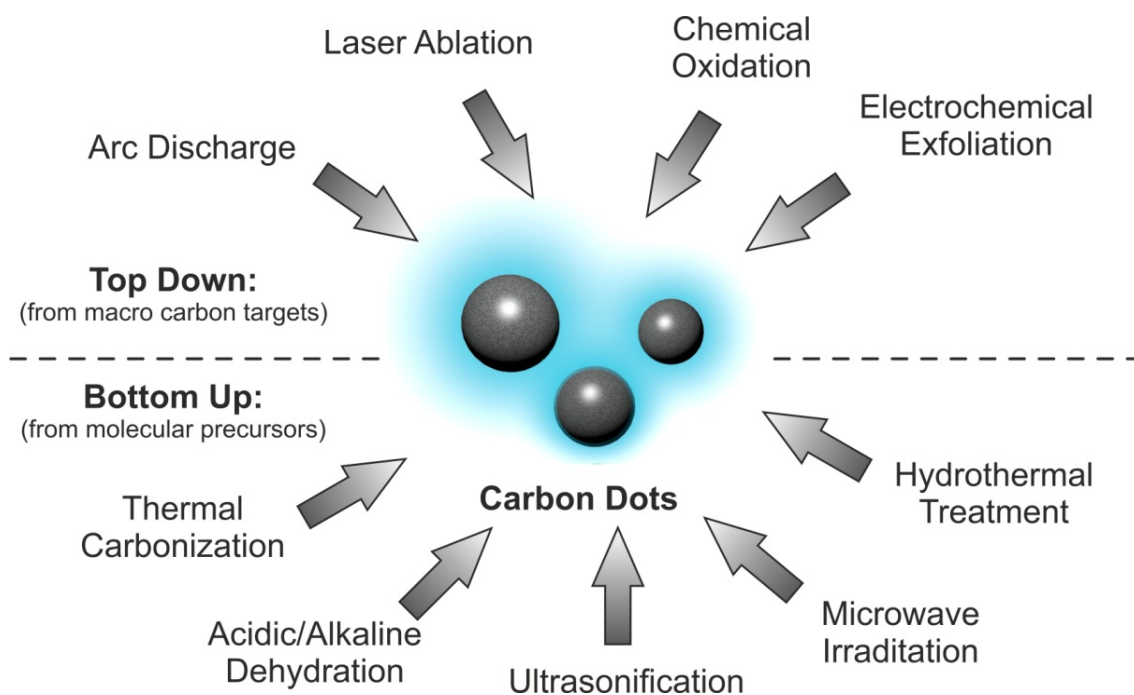


**Fig. 1.3:** Schematic overview on top-down and bottom-up preparation methods for C-dots.

Another top-down technique is the electrochemical exfoliation from graphite (Zheng *et al.* 2009). Here C-dots are released into aqueous solution from a graphite rod as working electrode during cyclic voltammetry (-3.0 to +3.0 V vs. Ag/AgCl). On such high potentials water is decomposed under formation of radicals which attack the electrode. These C-dots have an average size of 2.0 nm, emit blue luminescence under UV excitation and also show electrochemiluminescence (ECL). With a similar strategy carbon paste electrodes have been used as starting material for electrochemical preparation of C-dots by oxidation at +9 V vs. standard calomel electrode potential (SCE) in 0.1 M  $\text{NaH}_2\text{PO}_4$  aqueous solution (Long *et al.* 2012). The formation of C-dots is also possible through the electrochemical oxidation of water which leads to the formation of hydroxyl and oxygen radicals that attack the anode and generate water-soluble C-dots. These electrochemically formed C-dots darken the initially colorless solution gradually from yellow to brown (Lu *et al.* 2009). The particles show a high surface density of oxygen containing functional groups which explains their good water-dispersibility. Electrochemical preparation methods provide another interesting synthetic option: tuning of the luminescence properties of C-dots (Bao *et al.* 2011). In one strategy bundles of carbon fibers were used as working electrodes and different potentials were applied relative to a reference electrode. It was found that the applied voltage had significant influence on the release time of the particles (darkening of the suspension), on their size and - most interestingly - on their PL properties. It turned out that higher potentials lead to an increased oxidation of the C-dots' surfaces and, thus, influence the nature of the emissive sites on their surface which significantly alter their photo-physical properties (see below).

### Bottom-Up Preparation of C-dots

While the top-down approaches deal with the preparation of C-dots from carbon macro materials, the bottom-up approaches start from molecular precursors. One of the simplest ways to do so is *thermal carbonization* of the starting material. Bourlinos et al. reported "surface functionalized carbogenic dots" through thermal decomposition of different ammonium citrate salts (Bourlinos *et al.* 2008b). Citrate served as carbon source, while different organic amines act as surface modifier. The educts were mixed in solution, dried and calcinated at 300 °C in air for 2 h to obtain functionalized C-dots. Hydrophobic C-dots were prepared by using octadecyl ammonium citrate, while hydrophilic ones were obtained from 2-(2-aminoethoxy)-ethanol citrate. These C-dots have been characterized to be smaller than 10 nm, a quantum yield between 4 and 10 % and dispersibility in different solvents depending on their functionalization. When tris(hydroxymethyl)aminomethane (TRIS) is used as carbon source and betaine hydrochloride as surface modifier the resulting C-dots carry quaternary amine groups on their surface with a corresponding positive zeta potential of +43 mV. The particles show luminescence at  $\lambda_{\text{max}} \sim 460$  nm with a quantum yield of app. 4% and anion exchange properties (Bourlinos *et al.* 2012). Thermal decomposition is described for single precursor molecules or salts only. In this line the calcination of the complex ligand ethylenediamine-tetraacetic acid (EDTA) has turned out to be very useful. Typically, EDTA is calcinated at 400 °C under nitrogen atmosphere for 2 h. Through the decomposition, especially decarboxylation, nitrogen doped C-dots are formed. These were described to have an average size of about 7.5 nm and to show blue luminescence at  $\lambda_{\text{max}} \sim 400$  nm with a quantum yield of about 40% (Pan *et al.* 2010a; Zhou *et al.* 2012b; Deng *et al.* 2013).

Another bottom-up strategy is to perform the decomposition of molecular precursors not under dry conditions but in solution. This allows a very homogeneous carbonization of the starting material, obtaining C-dots which are already well dispersed in the solvent. Generally, particle formation from molecular precursors may be attributed to the polymerization of the molecules under dehydration and subsequent carbonization or decarboxylation (Li *et al.* 2014b). A simplified schematic example for the formation of C-dots from molecules in solution through dehydration reactions is shown in Fig. 1.4. Thereby, highly functionalized particles with delocalized electron systems are obtained.

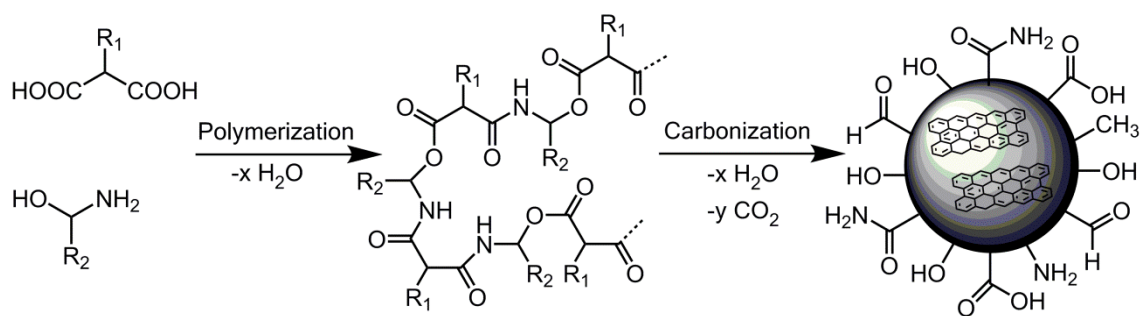


**Fig. 1.4:** Schematic for the formation of C-dots from molecular precursors through polymerization and carbonization by dehydration reactions.

One of the most popular C-dot preparation methods in solvents is the dehydration of carbohydrates. As implied from the name of these molecules, they formally consist of hydrated carbon so that dehydration provides pure carbon as a remnant, as indicated in Fig. 1.5. These dehydration reactions are often catalyzed by acids or bases, ultrasound exposure (Li *et al.* 2011a), microwave heating (Wang *et al.* 2011) or hydrothermal treatment (He *et al.* 2011). Practically, the dehydration process is not complete at all towards the end of the C-dot preparation, but the relative carbon content has increased considerably compared to the starting material. Under these conditions C-dots are formed with delocalized electron systems and a surface decoration that stems from the functional groups of the precursor molecules. In the case of carbohydrate starting materials surface groups are often hydroxyl-, aldehyde- and carboxyl-groups and the carbon to oxygen ratio depends on the dehydration rate (Yang *et al.* 2011). These functional groups provide high water-dispersibility on the one hand and the possibility for later surface modification on the other hand.

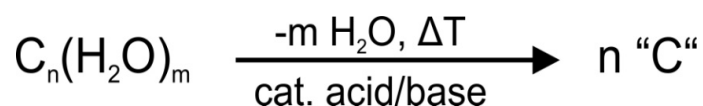


**Fig. 1.5:** Schematic for the bottom-up preparation of C-dots through dehydration of carbohydrates.

The simplest way for the preparation of C-dots from carbohydrates in aqueous solution is the acidic dehydration of glucose with concentrated sulfuric acid under stirring (Peng *et al.* 2009). Following this route Peng *et al.* obtained "black carbonaceous powder", which was further oxidized with nitric acid in a second step and passivated with 4,7,10-trioxa-1,13-tridecanediamine (TTDDA). These C-dots emit blue luminescence at  $\lambda_{\text{max}} \sim 440 \text{ nm}$  with a quantum yield of 13 % and an average size of 5 nm.

Modified preparation routes that basically follow the same strategies use different experimental conditions such as ultrasound exposure of the reaction mixture. A one-step route from carbohydrates to luminescent C-dots using ultrasound was reported by Li *et al.* (Li *et al.* 2011a). Typically, an aqueous glucose solution (1 M) is mixed with aqueous NaOH solution (1 M) and sonicated for 4 h. Within the reaction time the colorless solution turns gradually from yellow to dark brown due to C-dot-formation. This preparation method does

## Introduction

not require any passivation but provides directly blue luminescent C-dots ( $\lambda_{\max} \sim 450$  nm) with a size below 5 nm and a quantum yield of about 7 %. A similar procedure was reported by Ma *et al.* who treated a mixture of glucose and ammonia with ultrasound for 24 h (Ma *et al.* 2012). Those C-dots had an average diameter of 10 nm with very similar optical properties.

Microwave irradiation is also a very popular technique to assist a quick and easy carbonization of carbohydrates and other precursor molecules. For example, C-dots may be obtained by treating a mixture of glycerol (as carbon source) and TTDDA (as passivation agent) for only 10 min at 700 W in a microwave oven (Liu *et al.* 2011a). C-dot preparations via microwave heating has been performed using different pairs of carbon source and passivation agent such as: glycerol and poly ethylene imine (PEI) (Liu *et al.* 2012a), glucose and PEG (Liu *et al.* 2012b), amino acids and PEG (Lin *et al.* 2012) or citric acid and PEI (Salinas-Castillo *et al.* 2013). Such microwave treatment of these combinations has been shown to open up a direct route to passivated C-dots. It is noteworthy that passivation of C-dots is not strictly required as pyrolysis of only one precursor, sometimes acid or base catalyzed, has also been performed. Examples for such a synthetic route are microwave heating of glycerol (Wang *et al.* 2011), dextrin (Puvvada *et al.* 2012), polymers (Mitra *et al.* 2012), citric acid (Qu *et al.* 2012; Du *et al.* 2013), amino acids (Jiang *et al.* 2012) or even complex material such as egg shell membrane (Wang *et al.* 2012b), respectively. Microwave-assisted pyrolysis is one of the most popular preparation techniques of C-dots due to its high reproducibility and simplicity only outperformed with respect to the number of publications by hydrothermal synthesis.

Hydrothermal preparation of C-dots offers several distinct advantages which are the reason for its popularity. First and most important, hydrothermal synthesis is rather simple. Reactions are typically carried out in stainless-steel autoclaves with teflon lining. The precursors are suspended or dissolved (mostly) in water and transferred into the autoclave, which is tightly closed afterwards. Then the autoclave is heated in an oven or a muffle furnace. Carbonization takes place in solution assisted by high temperature and pressure provided within the closed system. Hydrothermal synthesis is fairly mild compared to microwave treatment, for example. Accordingly, this preparation method does not require sophisticated instrumentation and provides C-dots with rather high reproducibility. Please note that the experimental conditions (high temperature, high pressure) enable the carbonization and dehydration of rather stable materials so that a lot of different precursors can be used to prepare C-dots with a broad range of chemical compositions. Synthetic routes starting from carbohydrates are the most popular ones among all published hydrothermal procedures, since carbohydrates are a low-cost, sustainable mass material. For instance, He *et al.* reported the hydrothermal preparation of C-dots from glucose, sucrose and starch by using several acidic/alkaline additives (He *et al.* 2011). The obtained C-dots were highly water-dispersible and their

photoluminescence properties differed widely dependent on the additives in the reaction mixture. Yang et al. (Yang *et al.* 2011) showed that the hydrothermal formation of C-dots from glucose is influenced by the addition of  $\text{KH}_2\text{PO}_4$ , affecting particle size and photoluminescence. N-doped C-dots with amino-functionalization have been obtained directly from chitosan as precursor (Yang *et al.* 2012). However, not only carbohydrates may serve as precursors, several other classes of (bio-) molecules can be used in hydrothermal synthesis as well. Citric acid has been used as carbon source which gets decarboxylated during the process providing one of the brightest C-dot preparation so far with a quantum yield of up to 80 % ( $\lambda_{\text{max}} \sim 450 \text{ nm}$ ). The average size of these particles was 2.8 nm (Zhu *et al.* 2013a). Other examples for useful precursors are: amino acids (Hsu *et al.* 2012a), dopamine (Qu *et al.* 2013) or tetrachlormethane (Zhang *et al.* 2012). Surprisingly not only purified molecules have been used as precursors in hydrothermal preparation of C-dots but also complex biological materials like watermelon peel (Zhou *et al.* 2012a), orange juice (Sahu *et al.* 2012), pomelo peel (Lu *et al.* 2012), coffee grounds (Hsu *et al.* 2012b) or grass (Liu *et al.* 2012c).

A meaningful comparison of the different synthetic routes to luminescent C-dots requires a first categorization: *top-down* approaches need to be separated from *bottom-up* approaches. The physical approaches providing *top-down* preparation of C-dots require sophisticated instrumental devices such as arc discharger or laser set-ups for ablation. Moreover, ablation or exfoliation of C-dots from macroscopic carbon targets do not allow for doping C-dots with other elements, such as nitrogen. And please note, that both *top-down* approaches do not provide control over the C-dots surface functionalization in contrast to *bottom-up* approaches using well-defined molecules as precursors. Precursor fragments often remain on the C-dots surface so that surface decoration can be tailored by the selection of precursors. Another big advantage of *bottom-up* procedures is the experimental option to dope C-dots with other molecules or elements and their excellent reproducibility. According to the available literature doping is the key to high luminescence, quantum yield and functionalization for bioanalytical applications. Because of these tremendous advantages microwave- and hydrothermal-assisted C-dot preparations have become the most popular among the available preparation techniques. Table 1.1 summarizes the established synthetic routes to luminescent C-dots including individual advantages and disadvantages as well as the reported quantum yield.

**Table 1.1:** Comparison of different preparation methods for carbon dots (QY: Quantum Yield).

Type	Method	Advantage	Disadvantage	Typical QYs
Top Down	Arc Discharge	-	Complex Set-up, Low Reproducibility	<b>2%</b> (Xu <i>et al.</i> 2004)
	Laser Ablation	-	Complex Set-up	<b>4 - 10%</b> (Sun <i>et al.</i> 2006)
	Chemical Oxidation	Simple (exp.)	Precursor Material undefined	<b>2 - 12%</b> (Liu <i>et al.</i> 2007; Tian <i>et al.</i> 2009; Qiao <i>et al.</i> 2010)
	Electrochemical Exfoliation	Oxidation level easily controllable	Precursor needs to be conductive	<b>2 - 12%</b> (Lu <i>et al.</i> 2009; Li <i>et al.</i> 2010a; Bao <i>et al.</i> 2011)
Bottom Up	Ultrasonification	Degree of carbonization well controllable	Limited in choice of precursors	<b>~ 7 %</b> (Li <i>et al.</i> 2011a; Ma <i>et al.</i> 2012)
	Acidic/Alkaline Dehydration	Simple (exp.)	Limited in choice of precursors, no control of dehydration grade	<b>~ 13%</b> (Peng <i>et al.</i> 2009)
	Thermal Carbonization	Simple when only one precursor is needed	Inhomogeneity in mixing solid precursors	<b>4 - 40%</b> (Bourlinos <i>et al.</i> 2008a; Bourlinos <i>et al.</i> 2008b; Pan <i>et al.</i> 2010a; Bourlinos <i>et al.</i> 2012; Zhou <i>et al.</i> 2012b)
	Microwave Irradiation	Fast (< 10 min)	Temperature range depends on solvent (aqueous solutions)	<b>5 - 45%</b> (Wang <i>et al.</i> 2011; Jiang <i>et al.</i> 2012; Wang <i>et al.</i> 2012b; Du <i>et al.</i> 2013)
	Hydrothermal Treatment	Mild carbonization of various materials, good reproducibility	Complex optimization	<b>Up to 80%</b> (Dong <i>et al.</i> 2013a; Zhu <i>et al.</i> 2013a)

### Photoluminescence Properties

Among all properties of C-dots identified and reported so far, their intrinsic luminescence is the most interesting one. Compared to organic fluorophores C-dots show improved photostability and their luminescence is stationary and non-blinking in contrast to Q-Dots. Furthermore C-dots possess a very broad excitation band and it is possible to tune their emission. Even though their optical properties have been described and characterized



from many different perspectives, the quantum mechanical origin of C-dots luminescent properties is far from being understood and still under intense investigation.

Typically, C-dots have their absorbance maximum in the UV and their spectrum bottoms out over the whole visible light region up into the near infrared. It is a special feature of C-dots in this respect that the excitation wavelength may be varied to induce emission of differently colored light, as indicated in Fig. 1.6a.

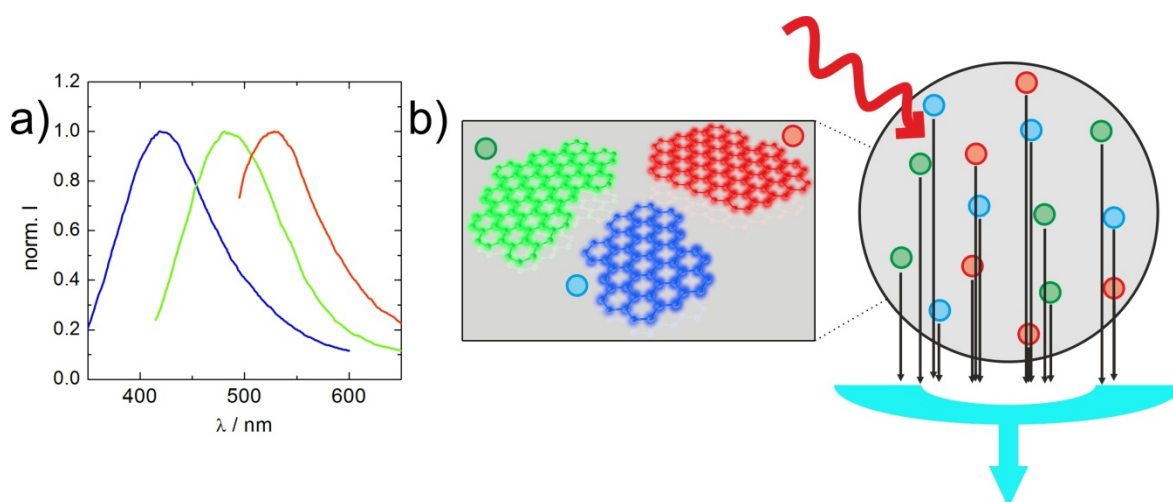


**Fig. 1.6:** Photoluminescence emission from C-dots upon variation of the excitation wavelength. a) Typical emission spectra of C-dots at different excitation wavelengths. b) Individual differently emissive fluorophores on the surface of C-dots, as possible explanation (Demchenko *et al.* 2013).

Researchers suggest two different mechanisms to explain this behavior: (i) C-dot preparations contain particles of different size and these show a size-dependent luminescence. Upon excitation at a given wavelength only a fraction of the entire population is excited and emits fluorescence (Zhao *et al.* 2008); (ii) multicolor photoluminescence arises from a distribution of different emissive trap sites on the particles surface (Liu *et al.* 2009). The strongest light absorbers are small-sized  $sp^2$  hybridized islands rich in  $\pi$ -electrons, in high amount and density. Their electronic excitations may be considered as the bandgap transitions forming excitonic states (Demchenko *et al.* 2013), shown as schematic in Fig. 1.6b. To date there is no completely convincing explanation available that verifies one mechanism and excludes the other. Furthermore, the doping of C-dots with nitrogen was reported to highly influence the QY of the particles through the addition of electron donor groups (Wang *et al.* 2015a). This influences the band gap of the emissive species and therefore enables brightest photoluminescence (Li *et al.* 2012c).

In the first publication about the systematic preparation of C-dots, Sun *et al.* compared the particles' photoluminescence with that from silicon nanocrystals (Sun *et al.* 2006). In this study the photoluminescence was attributed to surface energy traps which become emissive through their stabilization by surface passivation. This requirement for surface

## Introduction

passivation is similar for C-dots and silicon nanocrystals whose luminescence emission originates from radiative recombination of excitons (Wilson *et al.* 1993). The conclusions made by Sun *et al.* were the first attempts to explain the luminescence properties of C-dots which were challenged and improved by more in-depth studies over the years.

Q-dots are often used as a reference material in comparison to C-dots. The luminescence of semiconducting Q-dots depends on the size of the individual crystals. The smaller the crystal the larger is its band gap and thus, the higher is the frequency of the emitted light after excitation. Accordingly, the color of the light shifts from red to blue (to shorter wavelengths) with decreasing size of the Q-dots (Alivisatos 1996). However, such a strict size-dependent luminescence has not been observed in general for C-dots. Lee *et al.* reported a red-shift for larger C-dots by exfoliation from a graphite rod after size-separation of the resulting particles by column chromatography (Li *et al.* 2010a). In contrast Lu *et al.* reported an inverse dependency between luminescence and particle size for C-dots exfoliated from graphite rods in ionic liquid (Lu *et al.* 2009). Other authors claim that it is not the size but the functional groups decorating the particle surface which has the most significant influence on the electronic characteristics of C-dots (Bao *et al.* 2011).

C-dots have a more disordered solid state structure compared to crystalline Q-dots or nano-sized graphene. This has to be taken into account when different photoluminescence mechanisms are discussed (Fischer *et al.* 2011). A comprehensive description and explanation of C-dot luminescence has to include their internal composition, any surface functionalizations as well as the size of the particle itself. Thinking of the structure of C-dots as an amorphous or crystalline carbon core - mostly consisting of  $sp^2$ -carbons - and an oxidized carbon shell, it is generally considered that PL is likely to originate from the  $sp^2$ -carbons (Baker *et al.* 2010). Those confined and delocalized  $sp^2$ -carbon clusters exhibit PL due to recombination of electron-hole pairs acting as luminescence centers (Robertson 1996).

Yu *et al.* investigated the temperature dependent luminescence of C-dots from 77 K to 300 K (Yu *et al.* 2012). The authors observed asymmetric peaks in the luminescence spectra at each temperature, which they attributed to a superposition of two different sources of luminescence. One emission band originates from the C-dot core and another band is caused by emission from the particle surface. The individual emission bands (I and II) were fitted with two gaussian functions, resulting in a low and a high energy band peak. Furthermore, the authors demonstrated that C-dots show rather weak electron-phonon scattering, as there is only a very small red-shift of the band gap for increasing temperatures. Since band I and II are virtually temperature independent, mostly electron-electron scattering processes dominate the luminescence mechanism.

Other groups directed their research on the influence of surface states on C-dot luminescence (Ding *et al.* 2013). As such, C-dots were examined in different oxidation

states. Zheng *et al.* used C-dots prepared from soot which were oxidized with nitric acid before spectral characterization. Then these C-dots were treated with the reducing agent  $\text{NaBH}_4$  to bring all surface moieties to their reduced state. The spectroscopic properties of both particle types were compared to each other (Zheng *et al.* 2011). While the original C-dots showed only weak PL at a wavelength of 520 nm with a quantum yield of 6%, the reduced C-dots emitted at 440 nm with a drastically increased quantum yield of about 60%. The  $\text{NaBH}_4$ -based reduction process was found to be reversible by oxidation. Switching between reduced and oxidized states has been repeatedly performed in several cycles. The authors attribute the increase in quantum yield found for the reduced species to the increase of hydroxyl groups on the surface of the C-dots, since hydroxyl groups act as electron donors. Moreover, the emission of green luminescence is associated with the existence of surface energy traps (Sun *et al.* 2006), while blue emission arises from so-called *zig-zag sites* on the reduced C-dots (Pan *et al.* 2010a; Pan *et al.* 2010b). *Zig-zag* pathways along the C-C-bond-skeleton that go *zig-zag* (“ $\lambda$ ”) in comparison to others that describe an armchair shape (“ $\_/\_$ ”). It is noteworthy that the enhancement of PL through chemical reduction is not a unique phenomenon for one individual C-dot preparation, but it has also been reported for other preparation methods as well (Shen *et al.* 2012b; Zhu *et al.* 2013a).

The oxidation state of C-dots is not only tuned by chemical reduction, but also by electrochemical means. Bao *et al.* exfoliated C-dots from carbon fibers applying different potentials resulting in C-dots with potential-dependent spectroscopic properties (Bao *et al.* 2011). The higher the applied potential the higher is the oxidation state of the resulting C-dots and the more red-shifted is the emission peak. The authors attributed their observation to a change in the distribution of oxygen-containing emissive sites on the surface. Very similar observations were made by Long *et al.*, who used carbon paste electrodes for the electrochemical fabrication of C-dots (Long *et al.* 2012). They were able to control the C-dot surface to either show spectral red shifting of their luminescence or not.

Recently, a thorough investigation on the photophysical processes of single C-dots has been reported in literature (Ghosh *et al.* 2014), there the authors showed that PL from C-dots originates from surface emission sites. These involve a strong coupling between the electronic transition and collective vibrational modes of the lattice structure. Whereas the PL properties of individual C-dots resemble those of organic dye molecules, the temporal and spectral dispersion of their PL reflects the complex nature of the local chemical environment around each PL center. However, C-dots resemble a class of differently prepared carbon nanoparticles. As such, different mechanism could be possible among the nanomaterials.

## *Introduction*

Although many aspects of the C-dot PL have been worked out, the mechanism is still not fully understood. It may arise from a combination of emissive traps, excitons of carbon, quantum-confinement effects, free zig-zag sites, edge defects and/or aromatic/oxygen containing functional groups. A full understanding of the photophysical mechanisms is still in its infancy and requires further research endeavors (Song *et al.* 2012).

### Carbon Dots as Tools in Bioanalytics

Luminescent nanoparticles, like for instance Q-dots, have found widespread and multiple different applications in modern bioanalytics and they helped to solve several experimental challenges. Q-dots have been used in several ways as a label in optical imaging *in vitro* and *in vivo* due to their unique spectroscopic properties (Jaiswal *et al.* 2004). However, Q-dots often contain toxic heavy metals that may leach out from the particle and moreover Q-dots have been recognized as being phototoxic (Cho *et al.* 2007). C-dots by contrast are an entirely organic material with no heavy metals involved but they share very similar optical properties with Q-dots such as general photoluminescence, high photostability and upconversion photoluminescence (through NIR excitation). In addition to that C-dots have several advantages: non-blinking luminescence, absence of heavy metals and high water-dispersibility (da Silva *et al.* 2011). Considering all those properties C-dots are obviously very promising candidates to be used as labels in optical imaging. The next paragraphs provide an overview of the biocompatibility of C-dots and the application of them as contrast agent in optical microscopy.

### Cytotoxicity

In order to use C-dots as a label for live-cell imaging *in vitro* or as tracer in living organisms during *in vivo* imaging, these particles need to be inert and biocompatible with no significant cytotoxicity. Even though C-dots mostly consist of the non-toxic element carbon, their surface is decorated with a complex mixture of functional groups arising from oxidation or passivation processes. Thus, biocompatibility of C-dots has become an important issue and it has been addressed very prominently.

As C-dot preparations and the individual experimental conditions differ widely the resulting particles are most likely not perfectly alike with respect to their physicochemical properties and also with respect to their biocompatibility / cytotoxicity. So it is no surprise that many groups have studied C-dot cytotoxicity. Amino-functionalized C-dots prepared through hydrothermal treatment of chitosan (Yang *et al.* 2012) were tested for their cytotoxicity using *A549 human lung adenocarcinoma* cells and the well-established MTT-assay (Mosmann 1983). MTT assays read the metabolic activity of living cells and are therefore well suited to indicate any cytotoxic effect. The authors concluded from their experiments that C-dots can be categorized as a material with low cytotoxicity. However, this study was confined to concentrations smaller or equal 200 µg/mL, which is low compared to other

reports. Similar observations were made by Liu *et al.* who incubated human liver carcinoma cells (*Hep-G2*) with passivated C-dots from microwave heating of glycerol and TTDDA (Liu *et al.* 2011a). MTT assays revealed cell viability of about 100 % for concentrations below 240  $\mu\text{g}/\text{mL}$ . Higher concentrations of C-dots, however, induced a significant cytotoxic response.

By contrast, Hsu *et al.* prepared C-dots through calcination of coffee ground and evaluated the impact of these particles on the viability of pig kidney cells (*LLC-PK1*) for concentrations between 0 and 2.4  $\text{mg}/\text{mL}$  (Hsu *et al.* 2012b). The authors reported about uncompromised cell viability (> 95%) as long as C-dots concentrations were below 1.8  $\text{mg}/\text{mL}$  which renders them more biocompatible than Q-dots which get toxic beyond 100  $\mu\text{g}/\text{mL}$  (Rosenthal *et al.* 2011). Other C-dots like those exfoliated from graphite electrodes were shown to be non-toxic up to concentrations of 400  $\mu\text{g}/\text{mL}$  for human kidney cells (*293T*) (Zhao *et al.* 2008) and a similar threshold concentration was reported for C-dots from citric acid and ethylene diamine (hydrothermally) (Zhu *et al.* 2013a). Yang *et al.* (Yang *et al.* 2009) performed a comprehensive analysis of C-dot cytotoxicity and concluded that C-dots are nontoxic in concentrations up to 100  $\mu\text{g}/\text{mL}$  and may be used as high-performance fluorescence imaging agents. In their study human breast cancer cells (*MFC-7*) and human colorectal adenocarcinoma cells (*HT-29*) were incubated with PEG<sub>1500N</sub>-passivated C-dots from laser ablation (Sun *et al.* 2006). The cellular response was evaluated in terms of proliferation, mortality and viability via MTT-assay. As a control the authors treated the same cells with PEG-molecules alone under otherwise identical conditions. The results suggest that cell physiology is barely affected by C-dots in comparison to the PEG molecules alone. The toxic effect at high concentrations arises from the passivation agent itself which is known to induce cell fusion above certain threshold concentrations. As live cell imaging works well with lower concentrations of C-dots and requires significantly shorter exposure times, C-dots were considered as non-toxic for those applications, especially in comparison to Q-Dots. Similar studies with Q-Dots revealed a decrease in cell viability of about 25 % for human epidermal keratinocytes after exposure to PEG passivated CdSe/CdS Q-Dots (10 nM) for 24 h (Zhang *et al.* 2008). For comparison, viability of cells derived from the proximal tubules of a porcine kidney was compromised by 50% after a similar exposure to PEG passivated CdSe/ZnS Q-Dots (Stern *et al.* 2008).

In conclusion, it is difficult to make a general statement about the cytotoxicity of C-dots for multiple reasons: (i) the term 'C-dots' defines a rather broad class of materials with very different individual particles dependent on the starting materials and the preparation process. Polymer-passivated C-dots may be almost inert, while C-dots produced by oxidation processes have rather complex surfaces which may induce toxic effects or not dependent on the individual surface composition. (ii) Cytotoxicity studies have been performed with a wide variety of different cell lines. Some of these cell lines are less

## Introduction

sensitive and tolerate more xenobiotic impact than others. Accordingly, a general judgment on C-dot cytotoxicity requires an endless number of studies pairing all the different C-dots with all kinds of different cell lines. C-dots share this problem with all other nanomaterials that are considered for biomedical applications. (iii) Cytotoxicity studies using higher concentrations of C-dots may be affected by low molecular weight pyrolysis products that are difficult to separate from freshly prepared C-dots. It is almost impossible to rule out that these contaminants are inherently included in C-dot suspensions.

But the most severe cytotoxic effects have been observed for concentrations higher than required for biomedical imaging applications. Thus, C-dots can be considered as useful tools for labeling cells in live cell imaging or as tracers for *in vivo* studies. At the appropriate concentration they don't seem to be significantly more harmful to cells than regular organic fluorophores and fluorescent probes but they are less invasive and of better biocompatibility than Q-dots.

### Live Cell Imaging

Since C-dots show a unique photoluminescence, outstanding photostability and yet uncontested biocompatibility, they have been used as labels and probes in live cell imaging applications. The first approach in this respect was reported in 2006 by Sun et al. (Sun et al. 2006). The authors incubated *Escherichia Coli* ATCC 25922 bacteria with PEG<sub>1500N</sub>-passivated C-dots by adding the particles to the bacteria suspension. After 18 h of incubation the suspension was centrifuged, the bacteria got washed and re-suspended before they were examined by confocal laser scanning microscopy (CLSM). Similarly mammalian cells (*Caco-2*) were incubated with PPEI-EI-coated C-dots by adding the particles to the culture medium. After 1.5 h the cells were washed with phosphate buffered saline (PBS) and examined via CLSM. The labeling of both, bacteria and human cells, was clearly visible and attributed to the incorporation of the particles into the cytoplasm. Remarkably, the nuclei of most human *Caco-2* cells remained dark, indicating that C-dots may not be able to enter the nucleus. Likewise, Liu et al. incubated *E. coli* bacteria and *Murine P19 progenitor* cells with their C-dots that were prepared through carbonization of resols. The authors reported about similar observations as described above with respect to uptake and distribution of C-dots in prokaryotic and eukaryotic cells (Liu et al. 2009).

C-dots prepared according to the same procedure of laser ablation and passivation via PPEI-EI have also been described and tested as multiphoton luminophores for live cell imaging (Cao et al. 2007). The authors incubated MCF-7 cells with the particles for 2 h at 37 °C and examined the cells under two-photon excitation with a femtosecond laser pulse at 800 nm. Under these conditions the cells exhibited bright green luminescence in their cytoplasm with almost completely dark nuclei. In contrast, Ray et al. observed a homogeneous staining of the whole cell when Ehrlich ascites carcinoma cells (*EAC*) were exposed to C-dots from carbon soot (Ray et al. 2009).

Moreover, the uptake mechanism for C-dots into the cytoplasm of mammalian cells has been addressed. Here, cells were incubated with C-dots at 37 °C and 4 °C, respectively. All other experimental parameters except temperature were kept constant. Upon cooling the cells to 4 °C endocytosis-mediated particle uptake is disabled. Accordingly the authors did not observe any significant luminescence inside the cells indicating that endocytosis is the most-likely mechanism for the internalization of C-dots into cells.

With new preparation methods for C-dots coming up providing similar but not identical particles, several different unique species were analyzed with respect to their potential as a contrast agent for live cell imaging. Zhu et al. prepared C-dots hydrothermally from graphene oxide and dispersed this material in cell culture medium for uptake experiments (Zhu et al. 2011). Internalized C-dots showed bright green luminescence upon laser excitation at 405 and 488 nm from inside the cytoplasm of human bone osteosarcoma cells (*MG-63*). However, the authors also reported about a different, more complex uptake

## Introduction

mechanism when a murine pre-osteoblast cell line (*MC3T3*) was used in such uptake experiments.

To gain further insight into the question whether or not C-dots are taken up by endocytosis HeLa cells were incubated with C-dots in presence of several different molecular inhibitors of endocytosis. Since endocytosis is an energy-dependent cellular activity, low temperatures (Verma *et al.* 2008) and  $\text{NaN}_3$  (Schmid *et al.* 1990) are known to suppress this process. Moreover, it is well-known that the addition of sucrose or Methyl- $\beta$ -cyclodextrin (M $\beta$ CD) inhibit clathrin-mediated or caveolae-mediated endocytosis, respectively (Anderson 1998). However, analysis of intracellular fluorescence intensity after C-dot exposure in presence of the various inhibitors did not show any significant difference indicating that endocytosis may not be involved.

Taken together, there are conflicting results regarding the uptake mechanism of C-dots into adherent mammalian cells. The same is true for other nanomaterials as well whose uptake route has not been identified unequivocally (Geiser *et al.* 2005; Lajoie *et al.* 2007; Verma *et al.* 2008). Since C-dots are extremely small, a non membrane-mediated, passive diffusion of the particles across the membrane along their concentration gradient is not entirely ruled out but awaits further experimental support.

The distribution of C-dots after internalization *in vitro* has been extensively studied by Li *et al.* (Li *et al.* 2012b): human cervical carcinoma cells (*HeLa*) were incubated with C-dots and the luminescence distribution inside the cells was analyzed. According to these experiments the C-dots were primarily entrapped in endosomes, multivesicular bodies, and lysosomes with aggregation at the perinuclear region, which usually results from nanoparticle endocytosis. Such an intracellular distribution across different organelles might explain the inhomogeneous C-dot luminescence intensity observed in fluorescence micrographs with local intensity maxima. In a follow-up experiment HeLa cells were incubated with C-dots and the lysosomes/endosomes, golgi apparatus, mitochondria and endoplasmic reticulum were counterstained with specific, fluorescent organelle-markers. Merging the fluorescence images of both, the C-dots and the organelle-specific dyes provided a more precise intracellular localization of the particles. Besides diffuse distribution across the cells a significant fraction of the internalized particles has been localized to the lysosomes/endosome compartment. However, C-dot luminescence was mostly not exclusively in one organelle just preferentially. An exception from this was recently reported for C-dots through carbonization of PEG in presence of sodium hydroxide. These preferably stained the nuclei of HeLa cells, with particular binding to the nucleoli (Kong *et al.* 2014).

Although the internalization of C-dots is not completely understood, the particles can certainly be used for imaging applications and replace existing labels whenever they perform better. Fang *et al.* compared the photostability of C-dots with that of CdTe Q-Dots,



fluorescein isothiocyanate (FITC) and *Hoechst 33342* inside human embryonic kidney cells (*HEK 293*) (Fang *et al.* 2012). After 25 min of continuous observation in the fluorescence microscope (CLSM), the C-dot-label inside the cells was still detectable whereas the luminescence of the reference materials was not. Thus, C-dots obviously provide a significantly improved photostability compared to well-established fluorescence labels. Another interesting feature and added-value of C-dots is their multicolor emission which is dependent on the details of the experimental procedures (Liu *et al.* 2009; Liu *et al.* 2011a; Puvvada *et al.* 2012; Xu *et al.* 2013; Zhu *et al.* 2013a). For instance, Liu *et al.* incubated *Hep-G2* cells with TTDDA-passivated C-dots (0.1 mg/mL) for 24 h and examined the cells via CLSM afterwards (Liu *et al.* 2011a). The cells showed blue, green and red luminescence upon laser excitation at 405, 488 or 543 nm, respectively.

### Surface Modification

As the surface of C-dots is decorated by a variety of functional groups that arise from the oxidation or passivation steps during synthesis, these functional groups have been used as anchors to attach C-dots to biomolecules or indicator dyes. The whole set of established bioconjugation techniques can be used to couple and functionalize C-dots with other molecules such as N-hydroxysuccinimid (NHS) or 1-ethyl-3-(3-dimethyl-aminopropyl)-carbodiimid (EDC) chemistry. Biofunctionalization of C-dots may enable the particles (i) to report on the concentration of intracellular analytes when coupled to indicators, (ii) to be targeted preferentially to predefined intracellular structures when coupled to recognition sequences or (iii) to label individual cell types by interaction with their unique cell surface receptors when coupled to the corresponding ligands. Several examples for bioanalytical applications of C-dots that are based on a preceding biofunctionalization of their surface have been described already. Selected examples are highlighted below.

One of the first modifications of C-dots to comply with a given bioanalytical strategy has been reported by Li *et al.* in 2010 (Li *et al.* 2010b). PEG-passivated C-dots with amino termini were conjugated to *Transferrin* via EDC chemistry to specifically target cancer cells. *Transferrin* is a serum glycoprotein that is internalized by receptor-mediated endocytosis using the *Transferrin* receptor. The *Transferrin* receptor is commonly overexpressed by cancer cells so that it may serve as a label to preferentially address cancer cells but ignore non cancer cells (Qian *et al.* 2002). According to this study *Transferrin*-conjugated C-dots showed a significantly stronger internalization into HeLa cells than non-conjugated C-dots within identical exposure times. Moreover, the authors demonstrated that the uptake was mediated by *Transferrin* receptors, since HeLa cells pre-saturated with *Transferrin* did not show any internalization of C-dots. A similar targeting strategy for cancer cells was pursued by Song *et al.* who conjugated C-dots with folic acid (FA) (Song *et al.* 2012). The C-dots themselves were prepared via microwave treatment of an aqueous solution of glucose and TTDDA. Conjugation of FA with amino groups present on the C-dot surface

## Introduction

was achieved using NHS chemistry. Folic acid conjugated C-dots were used to distinguish between normal and cancer cells, based on the overexpression of folate receptors on the surface of cancer cells. In a proof-of-concept study a mixture of human cervical carcinoma cells (*HeLa*) and non-transformed mouse fibroblasts (*NIH-3T3*) was incubated with the FA-conjugated C-dots. Luminescence and thus, internalization of C-dots was only observed for the cancerous *HeLa* cells. Receptor-mediated endocytosis was confirmed as the primary uptake mechanism by pre-saturation of the *HeLa* folate receptors with free FA. These particular samples showed no luminescence inside the cells after incubation with FA-conjugated C-dots.

Other C-dot surface modifications were aiming for the detection of analytes inside living cells. One of them uses modified C-dots for a ratiometric measurement of the intracellular pH (Shi *et al.* 2012). Here C-dots were prepared from citric acid and TTDDA. The particles were then conjugated to the pH-sensitive fluorescein-isothiocyanate (FITC) and the pH-insensitive reference dye rhodamine B isothiocyanate (RBITC). The pH-sensitive C-dot-probe was used to quantify the intracellular pH of *HeLa* cells, while the latter was modulated by the  $H^+/K^+$  ionophore *nigericin*. Nigericin integrates into the plasma membrane and makes it permeable for protons such that the cytosol equilibrates with the pH of the extracellular medium (Tafari *et al.* 2002). The intensity of the green luminescence (FITC channel) increases with pH, while the intensity of the red luminescence (RBITC channel) remains roughly unaffected. The ratio of those two fluorescence intensities allows generation of a calibration curve for the intracellular pH value. Applying this calibration allows measuring the intracellular pH of *HeLa* cells that was determined to be  $7.4 \pm 0.2$ . The intracellular pH value of MCF-7 cells was found to be  $7.2 \pm 0.2$ . Both pH-values agree favorably with the results recorded with a commercially available pH probe (SNARF-1).

Zhu *et al.* used a dual emission nanohybrid of C-dots and Q-dots in order to image the concentration of copper ions (Zhu *et al.* 2012). These ratiometric nanohybrid probes consist of silica coated CdSe Q-dots that are conjugated with C-dots. While the C-dot fluorescence is quenched by copper ions, the Q-dot emission is inert and serves as reference. The probe was successfully applied for the imaging of  $Cu^{2+}$  concentrations in *HeLa* cells. After exposing the cells to exogenous copper by adding  $Cu^{2+}$ -ions to the culture medium, the fluorescence emission of the probe turned from green-yellow to red.

Yu *et al.* developed a ratiometric probe for hydrogen sulfide ( $H_2S$ ) through modification of C-dots for a *Förster resonance energy transfer* (FRET) based readout (Yu *et al.* 2013). The  $H_2S$  sensor is based on a naphthalimide-azide which was covalently attached to the surface of amino-terminated C-dots via EDC chemistry. In the absence of  $H_2S$  the C-dots emit blue light at 425 nm. The presence of  $H_2S$  leads to reduction of the azide, inducing a FRET from the C-dots' emissive states to the naphthalimide and the emission shifts from

blue to green at 526 nm. The C-dot-based probe was successfully applied to detect H<sub>2</sub>S in living cells, namely *HeLa* and murine aneuploid fibrosarcoma cells (L929). As a proof-of-concept H<sub>2</sub>S was added to the culture medium and the luminescence inside the cells shifted from blue to green.

C-dots have also been shown to assist the delivery of extracellular substances across the plasma membrane into adherent cells. Liu et al. reported about polyethylene-imine (PEI)-passivated C-dots for imaging and as nano-carriers for gene delivery (Liu *et al.* 2012a). Due to their PEI-coating these C-dots have a highly positive surface charge, which enables electrostatic interactions between the C-dots and DNA. These C-dot-DNA-complexes were used for plasmid transfection into COS-7 cells and Hep-G2 cells. The subsequent expression of the reporter gene encoded on the plasmid was similar compared to the transfection of the same plasmid with PEI25k. As an added value the carrier C-dots were used for optical imaging of the transfected cells. The C-dots emit blue, green and red luminescence upon laser excitation at 405, 488 or 543 nm, respectively. In this study the C-dots were found to be predominantly localized in endosomes without entering the nucleus.

Another set of C-dot-based drug delivery experiments was conducted by Lai et al. using C-dots incorporated inside mesoporous silica particles (C-dots@mSiO<sub>2</sub>) (Lai *et al.* 2012). These nano-composites were prepared via the calcination of glycerol inside mSiO<sub>2</sub>-particles. The resulting C-dots@mSiO<sub>2</sub> were subsequently passivated by PEG and loaded with the anti-cancer drug *doxorubicin*. Exposing *HeLa* cells to these particles revealed that the particle-mediated incubation was more toxic for the cancer cells than incubation with free *doxorubicin*, indicating a delivery into the cells. Moreover, the blue emission of the C-dots inside the mesoporous silica particles together with the red emission of doxorubicin provided the opportunity to track the drug release from the particles inside the cells.

In conclusion, existing studies have identified that C-dots have a considerable potential as a flexible and versatile contrast agent in live cell imaging. As their surfaces are accessible for established bioconjugation chemistry they can be easily modified, tailored and customized for specific bioanalytical applications. Even though C-dot research is still in its infancy, these particles have the potential to become a standard fluorescence label for bio assays, maybe even replacing Q-dots in selected applications. However, C-dots are commonly not as bright as their inorganic counterparts so that laser-based excitation is required. So it is obvious that a wider use of C-dots as a contrast agent in microscopic imaging requires improvements in specific molar absorption and quantum yield.

### Summary: Carbon Dots

In summary, chances that C-dots will evolve into a routine and widely accepted tool for imaging biological specimens are promising and justified based on the existing literature. The preparation of the particles C-dots is straightforward and performed under simplest experimental conditions. Low-cost and sustainable mass materials like, for instance carbohydrates, have been successfully used as precursor material. Processing of precursors and raw materials does not require any sophisticated and expensive instrumentation. The key step of C-dot preparation is a simple carbonization procedure. The resulting nanoparticles are highly stable, between 1 and 10 nm in diameter and do not contain any heavy metals like Q-Dots.

C-dots feature astonishing optical properties like an extremely broad range of suitable excitation wavelengths from ultraviolet light (UV) to visible (VIS) and further on to the near infrared (NIR). In particular, NIR is of predominant interest as excitation source for *in vivo* imaging because of its improved tissue penetration and reduced tissue auto-fluorescence. The emissive properties of C-dots can be tuned and customized for a given application. Electrochemoluminescence (ECL), based on potential-dependent changes of the emissive sites on the particles' surfaces, paves the way for using C-dots as reporters in redox assays and sensors.

The interaction of C-dots with living cells has been intensively studied throughout the last years. It has been found that C-dots are easily internalized into the cell interior. The exposure time required for C-dot uptake tends to be shorter than for other nanomaterials. The ease by C-dots to enter the cell interior makes them interesting base materials for intracellular probes after surface functionalization. Even though the uptake process has been attributed mechanistically to classical endocytosis, the full explanation seems to be more complex with other mechanisms involved. The existing cytotoxicity studies for carbon dots need to be handled with care and a good sense of proportion, as C-dots are often prematurely described as *low-toxic* imaging reagents. As long as they are applied in reasonably low concentrations that are, however, sufficient for *in vitro* and *in vivo* imaging, the material is indeed harmless. But cell viability was shown to be affected for concentrations much higher than needed for bioassays. When C-dots were tested for their suitability as contrast agent for *in vivo* imaging, they showed similar imaging characteristics compared to the well-established Q-dots with no significant evidence of toxicity. As the number of studies using C-dots as tracers in living organisms is still low, their broad application in this respect awaits further characterization. Taken together, the long-range prognosis for C-dots to become a standardized label and fluorescence marker in biomedical assays and similar applications are euphoric and optimistic.

### Graphene Quantum Dots

Since C-dots came into focus of research during the last years, their terminology is often inconsistent and mixed up with other nanomaterials. Usually, this involves confusion between C-dots and graphene quantum dots (GQDs). However, it should be noted that both are structural different materials derived from unequal precursors. While C-dots exhibit a non-defined chemical structure and may be prepared from various starting materials, GQDs resemble the plane aromatic structures of its precursors. Commonly, GQDs are top-down prepared from graphene and graphene oxide or from polycyclic aromatic hydrocarbon derivatives in bottom-up approaches (Pan *et al.* 2010b; Liu *et al.* 2011b). As such, GQDs are described to consist of one or few layers of small graphene-like fragments.

Concerning the inconsistencies, Song *et al.* made first attempts for a clear classification of the different carbon nanomaterials (Song *et al.* 2014). They designated GQDs as carbon nanoparticles with only very few graphitic layers. In contrast to this, C-dots exhibit a different crystal lattice. Bacon *et al.* stated that GQDs exclusively may be prepared from bulk graphene-based materials under harsh conditions or well defined from via organic synthesis from polycyclic aromatic compounds, as mentioned before (Bacon *et al.* 2014).

However, both, C-dots and GQDs, have in common that they are water-dispersible due to oxidized surfaces or passivation with hydrophilic polymers. Furthermore, both show a comparable emission behavior, being highly variable in photo-excitation. This results in the emission of light from different electronic sites of the particles depending on the wavelength of the excitation source (Li *et al.* 2013).

It can be expected that C-dots and GQDs are two kinds of unique carbon nanomaterial classes, because of their structural differences. Despite very similar luminescence properties, both materials may differ widely in other characteristics. Especially concerning the interaction with living cells. According to this, further research should include working out those differences.



## 2 Objectives

The synthesis of C-dots of bright luminescence has attracted lots of research in the last years. At present stage N-doped C-dots from amino acids and starch turned out to show highest quantum yields. Only little has been reported on a detailed characterization of the obtained material. Furthermore, it was shown that C-dots in principle may be useful as a contrast agent in live cell imaging agent under physiological conditions.

Based on this, the particles were meant to be characterized thoroughly for their physicochemical properties in terms of morphology and functionalization. Particular focus should be paid on the investigation of their spectroscopic characteristics, since these properties will be essential in multicolor cell imaging. Thus, the influence of the doping of C-dots with nitrogen should be addressed and the reason for the multicolor emission of the particles which enable multicolor imaging should be investigated. Furthermore, the characteristics of the C-dots had to be compared against those for GQDs from graphene oxide as precursor. Since both particle types are closely related and often mixed in up in literature, it was the aim of this work to clearly distinguish between these two classes of nanomaterials.

The influence of the C-dots on mammalian cells was to be characterized, since most of the particles' applications were suggested to be on living cells. Besides cytotoxicity and biocompatibility of the particles, distinct effects on cell behavior (adhesion, proliferation and migration) should be investigated. As the C-dots prepared in this work represent a novel nanomaterial with unique properties, the uptake process into mammalian cells and the ability of C-dots to pass biological barriers such as cell layers were meant to be studied. Possible advantages of the C-dots compared to established particles in terms of cellular uptake, translocation and stability should be worked out.

Additionally, the principle of the multicolor imaging of cell samples labeled with C-dots had to be investigated to recognize the full potential of the material for bioanalytical applications. Selective staining of tissue models, living cells and their compartments by C-dots should be studied and performed. Furthermore, modifications and encapsulations of the material should be worked out in principle for possible bioanalytical applications. Moreover, the C-dots additionally had to be examined for their suitability as actuator particle. Possible photochemical reactivity of the material should be studied in order to check the particles' usefulness as sensitizer in photodynamic therapy.

## Objectives

An overview on the main objectives of this work on C-dots is illustrated in Fig. 2.1. Thereby, a thorough investigation on the material characteristics is meant to be the base for further studies on biocompatibility and interaction with mammalian cells. The knowledge on the material and its interaction with mammalian cells shall peak in the application of C-dots in multicolor imaging, bioanalytical assays and theranostics.

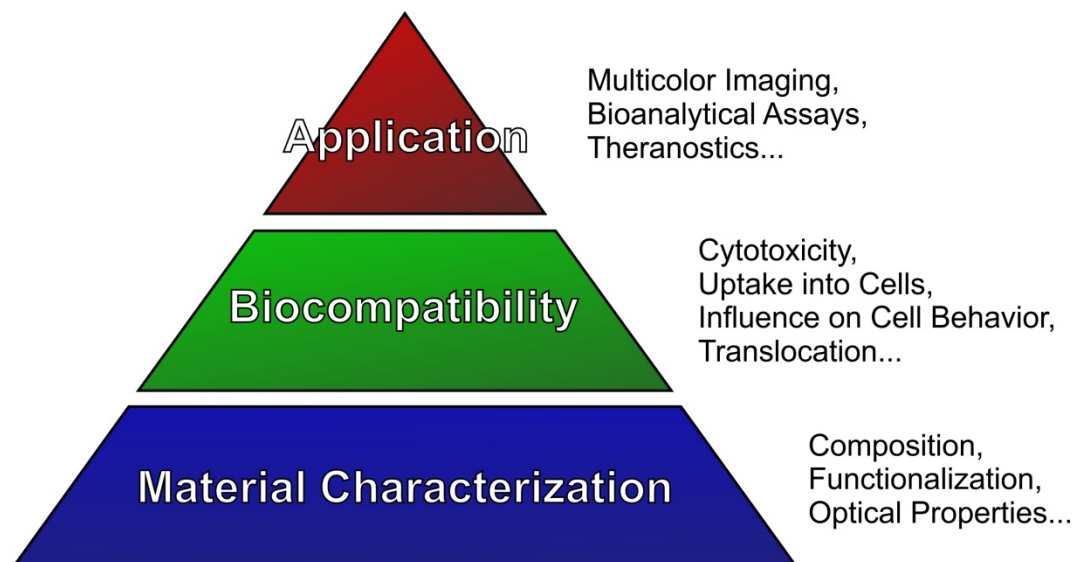


**Fig. 2.1:** Overview on the main objectives of this work on C-dots.

All together, fundamental characteristics of C-dots shall be studied in this work, setting this novel nanomaterial into the right light and leading to a better understanding of these particles' nature. Applications relying on the C-dots' unique properties should be developed, including a critical discussion of any limit of applicability.



## 3 Materials and Methods

### 3.1 Preparation of Photoluminescent Carbon Nanomaterials

#### 3.1.1 Hydrothermal Carbonization of Molecular Precursors

Hydrothermal synthesis is a method well known for its application in inorganic chemistry since mid of the 19<sup>th</sup> century (Byrappa *et al.* 2013). In a typical application, substances are crystallized from high-temperature aqueous solutions under high vapor pressures (Rabenau 1985). While inorganic chemistry uses this method for crystallization processes and the preparation of oxidic nanomaterials for example, hydrothermal treatment may also be applied to organic matter (Patzke *et al.* 2002).

As such, over 100 years ago Friedrich Bergius first described the *hydrothermal carbonization* (HTC), turning biomass into a coal-like material (Bergius 1913). This takes place under the influence of water, high pressure and temperature, resembling the charcoal formation process. His work in this field and the enormous significance of the hydrothermal transformation of organic materials earned Bergius the Nobel Prize in 1931.

The HTC processes may be classified with respect to two major applications fields and different temperature regions (Hu *et al.* 2010). On the one hand, high-temperature HTC is performed between 300 and 800 °C. In this temperature region organic materials typically do show decomposition into reactive gas molecules and carbon fragments, enabling the preparation of graphitic or activated carbon materials (Fujino *et al.* 2002; Salvador *et al.* 2007). Furthermore, distinct carbon nanomaterials and –structures, such as carbon nanotubes, may be fabricated using high temperature HTC (Gogotsi *et al.* 2000). By contrast to this, low-temperature HTC processes are carried out below 300 °C. These milder conditions allow for the preparation of water dispersible functional carbon materials by hydrolysis, dehydration and polymerization reactions (Sevilla *et al.* 2009b). Thereby, differently sized carbon structures may be prepared ranging from several micrometers (*carbon microspheres*) to very few nanometers (*C-dots*), depending on reaction conditions and starting material (Ryu *et al.* 2010; Yang *et al.* 2011).

The hydrothermal process itself is typically carried out in pressure vessels, so called *autoclaves*, so that highly corrosive solvents can be used at high temperatures and pressures, (Byrappa *et al.* 2013). For all hydrothermal preparations in this work, a stainless-steel autoclave with an inner liner, consisting of Polytetrafluoroethylene (PTFE), was used. The PTFE liner had an inner volume of about 50 mL and could be sealed with a lid consisting of the same material. For the sealing of the autoclave with its metal lid, six

standard screws were used. Photographs of the single components of the autoclave and its assembled version are shown in Fig. 3.1.

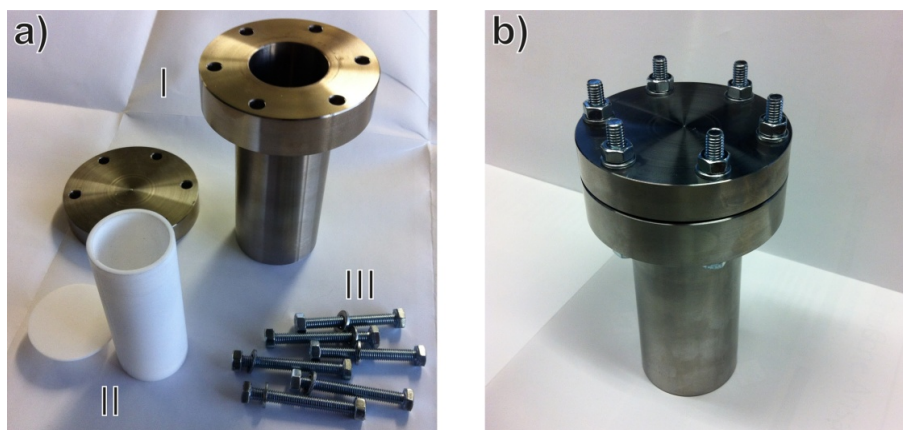


**Fig. 3.1:** a) Disassembled stainless-steel autoclave: I) Autoclave with lid, II) PTFE-liner (Inner volume ~ 50 mL) with sealing lid, III) Standard screws for fixation of the autoclave lid. b) Fully assembled autoclave.

For the hydrothermal preparation of C-dots, several precursor materials as carbon source were described in literature over the last years. Among them, complex materials have become very common for researchers to use in aqueous carbonization processes. These materials include: bamboo leaves (Liu *et al.* 2014a), egg (Wang *et al.* 2012a), gelatin (Liang *et al.* 2013), grass (Liu *et al.* 2012c), orange juice (Sahu *et al.* 2012), pomelo peel (Lu *et al.* 2012) and waste paper (Wei *et al.* 2014a), to name only a few examples. However, the preparation from these materials suffers the disadvantages of low reproducibility, as these materials may differ a lot in composition, depending on sampling and preparation. Furthermore, they do not allow for direct control over functionalization of the obtained carbon particles.

As such, pure molecular precursors are the carbon source of choice when it comes to highly controllable and reproducible hydrothermal C-dot preparations (Hsu *et al.* 2012a). These molecules should be easy to decarboxylate or dehydrate thermally, so that the formation of the carbon particles is enabled. Among those possible molecular precursors carbohydrates became a preferred carbon source in the preparation of C-dots (Peng *et al.* 2009; Wang *et al.* 2011; Kwon *et al.* 2012). These are considered as a sustainable, non-toxic and low-cost starting material. Furthermore, carbohydrates may be easily dehydrated thermally, resulting in more or less functionalized carbon nanoparticles, depending on the carbonization grade.

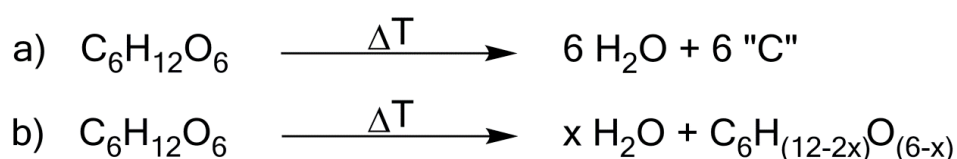


**Fig. 3.2:** Complete (a) and partial (b) dehydration reaction of carbohydrates.

As shown in Fig. 3.2, a complete dehydration of carbohydrates would lead to particles of pure carbon. Practically, in HTC processes a partial dehydration of the starting material is more likely (Fig. 3.2 b). Thereby, highly hydrophilic carbon-rich particles are formed. These are often described to consist of a hydrophobic carbon-rich core and a hydrophilic shell, decorated with several oxygen-containing groups (Sevilla *et al.* 2009a).

For the preparations of the C-dots mainly starch (from potato) was used as carbon source (Yan *et al.* 2015). A schematic of a possible mechanism of the formation of C-dots from starch is shown in Fig. 3.4 which was adapted from literature (Sevilla *et al.* 2009b; Ryu *et al.* 2010). During the hydrothermal treatment the polysaccharide is meant to undergo fragmentation and hydrolysis, partly to its monomer glucose. Further decomposition and dehydration may yield in reactive intermediates, such as several organic acids, aldehydes, furfural derivatives (5-hydroxymethylfurfural, furfural, 5-methylfurfural) and benzene/phenol derivatives (Luijckx *et al.* 1995; Kabyemela *et al.* 1999). These are assumed to serve as building blocks in polymerization/condensation or intermolecular dehydration reactions, forming aromatic systems and finally leading to particle formation.

The hydrolysis and dehydration reactions of carbohydrates may be catalyzed by acids or bases (Jin *et al.* 2011). Thus, hydrochloric and phosphoric acid or sodium hydroxide solutions are often used for the catalysis of C-dot formations from carbohydrates (He *et al.* 2011). However, these additives have the disadvantage of providing extreme pH-regions and high salt contents of the resulting suspensions. For the applications on living cells these suspensions have to be purified, which is difficult due to the small size of the particles. Furthermore, strong acids or bases do not allow to tune the dehydration grade very precisely, as dehydration efficiency is too good. To overcome those deficits, amino acids were chosen as catalysts for the dehydration of the carbohydrate starch (Du *et al.* 2014; Wei *et al.* 2014b), as shown in Fig. 3.3.

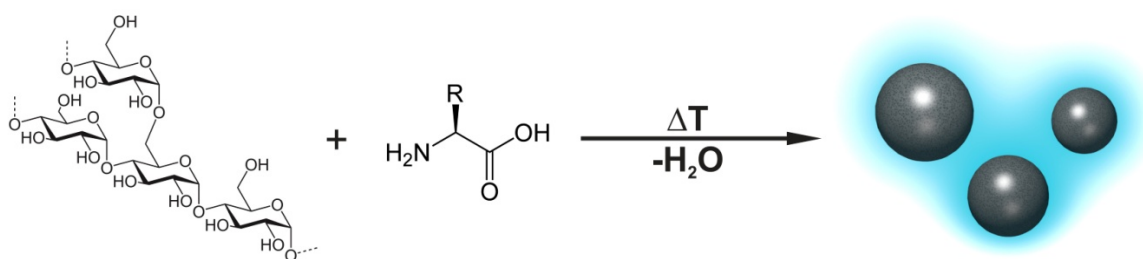


**Fig. 3.3:** Preparation scheme of C-dots (symbolized on the right) from starch and amino acids.

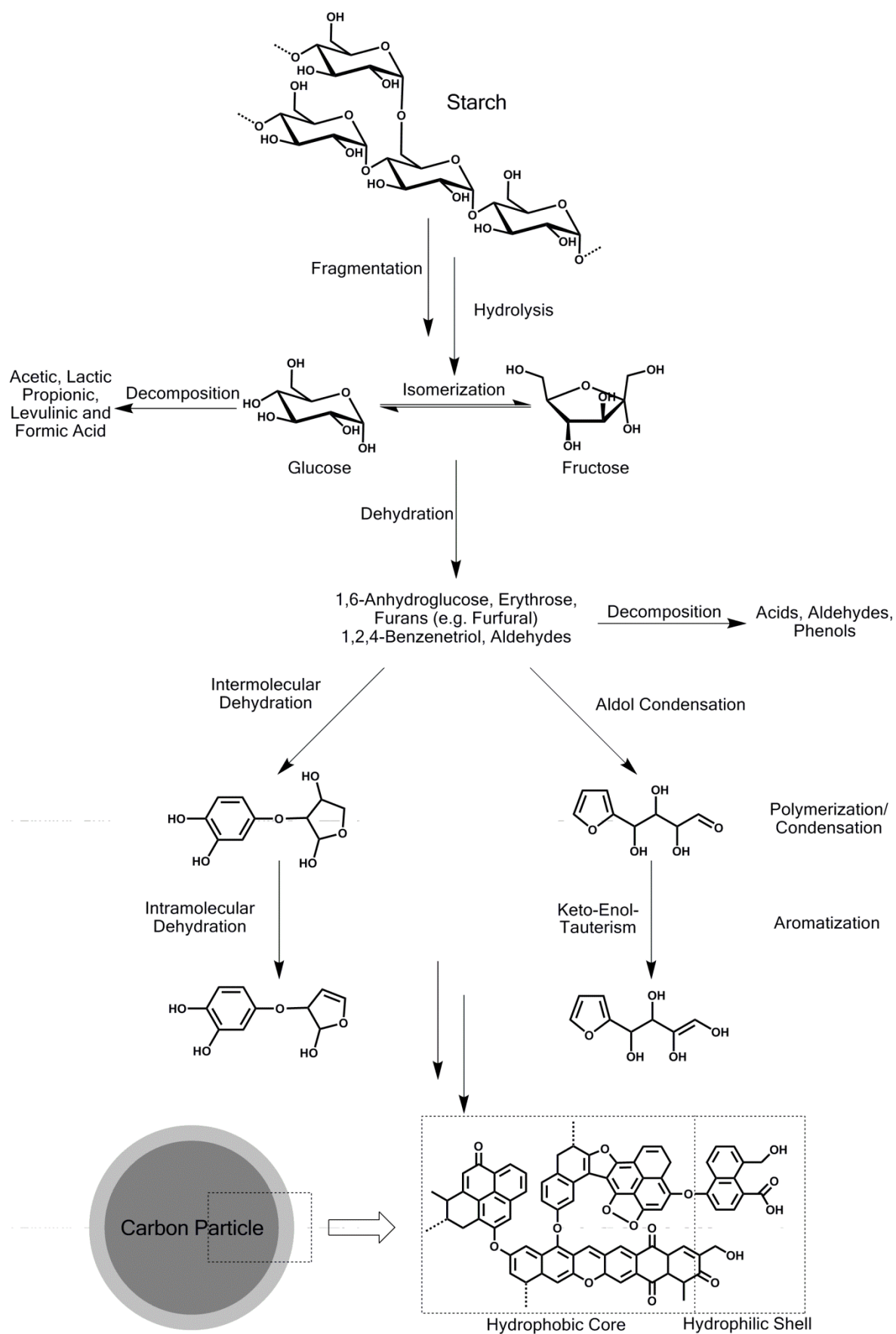


**Fig. 3.4:** Possible reaction scheme for the formation of carbon particles from starch, undergoing fragmentation, hydrolysis and dehydration. The resulting intermediates are supposed to polymerize or condensate and aromatize during particle formation (Sevilla *et al.* 2009b; Ryu *et al.* 2010).

Amino acids are biomolecules themselves. As such, residues of the additive in the resulting C-dot suspension are supposedly not harmful to living cells, compared to harsh reactive chemicals. Furthermore, they exhibit acidic and basic groups (due to carboxyl- and amino- functionalities) which are meant to catalyze the dehydration of starch. This happens under milder conditions than the treatment with strong acids or bases and therefore the carbonization grade may be easily tuned by adjustment of the reaction temperature or time. Additionally, using amino acids as additives allows for the doping of the particles with heteroatoms - in this case nitrogen. The doping of C-dots and GQDs with nitrogen was shown to influence the band-gap of the particles and as such changing their optical properties (Li *et al.* 2012c; Zhang *et al.* 2012; Wang *et al.* 2015a). In this work, the doping with nitrogen was used to achieve higher quantum yields for the particles' photoluminescence.

#### Carbon Dots from Starch and Amino Acids (N-doped C-dots)

Previous work in this field included the development and optimization of preparation protocols for C-dots from starch and amino acids. Here, the preparation was modified in terms of temperature, type and amount of the amino acid to enhance the photoluminescence of the particles. In an optimized preparation, 2.0 g starch from potato (Sigma Aldrich) and 1.71 mmol of the selected amino acid (for L-tryptophan, Trp, 350 mg, Sigma Aldrich) were suspended in 30 mL ultrapure water and transferred to a stainless steel autoclave with PTFE liner (~50 mL inner volume). The mixture was heated to 160 °C within about 1 h using a muffle furnace (Nabotherm: LT 15/3) and temperature was maintained for 12 h. After cooling to room temperature, the obtained raw brownish C-dot suspension was centrifuged 10 min with 2500 rcf to remove larger particles, aggregates and other contaminants which precipitate from the suspension. The supernatant was filtered through a 0.22 µm syringe filter with polyether sulfone (PES) membrane, resulting in a clear red-brownish suspension. Fig. 3.5 shows aqueous suspensions of the C-dots along the different preparation steps.

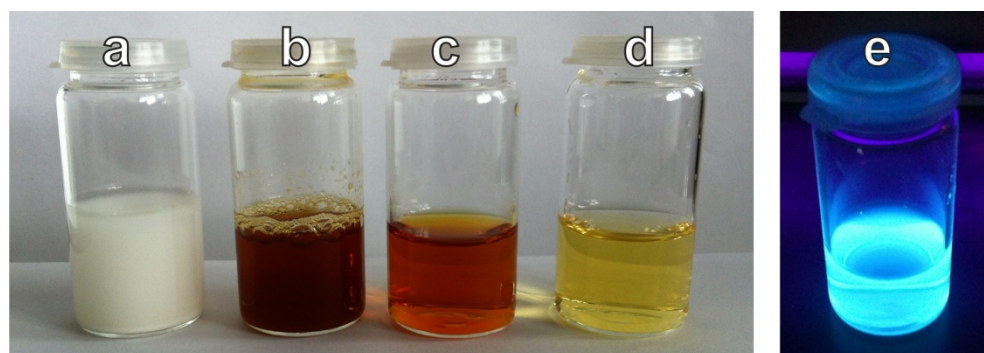


**Fig. 3.5:** Downstream processing of the C-dot preparation. a) Aqueous starch suspension, b) Raw C-dot suspension after carbonization, c) C-dot suspension after filtration, d) C-dot suspension after dilution to 1.0 mg/mL, e) diluted C-dot suspension under UV excitation in the dark (366 nm, 2x4 W).

## Materials and Methods

In order to prepare the particle suspension for the application on living cells, the C-dots had to be further purified. Therefore, size-exclusion chromatography (SEC) using a Sephadex® G-25 (fine, Sigma-Aldrich) column with ultrapure water as eluent was used to remove smaller molecular pyrolysis products. To monitor the progress of the elution, a UV-Lamp (366 nm; 2x4 W) was used to excite the fluorescent C-dots in the column, as shown in Fig. 3.6. The initially fluorescent fraction which eluted from the column was collected since the C-dots pass the column faster than smaller molecular pyrolysis products. Pictures of the purification process are shown in Fig. 3.6. The purified C-dot suspension was lyophilized and resuspended in phosphate buffered saline (PBS<sup>++</sup>) under a laminar air flow work bench to obtain an isotonic sterile C-dot suspension for cell treatment. Finally, the suspension was once more passed through a 0.22 µm syringe filter to remove aggregates from the lyophilization process and pathogenic germs.

The resulting mass concentration of the particle suspension was determined gravimetrically. Typically, 500 µL of the suspension were transferred into an aluminum pan. The water was evaporated, and the mass difference between the pan with the residue and its empty weight were used to calculate the suspensions mass concentration. The salt residue from PBS<sup>++</sup> was subtracted from the result.

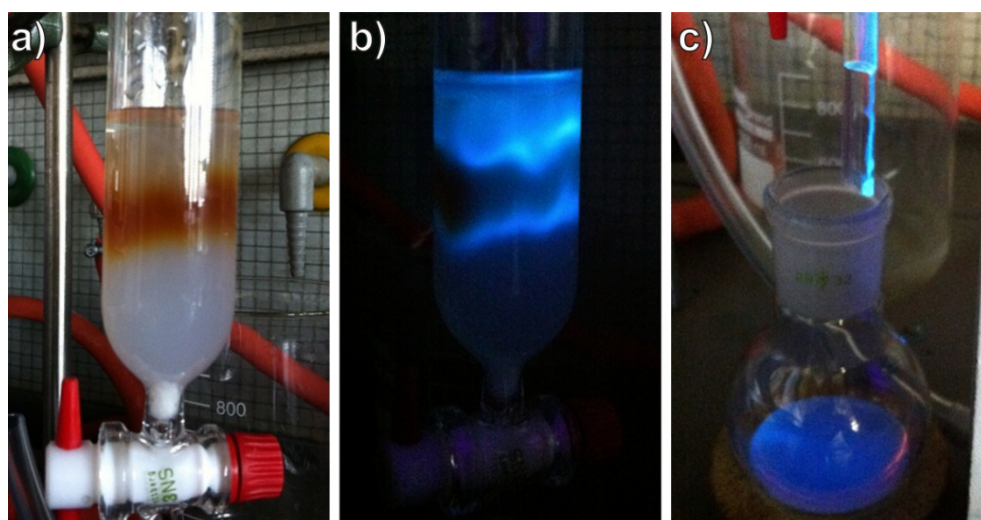


**Fig. 3.6:** a) Sephadex® G25 column loaded with C-dots prepared from starch and Trp, b) column under UV excitation, c) collection of the initial fluorescent fraction under UV excitation. For the excitation a standard UV lamp with 2x4 W at 366 nm was used.

In later chapters, all particles denoted as C-dots are referring to particles prepared via hydrothermal treatment of starch and Trp, if not denoted in a different way.

#### Carbon Dots from Starch (undoped C-dots)

For studying the influence of the nitrogen doping on the material and its optical properties, C-dots from pure starch were prepared. Therefore, the same protocol as mentioned before was used to prepare the particles, just without the addition of amino acids.

#### Carbon Dots from Citric Acid and Ethylenediamine

As reference material to the particles from starch and Trp in terms of cell imaging, a different hydrothermal preparation for C-dots from literature was used (Zhu *et al.* 2013b). Hereby, 456 mg citric acid monohydrate and 536  $\mu$ L ethylenediamine were dissolved in 10 mL ultrapure water. The colorless solution was transferred into a stainless steel autoclave as used for the other C-dot preparations. The autoclave was heated to 200 °C and temperature was maintained for 5 h. After cooling to room temperature the orange-brown particle suspension was purified, as described above for the other C-dot preparations.

### 3.1.2 Graphene Oxide via Hummers Method

*Hummers method* is a well established chemical exfoliation technique for the fabrication of graphene oxide (GO) since its publication “The Preparation of Graphitic Oxide” in the 1950s (Hummers 1958). More than half a century later, the method is more prevailing than ever, since graphene came into focus as alternative semiconducting material in electronic applications (Allen *et al.* 2010). The big advantage of this method is that it allows for the large scale fabrication of oxidized graphene-like structures in aqueous suspensions from bulk graphite with standard lab techniques, as shown in Fig. 3.7. While the “scotch tape method”, which was used when graphene was discovered, yields atomically thin graphene flakes (Novoselov *et al.* 2004), Hummers method produces a highly defective and oxygen-rich two dimensional carbon nanomaterial often consisting of several atom layers (Dikin *et al.* 2007). In further preparation steps GO may be reduced, with hydrazine for example, to lose several of its oxygen functionalities leading to large-area aromatization of the material, denoted in literature as *reduced graphene oxide* (rGO) (Stankovich *et al.* 2007).

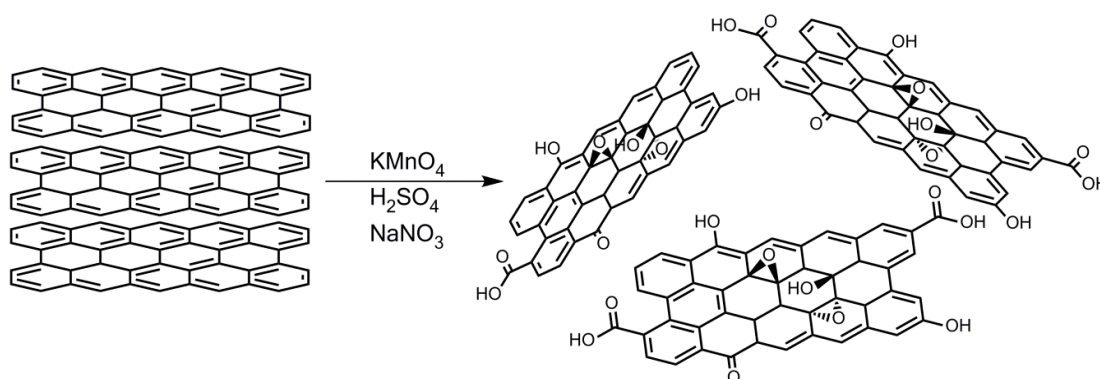


**Fig. 3.7:** Reaction scheme for the chemical exfoliation of bulk graphite to graphene oxide.

In this work, GO was prepared, based on Hummers method, to be used as precursor material for the fabrication of GQDs (Becerril *et al.* 2008). Therefore, 2 g of graphite (china flake graphite) were mixed with 1.5 g  $\text{NaNO}_3$ , 9 g  $\text{KMnO}_4$  and 150 mL conc.  $\text{H}_2\text{SO}_4$  in a 250 mL round bottom flask. The reaction mixture was treated with ultrasound for about 20 h, during which the color changed from green-black to grey-brown. It was stirred for two days at room temperature in order to complete the oxidation reaction, changing the mixtures color to brown. Afterwards it was transferred into a 500 mL round bottom flask and 280 mL of 5%  $\text{H}_2\text{SO}_4$  were added. The mixture was stirred at 100 °C until refluxing. Afterwards 6 mL of 30%  $\text{H}_2\text{O}_2$  were added and stirred for 1 h at room temperature. For the purification of the GO, the reaction mixture was centrifuged with 3000 rcf for 15 min and the supernatant was discarded. The precipitate was suspended in different solvents, centrifuged with 3000 rcf for 10 minutes and washed, as follows: 4x 3%  $\text{H}_2\text{SO}_4$  + 0.5%  $\text{H}_2\text{O}_2$ ; 2x 3% HCl; 2x ultrapure water. The last purification step yielded a stable brownish suspension. This was dialyzed for two weeks against ultrapure water. The water was



changed five times. The mass concentration of the suspension was determined gravimetrically.

### 3.1.3 Graphene Quantum Dots via Hydrothermal Treatment of Graphene Oxide

Graphene Quantum Dots (GQDs) are closely related to C-dots in terms of material composition, functionalization and photoluminescence properties (Li *et al.* 2013). While C-dots are described as quasi-spherical particles with sizes below 10 nm, GQDs show a broader distribution typically between 3 and 20 nm and possess a flake-like morphology (Shen *et al.* 2012a). However, the most important difference is that GQDs are prepared from graphene, GO or rGO in top-down approaches, while the precursor material of C-dots may vary a lot (Baker *et al.* 2010).

In this work, GQDs were prepared via hydrothermal treatment of GO in the presence of ammonia. Thereby, the GO sheets are cut into smaller fragments via nucleophilic substitutions of the oxygen moieties of the GO by ammonia (Lai *et al.* 2011). A scheme for the reductive amination reaction is shown in Fig. 3.8. The preparation method was adapted from literature and modified in terms of ammonia concentration, temperature and reaction time (Tetsuka *et al.* 2012).

For a typical preparation of GQDs, 10 mL of an aqueous GO suspension (0.5 mg/mL) were mixed with 90 mL ultrapure water and 30 mL aqueous ammonia solution (32%, Merck). The deep brown mixture was stirred vigorously and 30 mL of it were transferred into a stainless steel autoclave with PTFE liner (inner volume ~50 mL). Next, the autoclave was heated to 100 °C and temperature was maintained for 5 h. After cooling to room temperature the black suspension was boiled until about 8 mL of the liquid phase remains. This step removes the excess ammonia. Centrifugation with 21380 rcf yielded in a brownish supernatant which was further purified through filtration using a syringe filter membrane (0.2 µm, PTFE). The obtained yellow-brownish GQD suspension was used for further analysis.

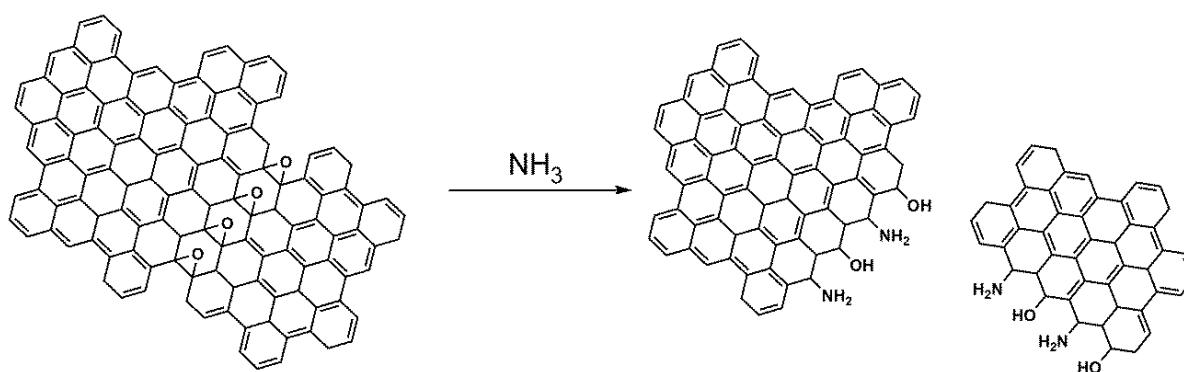


**Fig. 3.8:** Scheme for the fragmentation of GO via reductive amination reactions with ammonia under hydrothermal treatment.

## 3.2 Modification of Carbon Dots and Embedding in other Nanomaterials

All modifications and preparations in this chapter were performed using C-dots from starch and Trp, as described in chapter 3.1.1.

### 3.2.1 Modification of Carbon Dots with Oleic Acid

As the preparation method for the C-dots in this work was newly described, a method for the particle modification had to be developed. Therefore, an esterification between an organic carboxylic acid chloride and as well hydroxyl groups remaining on the C-dot surface was chosen. A scheme for the reaction is shown in Fig. 3.9. As surface modification reagent oleic acid was used, since a successful modification is clearly observable through increase of the hydrophobicity of the particles. Furthermore, oleic acid is also part of the monounsaturated derivative of 1,1'-dioctadecyl-3,3,3,3'-tetramethylindocarbocyanine perchlorate (DiI) D-3886, which is a fluorescent lipophilic cationic indocarbocyanine dye and used for the staining of cell membranes. Accordingly, an oleic acid modification of C-dots was expected to result in different cell staining behavior, such as intercalation into cell membranes. These particles are denoted as oleic acid modified (OAM) C-dots below.

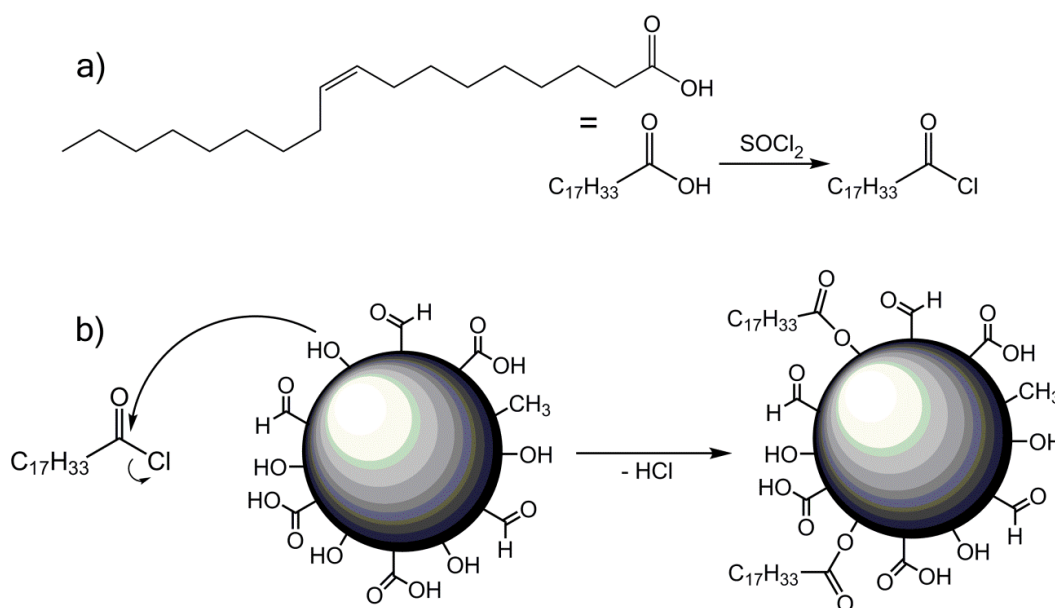


**Fig. 3.9:** Reaction scheme for the preparation of OAM C-dots. a) Activation of oleic acid with thionyl chloride to oleic acid chloride. b) Esterification between the oleic acid chloride and the hydroxyl groups of the C-dots.

## Materials and Methods

For the preparation of the oleic acid chloride, 500 mg oleic acid (Alfa Aesar) were dissolved in 25 mL dry dimethylformamide (DMF, Acros Organics) in a 50 mL round bottom flask under nitrogen atmosphere. Afterwards, 132  $\mu$ L thionyl chloride (Sigma Aldrich) were added. The solution turned brown during the addition. The reaction mixture was stirred for 2 h under reflux and nitrogen atmosphere and stirred further 30 min at room temperature.

In order to prepare the particles for the modification, 5 mL of an aqueous C-dot suspension ( $\sim$  80 mg/mL) were completely dried in an oven at 80  $^{\circ}$ C. The residue was resuspended in 5 mL DMF using vortexing and ultrasonic treatment. The particle suspension was added to the oleic acid chloride solution and the mixture was stirred for 48 h under nitrogen atmosphere. After that, the mixture was quenched with a saturated aqueous sodium bicarbonate solution (Merck) and the reaction mixture was extracted three times with 30 mL chloroform (Acros Organics). The organic phases were collected, combined and concentrated to about 5 mL at the rotary evaporator. The effort of the reaction was controlled using thin film chromatography (TLC). Hereby, the OAM C-dots showed a much longer migration in the mobile phase ethyl acetate (Acros Organics) during TLC than the unmodified particles. Photographs of the TLC plates are shown in Fig. 3.10 a and b.

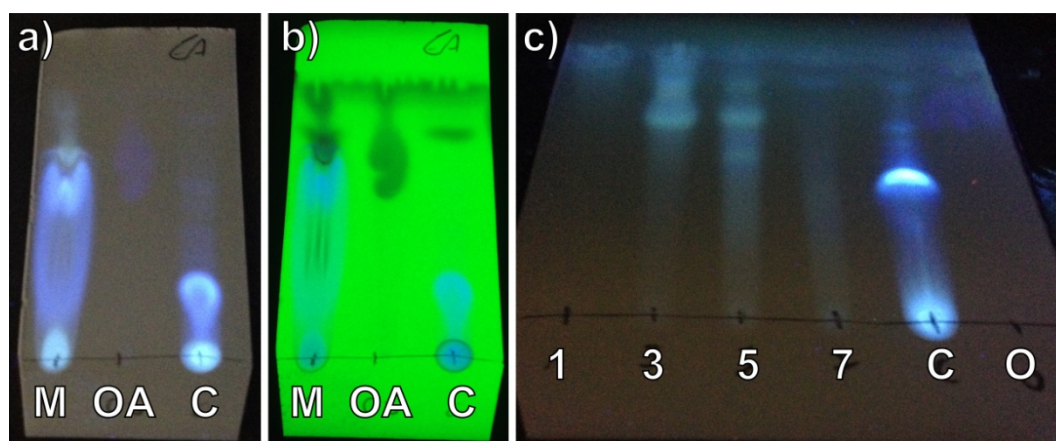


**Fig. 3.10:** TLC of the OAM C-dots using ethyl acetate as eluent. a) Reaction mixture (M), oleic acid (OA) and C-dots (C) after TLC upon excitation at 366 nm. b) Same as before upon excitation at 254 nm. c) TLC of the different fractions (1-7) eluated from the silica column, in comparison to unmodified C-dots (C) and oleic acid (O) upon excitation at 366 nm.

Subsequently, the product was further purified using a silica column and ethyl acetate as eluent. Thereby, the elution of the OAM C-dots was controlled using TLC upon UV excitation, as shown in Fig. 3.10 c. The luminescent fractions (3-5) which showed a similar migration as oleic acid were combined and concentrated at a rotary evaporator. As residue about 400 mg of dark-brown highly hydrophobic oil were obtained. This was dissolved in 1.6 mL dimethyl sulfoxide (DMSO, Acros Organics) to serve as stock solution for cell imaging experiments.

### 3.2.2 Preparation of Agarose Nanoparticles doped with Carbon Dots

Agarose hydrogels and particles are known to undergo swelling or shrinking depending on changes in the osmolarity of the surrounding environment (Viallat *et al.* 2004). Furthermore, fluorophores may be incorporated into hydrogels. These are able to undergo changes in their spectroscopic properties in response to an altered environment, such as the shrinking or swelling of a surrounding gel (Tellis *et al.* 2011). Since the photoluminescence of C-dots has appeared to be highly dependent on their concentration in suspension a change in the distance of the particles within a hydrogel was expected to be spectroscopically observable. In order to use C-dots as probes for measuring the osmolarity of aqueous solutions, they were incorporated into agarose nanoparticles. The preparation of these nanoparticles was adapted from literature and modified for the doping with C-dots (Wang *et al.* 1997). Hereby, an aqueous hot agarose solution is mixed with the dopant and emulsified in hot plant oil as organic phase. Cooling down the emulsion leads to solidification of the agarose droplets.

For a typical preparation of doped agarose nanoparticles, 20 mg of agarose (Sigma Aldrich) were mixed with about 2 mL of ultrapure water and a defined quantity of the aqueous suspension of C-dots (1 mg/mL). The aqueous phase was heated to 90 °C in a test tube in a water bath to ensure that the agarose was completely dissolved. Simultaneously, 150 mL of sunflower oil were heated to 60 °C in a round-bottomed flask in an ultrasonic bath. The two preheated phases were mixed and subsequently sonicated for 10 min while being stirred with a CPG-stirrer, as shown in Fig. 3.11.

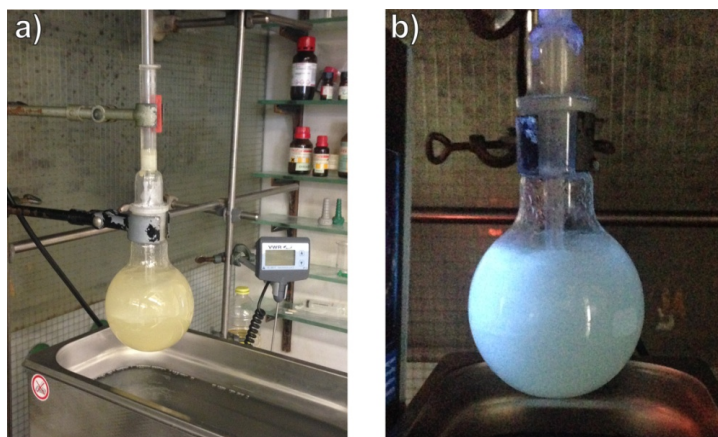


**Fig. 3.11:** Preparation of agarose nanoparticles. a) Suspension of the agarose particles in sunflower oil under stirring with a CPG-stirrer. Heating and ultrasonification were performed using a ultrasonic bath with temperature control. b) Under excitation with a UV lamp at 366 nm.

Afterwards, sonication was stopped and the mixture was cooled to room temperature under continuous stirring before being centrifuged for 15 min at about 3850 rcf. The supernatant was decanted and discarded whereas the sediment was suspended in 20 mL PBS<sup>++</sup>. The aqueous phase with the higher density was then removed from the vial using a pipette and afterwards filtered using a paper filter in order to obtain the desired suspension containing C-dots embedded in agarose nanoparticles.

### 3.2.3 Encapsulation of Carbon Dots in Liposomes

Liposomes are spherical entities surrounded by a lamellar phase lipid bilayer. For the preparation of the bilayer often phospholipids in varying compositions are used which encapsulate an aqueous solution compartment inside. These can be loaded with water-soluble drugs and fluorophores or aqueous suspensions of nanoparticles. The lipid bilayer may be prepared with chemically modified phospholipids which allow for the targeting of (cellular) receptors by using appropriate ligands (Torchilin 2005). Another phenomenon is that liposomes show swelling or shrinking upon changes of the external osmotic pressure. Thereby, the osmotic pressure of the inner compartment is equalized to the one of the surrounding medium by release or uptake of water (Mui *et al.* 1993).

In this work, liposomes loaded with C-dots were prepared to investigate whether liposomes may serve as delivery vehicles for C-dots into living cells. Therefore, two different types of liposomes were prepared. A preparation with high concentrations of C-dots encapsulated inside and another one with low concentrations of C-dots. The ratio of the mass concentrations was about 1:10.

For the preparation of liposomes with the highly concentrated aqueous C-dot suspension, a mass concentration of about 48 mg/mL with an osmolality of 290 mOsm/kg was used. For the liposomes with low concentrations, a C-dot suspension with about 4.8 mg/mL was used and osmolality was adjusted to 290 mOsm/kg by 4-(2-hydroxyethyl)-1-piperazineethanesulfonic acid (HEPES, Sigma Aldrich) buffer. Then 30 mg dipalmitoylphosphatidylcholine (DPPC, Avanti Polar Lipids), 15 mg dipalmitoylphosphatidylglycerol (DPPG, Avanti Polar Lipids) and 20 mg cholesterol (Sigma Aldrich) were solved in 3 mL chloroform and 0.5 mL methanol (Merck) and shortly ultrasonicated at 45 °C. Subsequently, 2 mL of the preheated (45 °C) C-dot suspension were added and ultrasonicated for 4 min. Afterwards, the solvent was removed on a rotary evaporator for 40 min at 45 °C at 380 mbar. The residue was mixed with further 2 mL of the aqueous C-dot suspension and thoroughly stirred. After short vortexing, the solvent was removed at a rotary evaporator for 20 min at 380 mbar and 20 min at 280 mbar. The residue was suspended in HEPES saline buffer, pH 7.5 (10 mM HEPES, 200 mM NaCl, 1.5 mM NaN<sub>3</sub> corresponding to 375 mosm/kg) and the dispersion transfused through an extruder 21 times back and forth with pore sizes of 1.0 µm first and then 0.4 µm. Purification was performed using a Sephadex® G-50 column with the HEPES buffer as eluent. Afterwards, the dispersion was dialyzed against the HEPES buffer for two days. The buffer was changed after one day during dialysis.

The preparation of the liposomes with the incorporated C-dots was performed by Christoph Fenzl at the Institute of Analytical Chemistry Chemo- and Biosensors, University of Regensburg.

### 3.3 Material Characterization Techniques

#### Atomic Force Microscopy (AFM)

Atomic Force Microscopy (AFM) is a high-resolution technique that belongs to the family of scanning probe microscopies. It allows for a resolution below the nanometer scale up to atomic resolution and is therefore about 1000 times better than the optical diffraction limit. The AFM was performed by Daniel Wastl in the group of Prof. Giessibl at the Department of Physics at the University of Regensburg. Details about the AFM technique as used may be found in literature (Wastl *et al.* 2013). In this work, AFM was used to visualize the particles and to measure their size distribution. Regarding the small size of the carbon particles and their material (low electron scattering) common optical and electron microscopy could not be used.

For the preparation of the measurement, a mica crystal (a type of sheet silicate) was cleaved to obtain an atomically smooth crystal layer. Thereupon a droplet of a 10 µg/mL particle suspension in ethanol was drop casted. The crystal was spun by hand for one minute in order to achieve uniform coating of the particles on the surface and to evaporate the ethanol. A sapphire tip was used as AFM probe. Height and width of the particles were analyzed by measuring the height profile of an adequate amount of particles via line scans with the WSxM 4.0 Beta 7.0 software.

#### Dynamic Light Scattering (DLS)

Dynamic Light Scattering (DLS) allows for the determination of the size distribution of particles in suspensions. Thereby, laser light is scattered in all directions (Rayleigh-Scattering) by impinging small particles in suspension. Since the distances of the scattering centers change due to Brownian motion, fluctuations of the scattered light intensity are detected over time. As such, a diffusion coefficient for the particles may be calculated which leads to their hydrodynamic diameter via Stokes-Einstein relation. (Berne *et al.* 2000)

For the DLS measurements in this work, a *Zetasizer Nano-ZS* from *Malvern* was used, which was equipped with a 632.6 nm laser. Due to the small size of the particles, relatively high concentrated suspensions were used. For the investigation of the C-dots, suspensions of about 20 mg/mL of freshly filtered (PES membrane 0.22 µm) C-dots in PBS at 25 °C were used. In all other measurements, the respective stock suspension was filtered and measured at 25 °C. Every measurement was carried out using semi-micro cuvettes made of poly (methyl methacrylate) (PMMA) from *Brand*. The hydrodynamic diameter distributions were plotted depending on three different aspects: The number plot represents a count over all particles and shows the occurrence of particles with the respective diameters. The volume plot shows the distribution of the particles which

## *Materials and Methods*

contribute the most to the total volume of all particles. The intensity plot shows the distribution for the particles contributing highest DLS signal intensities. Thereby, larger particles are highly overrepresented, since the diameter of each particle contributes to the fit of the signal to the power of six. However, this way of data presentation allows identification of contaminations or aggregates.

### Elementary Analysis (CHNX)

For the investigation of the elemental composition of the carbon materials elementary analysis was used. Therefore, the material is combusted into gaseous compounds and analyzed via infrared (IR) spectroscopy.

The analysis was carried out by the Central Analytical Services at the Faculty of Chemistry and Pharmacy of the University of Regensburg. 1 – 3 mg of the lyophilized particles were used for a single measurement to determine the mass fraction of carbon, hydrogen and nitrogen. The mass fraction of oxygen was calculated by subtraction.

### Energy-Dispersive X-Ray Spectroscopy (EDX)

Another analytical technique for the chemical characterization of a material is EDX. Hereby, the atoms of the sample are excited by an electron beam to stimulate the emission of specific x-rays from the samples distinct atoms. By analyzing the energy of the emitted radiation, the chemical composition of the specimen may be characterized.

In this work, aqueous suspensions of C-dots and GQDs were drop casted onto gold coated silicon wavers and the water was evaporated in a drying oven. The samples were analyzed with a JSM-6700F from *JOEL Inc.* with a 5 keV electron beam.

### Infrared Spectroscopy

Functionalization of the C-dots was analyzed via IR spectroscopy. The molecular vibrations of functional groups of the sample may be identified as distinct transmittance peaks in an IR spectrum. In this work an *IR-Spectrometer 3000* from *Varian* with sapphire optics was used. For the measurement, lyophilized C-dots were applied onto the optical bridge.

### Raman Spectroscopy

In Raman spectroscopy the inelastic scattering of monochromatic light (Raman scattering) by a sample is observed and analyzed. The excitation of different vibrational, rotational and other low-frequency modes allows conclusions on the chemical bonding states of the samples.



In this work, Raman spectra were recorded on a DXR Raman microscope from *Thermo Fisher Scientific Inc.* equipped with a 532 nm excitation laser (10 mW). For the sample preparation, aqueous particle suspensions were dried up on gold coated silicon wafers.

#### X-Ray Photoelectron Spectroscopy (XPS)

In x-ray photoelectron spectroscopy the number and kinetic energy of electrons emitted from the top 10 nm of the sample material under x-ray irradiation is detected and analyzed. This allows for the investigation of the elemental composition of the material and the chemical bonding states of each element in high resolution spectra.

The XPS measurements were performed at nanoAnalytics GmbH in Münster, Germany on lyophilized C-dots. The device which was used is an ESCALAB 250 from Thermo VG Scientific. For the excitation in spectroscopic mode monochromatic Al K $\alpha$  x-radiation was used (15 kV, 150 W, 500  $\mu$ m spot size). Overview spectra were recorded with 80 eV pass energy, high-resolution spectra with 30 eV.

#### Zetapotential

The zetapotential of particles in suspension gives information about their surface charge and therefore their colloidal stability. Furthermore, changes of the pH may result in alteration of the particle surface charge. This gives hints towards ionizable functionalities, such as carboxyl or amino groups.

The measurements were performed using a *Zetasizer Nano-ZS* from *Malvern*. The C-dots were analyzed as a 20 mg/mL suspension at 25 °C and at different pH values in aqueous HCl, NaOH and PBS solutions. For the measurements disposable capillary cells (DTS1070) from *Malvern* were used.

## 3.4 Optical Spectroscopy and Microscopy

### 3.4.1 Optical Spectroscopy and Fluorescence Lifetime Determination

#### Absorption Measurements

All absorption spectra in this work were recorded with a *Cary® 50* UV-VIS spectrophotometer from *Agilent Technologies*. Correction was realized through subtraction of the values and spectra of blank solutions with pure solvent. Absorption measurements below 300 nm were carried out in cuvettes from *Hellma* made of Suprasil® quartz with a light path of 10 mm. Those with absorptions at higher wavelengths than 300 nm were performed in single use cuvettes made of PMMA from *Kartell*.

#### Fluorescence Spectroscopy

Fluorescence intensities and spectra in this work were recorded with a FP-6300 spectrofluorometer from *JASCO Inc.* The device was equipped with a DC powered 150 W xenon lamp. Bandpass filters of the monochromators for excitation and emission were adjusted to 5 nm for every measurement. The same cuvettes were used as for the absorption measurements, depending on excitation above or below 300 nm.

Two dimensional fluorescence spectra were obtained by variation of the excitation wavelength in 5 nm steps and recording the respective emission spectra in 2 nm data pitches. The spectra were merged into a matrix and plotted as two dimensional maps with the x- and y-axis as excitation and emission wavelength. The fluorescence intensity at the respective combination was illustrated with a color code.

#### Fluorescence Lifetime

The fluorescence lifetime of C-dots was measured on a PicoQuant MicroTime 200 with UV optics. Excitation was accomplished using a 20 MHz (Nd:Van) laser at 355 nm with 12 ps pulsing and a beam diameter of 8 mm. An Olympus UPlanS Apo 60x/1.2W in water immersion was used as objective. Emission was filtered by a Chroma HQ 560 SP filter and detected with a MPD PDM 50 µm. All lifetime measurements were performed by Dr. Stefan Nagl at the Institute of Analytical Chemistry of the University of Leipzig.

The experimental data were fitted via exponential decay functions in order to obtain the fluorescence lifetimes of the material.

### 3.4.2 Imaging via Confocal Laser Scanning Microscopy

Confocal laser scanning microscopy (CLSM) uses a focused laser beam to scan across a specimen through a pinhole in order to increase lateral and axial resolution. The laser beam focused in the optical plane of the sample only excites fluorophores in its light path. The emitted fluorescence is detected by a photomultiplier tube with a confocal pinhole in front of it. 3D imaging is possible by moving the sample along the z-axis. By collecting the optical xy-sections at each z-position and subsequent reconstruction, layer-by-layer mapping may be performed (Pawley 2006).

The utilized CLSM in this work was a *Nikon Eclipse 90i* with a *C1* scanning unit which was used for all fluorescence micrographs. It was equipped with three different lasers (all from *Melles Griot*®) for the excitation of the specimen and three different emission detectors for the blue, green and red channel (RGB) of the recorded micrographs. The specifications of the lasers and detectors are shown in Table 3.1.

**Table 3.1:** Specifications of the CLSM lasers and its detectors for the blue, green and red channel.

Lasers:	Detectors:
<500 mW laser diode 400-405 nm	Blue: 435-450 nm (B)
<50 mW at 488 nm	Green: 515-530 nm (G)
<5 mW at 543.5 nm	Red: 650 nm LP (R)

The microscope was equipped with four objectives from Nikon: 10x/0.25, 20x/0.40, 50x/0.55 and 60x/1.00 (magnification/numerical aperture). For high-resolution fluorescence imaging of cells, the 60x magnification objective was used. It is a water immersion objective used for the analysis of biological samples under physiological conditions in aqueous environments. For these experiments every sample was covered with buffer and the objective was dipped into the solution. For overview fluorescence micrographs (such as photo wounds) and the imaging of whole spheroids the 10x magnification objective was mainly used. This is a dry objective, which means imaging was performed without contact to the buffer solution.

The scanning head of the microscope contained a variable detection pinhole whose size could be adjusted to four different diameters: S: 30  $\mu\text{m}$ ; M: 60  $\mu\text{m}$ ; L: 100  $\mu\text{m}$ ; O: 150  $\mu\text{m}$ . For the fluorescence pictures with C-dots and GQDs mostly pinhole adjustment L was used, as it allows more light to pass to the detector, so that the fluorescence could be detected more easily. Most pictures were recorded with a resolution of 1024 x 1024 pixels by the Nikon EZ-C1 software.

### 3.4.3 Reagents for Fluorescence Imaging Experiments

For the fluorescence imaging of interactions between C-dots and living cells the following reagents and labels were used:

#### FITC-labeled Annexin V and Propidium Iodide

Annexin V is a 35-36 kDa  $\text{Ca}^{2+}$  dependent binding protein with high affinity to the phospholipid phosphatidylserine. Phosphatidylserine is part of the membrane of living cells and is located exclusively in the inner membrane leaflet at the inside. Undergoing apoptosis, phosphatidylserine is translocated to the outer side of the membrane, exposing it to the cellular environment. As such, fluorescence labeled Annexin V (with fluorescein isothiocyanate, FITC) may bind to the membrane of apoptotic cells and serves as fluorescent probe for those cells (Vermes *et al.* 1995). In later stages of apoptosis, cells experience a loss of plasma membrane integrity and undergo cell death. For the staining of dead cells a vital stain such as propidium iodide (PI) may be used. While healthy cells exclude PI, it is internalized into the nuclei of dead cells. Late apoptotic and cells that have undergone necrotic pathways are both stained Annexin V and PI positive. An overview about the different cell stages and their labeling is given in Fig. 3.12.

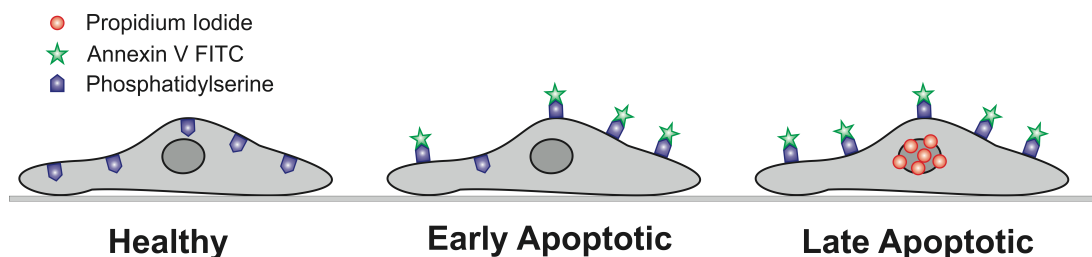


**Fig. 3.12:** Schematic overview showing healthy and apoptotic cells labeled with different apoptosis markers.

In this work, an apoptosis detection kit from *BD Biosciences* with product number 556547 was used. For the staining of the photo wounds the cells were incubated with 1:20 dilutions of each stock solution in EBSS<sup>++</sup> for 2.5 h. For the excitation of both Annexin V FITC and PI the 488 nm laser of the CLSM was used. For Annexin V FITC the 515-530 nm detector was used and for PI the 650 LP one.

#### Calcein Acetomethoxyester and Ethidium Homodimer-1

Calcein acetomethoxyester (AM) is used in cell biology as probe for the detection of living cells. The esterified version of calcein is membrane permeable and the acetomethoxy groups are removed by intracellular esterases. After cleavage the dye is able to bind  $\text{Ca}^{2+}$  ions which make it become strongly fluorescent and trapped inside the cell. A schematic of this process is shown in Fig. 3.13. Ethidium homodimer-1 (EthD-1) is similarly to PI membrane impermeable to healthy cells. By contrast, the dye may enter dead cells which

lost plasma membrane integrity and intercalate into dead cells DNA, staining its nucleus. Ethidium homodimer-1 becomes highly fluorescent upon DNA intercalation and therefore may be used as probe for dead cells (Horobin *et al.* 2002).

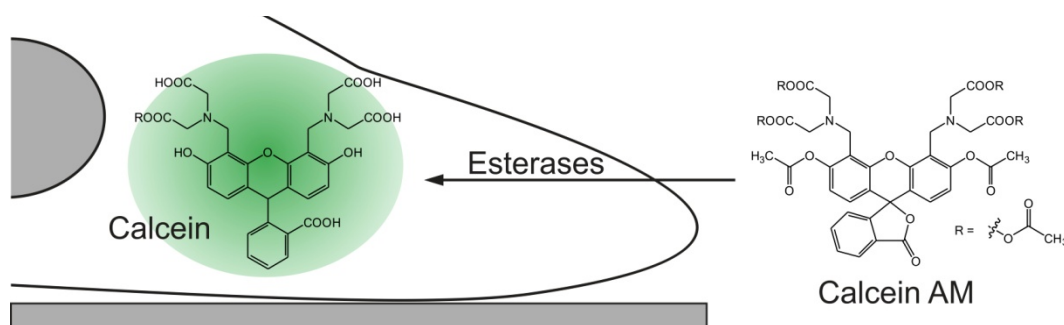


**Fig. 3.13:** Schematic for the transportation of calcein AM into living cells. Intracellular esterases hydrolyze the probe to free calcein, which becomes fluorescent and trapped inside the cell upon binding to Ca<sup>2+</sup>.

To distinguish between living and dead cells in this work a *LIVE/DEAD*® Viability/Cytotoxicity Kit for mammalian cells (L-3224) from *life technologies* was used. Cells were incubated with 2  $\mu$ M Calcein AM and 4  $\mu$ M EthD-1 solutions in PBS<sup>++</sup> for about 30 min at room temperature. Afterwards they were washed with PBS<sup>++</sup> and analyzed via CLSM. Calcein AM was excited at 488 nm and detected at 515-530 nm. EthD-1 was excited at 543 nm and emission observed using the 650 LP detector.

### Lysotracker green

For the staining of lysosomes inside living cells LysoTracker® Green DND-26 (L-7256) from *Life Technologies* was used, which is a fluorescent acidotropic probe for acidic organelles. The specific staining is based on fluorescence labeled weak basic amines which are freely permeable through cell membranes. In acidic cell organelles such as lysosomes, those weak amines get protonated and therefore get trapped in those organelles membranes. For the staining cells were incubated with a 1  $\mu$ M solution of the dye in PBS<sup>++</sup> for 30 minutes, washed and analyzed via CLSM. A schematic of the molecular structure of LysoTracker® Green and its staining pattern is shown in Fig. 3.14.

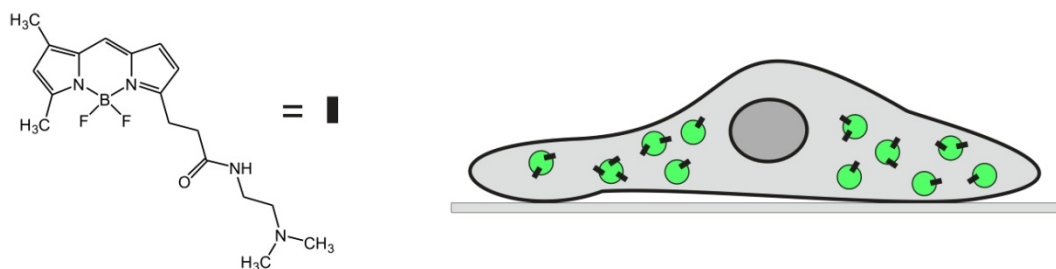


**Fig. 3.14:** Molecular structure of LysoTracker® Green on the left and a schematic for the staining pattern with the dye in cells on the right.

DNA Blotting and Staining with C-dots/EthD-1

Among others, investigations on the binding of C-dots to DNA were performed via staining of DNA structures. These were prepared via the following protocol. A custom made polydimethylsiloxane (PDMS) stamp with a fine lined structure was incubated with double stranded DNA (ds DNA, from herring sperm, Sigma Aldrich) with a concentration of 5 mg/mL in PBS<sup>++</sup> for 24 h in order to soak it with the DNA. Subsequently, the stamp was washed with PBS<sup>++</sup> and dried under nitrogen flow. Then, the stamp was pressed for 4 h on a culture Petri dish, which had been pre-incubated with a poly-L-lysine (as hydro bromide, Sigma Aldrich) solution, blotting the DNA on its surface. Thereupon, the stamp was removed and the DNA structure was incubated with 1.0 mg/mL C-dots in PBS<sup>++</sup>, or 4  $\mu$ M EthD-1 for 30 min, respectively. The Petri dish was washed with PBS<sup>++</sup> and analyzed with CLSM. A schematic for the preparation of the DNA structure is shown in Fig. 3.15.

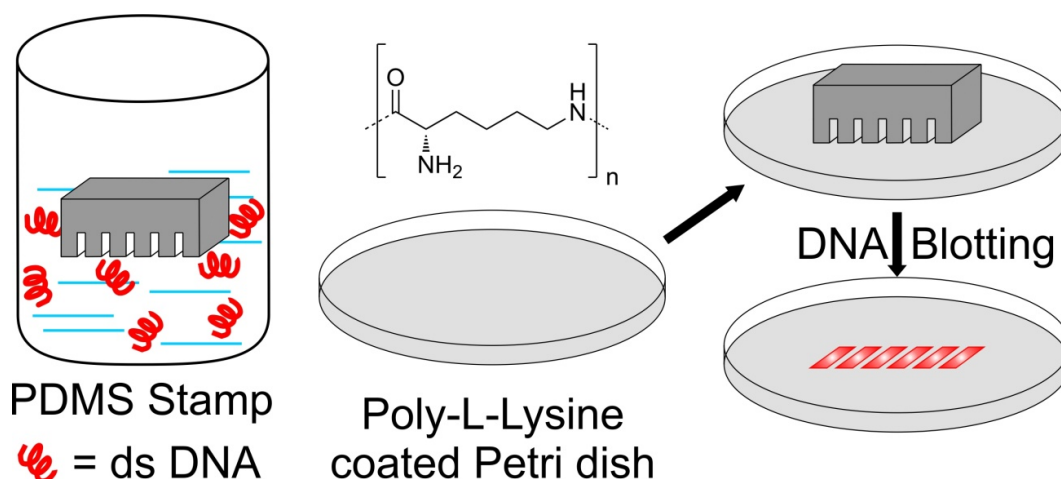


**Fig. 3.15:** Schematic for the preparation of defined DNA structures on Petri dishes to image the binding of C-dots to DNA.

## 3.5 Cell Culture Techniques

Avoiding microbiological contaminations and establishing aseptic conditions are requirements for working with cultures of animal cells. In order to ensure these conditions, all cell culture work was done under a laminar air flow work bench (Thermo Fischer Scientific Inc.). All consumables were autoclaved and only sterile medium and reagents were used. Cells were grown in culture flasks with a growth area of 25 cm<sup>2</sup> using 4 mL of culture medium. They were cultivated in an incubator (Thermo Fischer Scientific Inc.) at 37 °C with a 5% CO<sub>2</sub> humidified atmosphere. The cells were fed with fresh medium every three days and one day before every cell experiment. All reagents, buffers and media were warmed in a 37 °C water bath before usage and originate from Sigma Aldrich if not denoted differently.

### 3.5.1 Cultivation of Adherent Cell Lines

In this work, five different anchorage-dependent cell lines were used for experiments, which are described in more detail below. All cell lines originate from the *Leibniz Institute DSMZ – German Collection of Microorganisms and Cell Cultures*.

*Normal Rat Kidney* (NRK) cells were derived from rats of the species *rattus norvegicus*. The NRK cells used in this work (NRK-52E) are epithelial-like, adherently growing cells, which form homogeneous monolayers with a cobblestone-morphology, as shown in Fig. 3.16a.

The culture medium consisted of the following ingredients. *Dulbecco's Modified Eagle's Medium* (DMEM) with 3.7 g/L NaHCO<sub>3</sub> and 4.5 g/L D-Glucose + 5% (v/v) fetal calf serum (FCS, Biochrom), 1 mM L-Glutamine; 100 µg/mL Penicillin and 100 µg/mL Streptomycin.

*Madin-Darby Canine Kidney* (MDCK) I and II cells were both derived from an apparently normal adult female cocker spaniel kidney in September 1958 by S.H. Madin and N.B. Darby. These cells have been characterized as epithelial cells and grow to form a confluent monolayer similar to the NRK cells, as shown in Fig. 3.16b.

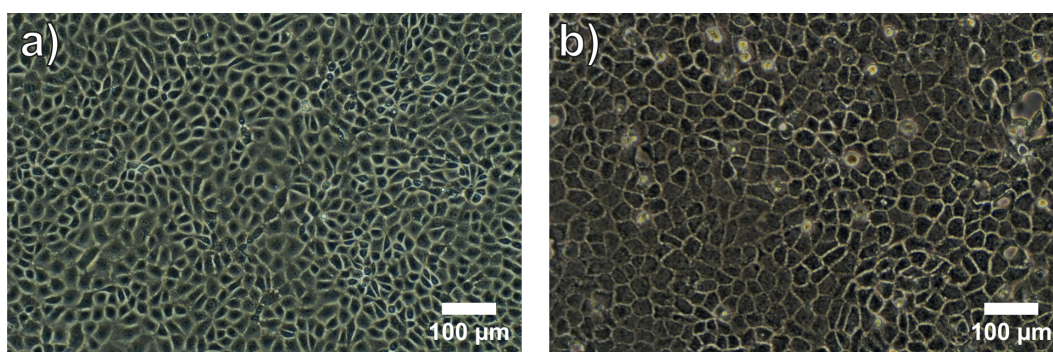


**Fig. 3.16:** Phase contrast micrographs of confluent monolayers of selected cell lines. a) NRK cells, b) MDCK II cells.

## Materials and Methods

The biggest difference between MDCK I and II cells is that MDCK I cells form very tight cell junctions and were derived from low passages of the parental cell line. MDCK II cells by contrast originate from higher passages of the parental cell line and exhibit “leaky” junctions (Barker *et al.* 1981). Furthermore, MDCK II cells are larger and taller, while MDCK I cells are more flat and irregular (Richardson *et al.* 1981).

The culture medium for both cell lines consisted of the following ingredients: *Earle’s Minimal Essential Medium* (MEM-Earle) with 2.2 g/L NaHCO<sub>3</sub> and 1 g/L D-Glucose + 5% (v/v) FCS; 4 mM L-Glutamine; 100 µg/mL Penicillin; 100 µg/mL Streptomycin.

*Chinese hamster ovary* (CHO) cells originate from the ovary of a Chinese hamster. The cell line CHO-K1 has been isolated by Theodore T. Puck from a female Chinese hamster in 1957, through single cell cloning (Wurm *et al.* 2011). These are epithelial cells typically exhibiting a long stretched morphology as shown in Fig. 3.17a.

The culture medium for CHO-K1 cells consisted of the following ingredients: *Nutrient Mixture F-12 Ham* (Ham’s F12) + 10% (v/v) FCS; 2 mM L-Glutamine; 100 µg/mL Penicillin; 100 µg/mL Streptomycin.

*Cultured human keratinocyte* (HaCaT) cells are a spontaneously transformed aneuploid immortal keratinocyte cell line isolated from adult human skin (Boukamp *et al.* 1988). These form an almost regular epidermal architecture when grown to confluence on their growth substrates, as indicated in the micrograph of Fig. 3.17b.

The culture medium for HaCaT cells consisted of the following ingredients: DMEM with 3.7 g/L NaHCO<sub>3</sub> and 4.5 g/L D-Glucose + 10% (v/v) FCS, 2 mM L-Glutamine; 100 µg/mL Penicillin and 100 µg/mL Streptomycin.

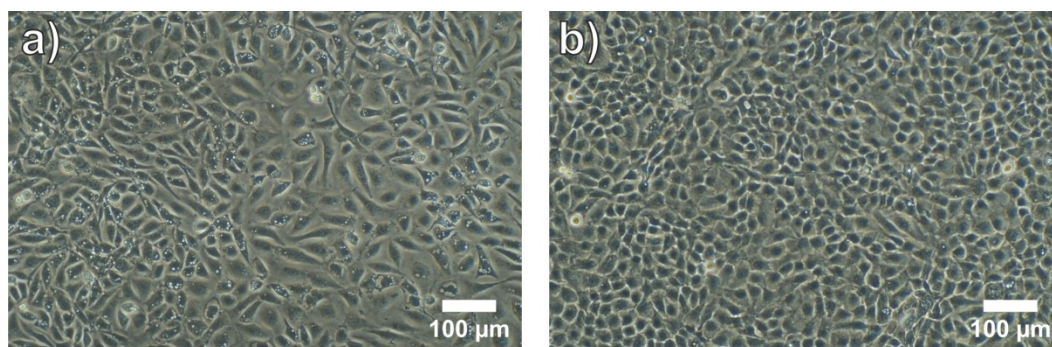


**Fig. 3.17:** Phase contrast micrographs of confluent monolayers of selected cell lines. a) CHO cells, b) HaCaT cells.



### Subcultivation

NRK, MDCK II and HaCaT cells were subcultured once a week using the following protocol. First, the confluent cell-layer was washed twice with 4 mL PBS<sup>-</sup> (phosphate buffered saline; w/o Ca<sup>2+</sup> and Mg<sup>2+</sup>) to remove dead cells and bivalent cations. Furthermore, the cells were incubated with a 1 mM solution of EDTA (ethylenediaminetetraacetic acid) in PBS<sup>-</sup> for 10 min at 37 °C. EDTA is a strong chelate-ligand which complexes bivalent cations, such as Ca<sup>2+</sup> and Mg<sup>2+</sup>, which are needed for the formation of functional cell-cell- and cell-ECM-contacts (extra cellular matrix). After removing the EDTA-solution the cells were treated with 1 mL of a 0.05% (w/v) trypsin-EDTA solution in PBS<sup>-</sup> for 10 min at 37 °C. Trypsin is an enzyme which belongs to the endopeptidases and cleaves peptides and proteins at the carboxylic side of the amino acids lysine and arginine. This is used to detach the cells from the surface of the growth substrate. Detachment was controlled with an inverted microscope and the activity of the enzyme was stopped through the addition of 10 mL culture medium to the cell suspension. The suspension was then transferred into a sterile centrifugation tube and centrifuged for 10 min with 110·g at room temperature. The supernatant was removed and the resulting cell pellet was resuspended in 4 mL of culture medium. Aliquots of this suspension were used to seed the cells again in new culture flasks (25 cm<sup>2</sup>) with 4 mL culture medium in dilutions of 1:10 or 1:20 with respect to the growth area.

MDCK I cells were subcultivated similarly, except that a 0.25% (w/v) trypsin-EDTA solution in PBS<sup>-</sup> was used for the detachment of the cells. Furthermore, incubation times for the EDTA- and trypsin-EDTA solutions were doubled to 20 min.

CHO K1 cells were subcultivated similarly to NRK cells, except that this was performed twice a week, incubating the cell-layer with 4 mL PBS<sup>-</sup> for 10 min, without the addition of EDTA. Afterwards the standard protocol applies.

### 3.5.2 Cultivation of Three Dimensional Multicellular Spheroids

Multicellular spheroids (MCS) are three dimensional spherical aggregates, typically a few hundreds of micrometers in size and consisting of several thousands of cells. They are used as *in-vitro* model for the investigation of tumor diseases and therapeutic approaches against cancer (Mueller-Klieser 1997).

In this work, MCS from *Michigan Cancer Foundation-7* (MCF-7) cells were used. MCF-7 is a human breast adenocarcinoma cell line, isolated in 1970 from a 69-year-old Caucasian woman. On adhesive surfaces, MCF-7 cells grow to epithelial-like confluent monolayers. For the formation of MCS the cultivation in non-adhesive culture ware was used, which is described as follows.

The culture medium consisted of the following ingredients: *Earle's Minimal Essential Medium* (MEM-Earle) with 2.2 g/L NaHCO<sub>3</sub> and 4.5 g/L D-Glucose + 10% (v/v) FCS (Sigma Aldrich); 110 µg/mL Pyruvate; 2 mM L-Glutamine; 100 µg/mL Penicillin; 100 µg/mL Streptomycin.

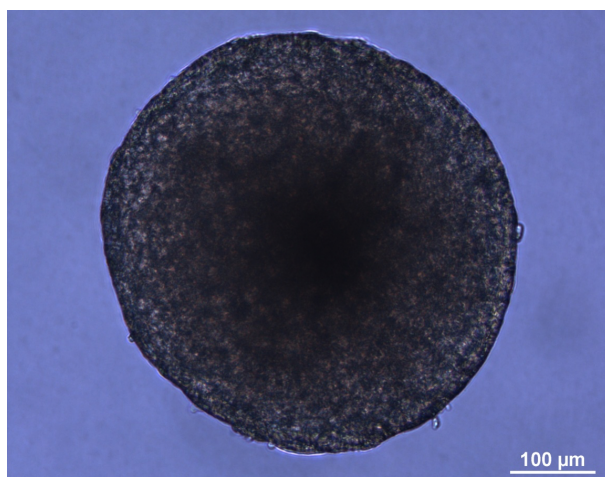


**Fig. 3.18:** Bright-field micrograph of a MCF-7 cell spheroid grown for 7 days in cell culture.

For the preparation of MCS, MCF-7 cells were grown in culture flasks with a growth area of 25 cm<sup>2</sup> using 4 mL of the medium mentioned before in an incubator at 37 °C with 5% CO<sub>2</sub>. Close to confluence, the cells were subcultivated by removing the culture medium and subsequent incubation with a 1 mM solution of EDTA in PBS<sup>-</sup> for 2 min at 37 °C. Afterwards, the buffer was removed and substituted for 1 mL of a 0.25% trypsin-EDTA solution for 3 to 4 min at 37 °C. Detachment of the cells was controlled using an inverted microscope and 4 mL of culture medium were added to stop the enzyme activity of trypsin. The cell suspension was then transferred into a sterile centrifugation tube and centrifuged for 5 min (200·g) at room temperature. The supernatant was removed and the resulting cell pellet was resuspended in 4 mL of culture medium. Cells were counted with a Burker hemacytometer and 3000 cells/well were seeded into agarose-coated 96-well plates.

Coating of the wells was carried out before, using 50  $\mu\text{L}$  of a sterile 1.5% (w/v) agarose solution in serum free MCF-7 culture medium per well. After seeding the cell suspensions, the plate was sealed with Parafilm® and incubated at 37 °C under orbital shaking for 4 h at 120 rpm and 50 rpm over night. Subsequently, the plate was transferred into a common incubator and in ideal cases every well contained one spheroid. Each MCS was allowed to grow for seven days before performing experiments with it. A bright-field micrograph of such a spheroid is shown in Fig. 3.18.

The preparation of the MCS was carried out by Christina Hupf at the Institute of Analytical Chemistry, Chemo- and Biosensors, University of Regensburg.

### 3.5.3 Cultivation of Beating Cardiomyocytes

Cor.At® cardiomyocytes are derived from transgenic mice embryonic stem cells (Kolosso *et al.* 2005) and were purchased from *Axiogenesis*. These cells are produced through *in vitro* differentiation of mouse embryonic stem cells and puromycin selection of cardiomyocytes. Cor.At® cells express cardiac-specific connexin-43, which indicates their ability for electric coupling between each other (Kolosso *et al.* 2006).

Since these cells are highly standardized from lot-to-lot, 99.9% pure and exhibit a fully functional cardiac phenotype, they can be utilized for cell-based *in vitro* assays, addressing cardiac pharmacology or toxicology. Moreover, this method is well suited to study the impact of any kind of stimuli on the regular cardiomyocytes beating.

The cells were seeded and cultured on fibronectin-coated 8W1E $\mu$  ECIS electrode arrays in the commercially available culture medium especially designed for Cor.At® cardiomyocytes and purchased from *Axiogenesis* (Ax-M-MC250E). Cultivation was performed in humidified incubators at 34 °C and a 5% CO<sub>2</sub>-atmosphere. Details on the ECIS based assays with the cardiomyocytes are described in chapter 3.6.2. Seeding of the cells was performed three days prior to the experiments with addition of puromycin as selection antibiotic agent. Two days before, the cardiomyocytes were fed with fresh medium containing puromycin and on the day before the experiment the medium was exchanged against a puromycin-free one. During these days establishment of the electric coupling between the cells and the accompanying synchronous cell contraction was monitored via ECIS. A phase contrast micrograph of Cor.At® cardiomyocytes seeded on an 8W1E $\mu$  ECIS array is shown in Fig. 3.19.

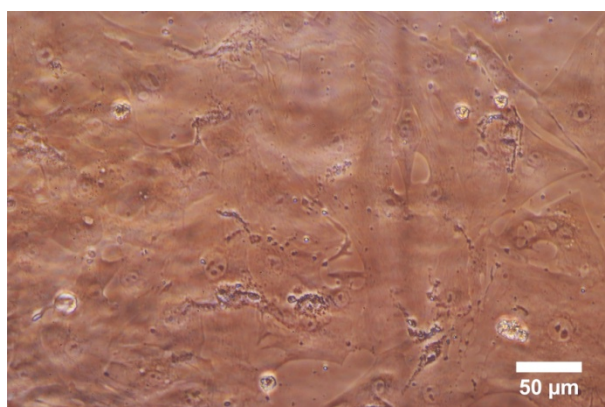


**Fig. 3.19:** Phase contrast micrograph of Cor.At® cardiomyocytes on an 8W1E $\mu$  ECIS electrode array.

### 3.6 Electric Cell-Substrate Impedance Sensing

Electrical Cell-Substrate Impedance Sensing (ECIS) is an impedance-based, non-invasive biophysical approach to monitor animal cell morphologies *in vitro* time-resolved. The technique was developed by Giaever and Keese in 1984 and has become a standard method to monitor cell-based assays with commercially available measurement systems (Giaever *et al.* 1984).

The principle of ECIS is shown in the schematic of Fig. 3.20 and is based on measuring the alternating current resistance (impedance) of cell-covered, planar gold film electrodes. Therefore, cells are seeded on gold films which serve as both, growth substrates and electrodes. A small working electrode is electrically connected to a much larger counter electrode via the surrounding culture medium. The size proportion ensures that the measured impedance is mostly determined through the working electrode. In low frequency ranges cells act as insulating particles, which force the electric current to flow underneath or between them. Accordingly, cell-free electrodes exhibit lower impedances than cell-covered ones. Furthermore, changes in cell morphology due to external influences may be observed, since a change in the three-dimensional cell structure leads to variations of the current paths. Consequently, impedance increases for electrodes with swelling cells and tighter cell-cell connections, as the space between them narrows. Vice versa, impedance decreases for shrinking cells. These phenomena may be used for cytotoxicity screenings as dying cells shrink and detach from their growth substrate.

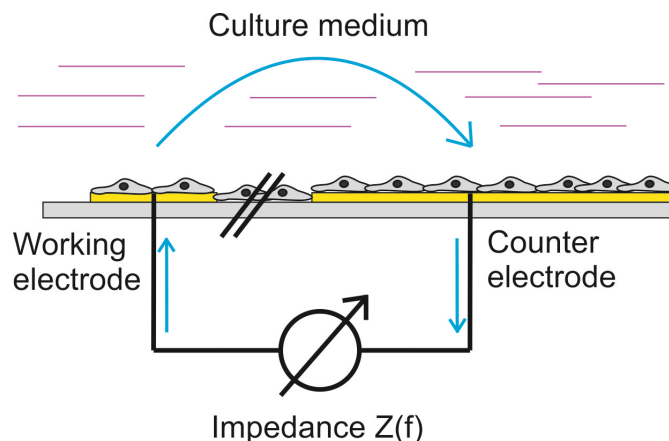


**Fig. 3.20:** Schematic illustrating the principle of ECIS. A small working electrode is electrically connected with a large counter electrode via the electrolytes of the culture medium. Impedance is measured as a function of frequency.

Additionally, ECIS provides the capacitance of the cell-covered electrode, which is especially interesting at higher frequencies. In higher frequency ranges, the current does not flow underneath and between cells but passes through them. As the capacitance depends on the permittivity of the surrounding medium, cell-free electrodes have a higher capacitance than cell-covered ones. That allows for a time-resolved monitoring of the fractional coverage grade of the electrode with cells.

### 3.6.1 Cell-based Assays using Commercially Available ECIS Arrays

For the ECIS experiments in this work, commercially available eight-well electrode arrays from *Applied BioPhysics Inc.* were utilized. These arrays consist of eight separate wells with a growth area of 0.8 cm<sup>2</sup> each and an inner volume of 600 µL per well. The substrate consists of Lexan® polycarbonate, which is coated with a thin gold film, covered with photopolymer. Photolithography is used to remove the polymer on the electrical contacts as well as on working and counter electrodes, exposing the gold film to the surrounding medium. Each of the wells contained one or more circular working electrodes with a diameter of 250 µm, depending on the respective array type, shown in Table 3.2. During a last manufacturing step an eight-well polystyrene chamber with lid is fixed on the base substrate with silicone glue to form eight individual measurement chambers. Subsequently, the arrays are exposed to an oxygen plasma which cleans the electrodes and sterilizes the chambers and lids.

**Table 3.2:** Specifications of commercial ECIS arrays according to *Applied BioPhysics Inc.* (<http://www.biophysics.com/cultureware.php>).

ECIS Array	Electrodes per Well	Electrode Area /mm <sup>2</sup>	Number of Cells measured
<b>8W1E</b>	1	0.049	50-100
<b>8W10E</b>	10	0.49	500-1000
<b>8W10E+</b>	40	1.96	2000-4000

#### Cytotoxicity and Cell Migration Assays

Cytotoxicity and cell migration assays were carried out in 8W1E arrays, as shown in Fig. 3.21. Therefore, NRK cells were seeded in a density of 200.000 cells/well two days prior to the experiment. One day before the experiment the cells were fed with fresh medium. Cytotoxicity assays were carried out by exposing the cells to increasing C-dot concentrations, keeping the cells permanently in contact with the particle suspension and monitoring impedance/capacitance over time. Cell migration was studied by first wounding the cell layers grown on the working electrodes by applying a lethal electric pulse (30 s, 5 V, 40 kHz). Recovery of the electrodes impedance and capacitance due to repopulation of the electrode by migrating cells then followed with time. Thereby, the impact of C-dots on the cells' ability to migrate was investigated.



**Fig. 3.21:** a) Commercially available 8W1E ECIS array from Applied Biophysics. b) Magnification of one well of the array with the small working electrode in the middle and the large u-shaped counter electrode on the bottom.

### Phototoxicity Assay

Phototoxicity evaluations with C-dots in suspension were performed using 8W10E ECIS arrays. NRK cells were seeded and fed similarly as mentioned before. On the day of the experiment, the cells were incubated with the 0.3 mg/mL C-dots in EBSS<sup>++</sup>/Glucose (1 g/L, EBSS<sup>++</sup>/G). After 10 min the suspension was irradiated with a standard UV lamp (366 nm, 2x6 W) for 10 min, as shown in Fig. 3.22. Subsequently, the array was transferred into an incubator, electrically connected and the time-courses of impedance/capacitance were recorded.

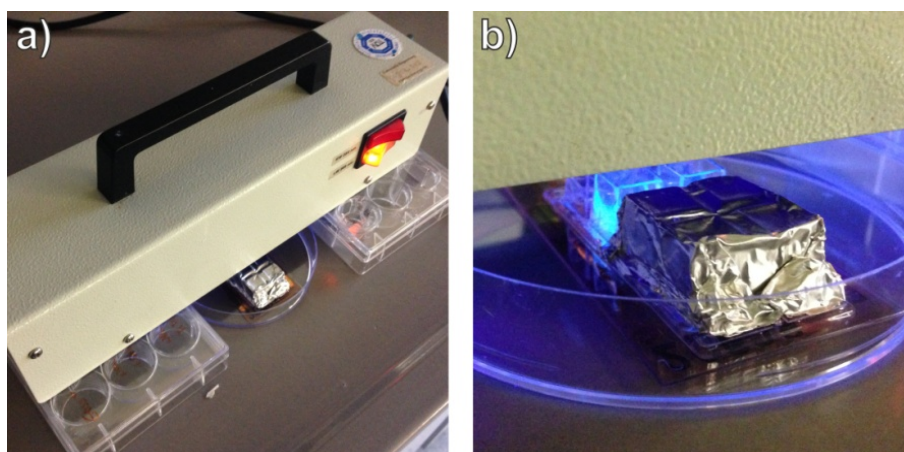


**Fig. 3.22:** Phototoxicity evaluation of C-dots in suspension. a) Set-up for the exposure of NRK cells to UV light (366 nm, 2x6 W) in 8W10E ECIS arrays. The cells are incubated in EBSS<sup>++</sup>/G containing 0.3 mg/mL C-dots. b) Closer view on the ECIS array. Control cells which were not meant to be irradiated were covered with aluminum foil.

### Cell Proliferation and Adhesion Assays

Cell proliferation and adhesion were measured in 8W10E+ ECIS arrays. This array type was preincubated with medium several hours before the experiment. Furthermore, the electrodes were cleaned via the “stabilize”-function of the ECIS software. For proliferation

## *Materials and Methods*

studies NRK cells were seeded in a density of 10.000 cells/well. Subsequently, the array was connected to an EICS device and impedance/capacitance was measured over time. After 6 h, the cells had adhered on the substrate and were then incubated with C-dots in serum-containing medium. For investigations on the influence of C-dots on cell adhesion, NRK cells were subcultivated and suspensions of the cells were incubated with the particles for 30 min. After incubation the cells were seeded in a density of 350.000 cells/well and changes of the impedance/capacitance were monitored over time.

All measurements with these arrays were carried out in humidified incubators at 37 °C and a 5% CO<sub>2</sub>-atmosphere. The arrays were electrically connected to a commercially available ECIS 1600R unit via an ECIS array holder, both from *Applied Biophysics*.



### 3.6.2 Monitoring the Impact of Carbon Dots on Cardiomyocyte Beating

Studies of the Cor.At® cardiomyocytes were performed in two commercially available 8W $\mu$ 1E ECIS arrays from *Applied BioPhysics Inc*, as shown in Fig. 3.23a. These are eight well arrays with 4 electrodes per well. Each electrode has an area of 0.196 mm<sup>2</sup>, so that 200 – 400 cells are monitored, according to the supplier. The arrays were modified by gluing silicone tube sections around the working electrodes in order to decrease the growth area and the number of cardiomyocytes needed. A photograph of one modified well of such an ECIS array is shown in Fig. 3.23b. Prior to the experiments the bottom of the wells were coated with fibronectin (from bovine plasma, *Sigma Aldrich*) in order to enable adhesion of the cardiomyocytes on the electrodes.

Before and after incubation with C-dots in medium, the regular beating of the cardiomyocytes was monitored via the rapid time collect (RTC) data acquisition provided by the commercial ECIS software from *Applied Biophysics Inc*. Impedance of the electrodes was monitored at 4 kHz, collecting 64 data points per second. The experiment was carried out on two ECIS arrays simultaneously, monitoring each electrode for 72 sec, cycling three times through all 16 wells per measurement. The obtained impedance time courses were analyzed for the amplitude and the frequency of the beating using a *LabView*® based software.

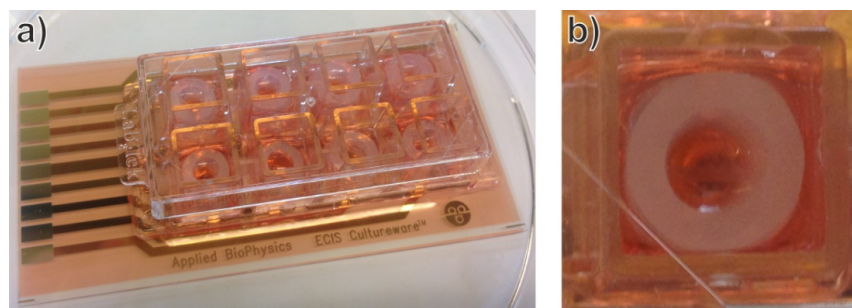


**Fig. 3.23:** a) Commercially available 8W1 $\mu$ E ECIS array from Applied Biophysics, each well modified with a silicone tube section. b) Magnification of one well of the array with the working electrodes in the middle, surrounded by a silicone tube section, yielding a smaller growth area.

All measurements with these arrays were carried out in humidified incubators at 34 °C and a 5% CO<sub>2</sub>-atmosphere. The arrays were electrically connected to a commercially available ECIS Z $\theta$  device via an ECIS array holder, both from *Applied Biophysics Inc*.

### 3.6.3 Monitoring the Phototoxicity of Carbon Dots by ECIS

The phototoxicity of internalized C-dots was investigated without particles in the surrounding medium, in order to study exclusively their intracellular impact via generation of reactive oxygen species (ROS). Therefore, a custom-made ECIS array with indium tin oxide (ITO) electrodes on a polymer substrate was used. As electrode layout an 8W1E design was chosen and the structure of the electrodes and connecting pads was defined with a photoresist (AZ ECI3027, AZ Electronic Materials GmbH) and photo-lithography. A photograph of one of those arrays is shown in Fig. 3.24a. The advantage of ITO as substrate is that it is electrically conducting and optically transparent at the same time. This allows for a well defined light exposure of the cells on the electrodes using an inverted microscope.

NRK cells were seeded and fed on the ITO arrays in a similar way as for cytotoxicity evaluations. On the day of the experiment the cells were incubated with C-dots (1.0 mg/mL in EBSS<sup>++</sup>/G) for 1 h. Afterwards, the cells were washed twice with EBSS<sup>++</sup>/G to ensure that only internalized C-dots remain in contact to the NRK cells. Subsequently those cells on the electrodes were focused and irradiated, as shown in Fig. 3.24b. Therefore, an inverted microscope (Nikon Diaphot) with a 10x/1.25 objective was used with a Nikon UV-2A filter block (excitation filter: 330-380 nm, bandpass) and a mercury vapor lamp (Nikon HB-10101AF) as light source.

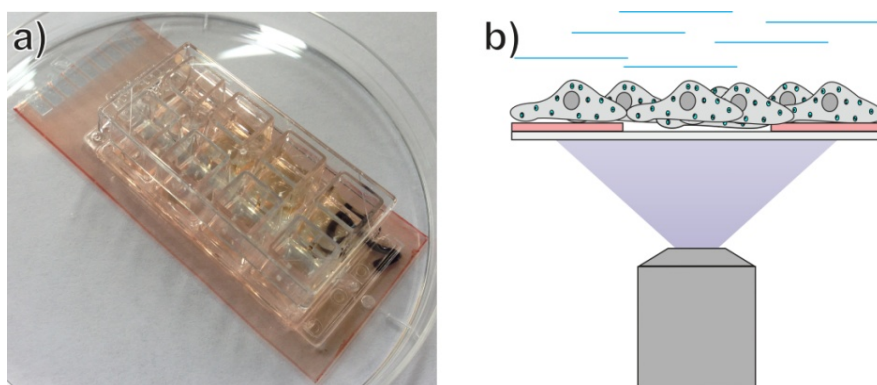


**Fig. 3.24:** a) Photograph of a custom-made 8W1E ECIS array with ITO as electrode material and photopolymer for the definition of electrodes and conducting pads. b) Schematic of the focused irradiation of internalized C-dots through the ITO substrate using an inverted microscope.

Impedance measurements were carried out on a custom-made device, using individual electronic components. The set-up consisted of an impedance analyzer (SI-1260, Solartron Instruments), an external frequency generator (Hewlett Packard: model 33120), a micro controller and a relay. The computer-controlled micro controller is used to switch between the impedance analyzer for non-invasive measurements and the frequency generator for manipulating cells. The relay connects the working electrodes with the respective counter electrode. Software written in LabView® collects the recorded data. For

the electrical connection of the electrode array a special holder (*Applied BioPhysics Inc.*) was used in a humidified incubator at 37 °C with 5% CO<sub>2</sub>.

The manufacturing of the ITO ECIS electrode arrays was performed by Romy Freund at the Institute of Analytical Chemistry, Chemo- and Biosensors, University of Regensburg.

### 3.7 Permeation Studies across Barrier-forming Cell Monolayers

Since C-dots are only a few nanometers in size and are well-known to easily penetrate cell membranes, the particles were investigated for their permeation kinetics through cell layers (Song *et al.* 2014). Therefore, porous cell culture inserts covered with cells monolayers were used. To pursue such a study, the analyte is added to the upper compartment of such an insert and it has to diffuse through the cell layer in order to equilibrate the concentration gradient and reach the lower compartment. The presence of the C-dots in the lower compartment can be easily detected by fluorescence spectroscopy.

As permeable cell culture substrates *Corning® Transwell®* filters (No. 3401) from *Costar* were used. These consist of a polycarbonate membrane with pore diameters of 400 nm and a density of  $10^8$  pores/cm<sup>2</sup> and a surface area of 1.12 cm<sup>2</sup>. A photograph of one of those filter inserts is shown in Fig. 3.25a. The filters were placed in a 12-well plate, with 1.5 mL cell medium in the lower compartment and 0.5 mL of the respective cell suspension in the upper compartment. NRK, MDCK I and MDCK II cells were seeded in densities of 500.000 cells/filter insert, two days prior to each experiment. To pursue the experiment, the medium was exchanged against EBSS<sup>++</sup>/G and the filters were transferred into a new 12-well plate with 1.5 mL EBSS<sup>++</sup>/G in the lower compartment. The upper one was filled with 0.5 mL of 0.3 mg/mL C-dots in EBSS<sup>++</sup>/G, respectively with 2 mg/mL FITC-labeled Dextran (4 kDa, Sigma Aldrich) as reference. The filters were placed in an incubator at 37 °C and 5% CO<sub>2</sub> and in distinct time intervals the fluorescence of the lower compartment was measured. Therefore, the filter inserts were taken out prior to every readout and fluorescence intensity was measured using a fluorescence plate reader *GENios* from *Tecan* (10 flashes, 40 μs, exc./em.: C-dots: 360/465 nm, FITC: 485/535 nm). After every measurement the filters were transferred back into the incubator. The principle of the experiment is shown in Fig. 3.25b as schematic.

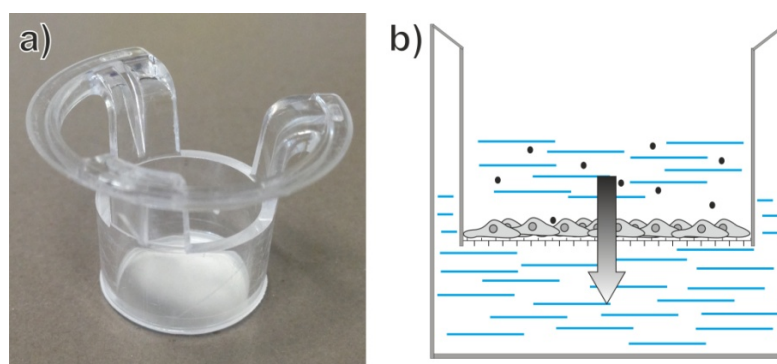


**Fig. 3.25:** a) Photograph of a Corning® Transwell® filter (No. 3401) from Costar. b) Illustration about the principle of the permeation experiment. Particles from the upper compartment have to diffuse through the cell layer to reach the lower compartment.

### 3.8 Protocols for *Loading* and Imaging of Mammalian Cells with Carbon Dots

In order to ensure constant quality of the staining and *loading* of mammalian cells with C-dots, standard protocols for the incubation with the particles were developed. Furthermore, CLSM imaging conditions were established for the application in a Live-Dead-Assay and for phototoxicity assays in a light-induced cell manipulation approach based on C-dots, as described later.

#### Live-Dead-Staining of Mammalian Cells via Carbon Dots

Since cytotoxicity of diverse toxicants was investigated via C-dots, the incubation with the particles should be as non-invasive as possible. Therefore very short incubation times of 30 min were chosen with 1.0 mg/mL C-dots in PBS<sup>++</sup> at 37 °C. Afterwards the cells are washed with twice with PBS<sup>++</sup> and analyzed via CLSM. The short contact of the cells to the particles should ensure that additional impairments of cell physiology are minimized and only the toxicants' effects on cell health are observed. A concentration of 1.0 mg/mL was chosen since this is below the EC<sub>50</sub> value and enables maximum uptake of C-dots along the short incubation time. The incubation at 37 °C was chosen to provide proper conditions for endocytosis, which is suggested to be the main uptake mechanism for C-dots into living cells. Upon laser excitation at 405 nm the cytoplasm of living cells exhibits blue luminescence due to uptake of the particles in low concentrations. Dead cells by contrast lost plasma membrane integrity and therefore C-dots may freely enter those cells' nuclei. The subsequent accumulation of the particles in the nuclei and binding to DNA is suggested to influence the optical properties of C-dots. As such, the nuclei of dead cells exhibit bright green luminescence upon laser excitation at 488 nm, as indicated in the schematic of Fig. 3.26a.

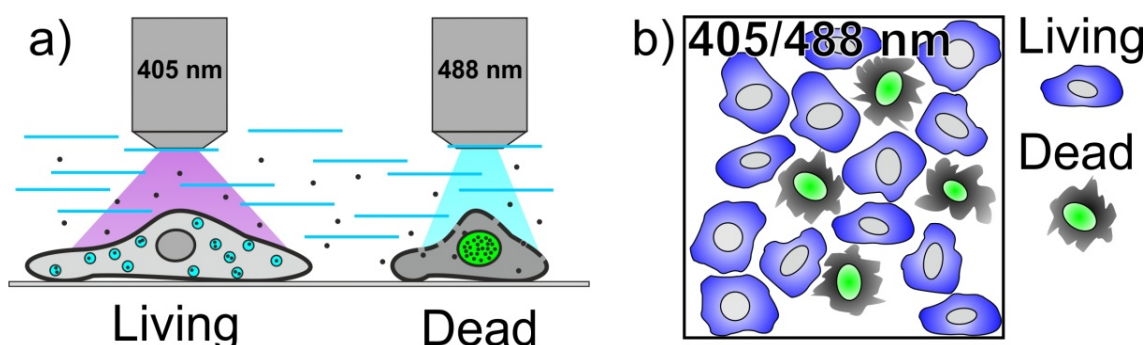


**Fig. 3.26:** Principle of the staining and CLSM imaging of living and dead mammalian cells with C-dots. a) Schematic side-view of living and dead cells upon exc. at 405 nm or 488 nm, respectively. b) Schematic of living and dead cells under simultaneous exc. at 405/488 nm.

## *Materials and Methods*

For the CLSM imaging of the C-dot stained cells, mostly a water immersion objective (60x/1.00) was used with Pinhole L and RGB detector gains of 130, see chapter 3.4.2. The imaging of a cell sample with simultaneous laser excitation at 405/488 nm, results in the different coloration of living and dead cells, as shown in the schematic of Fig. 3.26b.

### Loading of Normal Rat Kidney Cells with Carbon Dots to Combine Light-induced Cell Manipulation and Multicolor Imaging

For the *loading* of NRK cells with C-dots the short-term incubation protocol was slightly modified in order to maximize internalization of the particles. This should ensure that the generation of ROS inside living cells upon excitation of C-dots shows highest efficiency with respect to triggering apoptosis in target cells. At the same time, the physiology of those cells loaded with the particles but not being irradiated should be as unaffected as possible. Therefore, the incubation time was prolonged to 60 min with 1.0 mg/mL C-dots in EBSS<sup>++</sup>/Glucose (1 g/L) at 37 °C, 5% CO<sub>2</sub>. The buffer was adapted to a carbonate system, as the longer incubation was performed in standard incubators with CO<sub>2</sub> atmosphere. Afterwards, the cells were washed twice with EBSS<sup>++</sup>/Glucose and kept in the buffer during irradiation. 5 min of epi-illumination with the set-up described in chapter 3.6.3 induced distinct wounds of the cell layer after 1 – 3 h incubation time, at 37 °C, 5% CO<sub>2</sub>. The dead cells in the field of exposure exhibit bright green luminescent nuclei upon excitation at 488 nm via CLSM. At the same time, surrounding cells in healthy condition exhibit a bright blue cytoplasm upon excitation at 405 nm, as indicated in the schematic of Fig. 3.27a.

Irradiation of the cells via CLSM lasers for the light-induced manipulation approach on single cell level requires the extension of the set-up with a heating thermostat maintaining 37 °C during waiting time. Therefore, C-dot-loaded NRK cells grown in a small Petri dish are placed in a special copper thermostat with an external water heating and pumping device. This allows analyzing the cells after the waiting time without changing their position. At first, the cells are analyzed using 405/488 nm excitation. Target cells were then selected via digital zoom, and irradiated for 3 – 5 min with the 405 nm laser. After 1 h at 37 °C, the NRK cells are analyzed again by excitation at 405/488 nm. Thereby, irradiated cells exhibit the typical green luminescent nuclei surrounded by cells with a blue luminescent cytoplasm as shown in Fig. 3.27b.

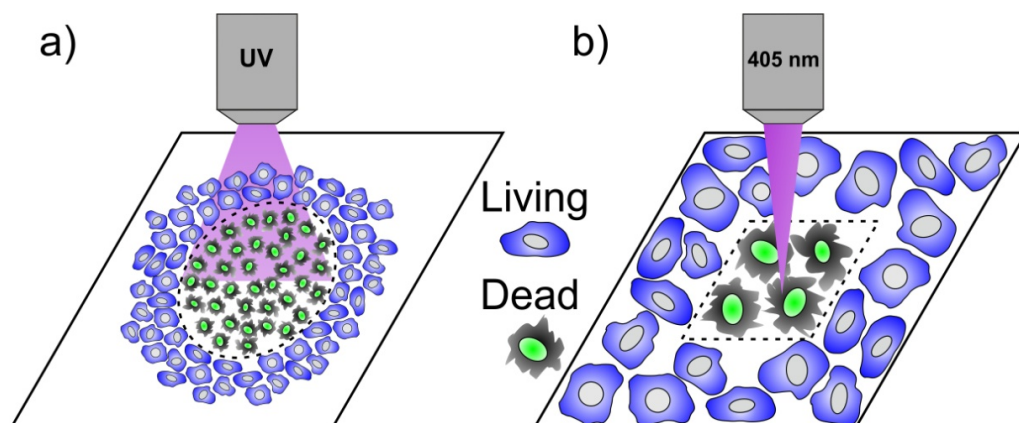


**Fig. 3.27:** Schematic for the light-induced cell manipulation based on C-dots. a) UV-Irradiation in large area via epiluminescence microscopy. b) Irradiation by 405 nm laser. Living cells exhibit a blue cytoplasm upon exc. at 405 nm, dead cells exhibit green nuclei upon exc. at 488 nm after the treatment.





## 4 Characterization of the Carbon Nanomaterials

The following chapter gives insight in the thorough investigations on the physicochemical and optical properties of the carbon nanomaterials, prepared in this work. Specifically, the characteristics of these are described in the following order: C-dots, GQDs, chemically modified C-dots and nanostructures with embedded C-dots.

### 4.1 Characterization of Carbon Dots

The characterization of the C-dots should at first verify the successful nanostructure formation from the precursor molecules. Furthermore, the dimensions and morphology of the particles was investigated. Based on this, the chemical composition and the spectroscopic properties of the C-dots were studied.

#### 4.1.1 Size Determination of Carbon Dots

##### Dynamic Light Scattering

Size distributions of the N-doped and undoped C-dots were studied at first in suspension by measuring the hydrodynamic diameter ( $d_H$ ) of the particles via DLS. The hydrodynamic diameter is in direct correlation to size and surface charge of the particles. Furthermore, it plays an important role for the application of C-dots in aqueous media, since the particles are internalized into living cells, for example, with their hydrate shell. Typical results for the DLS analysis of the particles in PBS are shown in Fig. 4.1a for N-doped C-dots and in Fig. 4.1b for undoped C-dots.

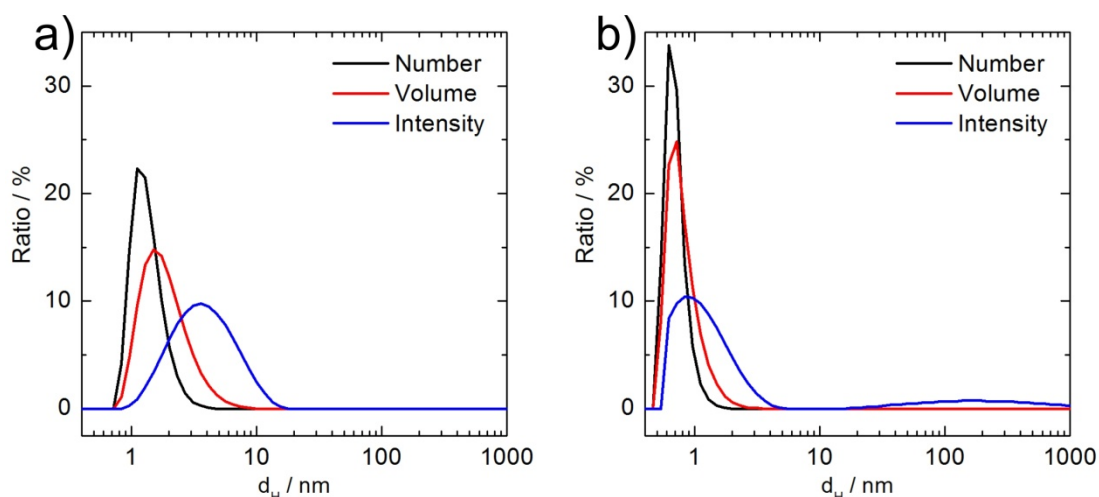


**Fig. 4.1:** Hydrodynamic diameter distributions expressed as number, volume or DLS intensity of the N-doped C-dots a) or the undoped C-dots b) in PBS at 25 °C.

A typical result of the DLS analysis of N-doped C-dots, such as the one shown here, yields hydrodynamic diameter distributions between 0.8 and 10 nm. Among different batches, these hydrodynamic diameter distributions are highly reproducible, varying only. In

contrast to these particles, the undoped C-dots were particularly smaller with distributions between 0.5 and 3.1 nm. Also the average values of the different distributions, shown in Table 4.1 confirm this tendency, since the averages for the particle number, volume and intensity are all at larger diameter for the N-doped C-dots. Hereby, it has to be mentioned that DLS is on the limit of the size determination with 0.6 nm. As such, these values may only be seen as indications for possible particle formations.

**Table 4.1:** Average values obtained from the distributions of the DLS measurements in Fig. 4.1 with standard deviations as error.

Peak	N-doped C-dots	Undoped C-dots
Number	1.4 ± 0.4 nm	0.7 ± 0.2 nm
Volume	2.0 ± 1.0 nm	0.8 ± 0.3 nm
Intensity	4.4 ± 0.2 nm	1.3 ± 0.7 nm

The observation of particularly larger hydrodynamic diameter for those C-dots prepared with Trp could be attributed to an important role of the amino acid in the particle formation process. Dehydration catalysis and chemical bond formation in the polymerization steps, as indicated in Fig. 1.4 and Fig. 3.4, may be linked to the presence of Trp. Larger C-dots from carbohydrates in presence of Trp are furthermore in accordance with reports from literature (Simoes *et al.* 2014). Since the zeta potential of the particles at physiological pH was found to be almost neutral, surface charge effects do only play a minor role for influences on the hydrodynamic diameter. More information on the effect of the addition of Trp on the chemical composition of the C-dots and the zeta-potential is given in chapter 4.1.2.

### Atomic Force Microscopy

For practical applications in cellular imaging, only the N-doped C-dots are of significant interest due to enhanced quantum yields, shown in chapter 4.1.3. As such, the morphology of this type of C-dots was characterized in detail via AFM. In Fig. 4.2a-c AFM micrographs of dried C-dots on mica substrate are shown with increasing magnification. The particles were analyzed for their height profile and a corresponding distribution for the measurement of 202 particles is shown in Fig. 4.2d.

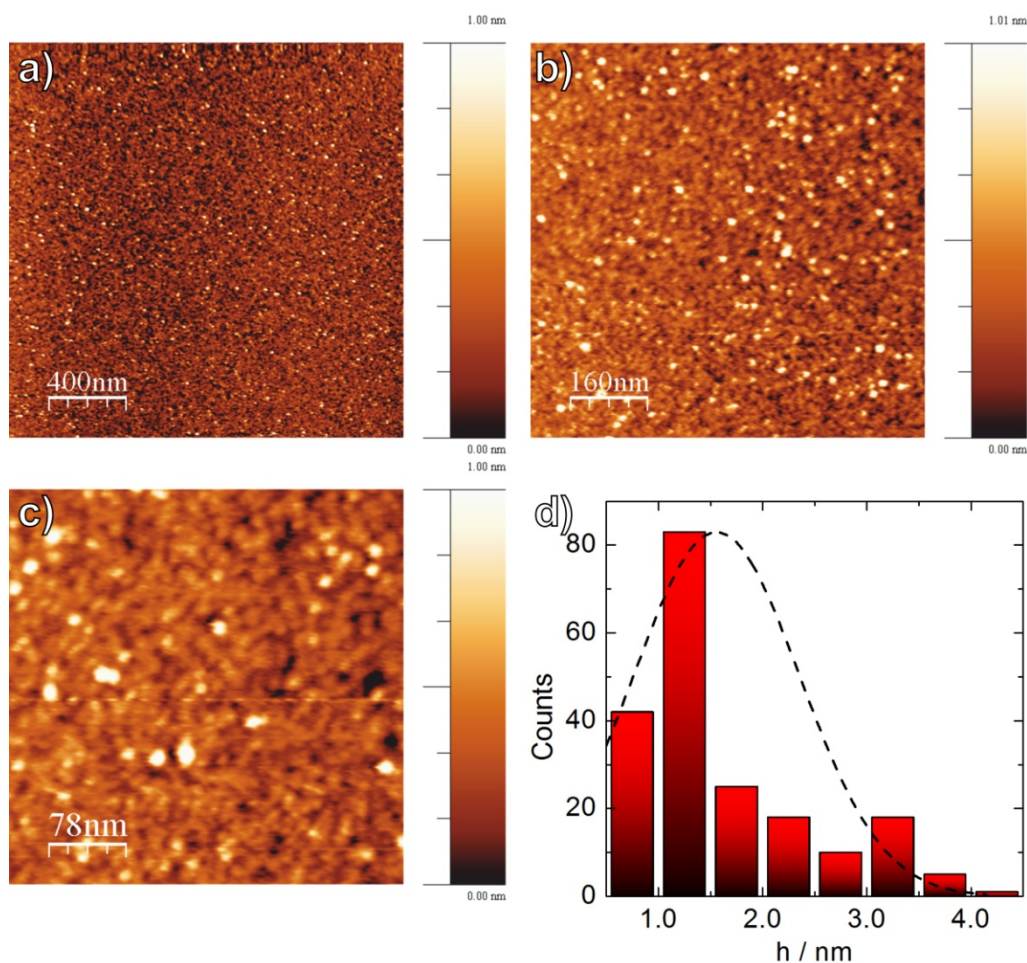


**Fig. 4.2:** a-c) AFM micrographs of dry N-doped C-dots on mica substrate. Magnification increasing from picture a) to c). d) Height distribution of N-doped C-dots measured over 202 particles, yielding an average of 1.6 nm with a standard deviation of 0.8 nm. The dashed line represents a normal distribution after least square optimization.

Analyzing the height of the N-doped C-dots reveals a distribution between 0.5 and 4.5 nm, with the majority of the particles between 1.0 and 1.5 nm and decreasing numbers towards larger particle heights. The average over all measured particles is 1.6 nm with a standard deviation of 0.8 nm. These results are consistent with those from DLS (average of 3.2 nm), since the diameter of the dry particle is always smaller than its hydrodynamic diameter.

In summary, the HTC process from starch and Trp apparently yields C-dots with a size distribution between 0.5 and 4.5 nm. While most of these particles are smaller than 2.0 nm, there are significant amounts of larger species. As such, the particles may have to be considered as a mixture of different species with possibly different spectroscopic and/or chemical properties.

### 4.1.2 Functionalization of Carbon Dots

The following chapter covers the characterization of the chemical composition and functionalization of N-doped C-dots from starch and Trp.

#### Elementary Analysis

Chemical groups and doping of the particles is indicated by their elemental composition. In order to study the composition of the C-dots and the influence of the addition of Trp on the efficiency of N-doping and dehydration, elementary analysis was carried out. The obtained mass ratios of the elemental composition from the analysis of starch as main precursor, as well as undoped and N-doped C-dots with varying amounts of added Trp for the HTC process are shown in Table 4.2.

**Table 4.2:** Mass ratios (w/w) of the elemental compositions of starch, undoped and N-doped C-dots. The composition of the brightest and mainly studied particles in this work is indicated in bold.

	<b>C</b>	<b>H</b>	<b>N</b>	<b>O<sub>(calc.)</sub></b>
Starch	40.4%	6.6%	0.0%	53.0%
C-dots undoped	40.1%	6.6%	0.0%	53.3%
C-dots 150 mg Trp	42.9%	6.3%	0.5%	50.3%
<b>C-dots 350 mg Trp</b>	<b>44.9%</b>	<b>6.1%</b>	<b>1.1%</b>	<b>47.9%</b>
C-dots 500 mg Trp	47.3%	6.0%	1.6%	45.1%

As demonstrated by the results, the hydrothermal treatment of starch without the addition of Trp led to marginal dehydration of the precursor material. Accordingly, undoped C-dots exhibit almost the same elemental composition as starch. The addition of Trp by contrast, yields an increasing content of carbon, while hydrogen and oxygen ratios are decreasing directly proportional to the amount of added Trp. This is due to increasing dehydration efficiency because of catalysis by Trp, as known for amino acids via Schiff' base reaction (Hodge 1979). As such, it may be assumed that Trp plays a significant role in the dehydration of starch and consequently for particle formation. Furthermore, the increase of the amount of Trp leads to a simultaneous increase in the nitrogen content of the obtained material. The N-doped C-dots which were used for all further studies exhibit a nitrogen mass content of 1.1%. Several reports on C-dots and GQDs indicate that doping with nitrogen drastically increases photoluminescence. As such, this might be the reason for the enhanced brightness of these C-dots. (Li *et al.* 2012c; Dong *et al.* 2013b).

## X-Ray Photoelectron Spectroscopy (XPS)

In order to retrieve information about the chemical binding of the elements within the C-dots XPS measurements were performed on lyophilized particles. The respective spectra are shown in Fig. 4.3.

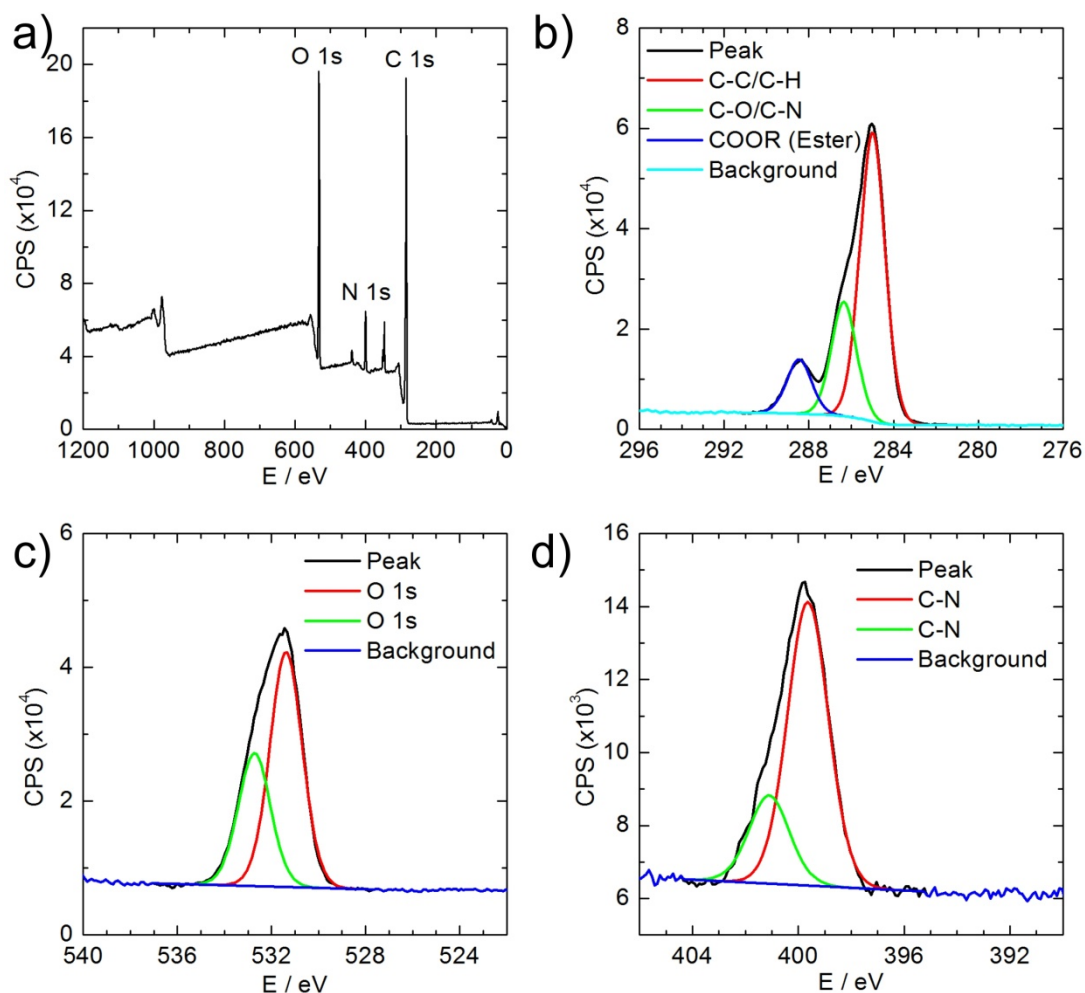


**Fig. 4.3:** XPS spectra of C-dots. Electron binding Energy E expressed in eV. a) Overview spectrum with assignment of the oxygen, nitrogen and carbon peak. b-d) High resolution spectra of the carbon (b), oxygen (c) and nitrogen (d) peaks.

X-ray photoelectron spectroscopy revealed the presence of carbon (C 1s, 285 eV), nitrogen (N 1s, 400 eV) and oxygen (O 1s, 532 eV). The expanded C 1s peak contains signals at 285.0 eV, 286.3 eV, and 288.5 eV, which correspond to COOR, C-O/C-N and C-C/C-H moieties. The expanded N 1s peak indicates two different C-N binding types with signals at 399.6 eV and 401.1 eV. According to the peaks in the XPS spectra the particles exhibit the following functionalities on their surface: C-OH, C=O, C-N, C=N. The carbon-nitrogen bonds are suggested to enable brightest photoluminescence due to influences on the emitters' band gap through the addition of electron donating groups (Li *et al.* 2012c; Wang *et al.* 2015a). C-NH<sub>2</sub> moieties would also be possible according to XPS signaling of the expanded N-peak, but the absence of these groups was verified via selective dye binding experiments.

### Detection of Amine Groups with Selective Chameleon Dyes.

The absence of chemically reactive primary amine groups on the C-dot surface was proven using the amine selective chameleon dyes S 0378 (FEW Chemicals) and Py-1 (Wetzel *et al.* 2004). Both of them did not show any chemical reaction with the particles, while positive controls using amines led to a clear change of their optical properties.

### Infrared Spectroscopy

Chemical moieties on the particles surface were also investigated via IR spectroscopy, applied to lyophilized C-dots. This method was chosen, since Raman spectroscopy is heavily disturbed through the C-dots intrinsic fluorescence. A typical IR spectrum of the particles is shown in Fig. 4.4.

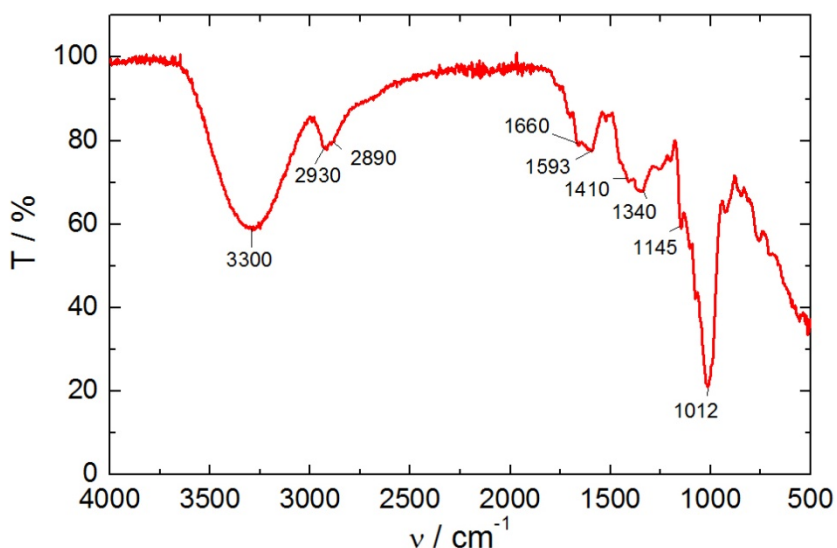


**Fig. 4.4:** IR spectrum of lyophilized C-dots with the wavenumbers of the most prominent peaks.

The spectrum exhibits characteristic peaks at 3600 – 3100  $\text{cm}^{-1}$  (-OH stretching vibration), 2930 and 2890  $\text{cm}^{-1}$  (symmetric and asymmetric C-H stretching vibration), and at 1410 and 1340  $\text{cm}^{-1}$  (C-H deformation vibrations). The peaks at 1660 and 1593  $\text{cm}^{-1}$  are assigned to the amide I and II stretching vibrations, while those at 1145 and 1012  $\text{cm}^{-1}$  result from C-O stretching vibrations.

As such, IR spectroscopy reveals that several functionalities of the precursor molecules remain in the particles. Among these, hydroxyl groups from starch are most likely to be particularly present. Interestingly, also amide stretching vibrations were detected with IR spectroscopy. This indicates that molecular fragments of Trp may be considered as parts of the C-dots nature through new chemical bond formations with starch during the preparation process.

### Zetapotential

Surface charge of a particle is determined by its chemical groups. As such, the zeta potential of the C-dots and its changes upon variation of the pH-value of the surrounding buffer may give information about their chemical functionalization (Cho *et al.* 2014). The normalized zeta potentials of aqueous C-dot suspensions at different pH values are shown in Fig. 4.5.

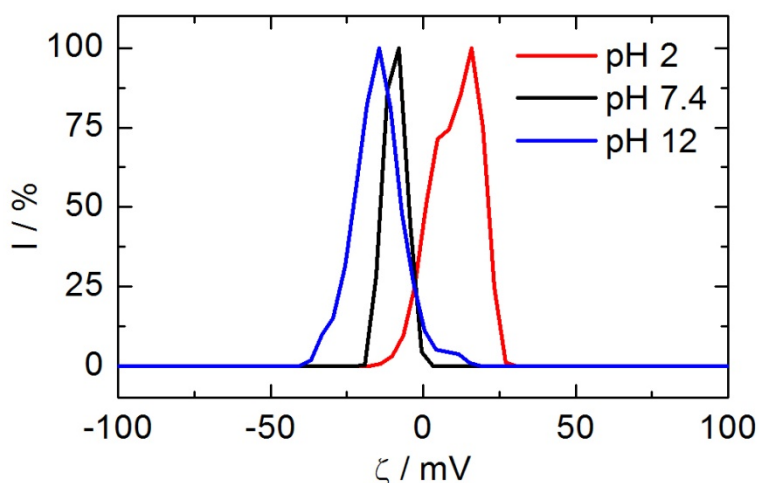


**Fig. 4.5:** Normalized zeta potentials of aqueous C-dot suspensions (5.0 mg/mL) at 25 °C. The particles were suspended in: HCl solution (pH 2), PBS (pH 7.4), in NaOH solution (pH 12).

As demonstrated by the results, the C-dots are marginally negatively charged at physiological pH of 7.4 with a zeta potential of  $(-9.3 \pm 3.5)$  mV. An increase of the pH to a value of 12, leads to a slightly more negative potential of  $(-14.7 \pm 8.3)$  mV which may be attributed to deprotonation at the particle surface. Since the change of the surface charge is rather small, basic groups such as amines seem to be rare on the particles surface. This is in accordance with the proven absence of amine groups, described in previous studies. In the acidic solution of pH 2 by contrast, the C-dots show a clearly positive zeta potential of  $(10.6 \pm 7.6)$  mV. This effect is rather strong and as such protonation of acidic groups such as carboxyl groups is the reason for the change of the surface charge.

In summary, the C-dots prepared via HTC of starch and Trp are obviously the result of dehydration reactions of the precursor molecules. This is evident from the increase of the carbon content and a simultaneous decrease of the oxygen and hydrogen content in comparison to starch. Furthermore, the doping with nitrogen by adding Trp as precursor molecule was successful, proven by IR spectroscopy, XPS and elementary analysis. Most likely, the particles exhibit hydroxyl and carboxyl groups as functional moieties, which are oxidized residues of the carbon source starch or direct remnants of Trp.

### 4.1.3 Spectroscopic Properties of Carbon Dots

The following chapter mainly describes the characterization of the optical properties of the N-doped C-dots and the effect of the doping with Trp. Furthermore, different influences on the particles photoluminescence were studied and discussed. All measurements were performed in aqueous suspensions.

General photoluminescence properties were studied by measuring the absorption, excitation and emission spectra of N-doped and undoped C-dots in aqueous suspension at a mass concentration of 1.0 mg/mL, which shows highest fluorescence intensity. The spectra of the N-doped C-dots are shown in Fig. 4.6a, those of the undoped C-dots in Fig. 4.6b.

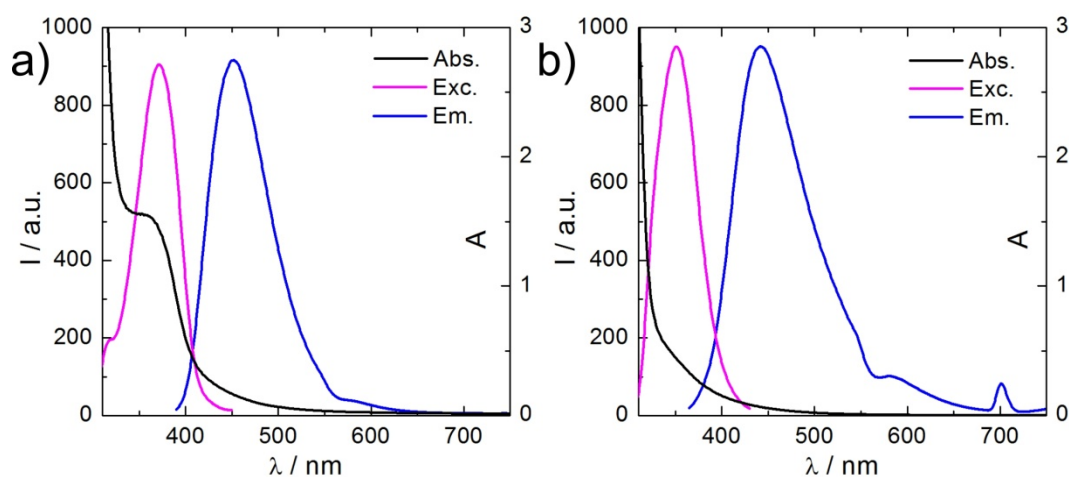


**Fig. 4.6:** Absorption, excitation and emission spectra of N-doped C-dots (a) and undoped C-dots (b) in aqueous suspension with mass concentrations of 1.0 mg/mL. Exc./Em. maxima 371/452 nm (a), 351/442 nm (b). The peak at 700 nm in the emission spectrum of undoped C-dots occurs due to second order light diffraction. Detector sensitivity settings were changed for undoped C-dots, due to their low quantum yields.

As shown in the spectra of Fig. 4.6a, such a suspension of N-doped C-dots exhibits an emission maximum at 452 nm, while highest fluorescence intensities may be achieved with excitation at 371 nm. The emission spectrum is surprisingly broad, covering the whole visible spectrum (VIS). While highest fluorescence intensities may be found between 400 and 550 nm, fluorescence intensity is weaker at higher wavelengths. An explanation for this behavior may be, that C-dots consist of different particle species with different optical properties. As such, the probability for the formation of particles with smaller delocalized electron systems (short wavelength emission) is more likely than for those with more expanded electron systems (long wavelength emission). The particles absorb light over the whole UV/VIS region and absorbance increases exponentially towards shorter wavelengths. Remarkably, N-doping results in high absorbance values in the region of the wavelength of the excitation maximum. Undoped C-dots by contrast, do not exhibit this “shoulder” in their absorption spectrum, as shown in Fig. 4.6b. Accordingly, the doping with



Trp may be responsible for the formation of highly photoluminescent C-dot species excitable in the near UV region. The maxima for the excitation and emission of undoped C-dots were found at 351 nm and 442 nm, respectively. Both values are at shorter wavelengths than those for N-doped C-dots. This could indicate that the addition of Trp may lead to the formation of particle species with more expanded delocalized electron systems of  $sp^2$ -hybridized carbon atoms. Furthermore, the incorporation of nitrogen may influence the band gap of the particles towards longer wavelength excitation and emission (Wang *et al.* 2015a).

#### Variation of the Excitation Wavelength

As described for other preparations in literature, the photoluminescence of C-dots is highly variable in terms of excitability (Li *et al.* 2012a; Long *et al.* 2012). The emission spectra of an aqueous suspension of N-doped C-dots for different excitation wavelengths between 300 and 500 nm in 20 nm steps and the corresponding normalized spectra are shown in Fig. 4.7.

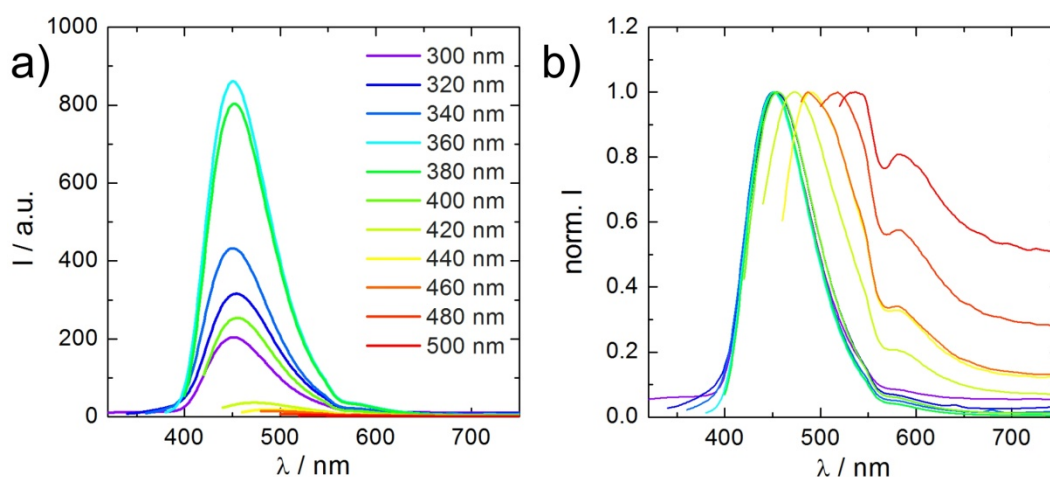


**Fig. 4.7:** Emission spectra of N-doped C-dots in aqueous suspension with a mass concentration of 1.0 mg/mL at 20 °C. Excitation wavelength was varied between 300 and 500 nm in 20 nm steps. a) Native emission spectra, b) emission spectra normalized to their respective maximum.

As demonstrated in the spectra of Fig. 4.7, the irradiation with wavelengths between 300 and 400 nm leads to excitation of particle species with 450 nm as emission maximum. Highest intensities are reached for an excitation at 360 nm, which decreases for shorter and longer wavelengths. The corresponding normalized spectra in Fig. 4.7b are highly congruent, confirming that emission occurs from the same photoluminescent species. At higher excitation wavelength, emission maxima are increasingly red shifted with increasing excitation wavelength but fluorescence intensity decreases further. Convergence of the normalized spectra was found a second time for excitation with 440 and 460 nm and an emission maximum at 487 nm. These observations could further indicate that the N-doped C-dots may consist of different photoluminescent species with distinct groups among them dominating the optical properties of the particle mixture. This would be in great accordance

to recent reports in literature that C-dots are supposed to be a “fluorescent cocktail of polycyclic aromatic hydrocarbons” (Fu *et al.* 2015). Furthermore, the data shows that the particles are highly variable in the wavelength of the photo excitation which is the base for multicolor imaging using different lasers in CLSM.

### Quantum Yield

In order to quantify the brightness of the photoluminescence of the N-doped C-dots and to qualify the effect of the doping with Trp the quantum yield (QY) of both types of C-dots was determined. Therefore, the emission spectra of aqueous suspensions of C-dots with absorbance values below 0.1 at their respective excitation maximum were recorded and the integrated spectra were plotted against the corresponding absorbance. Quinine sulfate in 0.1 M H<sub>2</sub>SO<sub>4</sub> was chosen as reference standard (QY = 54%) and the slopes of the linear fits for the plotting of the C-dots were compared against the one for quinine sulfate. The results for the QY determination are shown in Table 4.3.

**Table 4.3:** Quantum yields of undoped and N-doped C-dots determined via the “slope method” and quinine sulfate as reference standard. Values for N-doped C-dots originate from determinations of five different batches.

C-dots	QY
Undoped	0.6 ± 0.5%
N-doped	25.1 ± 2%

Obviously, the doping with nitrogen via addition of Trp to the HTC process leads to drastic increases in the QY of the particles. Thereby, the brightness of the N-doped C-dots exceeds the value of the undoped versions about thirty times. This is in accordance with reports from literature for higher QY for the C-dot doping with Trp (Simoies *et al.* 2014). As discussed before, the reason for this behavior are most likely changes in the band gap of the particles through the addition of nitrogen and furthermore the incorporation of Trp, resulting in larger delocalized electron systems able to show photoluminescence in the VIS. N-doped C-dots are therefore considered superior in the application for bioanalytical assays and multicolor imaging.

### Photoluminescence Lifetime

Photoluminescence lifetime of the N-doped C-dots was investigated to unveil the nature of the particles light emission and to clarify the possible presence of different C-dot species in suspension. In Fig. 4.8 a typical decay curve of the photoluminescence of 0.5 mg/mL N-doped C-dots in aqueous suspension is shown.

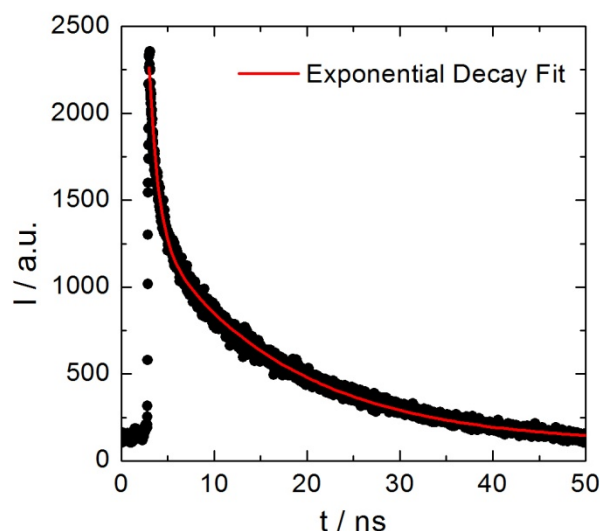


**Fig. 4.8:** Fluorescence lifetime measurement of N-doped C-dots in aqueous suspension with mass concentration of 0.5 mg/mL. The data was fitted via an exponential decay with the following formula:  $y = A_1 \cdot e^{(-x/t_1)} + A_2 \cdot e^{(-x/t_2)} + y_0$ , resulting in  $t_1 = 0.97 \pm 0.01$  ns and  $t_2 = 14.91 \pm 0.10$  ns,  $R^2 = 0.9954$ .

The exponential decay fit shown in Fig. 4.8 required at least two different decay times in order to fit the obtained lifetime data properly. Obviously the system is characterized by a short-term emission with a lifetime of  $0.97 \pm 0.01$  ns and a long-term emission of  $14.91 \pm 0.10$  ns. The length of the lifetimes suggests that the nature of the particles photoluminescence is fluorescence, which typically ranges between 0.5 and 20 ns (Lakowicz 2006). Single fluorescent species typically do only show one decay time. As such, the necessity of two different decay times for the fitting of the lifetime data may be a hint towards several luminescent species in suspension.

### Optical Properties in Dependency to Carbon Dot Concentration

In the following, the effect of the increase of the N-doped C-dot mass concentration on the fluorescence of the aqueous suspensions in PBS was studied. Therefore, two dimensional fluorescence plots were generated for particle suspensions with concentrations of 1, 5, 15 and 25 mg/mL in order to identify changes in their photo excitability and light emission behavior. With those plots, species which dominate the optical properties of the respective suspension are easily identified. The corresponding normalized fluorescence plots are shown in Fig. 4.9.

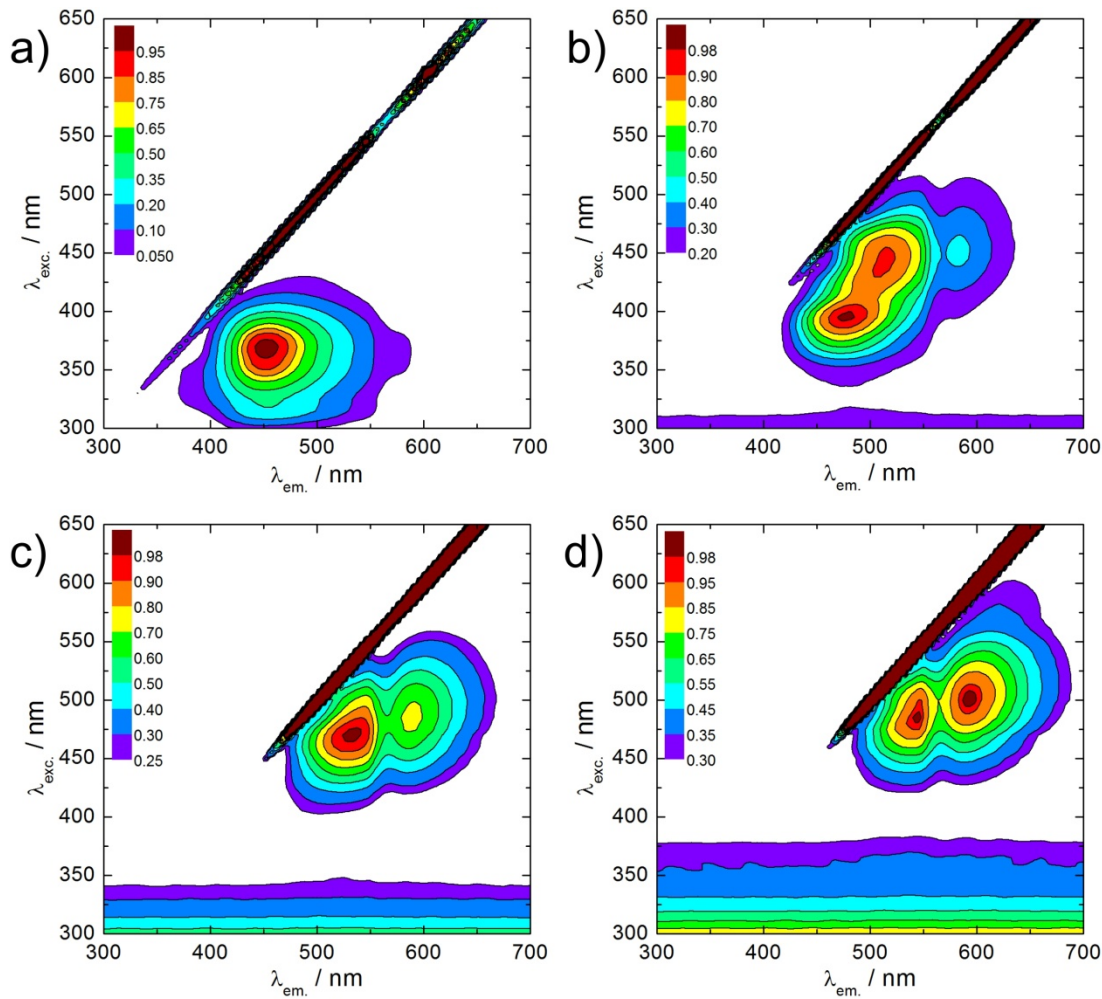


**Fig. 4.9:** Two dimensional fluorescence plots of N-doped C-dot suspensions in PBS with increasing mass concentrations at 20 °C. Each plot was normalized to the respective intensity maximum and the color code for the fluorescence intensity was adapted for each plot in relation to its maximum. The following N-doped C-dot suspensions were analyzed: 1 mg/mL (a), 5 mg/mL (b), 15 mg/mL (c), 25 mg/mL (d). High intensity diagonals in each plot occur due to stray light, where exc. and em. wavelength are equal.

Fluorescence intensity decreases in general with the increase of the particle concentration. In order to analyze the fluorescence qualitatively, the plots were normalized to their respective maximum. As shown in Fig. 4.9a, N-doped C-dot suspensions with a concentration of 1 mg/mL exhibit highest fluorescence intensities with excitation between 300 and 400 nm, while the emitted light has a wavelength between 400 and 600 nm. Highest fluorescence intensities may be achieved with exc./em. at 370/452 nm. Increasing the concentration to 5 mg/mL drastically changes these conditions, shown in Fig. 4.9b. Thereupon, three different intensity peaks occur in the two dimensional plot with the highest peak at exc./em. 395/476 nm. The two further fluorescence centers are at exc./em. 445/516 nm and 455/582 nm, respectively. Highest excitability is red shifted in general ranges between 350 and 500 nm, while emission occurs between 400 and 650 nm. Both, excitation and emission behavior are shifted towards longer wavelengths with the increase of the particle concentration. At 15 mg/mL, (Fig. 4.9c) the short wavelength excitable center seen in Fig. 4.9b does not occur anymore in the plot, while the maximum is here at

exc./em. 470/532 nm. The long wavelength excitable center at exc./em. 485/590 nm becomes more prominent at this concentration. Highest luminescence intensities may be recorded at excitation between 400 and 550 nm, while emission occurs between 450 to 650 nm. Again higher excitation and emission wavelengths yield higher fluorescence intensities with increasing particle concentration. At 25 mg/mL (Fig. 4.9d) the maximum fluorescence intensity comes from the long wavelength fluorescence center at exc./em. 500/592 nm, while the short wavelength component at exc./em. 485/544nm is almost at the same intensity level. Highest intensities are provided here with excitation between 425 and 600 nm, while emission occurs here at 500 to 700 nm.

Over all plots, a trend is evident that longer wavelength excitation and emission provides stronger fluorescence with increasing N-doped C-dots concentration of the suspensions. In general, three main fluorescence centers with emission in the blue, green and orange spectral region of the VIS were identified. An overview of these emission centers is given in Table 4.4.

**Table 4.4:** The peak maxima of the two dimensional fluorescence plots of Fig. 4.9. are categorized to the colors blue/green/orange.

<b>Emission</b>	<b>Exc./Em. /nm</b>	<b>Plot from Fig. 14</b>
<b>Blue</b>	370/452, 395/476	a, b
<b>Green</b>	445/516, 470/532, 485/544	b, c, d
<b>Orange</b>	455/582, 485/590, 500/592	b, c, d

The observation of distinct maxima in the plots with emission in the blue, green and orange may be attributed to different species in the N-doped C-dot suspensions. However, excitation and emission maxima of these species are concentration-dependent and are shifted towards longer wavelengths with increase of the concentration of the particle suspensions. This observation might be due to distinct species with different optical properties in the particle suspension.

For further clarification concerning the concentration dependency of the optical properties of the N-doped C-dots, absorption spectra of differently concentrated particle suspension were recorded. The spectra of these aqueous suspensions with concentrations of 1, 5, 10, 15 and 25 mg/mL are shown in Fig. 4.10.

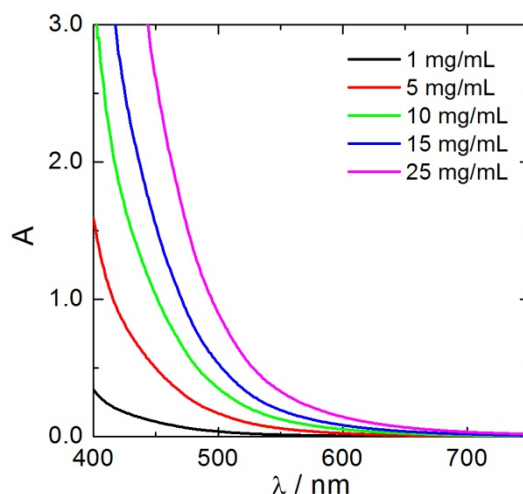


**Fig. 4.10:** Absorption spectra of N-doped C-dots in aqueous suspensions with varying mass concentrations.

As described before, absorption increases exponentially towards shorter wavelengths for N-doped C-dots. This effect amplifies drastically for higher concentrations, as shown in Fig. 4.10. The higher the particle concentration of the suspension the more reaches the absorption band towards longer wavelengths. According to this observation it may be suggested that at high concentrations short wavelength light is reabsorbed by the particles themselves and only the long wavelength light is detected. Furthermore, longer wavelength light would be necessary to excite a maximum amount of fluorescent species as light penetration is decreased for highly absorbing suspensions. This would be in accordance with the shift of the fluorescence excitation and emission maxima towards longer wavelengths for higher concentrated suspensions, described before.

#### Carbon Dot Fluorescence at Different Concentrations upon Excitation at the Wavelengths of the CLSM Lasers

Multicolor imaging experiments were performed via CLSM with three distinct laser wavelengths of 405, 488 and 543 nm. As such, the emission behavior of the particles in dependency to their concentration was studied at these wavelengths. Therefore, the emission spectra of aqueous suspensions of N-doped C-dots between 0.1 and 25 mg/mL were analyzed for their respective emission maximum. The fluorescence intensity and the wavelength of the emission maximum of each spectrum were plotted against the N-doped C-dot concentration in order to study possible changes of the optical properties. The respective fluorescence emission spectra and the C-dot concentration plots are shown in Fig. 4.11.

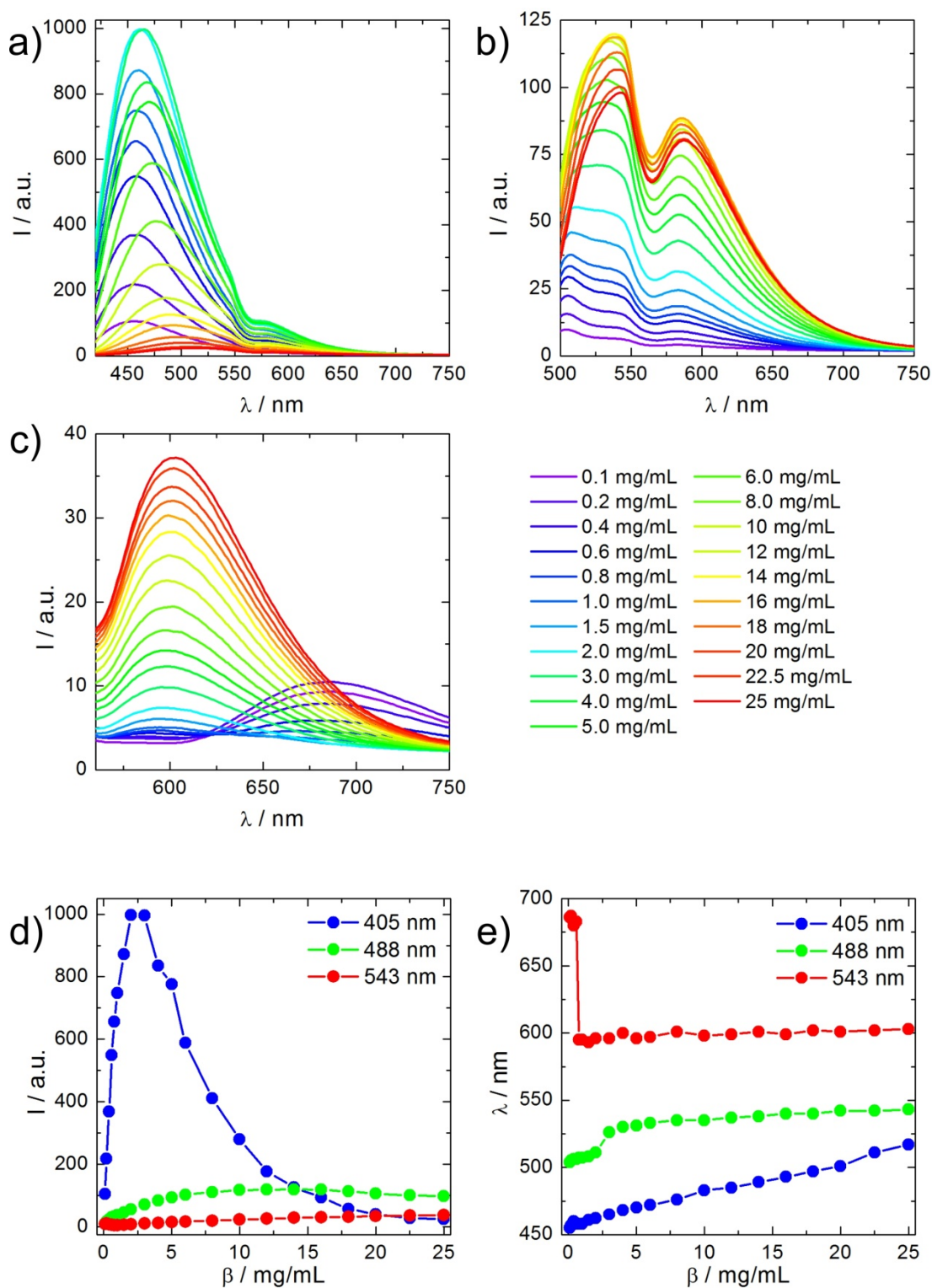


**Fig. 4.11:** a-c) Emission spectra of aqueous suspensions of N-doped C-dots with concentrations of 0.1, 0.2, 0.4, 0.6, 0.8, 1, 1.5, 2, 3, 4, 5, 6, 8, 10, 12, 14, 16, 18, 20, 22.5, 25 mg/mL, color-coded from violet to red. Excitation wavelengths: 405 nm (a), 488 nm (b), 543 nm (c). d) Plot of the fluorescence intensity of each spectrum's maximum against the particle concentration at the three different excitation wavelengths. e) Plotting of the emission wavelength of each spectrum's maximum against the particle concentration at the three different excitation wavelengths.

Obviously, fluorescence emission of the N-doped C-dots behaves very differently at the three excitation wavelengths with variation of the concentration of the particles. A superficial view on the spectra with excitation at 405 and 488 nm reveals second peaks or shoulders. Thus, irradiation with 405 nm light leads to excitation of the blue and green species. At 488 nm the green and orange species are excited, while 543 nm only excites the orange one. The main information of the emission spectra from Fig. 4.11a-c was extracted by plotting intensity (Fig. 4.11d) and wavelength (Fig. 4.11e) of the emission maxima against the particle concentration.

In the graphs of Fig. 4.11d it is shown that the excitation with 405 nm leads to a drastic increase of the fluorescence intensity with a maximum at 2 mg/mL. Further increase of the mass concentration results in an exponential decrease of the emission intensity. This effect may be attributed to self-quenching of the particles and reabsorption effects, as discussed before. For the excitation at 488 nm the emission intensity rises continuously with the increase of the mass concentration and reaches its maximum at 16 mg/mL. The plotted data follow the shape of a saturation curve in this case. Further increase of the particle concentration results in slightly lower fluorescence intensities. Interestingly, the excitation at 488 nm is stronger in terms of emission intensity compared to the excitation at 405 nm for higher concentrations. This effect is reflected in the observation of higher intensities for the 488 nm excitation at multicolor imaging experiments. Particle enrichments in the cells may cause this effect, which will be discussed in detail in chapter 6.1. The excitation with 543 nm generally leads to a linear rise of fluorescence intensity for concentrations above 1.0 mg/mL. Intensity of the emitted light is only stronger compared to the excitation at 405 nm at the highest concentration of 25 mg/mL.

The plotting of the wavelength of the emission maxima in Fig. 4.11e shows a shift of the emission wavelength for an excitation at 405 nm from 455 nm at the lowest concentration to 517 nm at the highest concentration. As such, emitted light changes from blue to green with the increase of the particle concentration. For the excitation with 488 nm the red shift is weaker starting from 505 nm at low concentrations to 543 nm at the highest one. With excitation at 543 nm the particles show emission at about 680 nm, however higher concentrations all show emission at about 600 nm.

Considering the optical changes caused by an increase of the N-doped C-dot concentration two explanations may be possible for this behavior. At first, reabsorption of emitted light, as discussed before, may result in longer wavelengths when the concentration of the particles increases. Secondly, if the suspensions are mixtures of different photoluminescent species, these could have different optical and (self-)quenching properties, as reported in the literature (Vinci *et al.* 2013; Fu *et al.* 2015).



Apart from that, the changes of the optical properties due to particle concentration may be used to unveil C-dot distribution and agglomerations in multicolor imaging via CLSM inside living cells.

#### Influence of Metal Ions on Carbon Dot Photoluminescence

As shown in chapter 4.1.2, N-doped C-dots are highly functionalized with hydroxyl, carboxyl and nitrogen-containing groups. These groups are well known to interact with metal ions and accordingly the particles possibly also interact with these. Consequently, possible bindings of certain metal ions and potential changes on the photoluminescence of the particles were studied. Therefore, 0.5 mg/mL aqueous suspensions of N-doped C-dots were incubated with metal ions in a concentration of 10 mM. The fluorescence intensities at exc./em. 370/450 nm were normalized with respect to particle suspensions without metals and plotted as bars in Fig. 4.12 for every metal ion type.

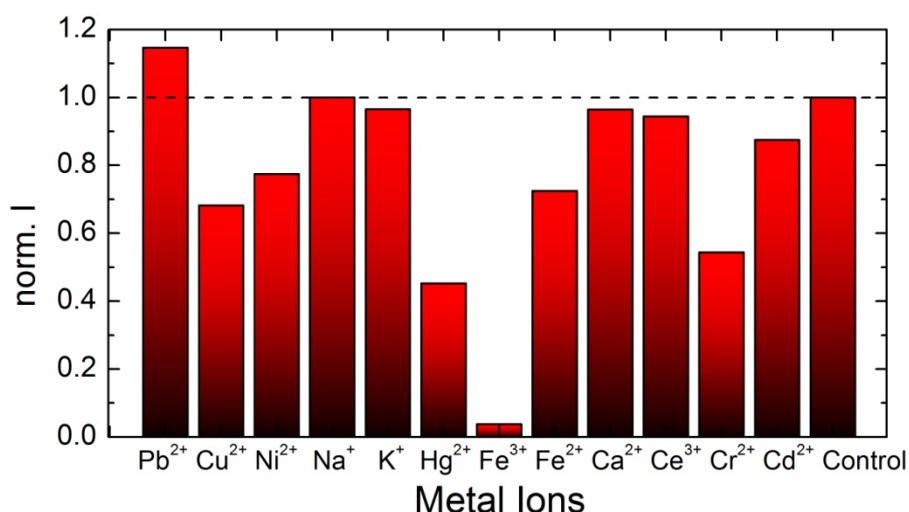


**Fig. 4.12:** Normalized fluorescence intensities of 0.5 mg/mL aqueous N-doped C-dot suspensions incubated with 10 mM of the corresponding metal ions. Normalization was performed against a particle suspension without metals denoted as “control”. The data originates from single measurements. Exc./Em.: 370/450 nm at 20 °C.

Decreases in the photoluminescence of the N-doped C-dots were found for several metal ions (Cu<sup>2+</sup>, Ni<sup>2+</sup>, Hg<sup>2+</sup>, Fe<sup>2+</sup>, Fe<sup>3+</sup> and Cr<sup>2+</sup>), as indicated in Fig. 4.12. However, among these only the incubation with Fe<sup>3+</sup> ions led to drastic fluorescence quenching below 5% of the value of the control suspensions. As such, it is assumed that N-doped C-dots show high affinity for Fe<sup>3+</sup> ions and that the formation of the metal-particle complex abolishes the emission ability of the particles. These data fit very well to observations of photoluminescence quenching by Fe<sup>3+</sup> for other C-dot preparations described in literature (Qu *et al.* 2013; Zhu *et al.* 2013b).

In order to quantify the interaction of the N-doped C-dots with the metal ion in more detail, particle suspensions with mass concentration of 0.5 mg/mL were incubated with  $\text{Fe}^{3+}$  in increasing concentrations. The emission spectra with excitation at 370 nm were recorded and analyzed, as indicated in Fig. 4.13.

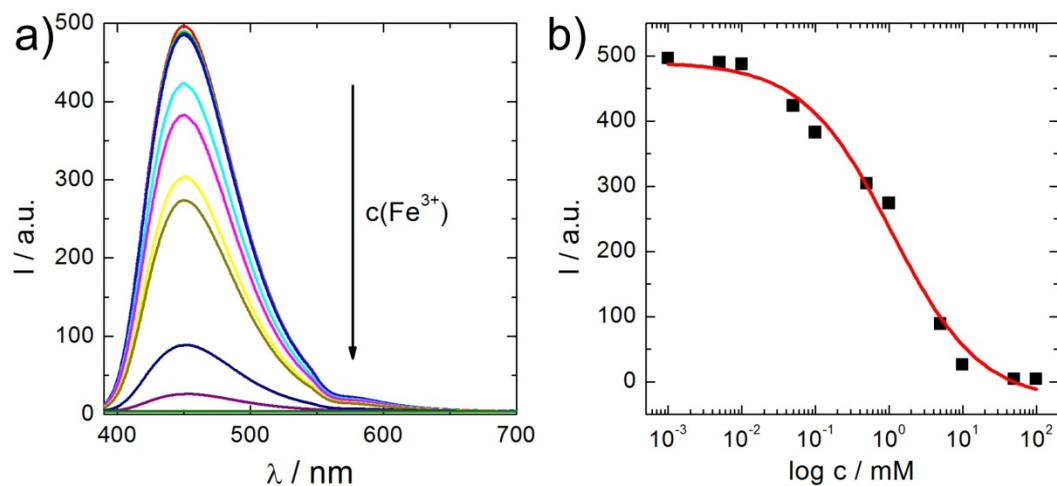


**Fig. 4.13:** a) Emission spectra of N-doped C-dots in aqueous suspension (0.5 mg/mL) incubated with  $\text{Fe}^{3+}$  in concentrations of 100, 50, 10, 5, 1, 0.5, 0.1, 0.05, 0.01, 0.005 and 0.001 mM. Concentration increases with the direction of the arrow. Excitation at 370 nm. b) Plot of the fluorescence intensity at the emission maximum against the  $\text{Fe}^{3+}$  concentration. Fitting of the data was performed with logistic function  $y=A_2+(A_1-A_2)/(1+(x/x_0)^p)$ ,  $R^2 = 0.9877$ .

The spectra in Fig. 4.13a show a decrease of the photoluminescence intensity with increasing  $\text{Fe}^{3+}$  concentration. The corresponding plot of fluorescence intensity against metal ion concentration and its convergent fit in Fig. 4.13b are in agreement with the law of mass action. Accordingly, it seems obvious that quenching of the particles photoluminescence comes hand and in hand with the binding to the metal ions. Most likely the type of quenching is static, through permanent interaction of the N-doped C-dots with  $\text{Fe}^{3+}$ . The fit of the dose-response data provided a linear detection region between 0.15 and 7.3 mM  $\text{Fe}^{3+}$ .

## 4.2 Characterization of Graphene Quantum Dots

Graphene Quantum Dots prepared from GO and ammonia were characterized in terms of size distribution, composition and optical properties in order to clearly differentiate this material from C-dots.

### Investigations on the Graphene Quantum Dot Size Distribution

Size distribution of the GQDs was determined in suspension by measuring the hydrodynamic diameter of the particles via DLS. Typical results for the DLS analysis of the particles in PBS are shown in Fig. 4.14.

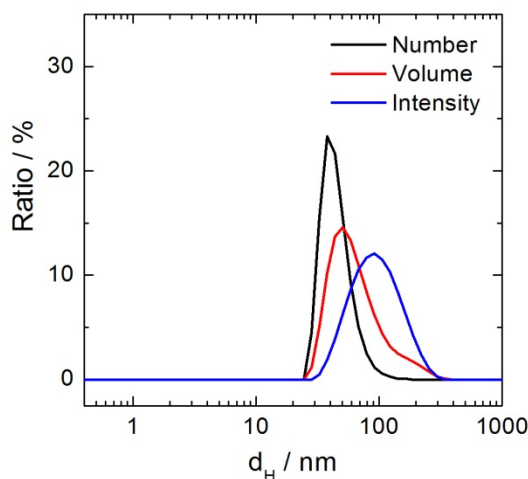


**Fig. 4.14:** Hydrodynamic diameter distributions plotted as a function of number, volume and DLS intensity of GQDs in PBS (0.1 mg/mL) prepared from GO and ammonia.

The DLS analysis of the GQDs yielded hydrodynamic diameter distributions between 28 and 255 nm. Thereby, the averages  $\pm$  standard deviation of the distributions are  $46 \pm 15$  nm (number),  $72 \pm 43$  nm (volume) and  $102 \pm 47$  nm (intensity). The top-down prepared GQDs exhibit a much larger hydrodynamic diameter than the hydrodynamic diameters determined for the bottom-up prepared C-dots. Obviously, this preparation results in larger carbonaceous nanostructures. Additionally, the resulting DLS distributions are very broad. This may be attributed to larger remnants of GO which are still part of the suspension after the filtration process.

More thorough investigations on the size distributions of the GQDs were performed via AFM, as this technique furthermore allows examining the particles' morphologies. Micrographs of GQDs recorded via AFM and analyzed on the particles width and height are shown in Fig. 4.15.

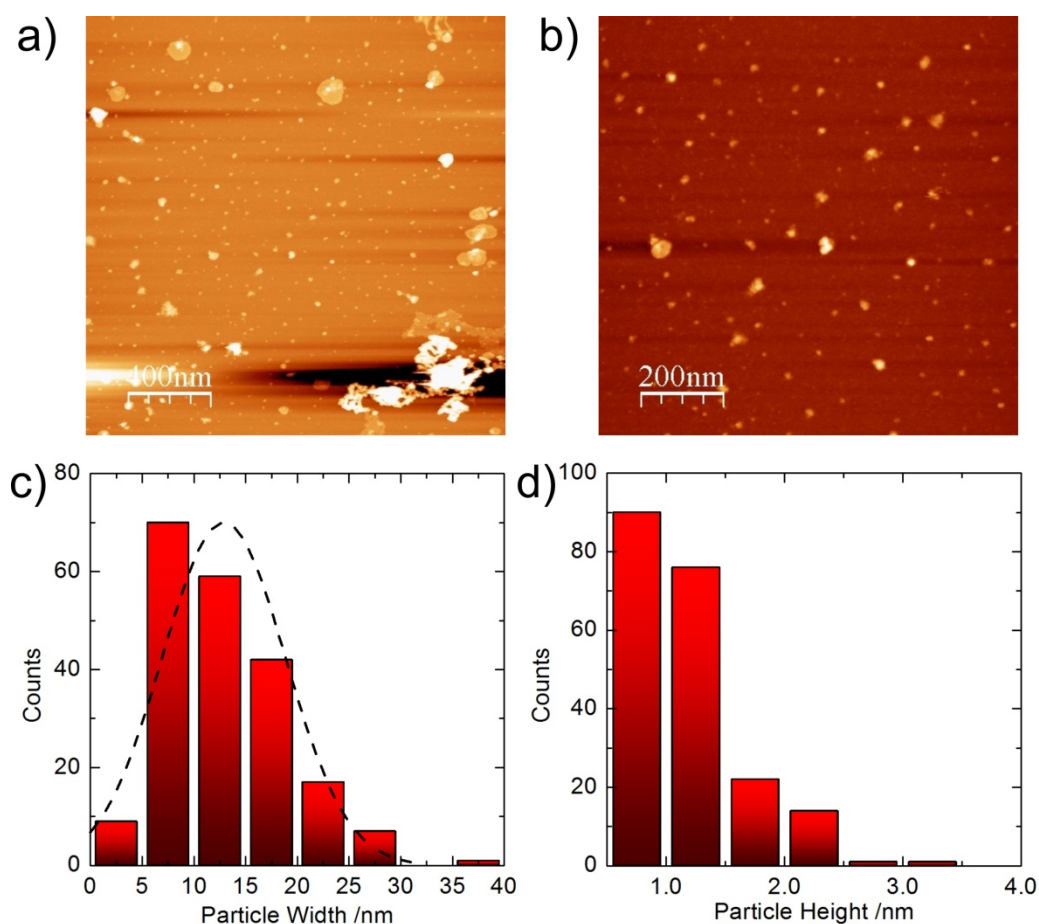


**Fig. 4.15:** a-b) AFM micrographs of GQDs on mica substrate. Magnification increasing from picture a) to b). c) Particle width distribution of GQDs measured over 205 particles, yielding an average of  $12.9 \pm 6$  nm. The dashed line represents a normal distribution after least square optimization. d) Particle height distribution of GQDs measured over 205 particles, yielding an average of  $1.2 \pm 0.5$  nm.

The AFM micrographs in Fig. 4.15a,b show non-uniform flake-like nanostructures in different extensions. These mostly have a much larger lateral extension than their actual height. Furthermore, it seems that several aggregates or larger fragments, possibly from GO, remain in the particle suspension. Analysis of the width of the GQDs shows that most of the particles are in a size range between 5 and 25 nm with an average of  $12.9 \pm 6$  nm. The height of most particles is between 0.5 and 1.5 nm with an average of  $1.2 \pm 0.5$  nm. As such, most GQDs consist of two to six graphene layers, assuming a graphitic structure of the particles with an approximate distance of 0.25 nm between the layers (Ohta *et al.* 2006).

In summary, the top-down preparation of GQDs from GO and ammonia results in much larger carbonaceous nanostructures than the bottom-up fabricated C-dots. While C-dots may be seen as almost spherical, GQDs exhibit the flake-like structure of its precursor material GO, but in smaller extension. Furthermore, the size distribution of C-dots may be described as much more homogenous, with peak width between 0.5 and 4.5 nm, while the flake-like GQDs reach sizes between 5 and 40 nm. These differences have to be considered comparing both materials.

### Composition of the Graphene Quantum Dots

Since elementary analysis of the GQDs could not be performed due to low amount of particles obtained per batch, composition was analyzed via EDX. Thereby, the particles were found to be highly oxidized with mass ratios of carbon and oxygen at similar levels.

Furthermore, Raman spectroscopy, as standard analysis method for graphene and its derivatives, was performed in order to study structural differences between the starting material GO, hydrothermally treated GO and GQDs prepared from GO and ammonia. The corresponding Raman spectra are shown in Fig. 4.16.

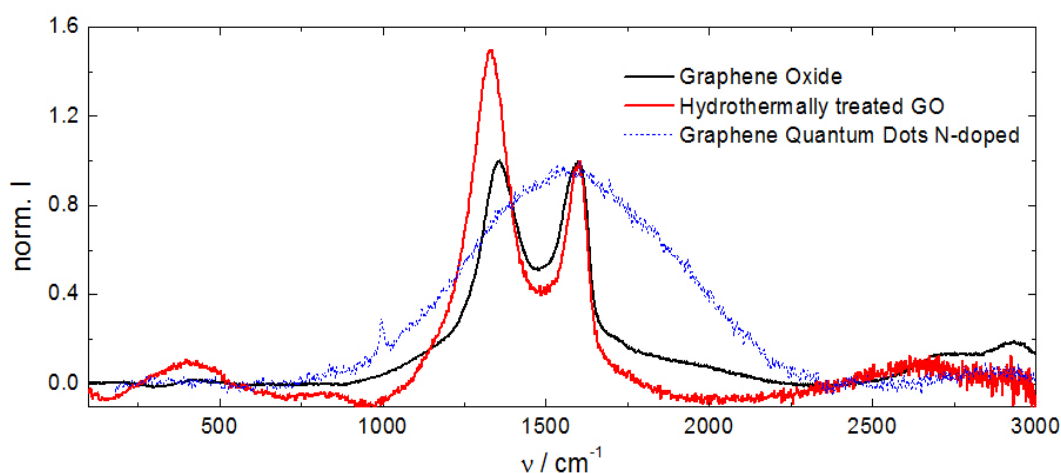


**Fig. 4.16:** Raman spectra of drop casted GO, hydrothermally treated GO and GQDs prepared from GO and ammonia. All spectra were normalized to the graphene peak at  $1600\text{ cm}^{-1}$ . The spectrum of the GQDs was plotted as dotted line due to strong fluorescence noise.

Graphene oxide prepared via Hummers method has its characteristic graphene (G) peak at  $1600\text{ cm}^{-1}$  and a defect (D) peak at  $1356\text{ cm}^{-1}$ . The ratio between D and G peak gives information about the defectiveness of the material and deviations from a completely  $\text{sp}^2$ -hybridized carbon atom layer. The hydrothermally treated GO shows an increase of the D/G-peak ratio to 1.5 which means the material gets even more defective. A possible explanation is an oxidative cutting of the GO flakes, resulting in highly oxygen functionalized flake edges and further disruption of the delocalized electron system. N-doped GQDs via hydrothermal treatment of GO with ammonia cannot be analyzed via Raman spectroscopy as signal generation was disturbed by fluorescence as shown in the spectra above. However, GQDs are likely to be rather similar in their defectiveness to hydrothermal treated GO due to cutting of the flakes and edge destruction. Further analysis on the functionalization, such as via IR, were not performed since the accessible amount of GQDs was insufficient.

### Spectroscopic Properties of Graphene Quantum Dots

Quantum yield of the GQDs was determined, similar to the method for C-dots and resulted in  $1.9 \pm 0.3\%$ , which is significantly lower as the  $25.1 \pm 2\%$  of the N-doped C-dots. Thus,

the formation of emissive sites and species is much more efficient in the bottom-up preparation of C-dots compared to the defect introduction in the top-down preparation of GQDs.

General optical properties were studied by measuring the absorption, excitation and emission spectra of GQDs in aqueous suspension at a mass concentration of 0.1 mg/mL. The corresponding spectra of the GQDs prepared from GO and ammonia are shown in Fig. 4.17.

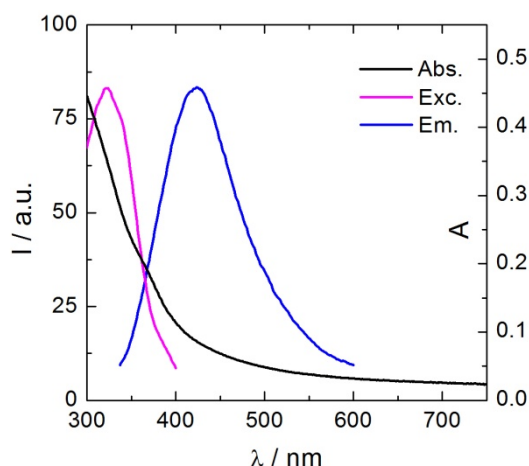


**Fig. 4.17:** Absorption, excitation and emission spectra of GQDs in aqueous suspension with mass concentrations of 0.1 mg/mL. Exc./em. maxima at 322/424 nm.

The GQDs show absorption over the whole UV/VIS region. Absorbance increases exponentially towards shorter wavelengths. No significant absorption “shoulder” appears in the spectrum. Highest fluorescence intensities are achieved with excitation at 322 nm and emission maximum is at 424 nm. Furthermore, the emission spectrum does not show secondary peaks or “shoulders” which would indicate the excitation of other species for example, as it was the case for C-dots. Compared to the N-doped C-dots excitation and emission wavelength are at shorter wavelengths. Since GQDs are much bigger in size, their photoluminescence has to originate from delocalized electron islands surrounded by defects on the flakes.

### Variation of the Excitation Wavelength

Similarly to the N-doped C-dots, the luminescence at different excitation wavelengths for GQDs was investigated. Therefore, the emission spectra of an aqueous suspension of GQDs (0.1 mg/mL) were recorded as a function of the excitation wavelength between 300 and 500 nm in 20 nm steps. The native emission spectra and the corresponding normalized versions are shown in Fig. 4.18.

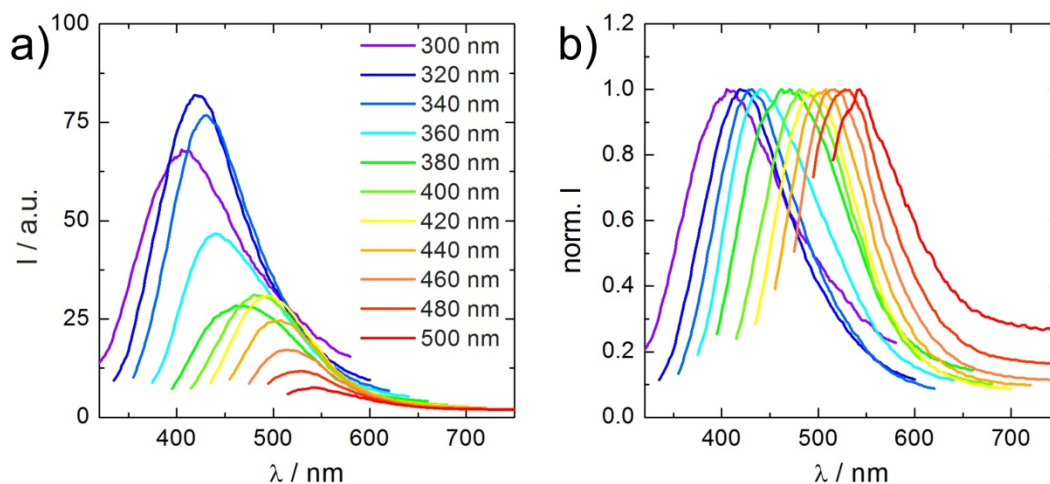


**Fig. 4.18:** Emission spectra of GQDs in aqueous suspension with a mass concentration of 0.1 mg/mL. Excitation wavelength was varied between 300 and 500 nm in 20 nm steps. a) Native emission spectra, b) emission spectra normalized to their respective maximum.

The variation of the excitation wavelength showed highest fluorescence intensities in the near UV region from 300 to 340 nm. However, significant emission intensities are also recorded with excitation up to 500 nm. Remarkably, the maxima of the emission spectra are shifted towards longer wavelengths for every increase of the excitation wavelength. This becomes particularly obvious from the normalized emission spectra in Fig. 4.18b. A linear correlation between excitation and emission wavelength is indicated. Furthermore, there is no overlap of the normalized spectra, which means these GQDs do not contain dominating species which are individually excited at different wavelengths. This is in contrast to the observation for N-doped C-dots, which seem to have distinct emissive species excited by various wavelengths.

Considering the collected facts about GQDs prepared from GO and ammonia, these particles are highly deviating from N-doped C-dots. At first GQDs are much bigger in size with a flake-like structure, while C-dots are spherical with both particle types having similar heights. This can mostly be referred to the two different precursor materials and the different preparation strategies, respectively: top-down vs. bottom-up. While chemical composition is not fully resolved, both materials seem to be highly oxidized carbon nanostructures. Furthermore, both materials show photoluminescence independent from excitation wavelength. While the wavelength of the emitted light of GQDs is directly correlated to excitation wavelength, N-doped C-dots emission seems to be dominated by a few species. Additionally, the C-dots emission maximum is at higher wavelengths with much higher quantum yields of more than a factor of ten. According to this, the N-doped C-dots seem to be more suitable for bioanalytical and imaging applications due to higher sensitivity at irradiation in the VIS.

## 4.3 Characterization of the Modified and Embedded Carbon Dots

### Characterization of Oleic Acid modified Carbon Dots

The OAM C-dots were characterized by analysis of hydrodynamic diameter distributions via DLS. These are shown in Fig. 4.19 for the liquid oleic acid particle conjugates in chloroform with a concentration of 0.2% (v/v).

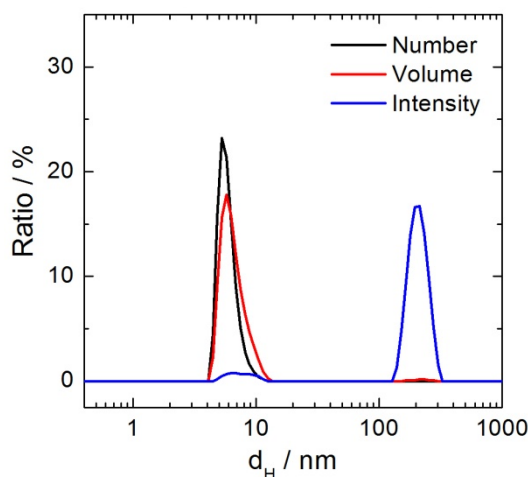


**Fig. 4.19:** Hydrodynamic diameter distributions of OAM C-dots in chloroform (0.2% v/v) expressed as number, volume or DLS intensity at T = 25 °C.

The DLS analysis of the OAM C-dots resulted in distributions at the expected diameter ranges, mostly between 4.5 and 9.6 nm. The average values  $\pm$  standard deviation were at  $5.9 \pm 1.1$  nm (number),  $6.5 \pm 1.5$  nm (volume) and  $7.6 \pm 1.8$  nm (intensity). Comparing these values with those of unmodified N-doped C-dots, the modification yielded an increase of the hydrodynamic diameter. Although both measurements were performed in different solvents (due to changed dispersibility), these results may indicate a successful modification with the long-chained fatty acids, resulting in larger particle diameters.

Photoluminescence was investigated by analyzing the emission spectra of OAM C-dots at different excitation wavelengths. Therefore, the emission spectra of the particles in chloroform (0.2% v/v) were recorded with variation of the excitation wavelength between 300 and 500 nm in 20 nm steps. The native emission spectra and the corresponding normalized versions are shown in Fig. 4.20.



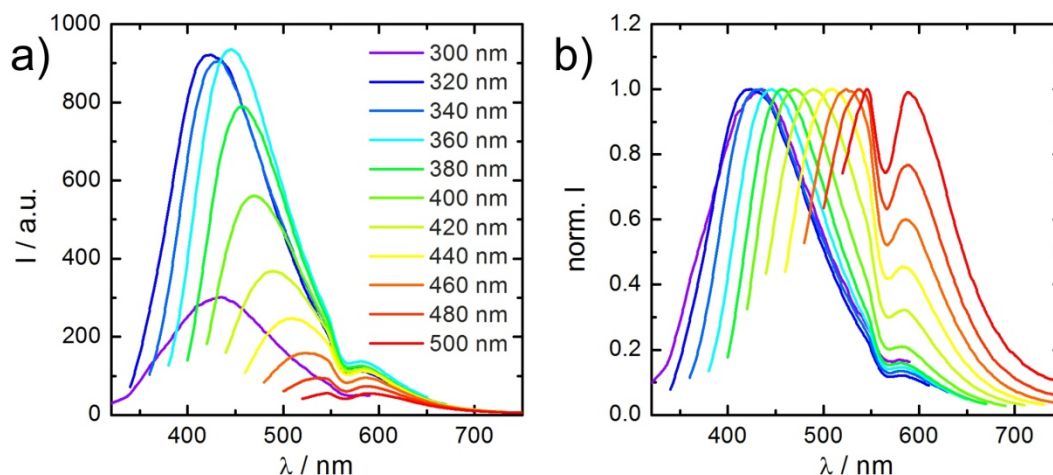


**Fig. 4.20:** Emission spectra of OAM C-dots in chloroform (0.2% v/v). Excitation wavelength was varied between 300 and 500 nm in 20 nm steps.  $T = 25\text{ }^{\circ}\text{C}$ . a) Native emission spectra, b) emission spectra normalized to their respective maximum.

Comparing the emission spectra of the OAM C-dots with those of the water-dispersible unmodified species shown in Fig. 4.7, significant deviations can be found. At first, variation of the excitation wavelength directly leads to a shift of the emission spectra maxima for OAM C-dots, while unmodified N-doped C-dots had several major emitting species. Furthermore, the emission spectra of OAM C-dots for excitations with wavelengths higher than 400 nm exhibit a more intense second emission maximum at about 590 nm becoming more dominant at higher excitation wavelengths, clearly present in the normalized spectra of Fig. 4.20b. As such, these particles are expected to emit longer wavelength light than unmodified versions at similar excitation using 405/488 nm laser sources during CLSM imaging experiments. Thereby, it has to be mentioned that this effect may be based on solvatochromism, as OAM C-dots were dispersed in chloroform due to their limited dispersibility in water. Other possibilities are that the modification process favors the long wavelength emitting species, leading to domination of these species in the OAM C-dot suspension or that the modification on the surface of the particles leads to this phenomenon.

#### Agarose Nanoparticles doped with Carbon Dots

The agarose nanoparticles doped with C-dots were characterized for their hydrodynamic diameter via DLS. Since the nanoparticles consist of agarose hydrogel, they would shrink or swell with varying osmolyte concentrations bringing the fluorescence particles closer together or further apart. As such, the influences of osmolality changes of the surrounding medium on the particles photoluminescence properties were studied.

In Fig. 4.21 DLS distributions for a typical agarose nanoparticle (with incorporated C-dots) suspension in PBS are shown. Additionally, the particles were dried on a gold surface analyzed via scanning electron microscopy (SEM) in order to confirm the obtained DLS data.

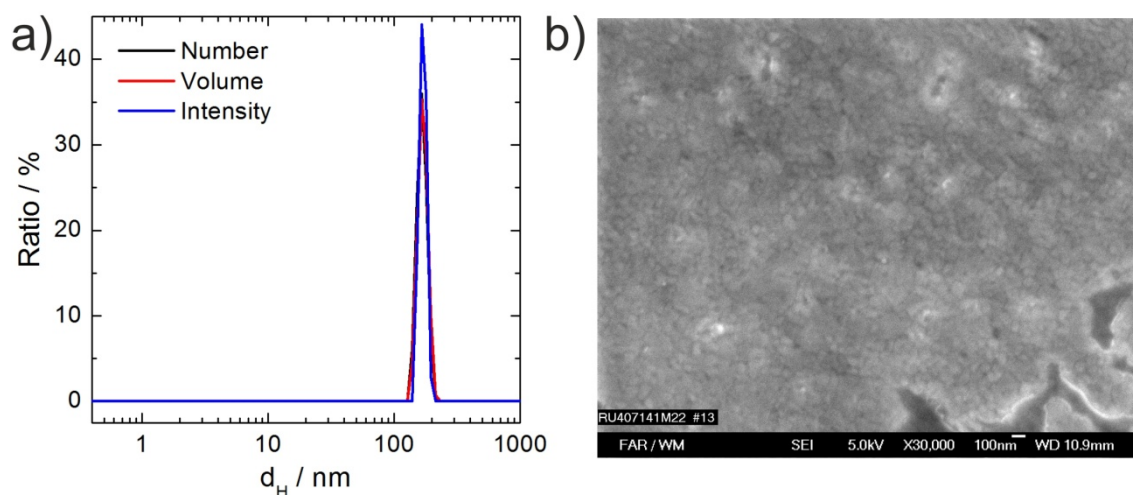


**Fig. 4.21:** a) Hydrodynamic diameter distributions of agarose nanoparticles doped with N-doped C-dots in PBS expressed as number, volume and DLS intensity. b) SEM micrograph of dried agarose nanoparticles doped with N-doped C-dots on a gold surface. The scale bar is indicated in the black bar at the bottom of the micrograph.

The hydrodynamic diameter distributions of the agarose nanoparticles in Fig. 4.21a show averages of  $167 \pm 15$  nm (number),  $167 \pm 21$  nm (volume) and  $169 \pm 11$  nm (intensity) with standard deviation as error. In addition to DLS, SEM micrographs of dried particles were recorded. In Fig. 4.21b, the particles may be seen as granular structure in the SEM micrograph. These structures are about 50 to 100 nm in size. Since the particles consist of a hydrogel and were dried for the SEM micrographs, these structures have to be significantly smaller than the hydrodynamic diameter. As such, a hydrodynamic diameter of about 167 nm may be realistic for the agarose nanoparticles.

The feature of the agarose hydrogel to swell and shrink depending on the osmolarity of the surrounding medium was used to investigate whether this affects the photoluminescence of the incorporated C-dots by expanding or reducing the distance between them. Since the N-doped C-dots showed changes of their optical properties with increasing concentration, possible effects on the emission of the incorporated N-doped C-dots were addressed.

For these studies, aqueous suspensions of agarose nanoparticles with incorporated N-doped C-dots were incubated with sucrose and sodium chloride as osmolytes in varying concentrations. After 2 h of incubation time, the suspensions were analyzed for their fluorescence intensities with exc./em at 370/450 nm. Additionally, bare N-doped C-dot suspensions served as control to clearly assign the changes in the photoluminescence to the shrinking of the agarose hydrogel matrix. The results of this study are shown in Fig. 4.22.

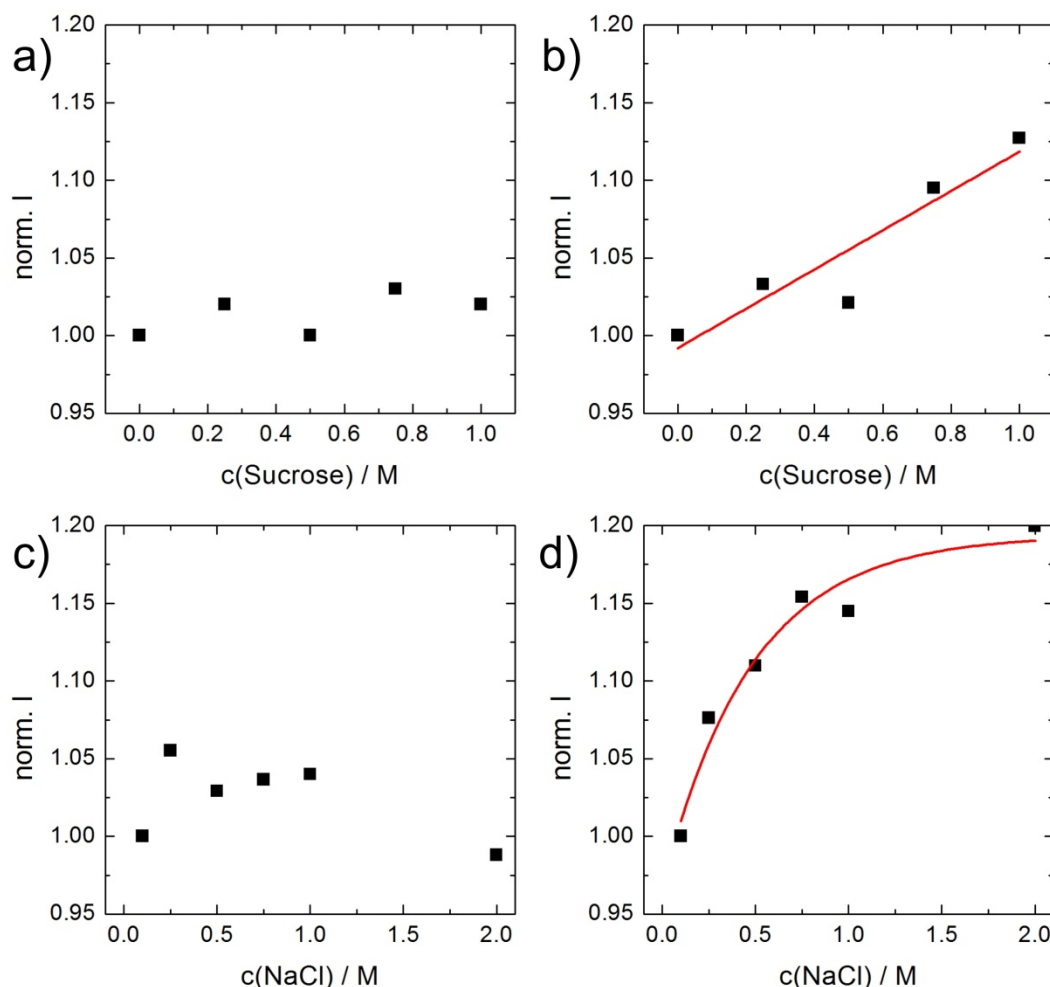


**Fig. 4.22:** Normalized fluorescence intensity plots of N-doped C-dots (a,c), or agarose nanoparticles doped with the N-doped C-dots (b,d), after incubation with different osmolytes, exc./em.: 370/450 nm. a) 0.5 mg/mL N-doped C-dots in aqueous suspension incubated with sucrose in increasing concentrations. b) Aqueous suspension of doped agarose nanoparticles (126  $\mu\text{g/mL}$ ) incubated with sucrose in increasing concentrations. Linear fit as red line: Slope:  $0.126 \pm 0.028 \text{ M}^{-1}$ ,  $R^2 = 0.8296$ . c) 0.05 mg/mL N-doped C-dots in aqueous suspension incubated with sodium chloride in increasing concentrations. d) Aqueous suspension of doped agarose nanoparticles (313  $\mu\text{g/mL}$ ) incubated with sodium chloride in increasing concentrations. Boltzmann fit as red line: Half maximum:  $0.48 \pm 0.73 \text{ M}$ ,  $R^2 = 0.8992$ .

The incubations of the bare C-dots with the osmolytes, shown in Fig. 4.22a (sucrose) and c (sodium chloride) did not show a distinct trend of the fluorescence intensity with increasing osmolyte concentration. Thereby, the intensities fluctuate approximately 5% relative to the base value at the different concentrations. The incubation of the agarose nanoparticles with sucrose in concentrations up to 1 M, led to a more or less linear increase of the fluorescence intensity with a maximum increase of 13%. This behavior is clearly in contrast to the observations for the bare C-dots. Incubation with sodium chloride was performed with concentrations up to 2 M. In doing so, fluorescence intensity increases by a maximum of 20% for the highest concentration. Plotting the intensity against the sodium chloride concentration shows the shape of saturation curve. In concentration regions up to 1 M, a linear increase of the fluorescence intensity is observed, similar to the incubation with sucrose, with a maximum intensity increase of about 15%.

The study on changes in the photoluminescence of the C-dot doped agarose nanoparticles at different osmolyte concentrations was performed just once. As such, this study does not claim to give statistical or quantitative information about the determination of osmolyte concentrations using agarose nanoparticles doped with C-dots. However, it was shown that the principle of a shrinking agarose hydrogel with incorporated C-dots significantly changes the particles photoluminescence properties and that these may be used for applications in this context.

### Liposomes with encapsulated Carbon Dots

The following chapter describes the characterization of two different kind of liposomes doped with C-dots. One sample was doped with low concentrations and another one with high concentrations of C-dots during the preparation process, as described in chapter 3.2.3.

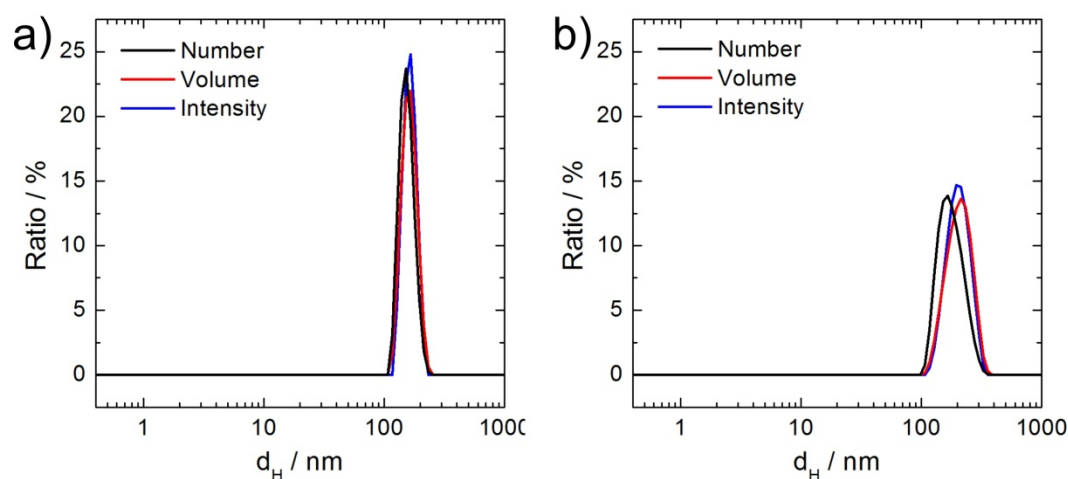


**Fig. 4.23:** Hydrodynamic diameter distributions of liposomes doped with N-doped C-dots as recorded by DLS. The liposomes were doped with C-dots in low (a) and high concentration (b) during the preparation process. The suspensions were measured in HEPES buffer and the distributions are expressed as number, volume and DLS intensity.

The DLS analysis of the liposomes with low concentrations of N-doped C-dots, shown in Fig. 4.23a, yielded hydrodynamic diameter distributions between 116 and 213 nm. The average values of the distributions  $\pm$  standard deviation are  $155 \pm 22$  nm (number),  $163 \pm 23$  nm (volume) and  $164 \pm 20$  nm (intensity). The measurement of the liposomes with the high C-dot concentration, shown in Fig. 4.23b, yielded hydrodynamic diameter distributions between 117 and 301 nm. Averages  $\pm$  standard deviation of the distributions were determined to be  $179 \pm 42$  nm (number),  $209 \pm 48$  nm (volume) and  $205 \pm 43$  nm (intensity). Comparing the results for both liposome preparations, these are roughly in similar size with different concentrations of encapsulated C-dots as main discrimination.

Among others, encapsulation of the N-doped C-dots inside the liposomes was performed to utilize the photoluminescence quenching of the particles close to each other. Undergoing shrinking or swelling of the liposomes, the optical properties of the C-dots

within were expected to be influenced by changes of the osmolarity of the surrounding medium, very similar to the behavior of doped agarose nanoparticles shown before. In a first experiment, liposomes prepared with high concentrations of C-dots were lysed using 20 mM sodium dodecyl sulfate (SDS). In cross-selectivity studies, it was shown that 20 mM SDS do not influence the C-dots photoluminescence. Through lysis of the liposomes the encapsulated C-dots are liberated and quenching of the photoluminescence reversed. In Fig. 4.24, the emission spectra of the two types of liposomes in aqueous suspension before and after lysis are shown with excitation at 370 nm.

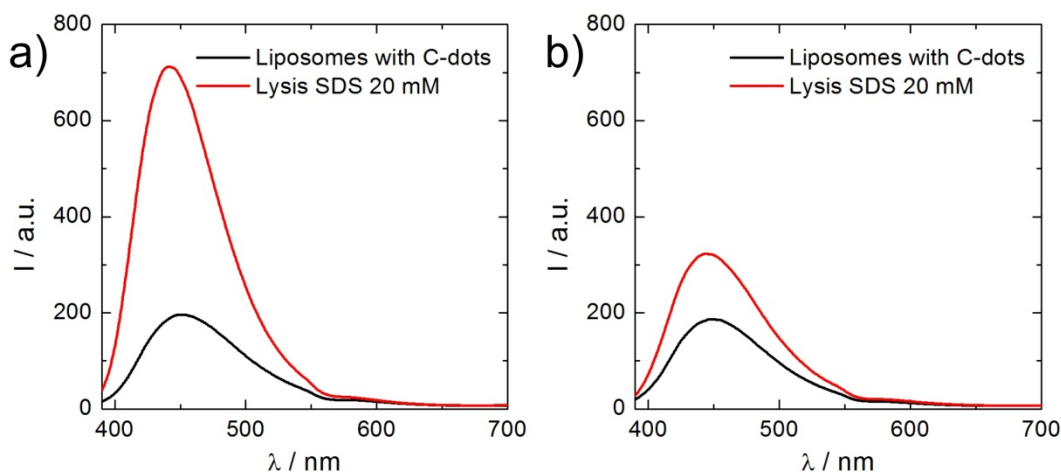


**Fig. 4.24:** Emission spectra of liposomes with low concentrated (a) and highly concentrated (b) encapsulated N-doped C-dots. Total phospholipid concentration of the liposomes: 0.23 mM (a) and 0.15 mM (b) in HEPES buffer before and after lysis with 20 mM SDS. Exc.: 370 nm, T = 25 °C.

As shown in the emission spectra of Fig. 4.24, lysis of both types of liposomes led to increasing fluorescence intensities. While the intensity of the liposomes with low concentration of encapsulated C-dots increased app. 72% at the emission maximum, those with the high concentrations of C-dots increased by 263%. On the one hand, these results indicate that the encapsulation of the C-dots inside the liposomes did quench their photoluminescence. On the other hand, the greater increase of the fluorescence intensity of the liposomes with higher content of C-dots is attributable to the release of a larger amount of particles into the buffer solution. C-dots were entrapped inside liposomes in different concentrations, by different preparation methods. The particles exhibit self-quenching when entrapped in sufficient high concentrations. This effect can be reversed by releasing the C-dots through lysis of the liposomes and is well known for organic dyes entrapped in liposomes (Edwards *et al.* 2006). Silica nanoparticles and inorganic Q-dots do not show this reversible fluorescence quenching effect upon release from liposomes (Chen *et al.* 2006). As such, C-dots behave like organic dyes, forming non-fluorescent aggregates upon static quenching, collisional quenching, and energy transfer from monomers to non-fluorescent dimers (Chen *et al.* 1988).

## *Characterization of the Carbon Nanomaterials*

In summary, the N-doped C-dots were successfully incorporated into other nanostructures, such as agarose nanoparticles or liposomes. Thereby, the particles photoluminescence properties may be influenced by shrinking of the matrix they are incorporated in due to osmolarity increase, as shown for agarose nanoparticles. The photoluminescence increase resulting from C-dot release from the liposomes is later on used as model for the intracellular release from endosomes, as described in chapter 7.2.

## 5 Interaction of Carbon Dots with Mammalian Cells

The following chapter describes studies addressing the influence of N-doped C-dots on the physiology of NRK cells and how these affect cell adhesion, proliferation and migration. Furthermore, studies on the uptake mechanism of the particles, their location inside cells and translocation through cell monolayer were performed. For most of the investigations, NRK cells were chosen since these form flat homogeneous monolayers and are well characterized for studies via ECIS. All studies were performed with N-doped C-dots which are denoted as *C-dots* in the following chapters for simplification.

### 5.1 Cytotoxicity Profile in Normal Rat Kidney Cells

Cytotoxicity of the C-dots in contact to confluent NRK cells was evaluated via *PrestoBlue*<sup>®</sup> assay. Therefore, an incubation time of 24 h was chosen with increasing C-dot concentrations between 0.1 and 4.0 mg/mL in full medium or serum-free medium, respectively. As such, influences on the cytotoxicity of C-dots in the presence and absence of FCS were studied. After incubation, the *PrestoBlue*<sup>®</sup> solutions above the cells were analyzed via fluorescence read-out (exc.: 544 nm, em.: 590 nm). Non-incubated cells served as negative control, while Triton X-100 (0.5% (v/v)) lysed cells were used as positive control. Cytotoxicity indices were calculated assigning the fluorescence intensities of the controls to 0 (negative) and 1 (positive). The resulting cytotoxicity indices plotted against C-dot concentration are shown in Fig. 5.1.

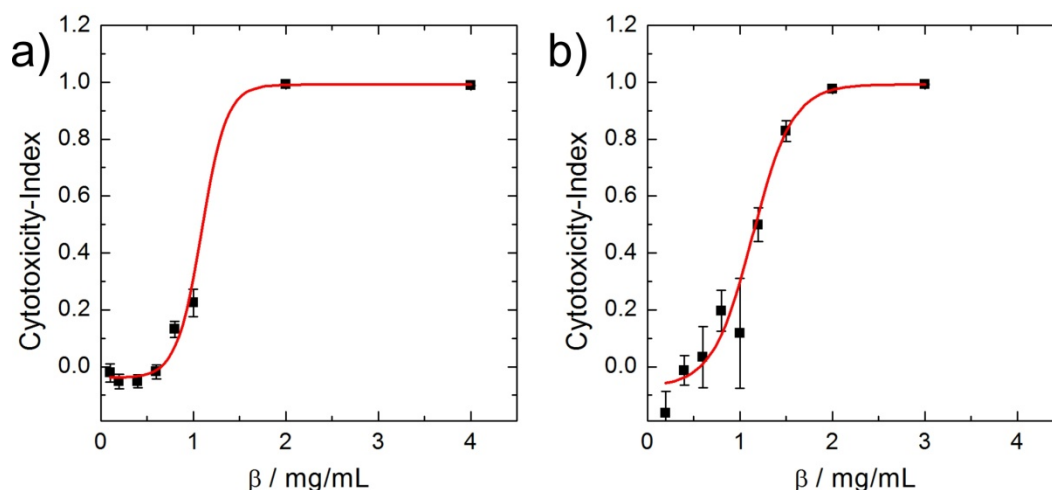


**Fig. 5.1:** Cytotoxicity evaluations via *PrestoBlue*<sup>®</sup> assay. Cytotoxicity indices plotted against C-dot concentration for the incubation of NRK cells in full medium (a) and serum-free medium (b) for 24 h. Fitting of the data via Boltzmann equation  $y=A_2-(A_1-A_2)/(1+e^{(x-x_0)/dx})$  shown as red line.  $n = 6$ . a)  $EC_{50} = 1.09 \pm 0.06$  mg/mL,  $R^2 = 0.9968$ . b)  $EC_{50} = 1.14 \pm 0.05$  mg/mL,  $R^2 = 0.9915$ .

Both cytotoxicity studies via PrestoBlue® show relatively sharp changes of cell viability with increasing C-dot concentration for the 24 h incubation. Thereby, a “critical mass concentration” of about 1.1 mg/mL was evaluated for both conditions, via fitting of the data, as shown in Fig. 5.1. This also represents the EC<sub>50</sub> value for the particles at the same time. In long-term incubations with C-dot concentrations below this value the majority of the NRK cells are also unaffected. By contrast, higher mass concentrations than 1.1 mg/mL in incubations for 24 h or longer are meant to seriously act cytotoxic and induce cell death. Comparable EC<sub>50</sub> values were described in literature for N-doped C-dots from glycerol with 0.4 mg/mL in contact to Hep-G2 cells (Liu *et al.* 2011a) or C-dot preparations from ginger with 1.4 mg/mL in contact to MDA-MB-231 cells (Li *et al.* 2014a).

The presence and absence of FCS did not show significant influence on the resulting EC<sub>50</sub> value for C-dots. As such, all following studies were performed in full medium to investigate the particles influence on mammalian cells under standard cultivation conditions.

For a differentiated and time-resolved investigation on the influence of C-dots on the viability of NRK cells, the ECIS technique was applied. Therefore, confluent NRK cells were incubated with C-dots in concentrations between 0.4 and 2.0 mg/mL in full medium. The impedance at 4 kHz and capacitance at 32 kHz were recorded over time for each population. Typical normalized time courses of the magnitude of the impedance and capacitance of such a study are shown in Fig. 5.2.

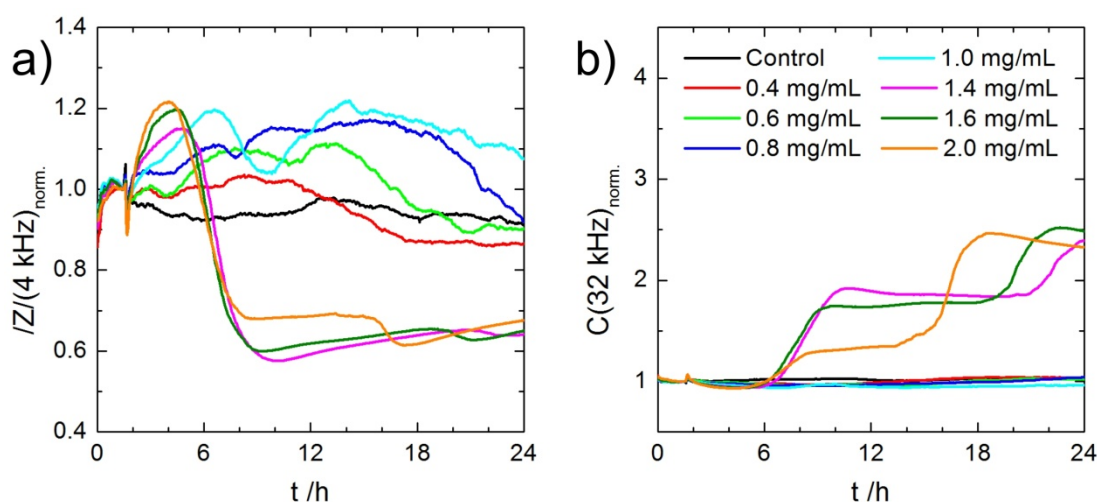


**Fig. 5.2:** Typical time courses of the normalized magnitude of the impedance at 4 kHz (a) and capacitance at 32 kHz (b) for the incubation of NRK cells with C-dots in concentrations between 0.4 and 2.0 mg/mL in full medium for 24 h at 37 °C. Time point of the addition of the particles t = 1.5 h.

As shown in Fig. 5.2a, the addition of C-dots at t = 1.5 h resulted in subsequent impedance increases. This effect is more pronounced for high C-dot concentrations between 1.0 and 2.0 mg/mL. This may be induced by swelling of the NRK cells through extensive uptake of the particles and subsequent tightening of the intercellular space. Similar observations of increasing impedance values before a final drop are described in literature for Caco-2 cells



undergoing cell death after incubation with peptide-coated silver nanoparticles (Bohmert *et al.* 2012). However, besides membrane damage due to the nanoparticles, no further explanation was discussed for this phenomenon.

Those cells incubated with particle concentrations higher than the  $EC_{50}$  value (1.4 - 2.0 mg/mL) undergo cell death in about 6 h indicated by decreasing impedance values. Thereby, NRK cells undergo cell death faster, the higher the C-dot concentration. Interestingly, a second drop of impedance may be observed a few hours later. As such, it may be suggested that the induced cell death is a two-step process. This possibly may include disintegration of cell junctions in a first step and detachment in a second step. In the “critical concentration” region (0.8 and 1.0 mg/mL) NRK cells undergo heavy reactions on the C-dot addition as indicated by the highly fluctuating impedance time course. However, these cells show similar impedance values as the non-incubated control group after 48 h. As such, these concentrations did not induce cell death, which is in accordance to the *PrestoBlue*® evaluations, since both assays therefore provide similar information (Opp *et al.* 2009). As this type of experiment was performed several times, it has to be mentioned that in rare cases the incubation with 1.0 mg/mL induced cell death during the study. As such, this concentration region may clearly be considered as “critical”. Lower C-dot concentrations (0.4 and 0.6 mg/mL) in contrast, show only marginal deviations from the non-incubated control group and may be assigned as non cytotoxic. The time courses of the capacitance in Fig. 5.2b confirm the assumptions from the impedance measurements. Hereby, no cell detachment is observed due to toxic effects for C-dot concentrations up to 1.0 mg/mL. For higher concentrations, clearly a two-step detachment process is observed. Interestingly, the first step of the capacitance increase seems to be independent from the particle concentration and occurs for all three concentrations at the same time point. The second and final increase is the faster, the higher the C-dot concentration. As such, particle concentrations higher than the “critical limit” seem to induce release of cell junctions instantly, while final detachment of the cells through cell death is directly dependent on C-dot concentration.

In summary, the ECIS studies are in accordance to the metabolic  $EC_{50}$  value of 1.1 mg/mL. For higher C-dot concentrations NRK cells undergo cell death in only a few hours. Furthermore, the permanent presence of the particles in the  $EC_{50}$  value region has to be considered highly invasive on NRK cells. As such, long-term studies should be performed in concentrations below this value, as described in chapter 5.3.

In contrast to the permanent presence of C-dot in the cells' bulk phase, applications of the particles described in chapter 6 and 7 only require short-term incubations between 30 and 60 min, for the staining and *loading* of the cells. In order to study the effect of this short-term incubation and to proof non-invasiveness, NRK cells were loaded with C-dots for just 60 min and monitored via ECIS. The corresponding time courses of the magnitude of the impedance and the capacitance in 4-fold determination are shown in Fig. 5.3.

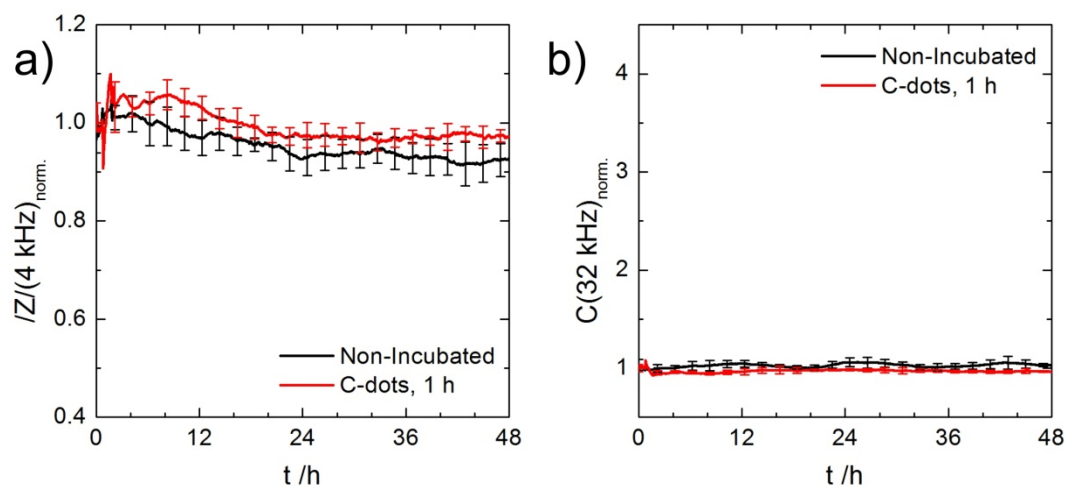


**Fig. 5.3:** Time courses of the normalized magnitude of the impedance at 4 kHz (a) and capacitance at 32 kHz (b) for the short-term incubation of NRK cells with 1.0 mg/mL C-dots in EBSS<sup>++</sup>/G for 1 h at 37 °C, shown as average  $\pm$  standard deviation,  $n = 4$ . Control NRK cells were not exposed to any particles. Addition of the particles was performed at  $t = 0.75$  h, while washing of the incubated cells was performed at  $t = 1.75$  h.

As observable in the impedance time course in Fig. 5.3a the addition of the C-dots at  $t = 0.75$  h resulted in similar impedance increases as observed for the long-term exposure. However, after the washing step impedance dropped to similar values as the non-incubated control group. Subsequently, the loaded NRK cells did not show any significant differences to the control groups. The time course of the capacitance shown in Fig. 5.3b, is in accordance with this observation. Thereby, detachment from the electrodes was not observed and the loaded NRK cells exhibit suitable capacitance values as the control groups. Accordingly, the short-term incubation with C-dots for the *loading* of NRK cells with the particles may be considered as not harming the physical conditions of the cells.

## 5.2 Uptake and Localization in Normal Rat Kidney Cells

In order to verify the suitability of the prepared C-dots as imaging agent and for other applications on mammalian cells, it was studied whether and how fast these particles are taken up by NRK cells. Therefore, confluent NRK cells were incubated with C-dots with a concentration of 1 mg/mL for varying incubation times. Before, it was shown that this concentration is not considered as acute toxic, especially for short incubation times of only a few hours. The uptake kinetics of the particles were analyzed via CLSM utilizing the C-dots intrinsic photoluminescence with excitation at 405 nm, as described in chapter 4.1.3. The resulting micrographs and the plots of their integrated fluorescence intensities against the corresponding incubation times are shown in Fig. 5.4.

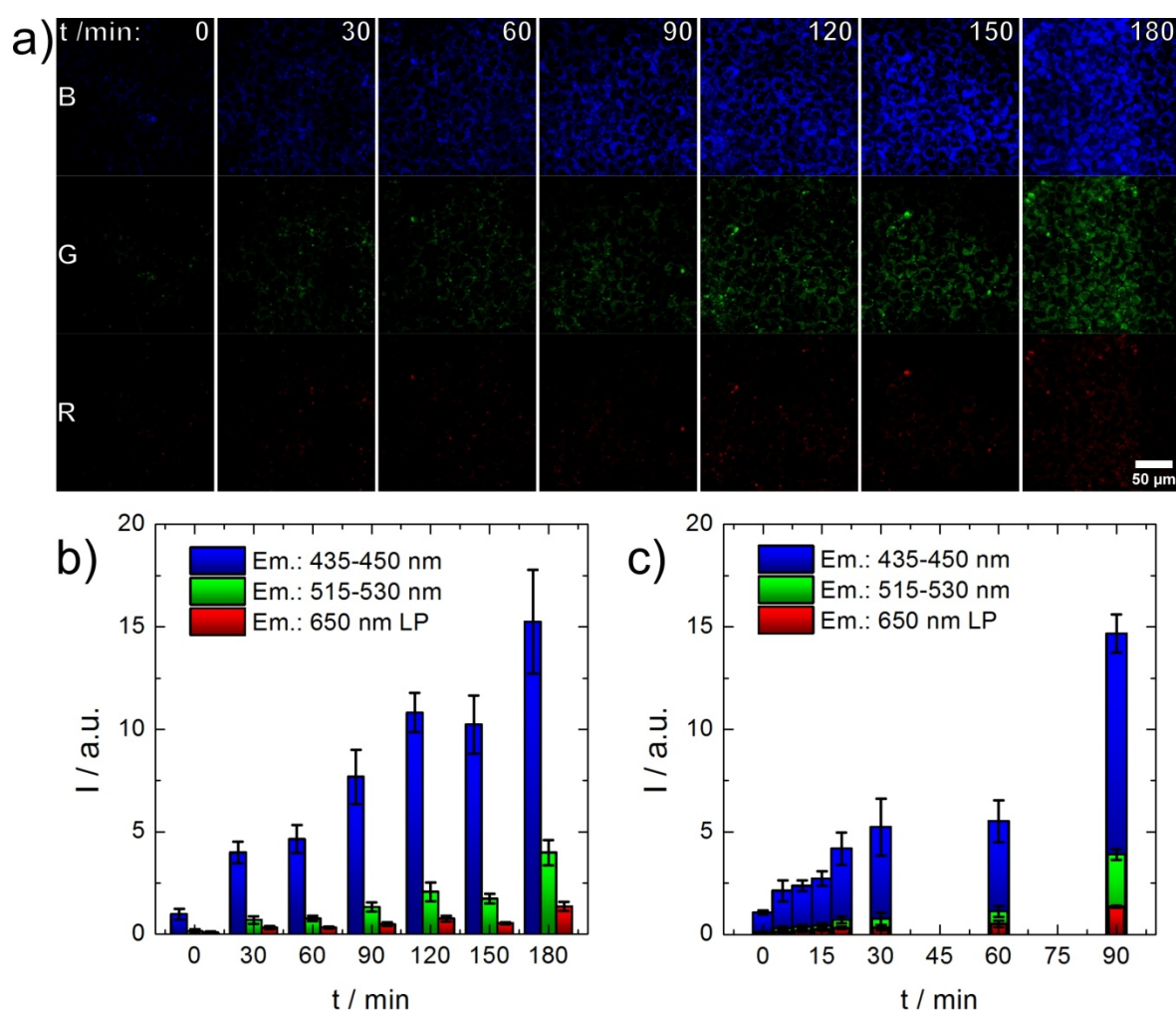


**Fig. 5.4:** Uptake kinetics of C-dots into NRK cells. a) Optical sections through NRK cells, after incubation with C-dots (1.0 mg/mL in EBSS<sup>++</sup>/G) at 5% CO<sub>2</sub> and 37 °C, washing and excitation at 405 nm. Incubation time was varied between 0 and 180 min in 30 min steps. Multicolor micrographs were split into their blue (B, 435 – 450 nm), green (G, 515 – 530 nm) and red (R, 650 nm LP) component for further analysis. b) Plot of the integrated intensities of the blue, green and red channel of micrographs from the study in (a) against the incubation time. c) Plot of the integrated intensities of the blue, green and red channel of micrographs from an independent study on the uptake kinetics with shorter incubation times. Experimental and microscopic settings were kept constant in both studies for comparison. The data of b) and c) are presented as average ± standard deviation, n = 5.

Increasing incubation times from 30 to 180 min obviously result in increasing fluorescence intensities, as it may be clearly seen in the micrographs of Fig. 5.4a. Thereby, the emission for all three channels (blue, green and red) increases. Highest intensities are observed with the blue detector, while longer wavelength emissions are weaker, in the order blue, green, red. Since this observation is in accordance with the characterization of the C-dots in aqueous suspension, it may be indicate that the particles are fully taken up by the cells. Furthermore, there is no preferred species in the uptake process among the C-dots, in the case of a mixture of different emitting species.

The plot of the integrated intensity of the micrographs for all channels against the incubation times, shown in Fig. 5.4b, enables quantification of the uptake kinetics. As such, an incubation of 180 min led to an increase of about 15-fold for the blue, 27-fold for the green and 17-fold for the red channel in comparison to the control cells (0 min). Following the time-course for the intensity of the blue channel, a stepwise increase may be observed. Thereby, saturations towards a fivefold increase is observed for incubations between 0 and 60 min, tenfold between 90 and 150 min and a further increase to 15-fold for 180 min.

For further verification of this stepwise increasing intensity, a second independent experiment with higher time-resolution was performed, whose results are shown in Fig. 5.4c. Here, the integrated intensity shows saturation to a fivefold value in comparison to the non-incubated cells (0 min) for incubation times between 5 and 60 min. Interestingly, increasing fluorescence intensities may already be observed after 5 min. As such, other uptake mechanisms than endocytosis may contribute to the incorporation of C-dots into NRK cells. From 60 to 90 min, a drastic intensity increase to a 15-fold value is observed, similar to the highest incubation time in Fig. 5.4b. This stays in contrast to other reports from literature, in which C-dots were described to be taken-up into HeLa cells during 1 h and further incubation only results in marginal additional incorporation (Li *et al.* 2012b).

The stepwise increase can possibly be assigned to different uptake mechanisms. Additionally, the achievement of maximum intensity values for increasing incubation times in the experiments can be attributed to a large number of incorporated C-dots. Cell viability is suggested to be affected for longer incubation times. As such, free diffusion of C-dots into the cells may play a role after a “partly permeabilization” of the cell membrane through the particles.

Unveiling the nature of the uptake mechanism of the C-dots into NRK cells, incubations with the particles at different temperatures were studied. Since, endocytosis is known to be inhibited at 4 °C (Goldenthal *et al.* 1984), the uptake of C-dots at 4 and 37 °C was analyzed and compared. Therefore, confluent NRK cells were incubated with C-dots for identical incubation times at 4 °C and 37 °C, respectively. Afterwards, the cells were analyzed via CLSM and the integrated fluorescence intensities of the micrographs were plotted against the incubation times. The results of this study are shown in Fig. 5.5.

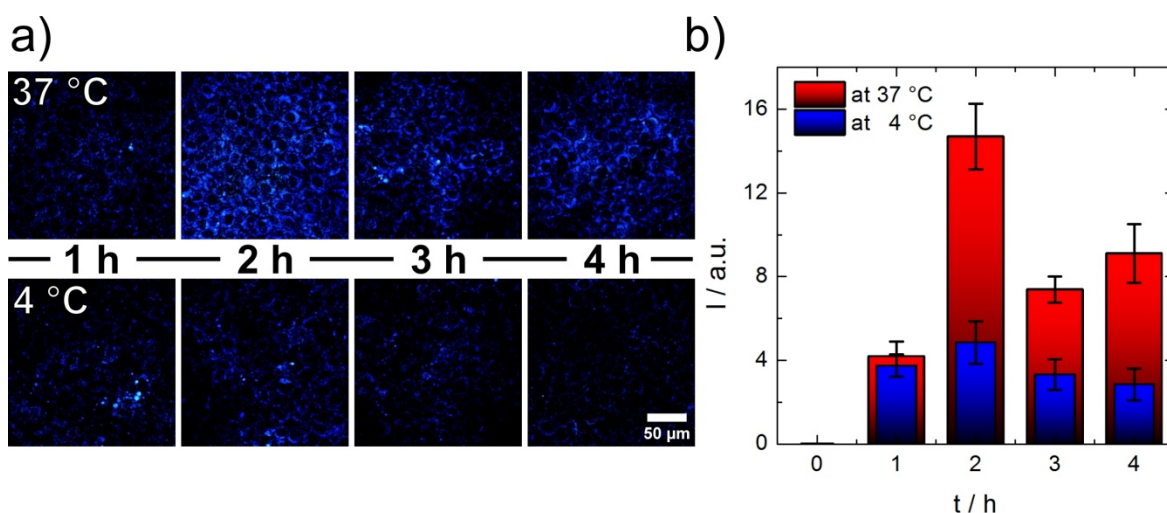


**Fig. 5.5:** Uptake of C-dots into NRK cells at different temperatures. a) Optical sections through NRK cells after incubation with C-dots (0.5 mg/mL) in PBS<sup>++</sup> for 1, 2, 3 and 4 h at 4 and 37 °C. Exc.: 405 nm, em. detectors: RGB. b) Plot of the average integrated intensities of the blue channel of the micrographs shown in (a) against the incubation time  $\pm$  standard deviation,  $n = 5$ .

As demonstrated in Fig. 5.5a, the incubation of NRK cells with C-dots at 4 and 37 °C results in bright blue luminescent cells already after 1 h. For longer incubation times, the fluorescence emission increases from cells under C-dot treatment at 37 °C. In contrast to this, the NRK cells incubated at 4 °C do not show significantly brighter emission from their cytoplasm. The plot of the integrated fluorescence intensity against the incubation times, in Fig. 5.5b mirrors this observation. After 1 h the two differently incubated NRK cell groups exhibit similar fluorescence intensities in the micrographs. Longer times show increasing intensities for the cells incubated at 37 °C while those at 4 °C remain roughly on the initial fluorescence intensity level. Similar observations are described in literature for the incorporation of C-dots into HeLa cells at different temperatures (Cao *et al.* 2007). As such, two uptake mechanisms are involved in the incorporation of C-dots into NRK cells. On the one hand, temperature-independent incorporation of the particles seems to take place in an early incubation phase. On the other hand, temperature-dependent endocytosis plays a significant role in the uptake process of C-dots into NRK cells when exposure time exceeds 1 h.

In order to confirm endocytosis as the main uptake mechanism for C-dots into NRK cells, the localization of the particles inside the cells was investigated. As such, NRK cells were incubated with C-dots and co-stained with LysoTracker® Green. This dye specifically stains lysosomes, which form from endosomes and are part of the endocytotic pathway. Colocalization of the particles and the dye fluorescence confirms localization of the particles inside lysosomes, as described in chapter 3.4.3. The micrographs of this study are shown in Fig. 5.6.

The highly magnified optical sections through the incubated NRK cells in Fig. 5.6a and d exhibit bright blue luminescence in their cytoplasm upon excitation at 405 nm, in a

heterogeneously dotted pattern leaving the nuclei free. Thereby, a higher degree of incorporated C-dots into the cells is observed for the incubation with 1.0 mg/mL (d), compared to the 0.5 mg/mL incubation (a). The staining with LysoTracker® Green in Fig. 5.6b+e shows green emission with a very similar pattern.

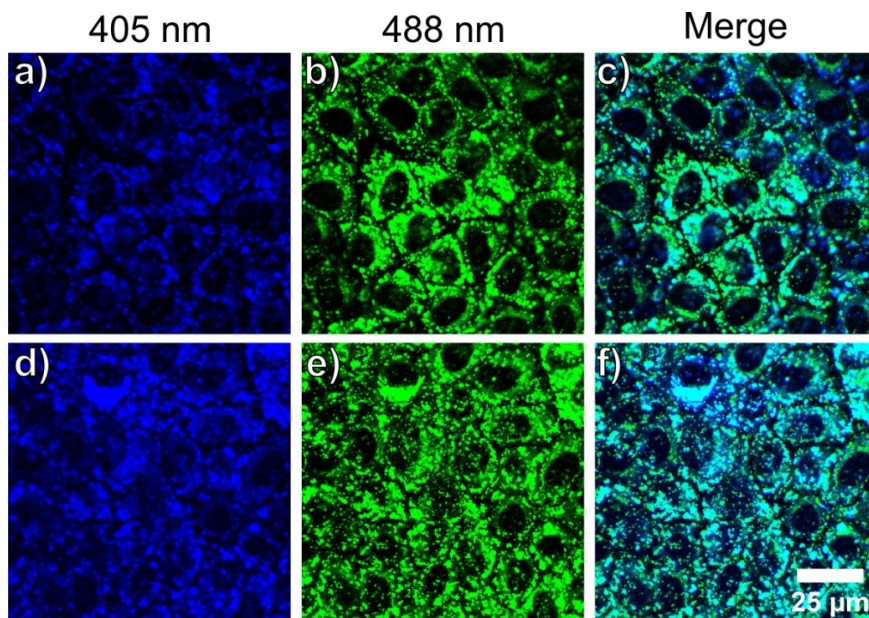


**Fig. 5.6:** Optical sections through NRK cells after co-staining with C-dots (a, b, c: 0.5 mg/mL and d, e, f: 1.0 mg/mL) and LysoTracker® Green for 30 min in full medium. a,d) Exc.: 405 nm, em. detector B. b,e) Exc.: 488 nm, em. detector G. c) Merge of picture (a) and (b). f) Merge of picture (d) and (e).

As such, the micrographs of both stainings were merged (Fig. 5.6c and f) in order to identify co-localization of the C-dot luminescence with the emission of the dye. The analysis of the merged images mostly shows co-localization of both patterns, indicated by the turquoise coloring. Accordingly, most of the C-dots are entrapped in lysosomes in the cytoplasm of the NRK cells. Therefore, endocytosis is highly suggested as main uptake mechanism for the C-dots. However, several purely blue spots are also observed in the merged micrographs. As such, it cannot be excluded that other uptake processes play a role in the incorporation of C-dots into NRK cells.

Reflecting the studies on the uptake of C-dots into NRK cells, it may be suggested that endocytosis may be the main uptake mechanism for the particles. The temperature-dependent uptake and the localization of the C-dots in lysosomes are strong hints for this issue. In literature, Q-dots and gold nanoparticles were described to be taken up via receptor-mediated endocytosis (Chithrani *et al.* 2006; Zhang *et al.* 2009). As such, analogies between the different nanoparticles can be seen concerning their internalization. However, most likely, C-dots are internalized via unspecific pinocytosis due to their ultra-small size, inducing vesicle-mediated incorporation.

Furthermore, it may be possible that the particles are incorporated into NRK cells via other pathways. Since the uptake of C-dots happens in minutes and not all of them may be found

in lysosomes, other mechanisms such as simple diffusion through “partly permeabilized” membranes of the ultra-small particles may be taken into consideration. Similarly, Li et al. stated that no special form of endocytosis could be connected to the intracellular uptake of C-dots, indicating the possible presence of a certain non-endocytic pathway which is energy independent (Li *et al.* 2012b).

### 5.3 Influence on Cell Adhesion, Proliferation and Migration

Impairments of mammalian cell physiology do not only involve cell death, but also processes, such as the adhesion on substrates, mitosis and cell proliferation, as well as the ability of adherent cells to migrate on substrates. For the study on the influence of C-dots on NRK cell behavior, the ECIS technique was used, which allows the non-invasive and time-resolved monitoring of cell response to different stimuli. For the studies in this chapter, NRK cells were treated with C-dots in increasing concentrations below the “critical concentration” of 1.1 mg/mL for long-term incubations, determined in chapter 5.1. Details on the different experimental set-ups are described in chapter 3.6.1.

#### Adhesion of NRK Cells Exposed to Increasing Concentrations of C-dots

For the investigation on the C-dots influence on NRK cell adhesion on substrates, cell suspensions in full medium were incubated in concentrations of 0.1, 0.3 and 0.5 mg/mL in two-fold determination. After 30 min of pre-incubation, the cells were seeded into 8W10E+ ECIS arrays in permanent presence of the C-dots. The time courses of the impedance and capacitance were recorded at multiple frequencies for the different populations. Fig. 5.7 shows the time courses of the normalized magnitude of the impedance and capacitance at different frequencies for this experiment.

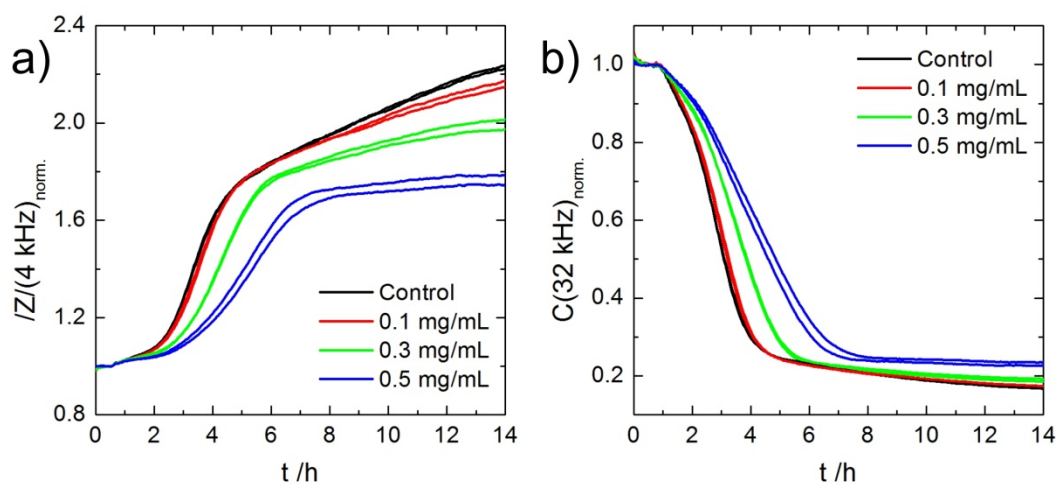


**Fig. 5.7:** Adhesion of NRK cells on 8W10E+ ECIS electrode arrays in presence of C-dots in concentrations of 0.1, 0.3 and 0.5 mg/mL in full medium at 5% CO<sub>2</sub>, 37 °C, n = 2. Control cells were not incubated with C-dots. NRK cells were preincubated with C-dots for 30 min at 37 °C. The time-point of cell inoculation is at t = 0.5 h. a) Time courses of the normalized magnitude of the impedance at 4 kHz. b) Time courses of the normalized capacitance at 32 kHz.

The time courses of the impedance in Fig. 5.7a show a direct correlation between concentration of the C-dots and the first impedance maximum, which can be assigned to adhered but not fully spread NRK cells. While non-incubated cells and those with the lowest C-dot concentration accomplish initial adhesion in 4 h, completion for the particle-



incubated cells is delayed with increasing concentration. Adhesion is accomplished here after about 5 h (0.3 mg/mL) and 6 h (0.5 mg/mL). Interestingly, the higher the C-dot concentration, the lower are the impedance values for the different cell groups. The time course of the capacitance in Fig. 5.7b confirms the observation of the direct correlation between C-dot concentration and the delay of cell adhesion. Additionally, slightly higher final capacitance values are observed for increasing particle concentrations. In further ECIS experiments, cell adhesion was studied for 0.6 mg/mL and higher concentrations. Thereby, no impedance increase was observed for 48 h. NRK cells do not adhere in permanent presence of C-dots at higher concentrations than 0.5 mg/mL.

According to these studies, it may be suggested that C-dots heavily affect NRK cell adhesion and that even lowest concentrations of 0.1 mg/mL show impairment. With increasing C-dot concentration NRK cells need longer time for the formation of a monolayer. Furthermore, it may be possible that the particles disturb the NRK cells ability to form cell junctions, which is reflected by the direct correlation between the final impedance/capacitance values and the C-dot concentration. While studies on the influence of C-dots on cell adhesion are not described so far in literature, established nanomaterials were therefore investigated. As such, disturbance of cell adhesion is a well-known phenomenon for some types of gold (Pernodet *et al.* 2006) and silica nanoparticles (Huang *et al.* 2010). Inhibition of the expression of adhesion proteins was attributed to the altered cell behavior.

#### Proliferation of NRK Cells in Presence of C-dots

Cell proliferation directly depends on mitosis and cell growth, which is significantly influenced by environmental factors such as toxicants. In order to study the impact of C-dots on cell proliferation, NRK cells were seeded and incubated with the particles in full medium after adhesion. The time courses of the impedance and capacitance at multiple frequencies were recorded in doublets for NRK cells with 0.2, 0.4 and 0.6 mg/mL C-dots in the medium, as well as non-incubated control cells. The corresponding normalized time courses are shown in Fig. 5.8.

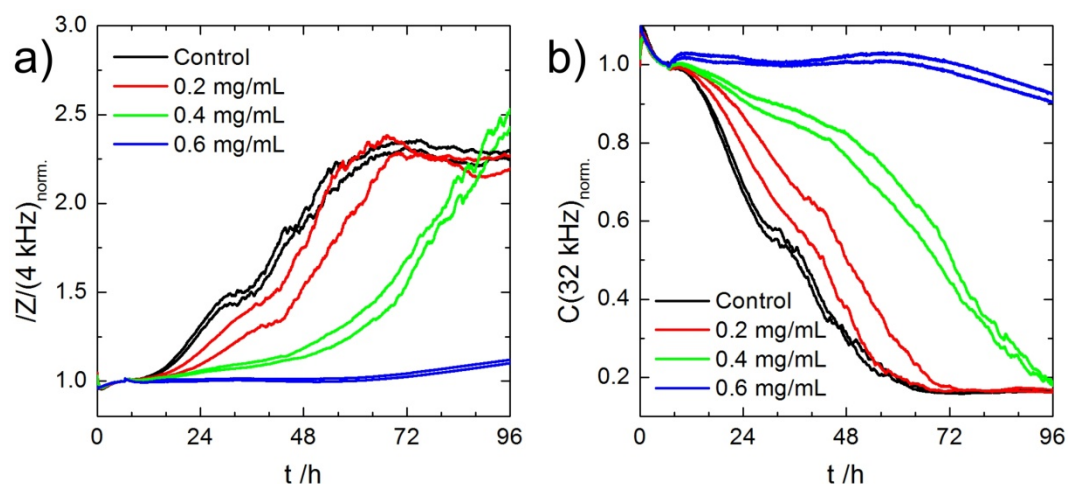


**Fig. 5.8:** Proliferation of NRK cells grown on 8W10E+ ECIS electrode arrays in presence of C-dots with concentrations of 0.2, 0.4 and 0.6 mg/mL in full medium at 5% CO<sub>2</sub>, 37 °C,  $n = 2$ . NRK cells were seeded in a density of 10.000 cells/well in order to monitor cell proliferation to monolayers. Control cells were not incubated with C-dots. Time point of the addition of C-dots at  $t = 6$  h. a) Time courses of the normalized magnitude of the impedance at 4 kHz. b) Time courses of the normalized capacitance at 32 kHz.

From the time courses of the normalized impedance in Fig. 5.8a, a direct correlation between C-dot concentration and the time for the formation of an NRK monolayer are observed. While the incubation with 0.2 mg/mL leads to short delays for the formation of the monolayer, the 0.4 mg/mL drastically slows down proliferation. For the cells incubated with this concentration higher impedance values were recorded for the monolayer. This effect can be related to the observation of increasing impedance values in the cytotoxicity evaluations, possibly due to cell swelling because of extensive C-dot uptake, or tightening of cell-cell contacts, described in chapter 5.1. For the incubation with 0.6 mg/mL, proliferation seems to be largely inhibited, since impedance shows no increase for 72 h. However, the slight increase in the last 24 h of the experiment may be attributed to a small minority of NRK cells showing no inhibition of mitosis at this concentration. The time course of the normalized capacitance in Fig. 5.8b allows of a more accurate view on the increasing coverage grade of the electrodes with the NRK cells. Non-incubated cells seem to fully establish a monolayer after about 60 h. Those which were incubated with 0.2 mg/mL do show a similar time course with only short delays of about 6 h for the establishment of a full monolayer. The incubation with 0.4 mg/mL shows significant delays, as seen in the impedance time courses. These cells need about 96 h for the full coverage of the ECIS electrodes. For the highest concentration, capacitance remains at the values for a cell-free electrode for a very long time. However, after 64 h capacitance begins to decrease. As mentioned before, it may be possible that mitosis of a very small population of NRK cells was not inhibited by the C-dots, explaining this observation. The observation of cell proliferation inhibition through C-dots was also described in literature for particle concentrations above 0.2 mg/mL for MCF-7 and HT-29 cells (Yang *et al.* 2009). However, analysis and discussion of this biocompatibility parameter of C-dots may scarcely be found

in literature so far. In contrast to this, properly capped Q-dots are described to show no influence on cell proliferation (Alivisatos *et al.* 2005). Since C-dots without passivation are able to interact with cellular biomolecules, they can disturb proliferation processes.

### Migration of NRK Cells Exposed to Increasing Concentrations of C-dots

The migration of NRK cells in the presence of increasing concentrations of C-dots was studied by wounding a confluent NRK monolayer with an electric pulse and monitoring the remigration of the cells into the center of the electrode. The time-courses of the normalized magnitude of the impedance at 4 kHz and the normalized capacitance at 32 kHz of such an experiment is shown in Fig. 5.9.

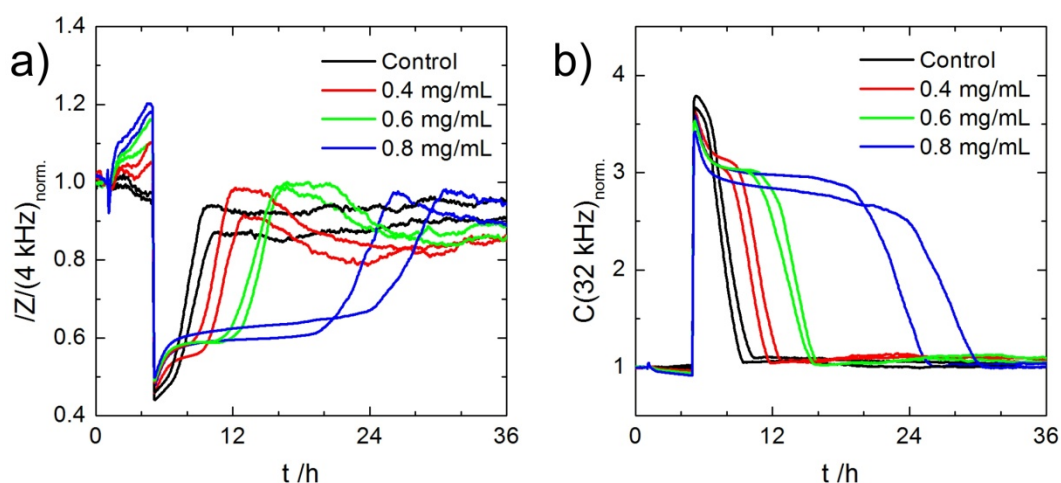


**Fig. 5.9:** Migration of NRK cells on 8W1E ECIS electrode arrays in presence of C-dots with concentrations of 0.4, 0.6 and 0.8 mg/mL in full medium at 5% CO<sub>2</sub>, 37 °C, n = 2. Control cells were not incubated with C-dots. Particles were added at t = 1 h. The electric pulse (30 s, 5 V, 40 kHz) was applied at t = 5 h. a) Time courses of the normalized magnitude of the impedance at 4 kHz. b) Time courses of the normalized capacitance at 32 kHz.

For the investigation of the influence of the C-dots on NRK cell migration the time courses of the impedance and capacitance after the application of the electrical pulse are studied. Prior to the wounding pulse, impedance values for NRK cells incubated with C-dots drastically increase over time. This effect is more pronounced the higher the particle concentration and may be attributed to the possible swelling through C-dot incorporation, described in chapter 5.1. Directly after the application of the electric pulse, all impedance time courses drop to the values of cell-free electrodes, due to the damaging of the cells on the electrodes. Afterwards, the impedance time courses in Fig. 5.9a show increasing values towards the level of the fully cell covered electrode prior to wounding for the non-incubated cells and for those incubated with C-dots in different concentrations. This is due to the re-population of the electrode with NRK cells. Time courses of the impedance increases are delayed for the C-dot incubated cells. While control cells completely covered the electrodes 5 h after wounding, those in the presence of 0.4 mg/mL C-dots needed 7 h

and those with 0.6 mg/mL needed 10 h. The incubation with 0.8 mg/mL drastically increased the delay to 20 - 25 h. This may indicate that migration is drastically impaired at these high particle concentrations.

Further experiments showed that NRK cells exposed to C-dots in higher concentrations did not show migration onto the electrode after wounding. As such, there is critical C-dot concentration for migration due to toxic effects. Interestingly, fully cell covered electrodes incubated with C-dot exhibit higher impedance values shortly after reaching confluence. Furthermore, the impedance signals after migration is complete are not as stable as they are for the control cells. This can be attributed to the impairment of the formation cell junctions by the particles. The time courses of the capacitance in Fig. 5.9b confirm the discussed observations of the time delay for the full recovering of the electrodes with NRK cells in presence of C-dots. Additionally, the slight capacitance increase for the C-dot incubated cells towards prolonged observation times may be interpreted by impairments of the formation of stable cell monolayer through the particles.

Compared to other nanomaterials, C-dots seem to show reverse affection of cell migration in the case of gold and silica nanoparticles. Both, silica and gold nanoparticles were described to prompt migration rates of cells incubated with these materials. Huang *et al.* showed this effect via scratch-assay on A375 cells having incorporated silica nanoparticles (Huang *et al.* 2010). Gold nanoparticles were shown to accelerate migration of HUVEC cells and A549 cells, possibly through redox signaling (Liu *et al.* 2014b; Nethi *et al.* 2014). Both, suppression and promotion of cell migration are disadvantages for a desired non-invasive label.

### Migration of NRK Cells after Short-term Incubation with Carbon Dots

Since staining of adherent cells with C-dots only requires short-term incubations of 1.0 mg/mL in EBSS<sup>++</sup>/G for 1 h, the migration of NRK cells loaded under these conditions was investigated and compared against control cells not incubated with particles. The analysis of cell behavior is therefore especially interesting, since C-dots are used for the active wounding of cell layers, as described in later chapters. Thereby, the bare internalization of the particles itself should be as non-invasive as possible. The resulting time-courses of the normalized magnitude of the impedance at 4 kHz and the normalized capacitance at 32 kHz of NRK cells exposed to 1.0 mg/mL C-dots for 1h compared against particle-free control groups are shown in Fig. 5.10.

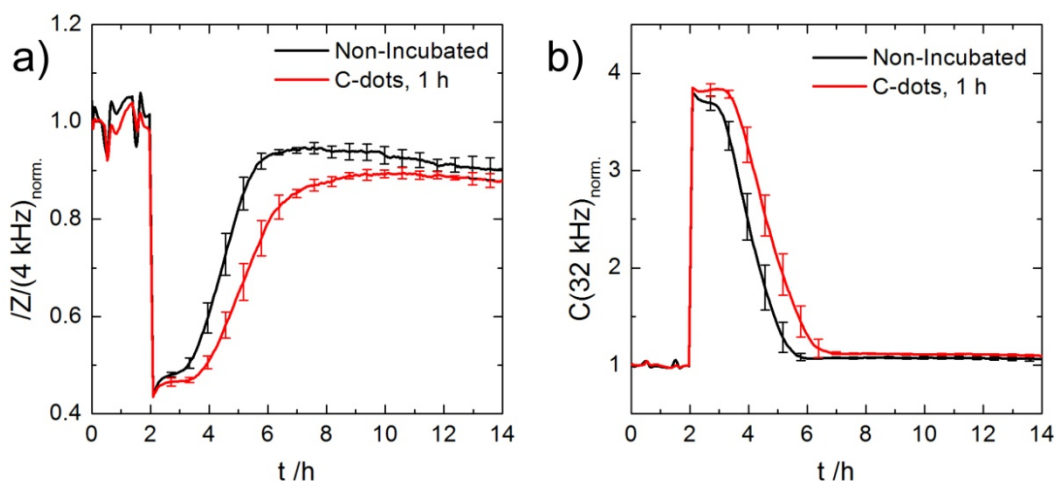


**Fig. 5.10:** Migration of NRK cells on 8W1E ECIS arrays after loading with C-dots. Time courses of the normalized magnitude of the impedance at 4 kHz (a) and capacitance at 32 kHz (b) as averages  $\pm$  standard deviation for the short-term incubation of NRK cells with 1.0 mg/mL C-dots in EBSS<sup>++</sup>/G for 1 h at 5% CO<sub>2</sub>, 37 °C, n = 4. Control NRK cells were not exposed to any particles. Time point of the addition of the particles is at  $t = 0.5$  h. Time point for the washing of the incubated cells is at  $t = 1.5$  h. The electric pulse was applied at  $t = 2.0$  h.

The time courses of the impedance in Fig. 5.10a show that the control NRK cells which were not exposed to C-dots re-populate the electrodes within 4 h after pulsing, while it took about 5 h for the *loaded* cells. Besides the short time-delay of 1 h, comparable impedance values were observed for both cell groups after reaching full coverage of the electrodes. The time courses of the capacitance in Fig. 5.10b are in accordance with the observation of a time delay of 1 h. Furthermore, both cell groups regain capacitance values of fully confluent electrodes as observed prior to pulsing. As such, it may be suggested that the *loading* of NRK cells with C-dots has only marginal effects on migration and wound healing ability of the cells. Furthermore, these cells may be considered as fully viable, consistent with the observations in the cytotoxicity evaluations for short-term incubations in chapter 5.1.

In summary, the ECIS studies showed that the permanent presence of C-dots in the cell culture medium heavily affects various cell processes. A direct correlation between C-dot concentration and time delays for adhesion, proliferation and migration was observed for all three cell processes. While adhesion is already affected at a very low C-dot concentration (0.1 mg/mL), migration is only inhibited relatively high concentrations (>0.8 mg/mL). Other nanoparticles, such as gold and silica also show influence on these cell processes, as discussed before. Accordingly, the utilization of these materials for analysis of cell behavior has to be seen critical. However, applications of the C-dots described in later chapters do not afford particles in the bulk phase and rely entirely on incorporated particles. As such, these harmful effects may be considered as highly suppressed, as demonstrated for the migration of C-dot-*loaded* NRK cells.

## 5.4 Permeation across Mammalian Cell Monolayers

Among nanoparticles, C-dots belong to the smallest representatives of their class. Additionally, these particles are highly water dispersible and are suggested to exhibit several functional groups on their surface. As such, C-dots are likely to easily penetrate cell membranes, layers and tissues. In order to quantify the particles ability to pass biological barriers Transwell® filters were used. Different mammalian cell lines were grown to confluence on these filters and the permeation of the C-dots across the cell layers was studied utilizing the particles intrinsic photoluminescence. Among the cell layers under study, MDCK I cells exhibit the tightest and NRK cells the leakiest junctions. MDCK II cells may be considered to be in the middle of both cell lines. This characteristic is reflected in the different transepithelial electrical resistances (TEER) of the cell lines: 400-3500  $\Omega \cdot \text{cm}^2$  (MDCK I), 40-100  $\Omega \cdot \text{cm}^2$  (MDCK II), 12  $\Omega \cdot \text{cm}^2$  (NRK-52E) (Wegener *et al.* 1996; Limonciel *et al.* 2012). As reference a FITC labeled dextran with molecular weight of 4 kDa was used, as this exhibits a similar hydrodynamic diameter of 1.4 nm (Watson *et al.* 2013). Furthermore, the unhindered diffusion through empty filters was investigated for comparison. The increasing fluorescence intensities in the lower compartments were normalized with respect to the fluorescence intensities obtained after mixing both compartments at the end of each experiment. Plots of the relative fluorescence intensity against the corresponding incubation times are shown in Fig. 5.11. From the plots different information about the diffusion kinetics were extracted. Since the data sets are in the shape of saturation curves, the slopes of the linear part of the curves starting from the first three data points were used for quantification of the diffusion kinetics through the cell layers. These were used for the calculation of the apparent permeability coefficients ( $P_{app}$ ) of C-dots and FITC-dextran, using the following formula (1) (Youdim *et al.* 2003).

$$P_{app}(\text{cm}/\text{sec}) = \left( \frac{V_D}{A \cdot m_{D0}} \right) \cdot \left( \frac{\Delta n_R}{\Delta t} \right) \quad (1)$$

In this equation,  $V_D$  is the apical “donor” volume ( $\text{cm}^3$ ),  $A$  is the surface of the membrane ( $\text{cm}^2$ ),  $m_{D0}$  is the amount of substance in the donor compartment at time point zero and  $\Delta n_R/\Delta t$  is the change of the permeation marker in the basolateral compartment over time (%/sec). The later is represented by the slope of the starting values for the different data sets. The following parameters were used in the calculation, as specified in Table 5.1.

$$\frac{1}{P_C} = \frac{1}{P_{app}} - \frac{1}{P_{Filter}} \quad (2)$$

**Table 5.1:** Parameters for the calculation of the  $P_{app}$  values for C-dots and FITC-dextran.

Parameter	Value
$V_D$	0.5 cm <sup>3</sup>
$A$	1.12 cm <sup>2</sup>
$m_{D0}$	0.15 mg (C-dots) 1.0 mg (FITC-dextran)

$P_{app}$  values for C-dots and FITC-dextran (4 kDa) were corrected for the values of empty filters according to formula (2).  $P_C$  is the permeability coefficient of the corresponding cell line and  $P_{Filter}$  is the one for empty filters.  $P_{Filter}(C-dots)$  was determined to  $7.89 \pm 2.60$  cm/s  $\cdot 10^{-3}$  and  $P_{Filter}(FITC-dextran)$  to  $10.94 \pm 2.83$  cm/s  $\cdot 10^{-3}$ . The calculated  $P_C$  values are shown in Table 5.2.

**Table 5.2:**  $P_{app}$  values derived from the linear parts of the data in Fig. 5.11 calculated from the first three data points of the curves. Values for the empty filters were averaged from three different experiments and were used for the calculation of  $P_C$  for the different cell lines.  $P_{app}$  values for C-dots originate from three independent measurements, while those for FITC-dextran were obtained from single measurements.

$P_C/cm/s \cdot 10^{-3}$	C-dots	FITC-D. 4 kDa
<b>NRK</b>	4.33 $\pm$ 0.98	1.55 $\pm$ 0.80
<b>MDCK II</b>	2.70 $\pm$ 0.75	0.51 $\pm$ 0.57
<b>MDCK I</b>	2.03 $\pm$ 0.53	0.13 $\pm$ 0.57

The  $P_{app}$  values of the C-dots and the FITC-dextran are highest for the empty filters, since these allow for unhindered diffusion between the compartments. For the permeation across the cell layers significantly slower increase rates and as such smaller  $P_{app}$  values were found for both tracers. These decrease in the order NRK – MDCK II – MDCK I, which is in great accordance with the TEER values of the cell lines. As such, the data suggests that the C-dots are mainly permeating paracellularly, leaking through the cell junctions.

Comparing the  $P_{app}$  values of C-dots against those of FITC-dextran, a much faster permeation of C-dots is observed for all three cell lines. This is 2.7 times faster for NRK cells, 4.8 times faster for MDCK II cells and 9.6 times faster for MDCK I cells. Apparently, C-dots are not as strongly hindered by tight cell junctions as the FITC-dextran, this could indicate that they are partly transported on transcellular pathways, e.g. undergoing endo- and exocytosis. This would be in accordance to recent studies on the permeation of GQDs through MDCK monolayers (Wang *et al.* 2015b).

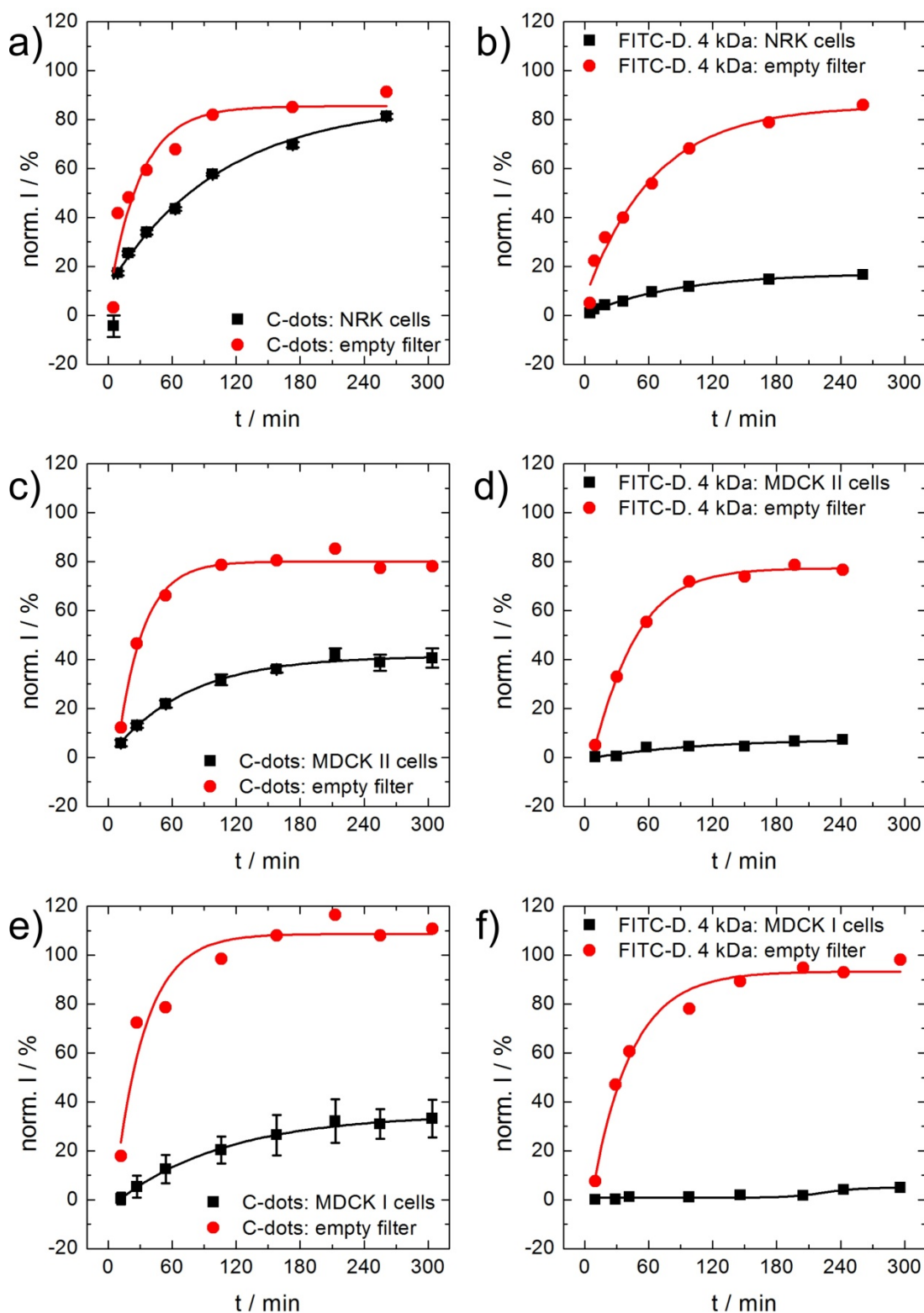


**Fig. 5.11:** Studies on the permeation of C-dots across mammalian cell monolayers grown on Transwell® filter. FITC labeled dextran (4 kDa) was used as reference. The graphs show the fluorescence intensities of the lower compartment normalized against the fluorescence intensities obtained after mixing both compartments at the end of each experiment. These were plotted against the incubation times. Permeation of C-dots across mammalian cell monolayer was performed in triplicate, all others in single experiments. The data were fitted with Boltzmann equation  $y=A_2-(A_1-A_2)/(1+e^{(x-x_0)/dx})$ . a,c,e) C-dot permeation across cell monolayer and empty filters. b,d,f) Permeation of FITC-dextran (4 kDa) across cell monolayer and empty filters. Cell lines: a,b) NRK; c,d) MDCK II; e,f) MDCK I.



For further analysis, the final fluorescence intensities were compared at the end of each experiment (after about 5 h) for both tracers. A list of these rates is shown Table 5.3.

**Table 5.3:** Final fluorescence intensities (after ca. 5 h incubation) normalized against the fluorescence intensities obtained after mixing both compartments at the end of each experiment. n = 3, for C-dots, n = 1 for FITC-dextran.

	C-dots	FITC-dextran 4 kDa
<b>NRK</b>	81.2 ± 1.1%	16.6%
<b>MDCK II</b>	40.6 ± 4.0%	7.2%
<b>MDCK I</b>	33.2 ± 7.8%	4.9%

The trends of the final fluorescence intensities for the different cell lines are in accordance with the increase rates of Table 5.2. Both, C-dots and the FITC-dextran, show decreasing final intensities for cell lines with higher TEER values in the order NRK – MDCK II – MDCK I. This also indicates that permeation of the C-dots is mainly paracellular. Among the samples, much higher rates of translocated C-dots were found than those for the FITC-dextran, for all cell lines. These are 4.9 times higher for NRK cells, 5.6 times higher for MDCK II cells and 6.7 times higher for MDCK I cells. As such, transcellular transportation of the C-dots may not be excluded, since high translocation rates can even be observed for cell layers with tightest junctions.

The studies on the interaction of C-dots with mammalian cells showed that there is an explicit critical mass concentration of 1.1 mg/mL for the long-term incubation of NRK cells with C-dots in full medium. However, for the *loading* of NRK much shorter incubation times are necessary as the incorporation of the particles happens fast, in the time range of minutes. For the standard incubation conditions of 1.0 mg/mL C-dots for 1 h in EBSS<sup>++</sup>/G no significant toxic effect was observed. Adhesion, proliferation and migration of the NRK cells are clearly restrained in the permanent presence of C-dots at subtoxic concentrations levels. This effect increases for higher particle concentrations and is most pronounced for cell adhesion and least for migration. The studies on the permeation of the C-dots across the cell layer obviously showed the high potency of the particles to pass biological barriers. Compared to  $P_{app}$  values of other nanomaterials in the literature, those for C-dots are two to three orders of magnitude higher. For example,  $P_{app}$  values for Q-dots and silica nanoparticles evaluated on a blood-brain barrier model are  $(1 - 6) \cdot 10^{-6}$  cm/s (Hanada *et al.* 2014). An evaluation of  $P_{app}$  of GQDs on MDCK cells resulted in  $(1 - 3) \cdot 10^{-6}$  cm/s GQDs in a sized of 12 nm and  $(0.5 - 1.5) \cdot 10^{-6}$  cm/s for GQDs in a sized of 3 nm (Wang *et al.* 2015b). This clearly shows the ability of C-dots to pass biological barriers. Together with fast uptake times into cells, these properties mark C-dots as highly interesting particle systems for the application as labels or probes in mammalian cells with deep tissue penetration.

### 5.5 Impact of Carbon Dots on Beating Cardiomyocytes

As described in chapter 3.6.2, the influence of C-dots on the contraction of Cor.At® cardiomyocytes was analyzed via ECIS. Therefore, the impedance time-courses of several cell populations were recorded prior to the C-dot addition as reference. Subsequently, the cardiomyocytes were incubated with C-dots in concentrations between 0.2 and 0.9 mg/mL. The high resolution impedance time courses for each population were recorded 2, 4, 6, 8 and 24 h after particle addition. Control cardiomyocytes that were not exposed to C-dots served as control to account for cell behavior changes over time. From the different conditions, selected impedance time courses are shown in Fig. 5.12, in order to illustrate typical results of this study.

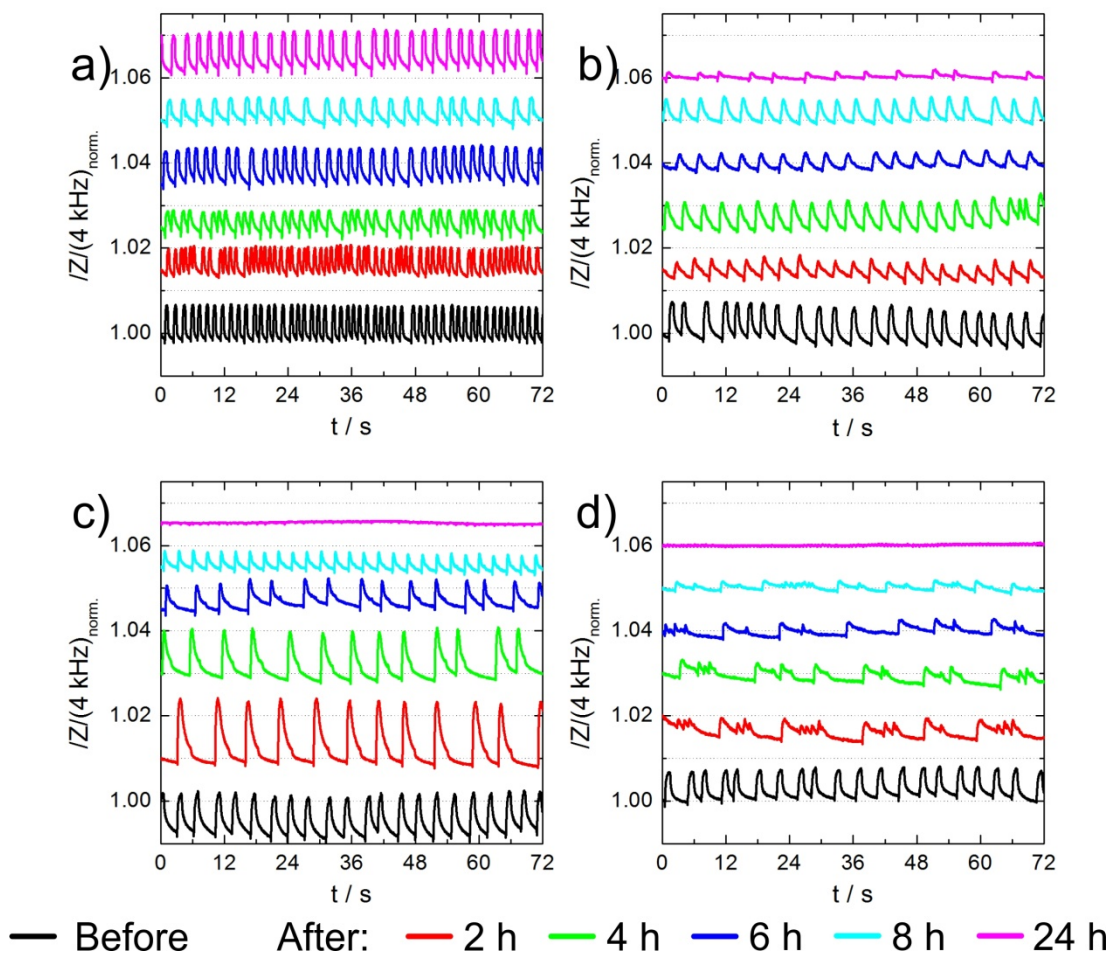


**Fig. 5.12:** High resolution time courses of the normalized impedance magnitude at 4 kHz for contracting Cor.At® cardiomyocytes on 8W1E $\mu$  arrays at 5% CO<sub>2</sub>, 34 °C. Time courses were normalized to their starting values and are plotted with offset towards each other. Recording was performed before and after incubation with C-dots at different times after particle addition in medium. In the plots the following incubation conditions were examined: a) Without C-dots, b) 0.4 mg/mL, c) 0.5 mg/mL, d) 0.7 mg/mL.

The impedance time courses of the control cardiomyocytes in Fig. 5.12a show rhythmic impedance peaks with about 55 beats per minute (bpm) and amplitudes of about 0.7% in the first measurement (black line). This indicates the synchronous contraction of the cardiomyocytes on the ECIS electrodes. Over time, the amplitudes of the later time

courses seem to vary randomly, while the contraction rate slows down to 23 bpm after 24 h (magenta line). As such, the contraction rates of the cells decrease over time even under control conditions.

The impedance time courses, before and after the incubation with 0.4 mg/mL C-dots are shown in Fig. 5.12b. Prior to incubation the cardiomyocytes show contraction rates of 17.5 bpm with amplitudes of about 0.8% (black line). After the addition of the particles, the amplitudes of the impedance spikes get smaller. However, no significant deviation from the control cells can be observed between 2 and 8 h. After 24 h (magenta line), the amplitudes of the impedance spikes reach only values lower than 0.1% with about 11 bpm. Thus, C-dots at a concentration of 0.4 mg/mL weaken the contraction of cardiomyocytes for exposure times close to 24 h.

Incubations with a higher C-dot concentration of 0.5 mg/mL result in a complete stop of the cell contractions after 24 h incubation, as indicated in Fig. 5.12c. The impedance signal exhibited 19 bpm with amplitudes of 1.0% (black line) before incubation. Interestingly, the amplitude increases to 1.45% after 2 h (red line) and decreases afterwards to 0.4% after 8 h (cyan line). At the same time, the contraction rate increased to 22.5 bpm. This may be assigned to the same phenomenon observed for the incubation of NRK cells with C-dots, described in chapter 5.1. In experiments addressing acute toxicity, the impedance also increased for several hours directly after particle addition before decreasing drastically for toxic C-dot concentrations.

Acute toxicity can be observed for particle additions of 0.7 mg/mL, well observable from the impedance time courses in Fig. 5.12d. Prior to the incubation with C-dots the cardiomyocytes show rhythmic contraction indicated by the impedance increases with 16.5 bpm and an amplitude of 0.7% (black line). Already after 2 h (red line), contraction of the cells becomes unrhythmic with decreased rates of 5 bpm and decreasing impedance values. After 8 h (cyan line), the amplitudes of the impedance spikes are barely detectable with values of 0.1%. The last impedance time course after 24 h (magenta line) shows constant impedance values, indicating complete loss contraction ability.

The results of this study indicate that there is a critical C-dot concentration of about 0.4 mg/mL for Cor.At® cardiomyocytes with respect to their beating. Lower concentrations (in this case 0.2 mg/mL) did not affect contraction of the cells, while higher concentrations led to a loss of beating within 24 h. Acute toxicity is observed for 0.7 mg/mL and higher concentrations. Thereby, the cells immediately change their contraction behavior, possibly due to the internalization of C-dots in large amounts. Most likely, these affect intracellular signaling pathways, disturbing the cells ability for rhythmic contraction (Peters *et al.* 2015). For the first time, this disrupting effect of C-dots on the beating of cardiomyocytes was described. However, literature shows that other nanomaterials also show impairments of cardiomyocyte contractility. Among them, the degradation of TiO<sub>2</sub> nanoparticles heavily

### *Interaction of Carbon Dots with Mammalian Cells*

affects cardiomyocyte contraction through release of inorganic ions (Jawad *et al.* 2011). 2,3-dimercaptosuccinic acid modified Fe<sub>2</sub>O<sub>3</sub> nanoparticles were reported to show no impact on the beating, up to concentrations of 0.1 mg/mL (Mou *et al.* 2015). As such, a proper characterization of the nanomaterials interactions with different cell types has to be performed before utilization as label or probe.

## 6 Multicolor Cell Imaging using Carbon Nanomaterials as Luminescent Probes

The following chapter describes studies on the application of C-dots and GQDs in NRK cells for multicolor imaging. The fast incorporation of the particles into the cells and their unique optical properties, described in chapters before, were utilized for a functional staining of the cells. Multicolor imaging was performed via CLSM in combination with the proper laser wavelength for excitation and the selective use of the RGB emission detectors, described in chapter 3.4.2.

### 6.1 Carbon Nanomaterials for Multicolor Imaging of Normal Rat Kidney Cells

In chapter 4.1.3 the change of the optical properties of the C-dots due to concentration variations was described. Thereby, the emission is red-shifted into the green spectral region upon excitation with 405 nm for high particle concentrations. Furthermore, the excitation at 488 nm results in highest fluorescence intensities for large particle concentrations. In order to investigate the multicolor imaging applicability of the C-dots based on enrichment in certain cell compartments living and lysed NRK cells were incubated with the particles. Subsequently, the cells were analyzed via CLSM and the corresponding optical sections are shown in Fig. 6.1.

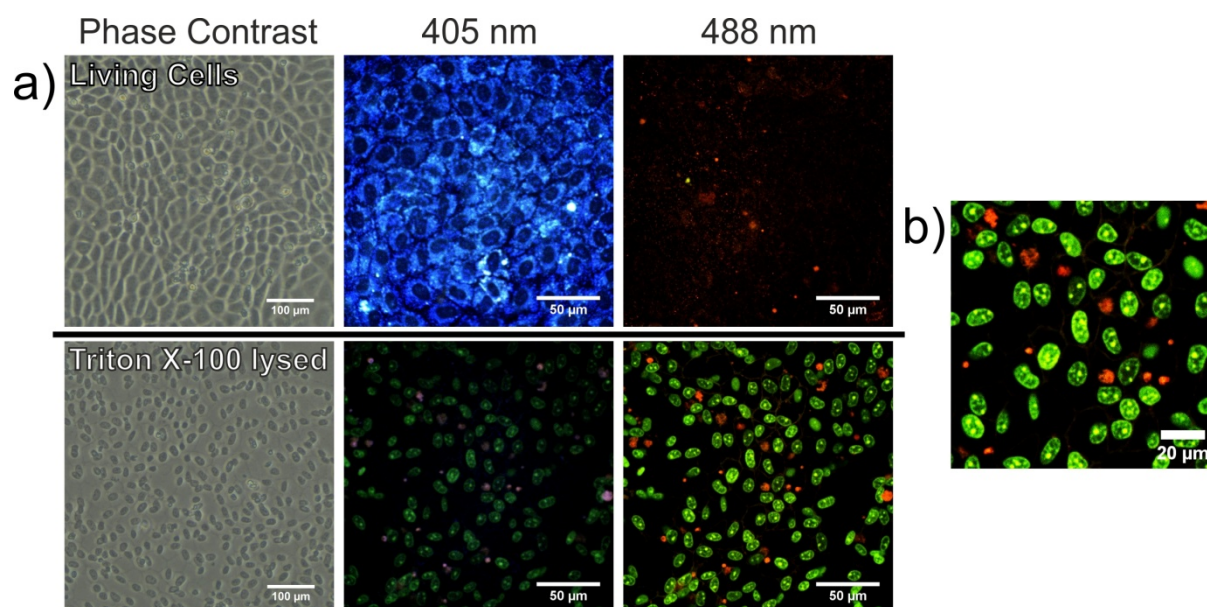


**Fig. 6.1:** a) Micrographs of NRK cells with and without lysis before staining with C-dots. Living cells were incubated with 1.0 mg/mL C-dots in PBS<sup>++</sup> for 30 min at 37 °C. Lysed cells were treated with 0.5% Triton X-100 in PBS<sup>++</sup> for 30 min, before staining. Cells are shown under phase contrast and as optical sections via CLSM with 405 nm, respectively 488 nm, laser excitation. RGB detector settings were kept constant for all optical sections. b) Magnification of Triton X-100 lysed and C-dot stained NRK cells from (a).

As demonstrated in the micrographs of Fig. 6.1a, the living NRK cells which were incubated with the C-dots exhibit their typical morphology without any sign of toxic effects in phase contrast. Upon excitation with 405 nm via CLSM the cytoplasm of these cells shows bright blue luminescence with the cell nuclei remaining unstained. The irradiation with the 488 nm laser does not result in particular fluorescence emission. From the NRK cells which were lysed with Triton X-100 only the nuclei remain clearly visible in phase contrast. The incubation of these samples with the C-dots significantly changed the emission behavior of the particles. While the excitation at 405 nm results in weakly green fluorescing nuclei, the excitation at 488 nm shows them brightly green. Interestingly, the nucleoli inside each cell nucleus appear particularly bright, as indicated in Fig. 6.1b. Selective nucleoli staining was also reported for other C-dot preparations in literature and therefore this behavior is consistent with other studies. As such, Kong *et al.* described green fluorescent C-dots prepared from PEG 200, which particular staining the nuclei and nucleoli of living HeLa cells (Kong *et al.* 2014). Another report from literature showed that the modification of C-dots with basic amines induces selective staining of nucleoli with the particles. The authors claim that this enables cross-linking of the modified C-dots' primary amino groups with proteins or DNA and therefore explain ribosomal affinity (Barbosa *et al.* 2015). However, for the C-dots in this work no reactive primary amine groups were detected using selective dyes, as shown in chapter 4.1.2.

This observation is in great accordance to the change of the C-dots optical properties with increasing concentration. As such, it may be assumed that living NRK cells incorporate the particles in small amount, mostly via endocytosis, as described in chapter 5.2. Thereupon the C-dots seem to be trapped in the endosomes, not being able to freely enter the cell nuclei, which would explain the absence of luminescence in the nuclei. By contrast, the direct contact to the bulk phase after membrane permeabilization enables binding and access of the C-dots to the nuclei. The subsequent accumulation of the particles may result in high local concentrations of the C-dots which is responsible for the observed changes in emission behavior. A possible explanation for the more bright nucleoli might be the different binding behavior of the particles towards DNA, RNA and/or proteins of which this compartment mainly consists.

However, it has to be mentioned that the optical properties of the C-dots were characterized in solution. Thereby, reabsorption effects and varying self-quenching behavior of diverse C-dot species were discussed to be responsible for this phenomenon. Accordingly, a second possibility for the different coloration might be that preferably the green emitting species binds to the DNA in the cell nuclei or that the binding itself changes the optical properties of the C-dots. Further investigations on the specific staining of living and dead cells as well as reasons for the different emission behavior are described in chapter 6.2.

Recently, red-shifted fluorescence was described in literature for carbon fluoroxide particles upon accumulation in the nuclei of 3T3-L1 fibroblast cells, in contrast to low concentrated particles in their cytoplasm. The authors claim that this effect may be observed for unharmed cells and that the particles incorporation did not induce significant changes in size and shape of the cells (Kharin *et al.* 2015). This stays in contrast to the particular accumulation of C-dots in the nuclei of dead NRK cells. However, the observation of changed optical properties of the C-dots from starch and Trp does not seem to be unique among photoluminescent carbon nanoparticles. In literature, the localization of this kind of nanoparticle is described to be highly dependent on the surface charge. Negatively and neutrally charged silicon carbide nanoparticles were found to be located in the cell nuclei, while positively charged particles are located in the cytoplasm (Serdiuk *et al.* 2012). The N-doped C-dots from starch and Trp meet this criterion, as indicated by their slightly negative zeta potential, as shown in chapter 4.1.2.

#### Multicolor Imaging with Carbon Dots in fixed NRK Cells

Since it has been demonstrated that multicolor imaging of cells and cell compartments is possible, the principle behind the diverse staining was further investigated. Therefore, NRK cells were fixed with para-formaldehyde (PFA) to preserve cellular morphology and to partly permeabilize their membrane. These cells were incubated with C-dots for different periods of time in order to let the particles accumulate inside the cells. Subsequently, the cells were analyzed via CLSM utilizing all three lasers to identify deviations in the staining of the cells at different excitation wavelengths. The optical sections of the C-dot stained and fixed NRK cells are shown in Fig. 6.2.

As demonstrated in Fig. 6.2, all fixed NRK cells incubated with C-dots exhibit bright luminescence throughout the whole cell bodies upon all three laser irradiations at different wavelengths. The control cell group exhibits only very marginal fluorescence emission for the given detector settings. For the irradiation with 405 nm laser light the most interesting deviations between cells exposed to C-dots for increasing times were observed. Among them, the cells which were incubated for 1 h show bright blue cytoplasmic fluorescence with nuclei appearing darker but with brighter nucleoli inside. Those cells which were incubated for 4 h do show a similar pattern with a greenish luminescence, while the 24 h incubated cells appear green-reddish. As such, the extension of the incubation times results in increasing intensities for the green and red detector channels for the 405 nm excitation. This is also indicated for the irradiations with the 488 and 543 nm laser light. Thereupon, the emission intensities increase for both excitation wavelengths and prolonged incubation times.

In summary, longer incubation times with C-dots result in accumulation of the particles inside the fixed NRK cells. As annotated in chapter 4.1.3, higher concentrations of the C-dots result in altered emission behavior of the stained cells for the three different laser wavelengths. The observation of the green shift to longer incubation times for excitation at 405 nm is in great accordance with the spectroscopic characterization. Additionally, the fluorescence intensity increase for the 488 and 543 nm excitation after prolonged incubation times, observable in the cell imaging experiment, may also be observed for increasing concentrations in suspension. Accordingly, different local C-dot concentrations may be responsible for the multicolor staining. The observation of darker nuclei with brighter nucleoli may be due to diverse binding behavior of the particles towards the local biomolecules: DNA, RNA and proteins. As such, accumulation and binding (of possibly specific subpopulations) of C-dots in cell compartments and on biomolecules may be responsible for the multicolor staining effect.



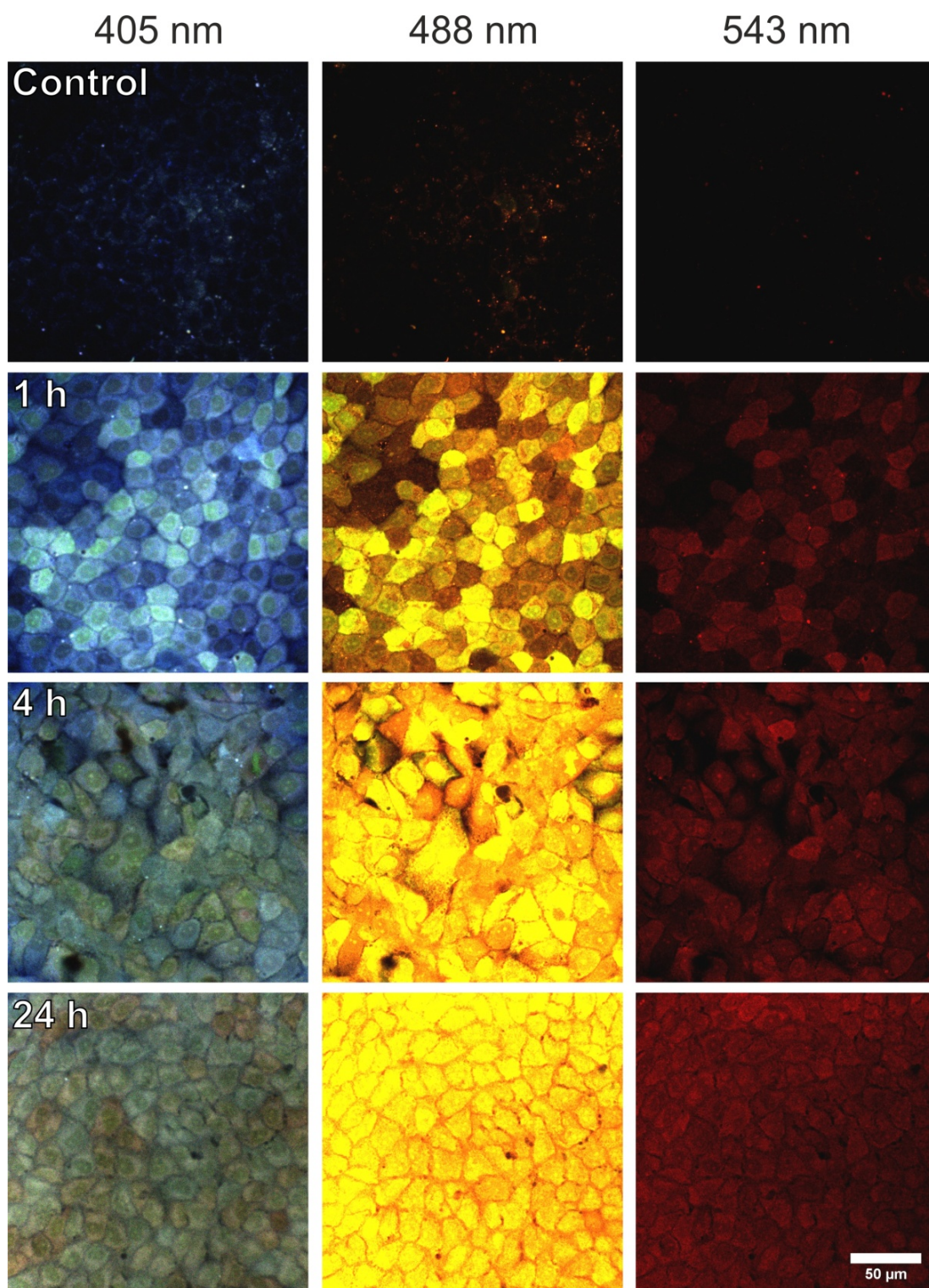


**Fig. 6.2:** Optical sections via CLSM through NRK cells after fixation with 4% PFA (w/v) in PBS<sup>++</sup> for 15 min and staining with 1.0 mg/mL C-dots in PBS<sup>++</sup> at 37 °C for increasing incubation times, from three different experiments. After every incubation step the cells were washed with PBS<sup>++</sup>. PFA-fixed NRK cells, which were not exposed to C-dots served as control. The cells were irradiated with 405 nm, 488 nm and 543 nm, respectively. The RGB detector settings were kept constant for all micrographs.

### Incorporation and Imaging of Liposome encapsulated C-dots in NRK Cells

For the application of nanoparticles in bioanalytical (imaging) assays a specific staining or detection of target structures or molecules is often desired. In the case of C-dots the utilization of liposomes as delivery vehicle was investigated. Therefore, the staining of NRK cells with free C-dots was compared to a staining with liposome encapsulated C-dots. Typical optical sections via CLSM are shown in Fig. 6.3.

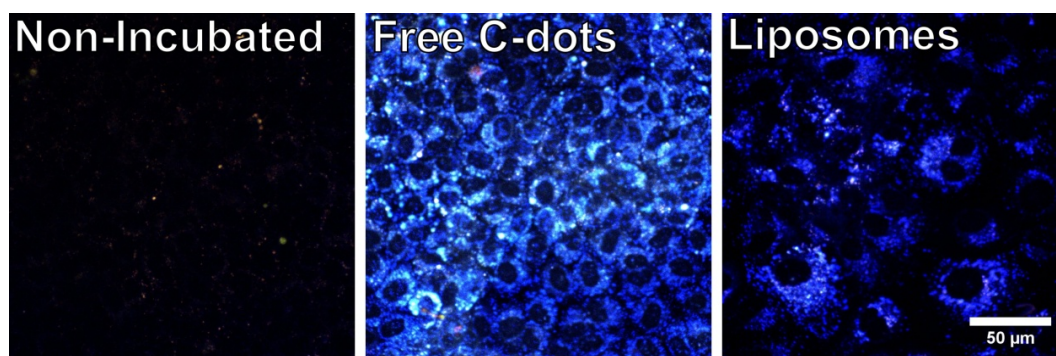


**Fig. 6.3:** Optical sections via CLSM through NRK cells incubated with C-dots (1.0 mg/mL) and liposomes with encapsulated C-dots (total phospholipids conc.: 1.1 mM), all in full medium for 1 h at 37 °C. NRK cells which were not exposed to the particles served as control. Exc.: 405/488 nm simultaneously. The magnification and the RGB detector settings were kept constant for all micrographs.

The comparison of both micrographs reveals a very different staining pattern for the two different cell groups. While the incubation with free C-dots results in a fully packed cytoplasm of all NRK cells, the liposome incubated cells exhibit a more heterogeneous staining pattern. The luminescence in these cells appears coarser, often enriched in one half of the cells. This may indicate incorporation into the Golgi complex. Furthermore, the cells appear much larger and not as densely packed as those incubated with free C-dots, although both cell samples were seeded in similar conditions. Possibly, the internalization of C-dots through this uptake process is more invasive than the uptake of free particles. In summary, C-dots are steadily encapsulated inside the liposomes and are not set free during the uptake process into NRK cells. Furthermore, the modification of those liposomes might be used to specifically target distinct structures or compartments inside cells.

### Oleic Acid modified C-dots for the Imaging of fixed NRK Cells

Carbon dots were modified with oleic acid in order to change their staining pattern for mammalian cells. In order to distinguish differences in the staining behavior of both, modified and unmodified C-dots, fixed NRK cells were incubated with the particles. Furthermore, fixed NRK cells were additionally lysed for the staining experiment. This allows the free diffusion of the C-dots into the cell bodies. After incubation with the particles, the cells were analyzed via CLSM. The corresponding micrographs are shown in Fig. 6.4.

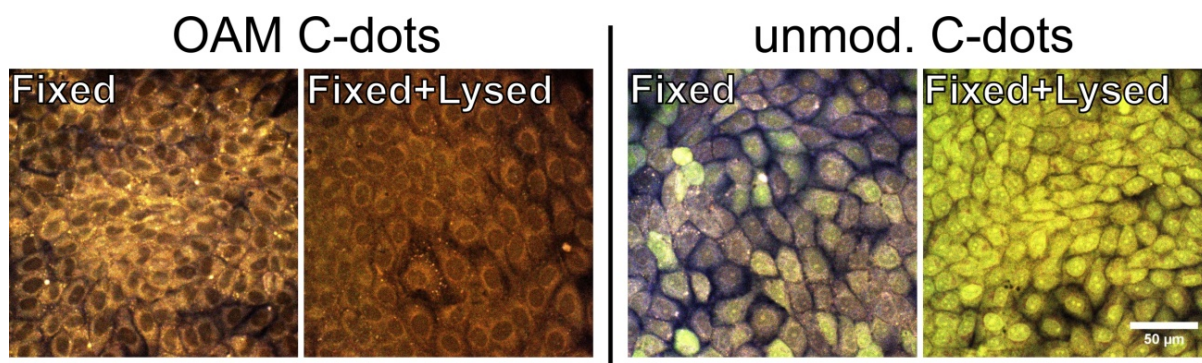


**Fig. 6.4:** Optical sections via CLSM through PFA-fixed NRK cells incubated with OAM C-dots (1.0% v/v) and C-dots (1.0 mg/mL), all in PBS<sup>++</sup> for 45 min at 37 °C. Fixed NRK cells were treated with PFA (4% in PBS<sup>++</sup>) for 15 min prior to staining. Fixed and lysed NRK cells were additionally treated with Triton X-100 (0.5% in PBS<sup>++</sup>) for 15 min prior to staining. Exc.: 405/488 nm simultaneously. The magnification and the RGB detector settings were kept constant for all micrographs.

Comparing the staining of the fixed NRK cells, a different coloration for either C-dot type is obvious. While the modified versions exhibit long wavelength emission (orange-red) for the two cell groups, the unmodified C-dots show emission in the shorter wavelength light region. Among them, the non-lysed cells appear mostly bluish, probably due to low concentrations of incorporated C-dots. The lysed cells appear brightly yellow, most likely due to the free diffusion of large amounts of particles into the cell body. Again a concentration dependent emission wavelength-shift may be the explanation for this behavior. The long wavelength emission of the OAM C-dots is in accordance with spectroscopic characterization of the particles in chapter 4.3. The observations have been attributed to solvatochromism or a dominating contribution of a long wavelength emitting species in the particle suspension, as discussed before. Interestingly, the OAM C-dots do not show accumulation inside the nuclei of both cell groups, non-lysed and lysed. In contrast to this, unmodified C-dots clearly show this behavior. Since the particles have direct access to the cell nuclei they accumulate in this compartment, undergoing changes of their emission properties. Thereby, several nuclei of the non-lysed cells appear greenish, while the lysed cells' nuclei appear bright yellow. Here, it has to be mentioned that PFA partly permeabilizes the cell membrane, enabling direct contact of the nucleus to the bulk phase. As such, the interaction of unmodified C-dots is obviously based on their small size and functional groups on the surface for electrostatic interactions. These properties were changed through the modification with the long chain fatty acids and obviously inhibit the binding to DNA inside the nuclei. Further investigations on this issue are described in the next chapter.

Incorporation and Imaging of GQDs in NRK Cells

In literature, terminology of GQDs and C-dots does often not clearly distinguish between the two species. One of the objectives of this work is to work out differences between both materials. As such, the applicability of GQDs as imaging materials in NRK cells was investigated and compared against characteristics of C-dots. In Fig. 6.5 micrographs of GQD incubated NRK cells are shown.

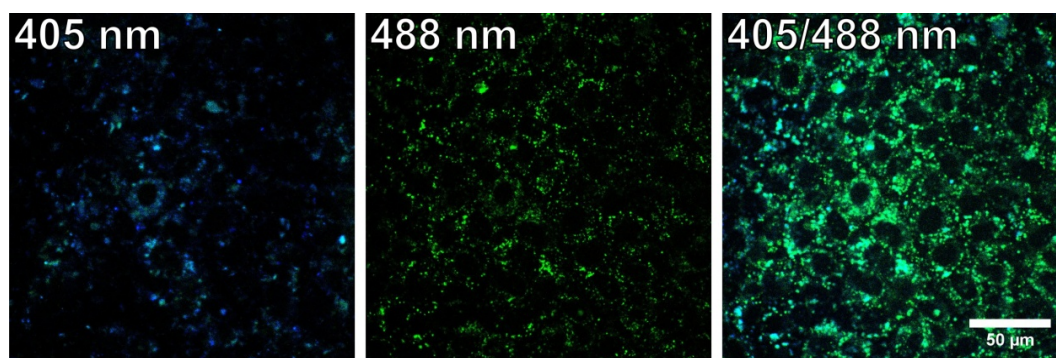


**Fig. 6.5:** Optical sections via CLSM through NRK cells incubated with GQDs (~ 0.1 mg/mL) for 2 h in EBSS<sup>++</sup> at 37 °C. Exc. at 405 nm, 488 nm and 405/488 nm simultaneously, RGB detector settings were kept constant for all micrographs.

The incorporation of GQDs into NRK cells led to a rather weak fluorescence emission inside the cells upon excitation at 405 or 488 nm. This shows blue-green emission with excitation at 405 nm and green emission with excitation at 488 nm. The relatively weak fluorescence has to be attributed to the low quantum yields of the material, described in chapter 4.2. Only the simultaneous excitation with both lasers results in significant fluorescence intensities. Thereby, the nuclei stay luminescence-free and the emission in the cytoplasm appears speckled. This may be attributed to a vesicular incorporation of the GQDs, which is similar to the incorporation of C-dots. Since both materials are meant to exhibit vastly different functional groups on the surfaces, it may be suggested that they are mostly incorporated via endocytosis using different or no receptors on the cell membrane surfaces.

## 6.2 Distinguishing Between Living and Dead Mammalian Cells Using Carbon Dots

In the previous chapter, it was shown that C-dots enable multicolor imaging of mammalian cells. Thereby, living cells most likely take up C-dots in low concentrations via endocytosis. These particles are suggested to be trapped in endosomes not being able to freely enter the nuclei of the cells. This results in bright blue emission of the cytoplasm of those cells upon excitation at 405 nm. Damaged or dead cells by contrast, undergo loss of plasma membrane integrity, enabling direct contact between the cell nuclei and the bulk phase. As such, C-dots are suggested to freely pass the nuclear pore complex inside the cell due to their small size and accumulate inside the nucleus. Since nuclei mainly contain DNA, C-dots are thought to bind to DNA in large number. The high local concentration of the particles may be responsible for the observed emission shift towards bright green fluorescence of the nuclei upon excitation at 488 nm. Alternatively, it may be possible that within a C-dot preparation as mixture of different species long wavelength emissive species favorably bind to DNA explaining the red-shift. Another possibility might be that the binding to DNA itself influences the spectroscopic properties of the C-dots due to a changed environment. In order to investigate this phenomenon, the following chapter describes studies on the interaction between C-dots and DNA. Furthermore, the specific staining of living and dead cells was used for the evaluation of cytotoxicity assays of several chemicals on NRK cells via CLSM.

### Studies on the Interaction between C-dots and DNA

As a first verification of the suggested binding of C-dots to DNA, blotted DNA structures were incubated with C-dots and analyzed via CLSM utilizing the particles' intrinsic fluorescence. As control, EthD-1, a well-known DNA intercalating and staining agent was applied to the same DNA structures. Details on the preparation of the structures and the staining are described in chapter 3.4.3. The obtained micrographs are shown in Fig. 6.6.

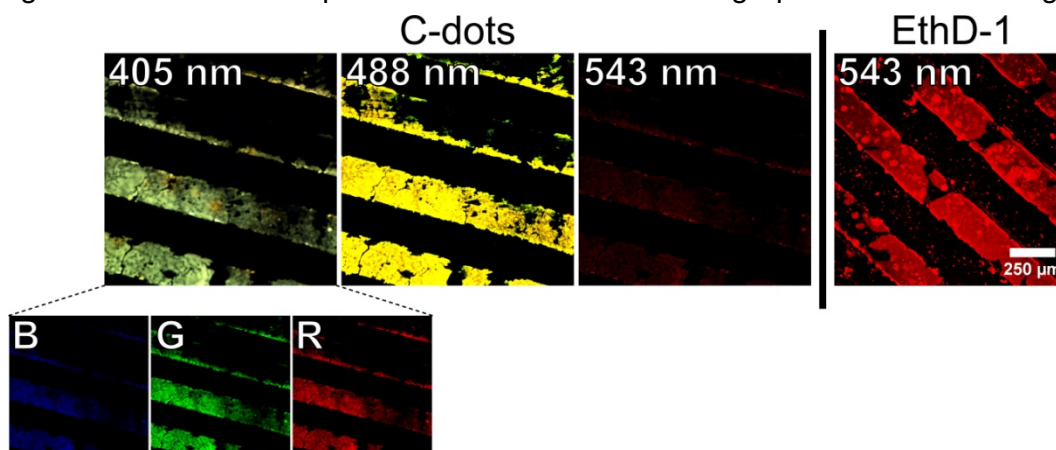


**Fig. 6.6:** Blotted DNA stained with C-dots and EthD-1 under laser excitation with different wavelengths. The micrograph of the 405 nm excitation was split into its blue, green and red channel. RGB detector settings were kept constant for the C-dot micrographs.

Examining the micrographs in Fig. 6.6, the structures of the blotted DNA are clearly visible for both, the C-dot and the EthD-1 staining. The DNA incubated with C-dots exhibits green emission upon excitation at 405 nm, yellow with excitation at 488 nm and weak red for irradiation with 543 nm laser light. By contrast, the EthD-1 stained DNA structure exhibits brilliant red fluorescence emission, as expected. As such, the data shows that C-dots selectively bind to DNA very similar to the organic dye. The coloration of 405 nm excited DNA appears greenish, which is in accordance with the observation in the cell experiments. Thereby, the nuclei of dead cells also show weak green fluorescence upon excitation at 405 nm, which can be seen in Fig. 6.1a. The splitting of the micrograph into its blue, green and red channel shows very weak blue emission, while green emission is superior and red emission relatively strong. The 488 nm excited DNA exhibits brilliant yellow emission, with green and red emission at similar intensity levels, which differs from the green nuclei observed in cell experiments. This may be explained by higher local concentration of C-dots in the blotted DNA structure, resulting in a stronger red-shift of the emission. This would be in accordance to the concentration dependent emission changes of C-dots in solution described in chapter 4.1.3. As such, the different coloration via CLSM may be attributed to local C-dot accumulations.

For a more detailed examination of the interaction between C-dots and DNA, the photoluminescence of the particles was studied in solution upon incubation with DNA. Therefore, 0.5 mg/mL C-dots in PBS were mixed with increasing concentrations of ds DNA and the emission spectra were recorded with excitation at 488 nm. The corresponding averaged emission spectra for the particle mixtures and the DNA preparation, as well as integrated intensity values of the spectra are shown in Fig. 6.7.

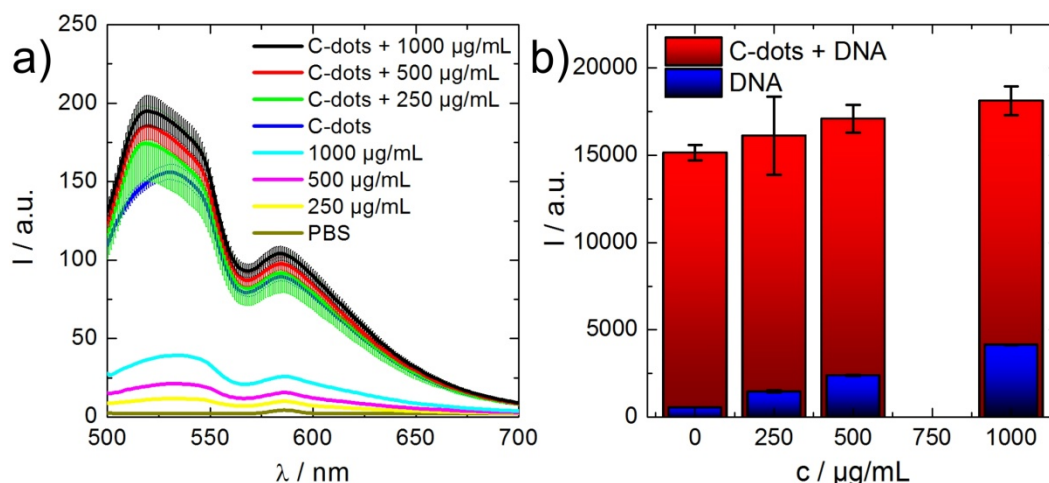


**Fig. 6.7:** Influence of ds DNA on C-dot fluorescence. a) Emission spectra of C-dots (0.5 mg/mL) with and without ds DNA in increasing concentrations in PBS. Spectra were recorded at room temperature upon excitation at 488 nm and plotted as average  $\pm$  standard deviation,  $n = 3$ . b) Integrated fluorescence intensities of the emission spectra from (a) plotted against ds DNA concentration, as average  $\pm$  standard deviation,  $n = 3$ .

Under the given assay conditions, the bare DNA solutions in PBS show increasing fluorescence emission for higher DNA concentrations with a maximum at 535 nm, upon excitation at 488 nm. This possibly may be attributed to additives or residues in the DNA preparation. The pure C-dot suspension has its emission maximum at 530 nm. In contrast to this, the incubation of the particles with the DNA led to a shift of the emission maximum to 519 nm with increasing fluorescence intensities for higher DNA concentrations. Analyzing the integrated fluorescence intensities of the spectra given in Fig. 6.7b, the increase of the intensities of the C-dot-DNA suspensions may be attributed to addition of the DNA preparation. Thus, the conclusion applies that there is no increase in the quantum yields of C-dots through the binding to DNA. However, the emission maxima of the mixtures are significantly blue-shifted. This may not be attributed to the DNA preparations themselves, since these have their maxima at longer wavelengths. Accordingly, the changed environment through the binding to DNA could induce effects on the spectroscopic properties of the C-dots. As the green detector of the utilized CLSM is sensitive for light between 515 and 530 nm, the blue-shift of the particles emission maximum may result in higher intensities for the green channel of the obtained micrographs. This may explain the different coloration of C-dot incubated DNA and cell nuclei.

In summary, it has to be said that only suggestions can be made on the diverse staining of DNA and cell nuclei. However, the described studies have shown that possibly two effects play a role in the changed emission behavior of the C-dots. On the one hand, high local concentrations of the particles together with reabsorption of the emitted light and diverse self-quenching behavior of different species might induce a general red-shift of the emitted light. On the other hand, the binding of the C-dots to DNA might change the particles spectroscopic properties in such a manner that the utilized detector for the green light emission records higher fluorescence intensities. Both effects might contribute to this phenomenon as well.

#### Multicolor Imaging of Mammalian Cell Viability with a Live-Dead-Assay using C-dots

In order to examine the applicability of C-dots for cytotoxicity investigations via imaging, NRK cells were treated with increasing concentrations of saponin. These are amphiphilic glucosides, acting on mammalian cells by plasma membrane permeabilization. After the treatment, the NRK cells were incubated with C-dots and analyzed via CLSM. Thereby, the individual staining of the cytoplasm of living cells and the dead cells nuclei was to be utilized for quantitative analysis. As comparison, a commercially available staining kit designed to distinguishing between living and dead cells by Calcein AM and EthD-1 was applied to a control cell group. The corresponding micrographs of the differently stained NRK cell groups are shown in Fig. 6.8.

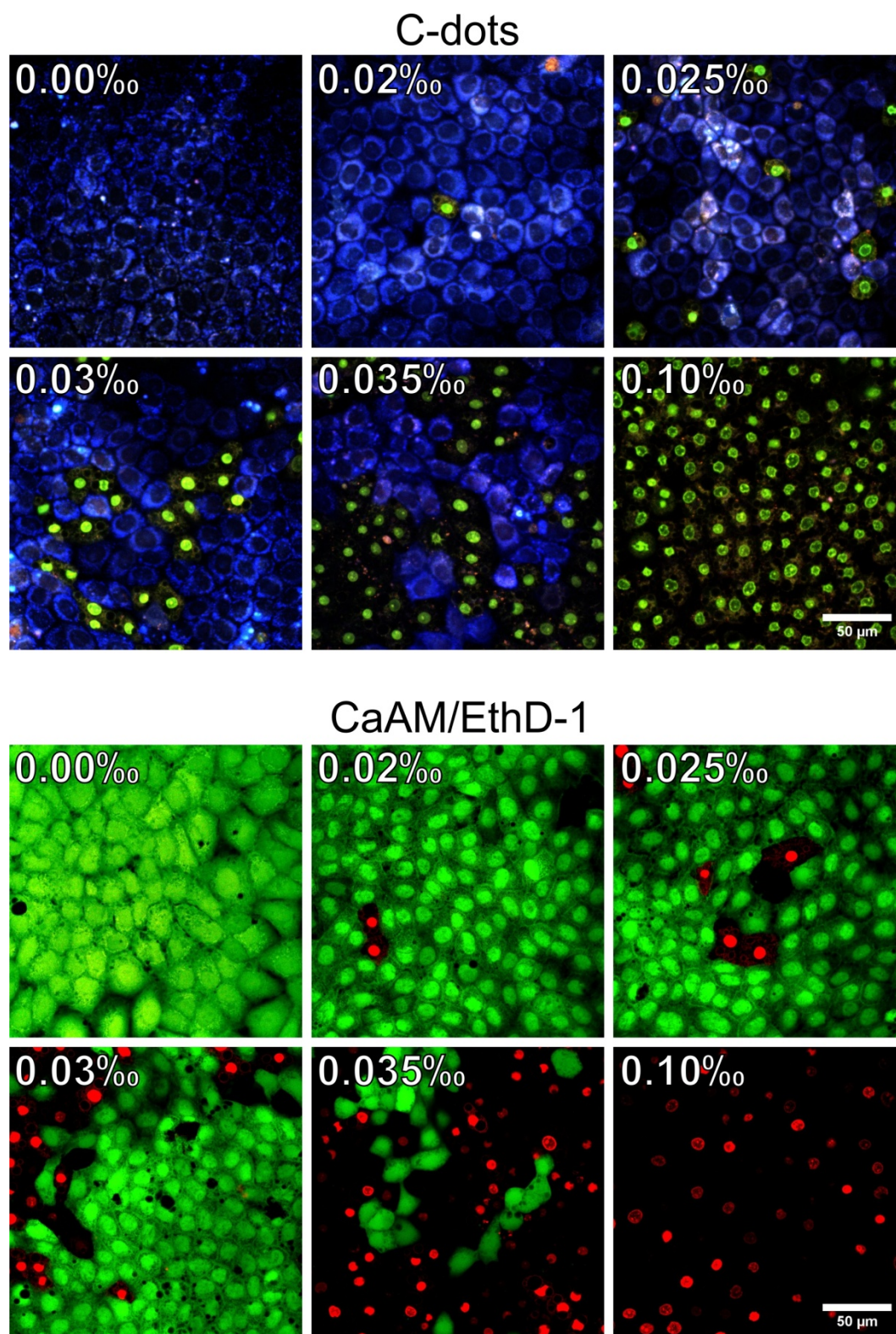


**Fig. 6.8:** Optical sections via CLSM through NRK cells incubated with saponin in varying concentrations (0.02 - 0.10‰) in PBS<sup>++</sup> for 30 min at 37 °C prior to staining. Carbon dot staining was performed with 1.0 mg/mL C-dots in PBS<sup>++</sup> for 30 min at 37 °C. Exc.: 405/488 nm simultaneously. Control staining was performed with 2 μM CaAM/ 4 μM EthD-1 in PBS<sup>++</sup> for 30 min at room temperature. Exc.: 488/543 nm simultaneously. The magnification and RGB detector settings were kept constant for all micrographs among the particular staining groups.



The comparison of the two different staining methods in Fig. 6.8, via C-dots and CaAM/EthD-1 shows that both provide similar information at the individual saponin concentrations. With increasing toxicant concentration NRK cells that were stained by C-dots show a decrease of the blue cytoplasmic luminescence (living cells), while the number of green luminescent nuclei (dead cells) increases. Similar observations can be made for the CaAM/EthD-1 stained NRK cells. There, the number of green fluorescent cells (living) decreases while the number of red fluorescent nuclei (dead cells) increases for higher saponin concentrations. Thus, C-dots are as suitable for cytotoxicity evaluations via imaging just as the commercially available assay.

Further verification of the distinct staining of living and dead cells via C-dots was performed through the labeling of adherent cells after wounding with an electric pulse using ECIS. This ensures that the staining is independent from chemically induced cell death. NRK cells in 8W1E arrays were wounded with an electric pulse and stained with C-dots subsequently for increasing times after wounding. The remigration of the NRK cells onto the electrode might become visible. For comparison, control cells were exposed to the same wounding pulse as the C-dot-treated cells before and stained with CaAM/EthD-1. Both cell groups were analyzed via CLSM and the recorded optical sections are shown in Fig. 6.9.

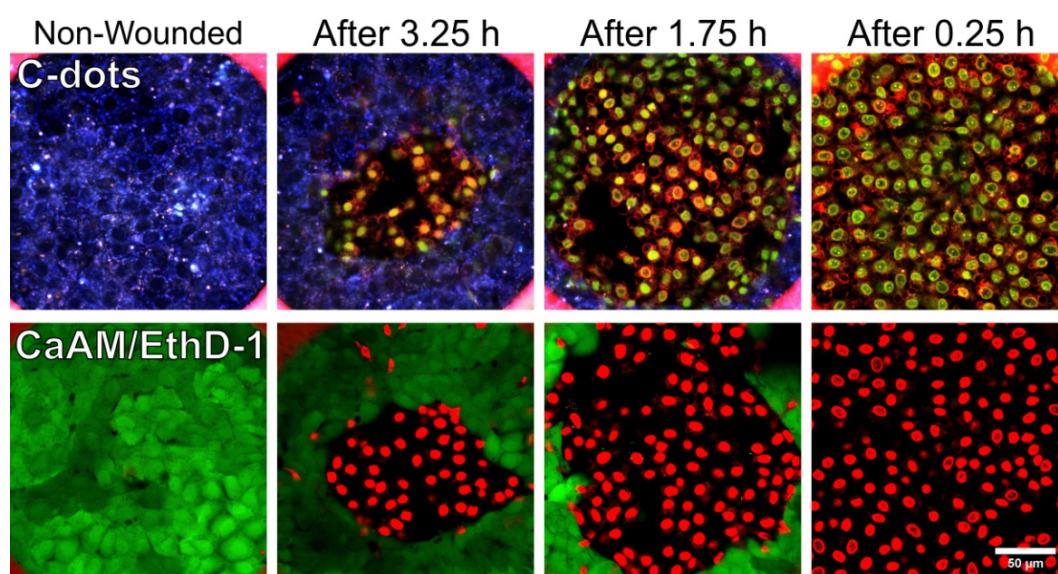


**Fig. 6.9:** Optical sections via CLSM through NRK cells after wounding via ECIS in 8W1E arrays (30 s, 5 V, 40 kHz) and staining with C-dots or CaAM/EthD-1, respectively, for increasing times after wounding. Carbon dot staining was performed with 1.0 mg/mL C-dots in PBS<sup>++</sup> for 30 min at 37 °C. Exc.: 405/488 nm simultaneously. Control staining was performed with 2 μM CaAM/ 4 μM EthD-1 in PBS<sup>++</sup> for 30 min at room temperature. Exc.: 488/543 nm simultaneously. The magnification and RGB detector settings were kept constant for all micrographs among the particular staining groups.

As indicated through the micrographs in Fig. 6.9 both staining protocols provide similar information about the coverage grade of the electrodes with NRK cells. Non-wounded cells of course exhibit complete coverage with living cells. With and increasing time delay between staining and time of the wounding pulse the coverage grade of the electrode with

living NRK cells increases since cells start to migrate onto the free electrode area. This is indicated by the increasing number of blue luminescent cells for the C-dot staining and green luminescent cells for the CaAM staining. As such, differentiation between living and dead cells with C-dots is independent from the mechanism by which death is induced.

#### Quantitative Cytotoxicity Assay using Carbon Dots: Impact of tBuOOH on NRK Cells

Since it was proven that C-dots can be used for a distinct staining of living and dead cells, the particles were studied for their applicability in the quantification of cytotoxic effects via imaging. Therefore, NRK cells were treated with tert-Butyl hydroperoxide (tBuOOH) for 3 h which induces oxidative stress and finally apoptosis at higher concentrations (Ritter *et al.* 1999; Lash *et al.* 2002). The cells treated in this manner were stained with C-dots and examined via CLSM, as shown in Fig. 6.10a.

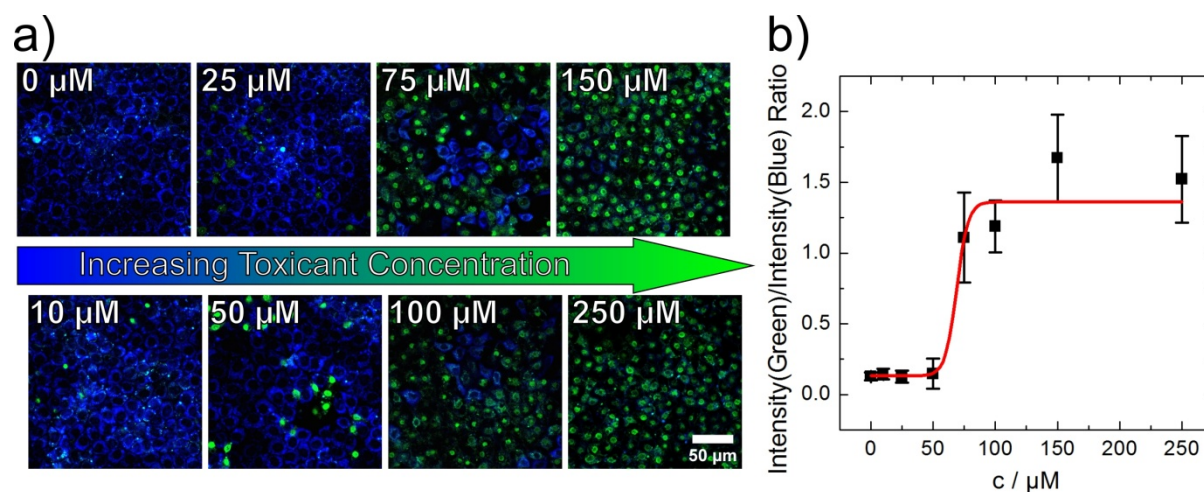


**Fig. 6.10:** EC<sub>50</sub> evaluation for NRK cells treated with tBuOOH. a) Optical sections via CLSM through NRK cells incubated with tBuOOH in concentrations between 10 and 250 µM in PBS<sup>++</sup> for 3 h at 37 °C prior to staining. Carbon dot staining was performed with 1.0 mg/mL C-dots in PBS<sup>++</sup> for 30 min at 37 °C. Micrographs as merges of channel blue (exc. 405 nm) and channel green (exc. 488 nm). b) Plot of the ratio between the integrated intensity of the green channel (515-530 nm) of the micrographs upon excitation at 488 nm and the corresponding blue channel (435-450 nm) upon excitation at 405 nm against tBuOOH concentration. Ratios were calculated from at least six different pairs of micrographs for each concentration and the averages ± standard deviation were used for the plot. Data was fitted via Boltzmann equation  $y=A_2-(A_1-A_2)/(1+e^{(x-x_0)/dx})$ , shown as red line.  $x_0 = 69.0 \pm 6.5 \mu\text{M}$ ,  $R^2 = 0.9530$ .

Similarly to the studies with saponin, selective staining of living and dead NRK cells is performed using C-dots. As such, the staining may be considered as independent from the cell death inducing toxicant. Additionally to the bare observation of the micrographs, they were analyzed for their integrated intensity of the blue channel upon excitation at 405 nm and the one for the green channel upon excitation at 488 nm. While the blue intensity may be considered as a measure for living cells, the green intensity serves as measure for dead cells. Integration over the whole micrographs allows the utilization of the emission red-shift for increasing local C-dot concentrations. The staining with C-dots seems not to be an “all or nothing” phenomenon, which may especially be seen for the slightly green

nuclei of the NRK cells treated with 25  $\mu\text{M}$  tBuOOH and the remaining blue-purple cells incubated with 75 and 100  $\mu\text{M}$  tBuOOH in the micrographs of Fig. 6.10a. Partly damaged cells and cells in very early stages of apoptosis contribute to both integrated intensities, or in the other way, not as strongly as completely intact or dead cells to each intensity. The ratio between the calculated green and blue intensities serves as measure for cytotoxicity and reduces errors induced by variances of the z-plane in the different micrographs for every cell population under test. Furthermore, the usage of the green/blue intensity ratio makes this application independent from the amount of cells in a single micrograph. As such, cytotoxicity evaluations may even be performed on non-confluent cultures with different cells densities. These green/blue intensity ratios were plotted against the corresponding tBuOOH concentrations as shown in Fig. 6.10b. While the green/blue intensity ratio is about 0.1 for living NRK cells, the ratio increases drastically to 1.5 for completely dead cells. Through fitting of the data, an  $\text{EC}_{50}$  of  $(69.0 \pm 6.5)$   $\mu\text{M}$  was determined. This is in good agreement to the  $\text{EC}_{50}$  of 100  $\mu\text{M}$  tBuOOH described in literature for *PC12 pheochromocytoma* cells by *fura-2* assay (Lu *et al.* 2002). Accordingly, the data suggests that the imaging of C-dots in NRK cells allows the evaluation of effective concentrations of toxicants via CLSM imaging.

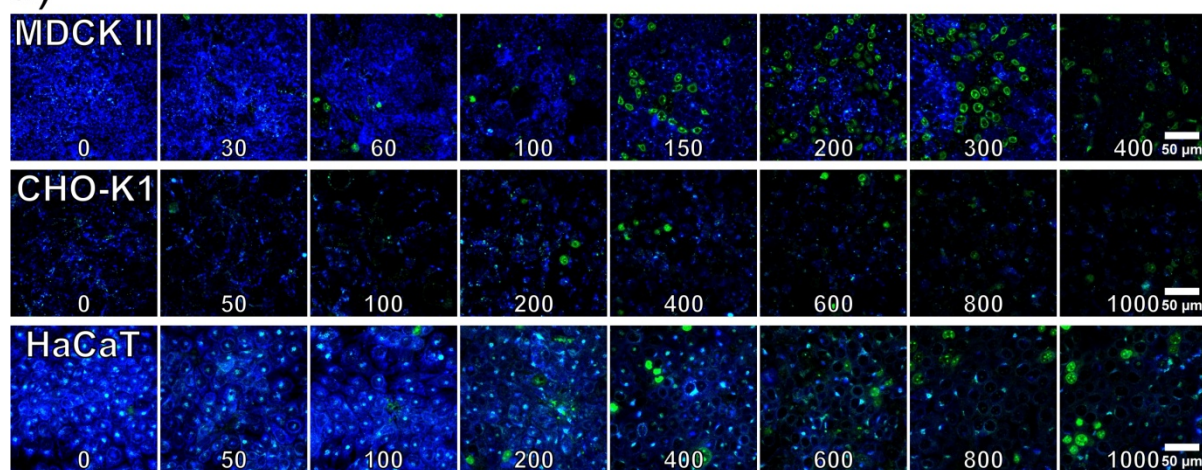
#### Evaluation of $\text{EC}_{50}$ Values of tert-Butyl hydroperoxide for different Mammalian Cell Lines

Further verification on the suitability of C-dots as cytotoxicity evaluation imaging agent for mammalian cells were performed on different cell lines. This should ensure the applicability of the particles as general imaging agent independent of the cell line. Furthermore, the imaging of the different cell lines stained with C-dots is used to compare cytotoxicity of tBuOOH in contact to different cell lines. Therefore, MDCK II, CHO-K1 and HaCaT cells were treated with tBuOOH in increasing concentrations under similar conditions as described for the NRK cells before. The cells were stained with C-dots, examined via CLSM and the micrographs were analyzed for their green/blue intensity ratios. The results of this study are shown in Fig. 6.11.

As demonstrated in the selected micrographs of Fig. 6.11a, healthy MDCK II and HaCaT cells tend to incorporate C-dots in large amounts, indicated by the strong blue luminescence from cells incubated with low concentrations of tBuOOH and control cells upon excitation at 405 nm. CHO-K1 cells show a significantly lower incorporation of C-dots, but still an adequate amount for analysis. Generally, all three cell lines under study show weaker blue luminescence with the increase of the tBuOOH concentration. This may be attributed to cell death and the associated stop of incorporation of the C-dots through endocytosis. Green luminescent nuclei were observed for all three cell lines upon excitation at 488 nm increasing for higher toxicant concentrations. However, in contrast to the previously studied NRK cells, only a few of the dead exhibit green stained nuclei. Other dead cells among the different cells at higher tBuOOH concentrations only feature very

low blue C-dot luminescence in their cytoplasm. This may be attributed to dead cells but dead cells in out-of-focus positions relative to the adherent cells. Furthermore, the staining with C-dots and the 3 h treatment with tBuOOH was optimized for NRK cells, to yield apoptosis in the majority of cells. Therefore, the treatment may have left a majority of the cells in another stadium of cell death or induce a different cell death pathway such as necrosis, compared to NRK cells. As such, for most of these cells the plasma membrane diffusion barrier may still be intact, hindering the C-dots to accumulate in the dead cells' nuclei. This results in weaker blue intensities, with only marginally increasing green intensities for the micrographs of damaged or dead cells. According to this, the EC<sub>50</sub> evaluation utilizing the green/blue intensity ratio of the micrographs cannot be performed as exact as for NRK cells, described before.

a)



b)

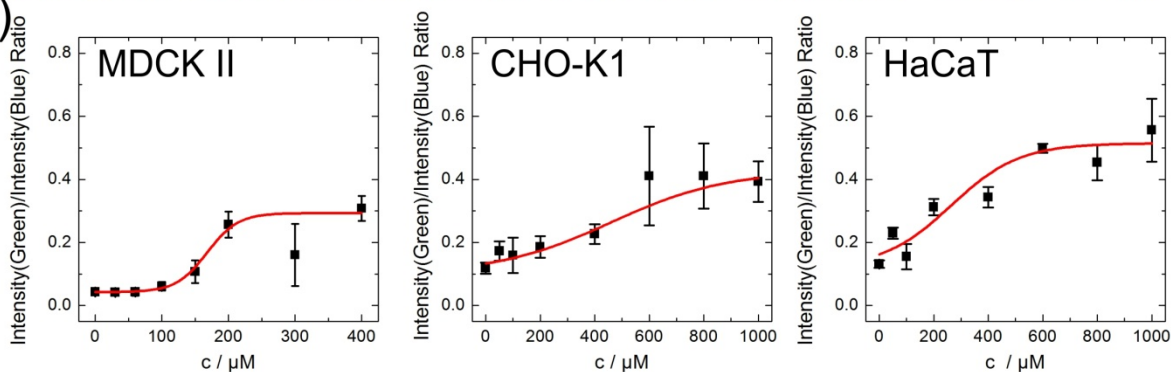


**Fig. 6.11:** a) Optical sections via CLSM through MDCK II, CHO and HaCaT cells (from top to bottom) incubated with tBuOOH in increasing conc. (MDCK II: 30–400 μM, CHO-K1/HaCaT: 50–1000 μM) in PBS<sup>++</sup> for 3 h at 37 °C prior to staining. Carbon dot staining was performed with 1.0 mg/mL C-dots in PBS<sup>++</sup> for 30 min at 37 °C. Micrographs are shown as merges of their blue (exc. 405 nm) and green (exc. 488 nm) channel. b) EC<sub>50</sub> evaluation for MDCK II, CHO-K1 and HaCaT cells treated with tBuOOH by plotting the ratio between the integrated intensity of the green channel (515–530 nm) of the micrographs upon excitation at 488 nm and the corresponding blue channel (435–450 nm) upon excitation at 405 nm against tBuOOH concentration. Ratios were calculated from at least five different pairs of micrographs for each concentration and the averages of the ratios ± standard deviation were used for the plot. The data was fitted via Boltzmann equation, shown as red line. MDCK II:  $x_0 = 167.8 \pm 12.5 \mu\text{M}$ ,  $R^2 = 0.9411$ , CHO-K1:  $460.5 \pm 139.9 \mu\text{M}$ ,  $R^2 = 0.8548$ , HaCaT:  $263.9 \pm 123.6 \mu\text{M}$ ,  $R^2 = 0.8976$ .

Plot of the green/blue intensity ratios of the micrographs against the tBuOOH concentration for all three cell lines, shown in Fig. 6.11b, allowed a rough evaluation on the corresponding EC<sub>50</sub> values. These are summarized in Table 6.1, together with the values for NRK cells. Furthermore, EC<sub>50</sub> values were calculated through the fitting of the data for the decreasing blue intensities of the micrographs only for higher tBuOOH concentrations, resulting from reduced incorporation of the C-dots. This is independent of the highly variable green intensities from the few stained nuclei, allowing more precise fits in this case. The corresponding results are also shown in Table 6.1.

**Table 6.1:** Comparison of EC<sub>50</sub> values for tBuOOH determined via CLSM imaging with C-dots. Evaluation was performed via the green/blue intensity ratio and the integrated intensity of the blue channel of the micrographs for various mammalian cell lines respectively. (\*: Error could not be determined.) The concentrations were calculated via fitting of the obtained data using the Boltzmann function. Each data point resulted from averaging the ratio or intensity, respectively, of at least five micrographs per sample ± standard deviation.

Cell Line	EC <sub>50</sub> /μM (G/B-Ratio)	EC <sub>50</sub> /μM (Blue Int.)
NRK	69.0 ± 6.5	56.4 ± 13.9
MDCK II	167.8 ± 12.5	116.1 ± 51.8
CHO-K1	460.5 ± 139.9	402.8 *
HaCaT	263.9 ± 123.6	137.1 ± 42.1

The determined EC<sub>50</sub> values from the green/blue intensity ratio are roughly in accordance to the observed morphology changed cell damage and death among all cell lines. The evaluation using the integrated blue intensities resulted in similar values. Thereby, the comparison of the errors of the calculated EC<sub>50</sub> values for NRK and MDCK II cells indicate the benefits of the usage of the green/blue intensity ratio. It combines the decreasing blue intensities with the increasing green intensities for higher toxicants concentrations. Furthermore, it is independent of cell density or variations of the focal plane between the different micrographs per sample. For the other cell lines without the constant feature of direct correlation between green stained nuclei and toxicant concentration, the fitting of the blue intensity data resulted in higher precisions for the EC<sub>50</sub> evaluations.

However, it has been shown that the blue staining of living cells due to endocytosis of low concentrations of C-dots and the green staining of dead cells' nuclei due to accumulation of the particles is observed for all cell lines. As such, the principle of the staining is not only limited to the application on NRK cells, but surely for most adherent mammalian cell lines. The usage of the green/blue ratio of the micrograph intensities can most likely be optimized to reach higher precision for the EC<sub>50</sub> determination. Thereby, the incubation of the different cell lines with C-dots, as well as the toxicant treatment might be optimized to achieve this goal.

Established methods from literature using commercially available staining kits, such as Calcein AM/Eth hd-1 also rely on quantifying cytotoxicity via fluorescence microscopy. Therefore, the intensities or cell numbers of the different emission channels in the micrographs are analyzed (Kummrow *et al.* 2013). However, most commonly quantification and analysis of fluorescent dye stained cells is analyzed via flow cytometry, since it allows high-speed quantitative multi-parameter analysis of cells in suspension. In the following the applicability of C-dots for a detectable staining in the flow cytometry analysis of NRK cells was studied.

Flow Cytometry as Method for the Analysis of C-dot-stained NRK Cells

Independence of the analysis method of C-dot-stained NRK cells from CLSM was verified via fluorescence activated cell sorting (FACS). Therefore, NRK cells were treated with 150  $\mu\text{M}$  tBuOOH for 3 h in PBS<sup>++</sup>/Glucose (1 g/L) prior to staining with C-dots (1.0 mg/mL in PBS<sup>++</sup> for 30 min). This treatment induces apoptosis among the NRK cells, enabling the detection of the green fluorescent C-dot stained nuclei. Control cells were not treated with the toxic agent before staining. Fluorescence of the internalized particles was analyzed upon excitation at 488 nm and emission between 515 and 545 nm, as required for the detection of dead cells stained with C-dots. For comparison, NRK cells from the same samples were incubated with propidium iodide (PI) for the selective staining of dead cells. These cells fluorescence was detected upon excitation at 488 nm with a 670 nm longpass filter. The dot plots of the fluorescence intensities against the forward scattered light (FSL) intensities from this study are shown in Fig. 6.12.

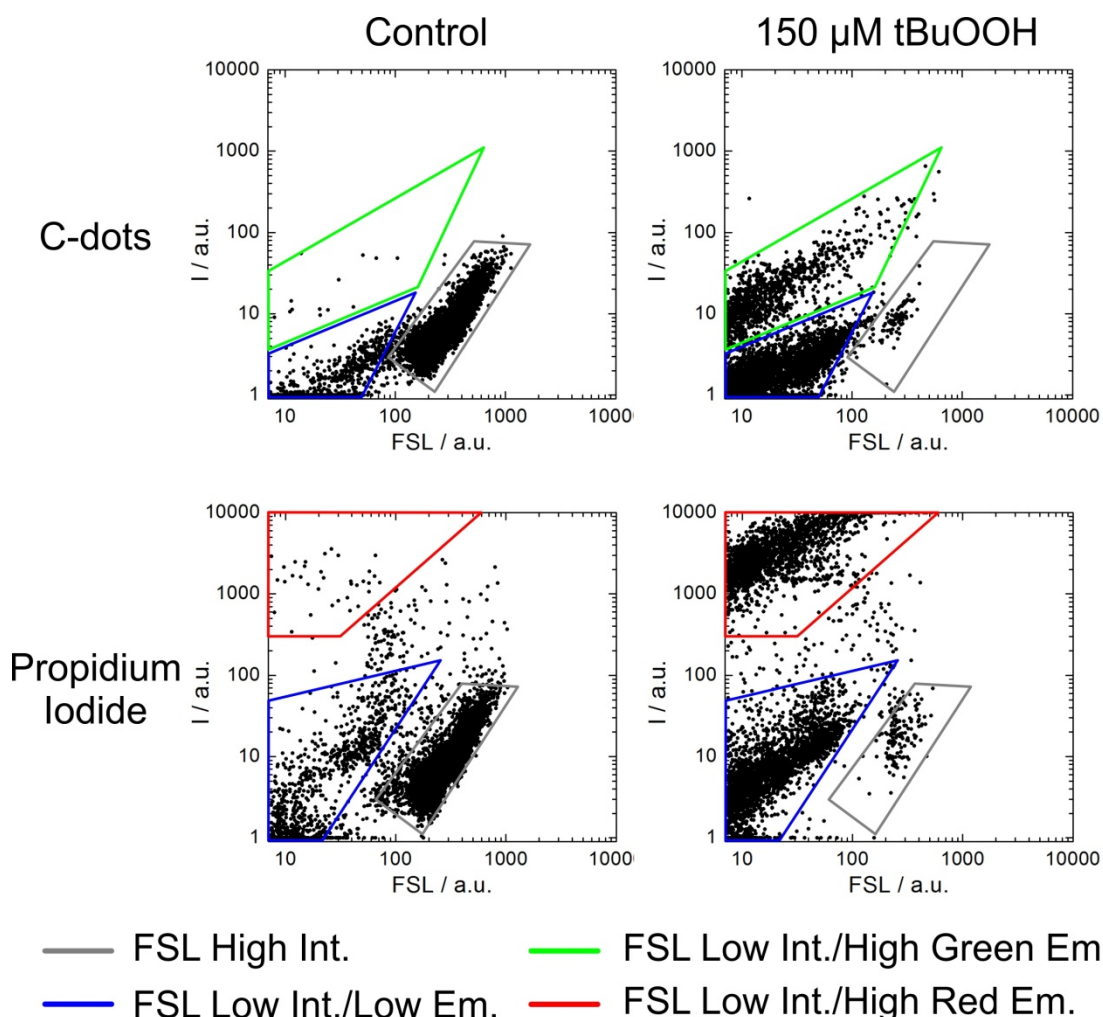


**Fig. 6.12:** Dot plots of the fluorescence intensity against the FSL intensity from the FACS analysis of C-dot and propidium iodide stained NRK cells. Control cells were not treated prior to staining, sample cells were treated with 150  $\mu\text{M}$  tBuOOH in PBS<sup>++</sup>/Glucose (1 g/L) for 3 h before staining. Fluorescence of the C-dot stained NRK cells was analyzed upon exc. at 488 nm with a 515 - 545 nm em. filter. Propidium iodide em. was analyzed upon exc. at 488 nm with a 670 nm longpass filter. From the controls 10.000 cells and from the tBuOOH incubated sample 5.000 cells were studied per analysis. The experiment was performed three times, obtaining similar results.

The dot plots from the FACS analysis of the C-dot-stained NRK cells in Fig. 6.12 allow the classification of three different cell populations per sample. From the control, the majority of the dots are located in the grey marked region with high FSL intensities and medium fluorescence emission intensities. Since FSL is a measure for cell volume and apoptotic NRK cells undergo shrinking, it may be suggested that those cells in the grey region are healthy with only moderate green fluorescence emission. This emission behavior can also be observed for intact C-dot stained NRK cells via CLSM analysis. A minority of the dots is located in the blue marked region, indicating small cell volumes with only marginal fluorescence intensities. These cells may have undergone cell death without being stained by C-dots due to intact plasma membranes or apoptosis after staining with the particles. Only very few dots are located in the green marked region, which exhibits low FSL intensity and higher green fluorescence intensities. This small number of cells shows the typical characteristics of dead C-dot-stained nuclei, a low cell volume together with green fluorescence emission. As expected the control sample consists of only very few of those cells, since these were not treated with the toxic agent prior to the staining with C-dots. The tBuOOH-treated sample by contrast, exhibits very few dots in the grey marked region, indicating that only a small number of the NRK cells survived the treatment with tBuOOH. Most of the dots are located in the blue and green marked region with low FLS intensities. As such, the majority of the NRK cells is suggested to have undergone apoptosis with a shrinking cell volume. The dead cells are split into two different populations, those with high green fluorescence emission and those showing only marginal intensities. According to this observation it may be suggested that the tBuOOH-treatment did not induce loss of plasma membrane integrity among all apoptotic cells. As such, only parts of the dead cells nuclei were stained with the particles.

A similar observation can be made for the PI stained NRK cells. While most of the dots in the plot of the control sample are located in the grey marked region, a minority can be found in the blue and only a very small number in the red region with high red fluorescence intensities. This indicates that, analog to the C-dot staining, most of the NRK cells can be considered healthy, with only a very small number of dead cells nuclei stained red fluorescent. The tBuOOH and PI treated sample significantly supports the notion of two different dead cell populations. While parts of the dead cells exhibit bright red fluorescence, the other part shows only marginal intensities. As such, also the organic dye could only stain some of apoptotic NRK cells. This indicates that plasma membrane integrity was maintained among a large number of cells. The organic dye shows a similar staining behavior for the NRK cells as the C-dots. Again only a few dots can be found in the grey marked, which shows that most of the cells underwent death.

A detailed analysis of the amount of cells among the diverse treated and stained NRK cell populations identified via FACS is shown in Table 6.2.



**Table 6.2:** Amount of cells in % among the diverse treated and stained NRK cell populations identified via FACS. Data was obtained from three different cell samples, shown as averages  $\pm$  standard deviation.

<b>NRK Populations</b>	<b>Control (C-dots)</b>	<b>Control (PI)</b>	<b>tBuOOH (C-dots)</b>	<b>tBuOOH (PI)</b>
<b>Healthy Cells (Grey)</b>	90.2 $\pm$ 0.4%	85.1 $\pm$ 3.3%	3.0 $\pm$ 0.8%	2.3 $\pm$ 1.0%
<b>Dead Cells / Low Em. (Blue)</b>	9.9 $\pm$ 0.6%	8.2 $\pm$ 1.4%	76.8 $\pm$ 0.5%	59.3 $\pm$ 5.6%
<b>Dead Cells / High Em. (Green/Red)</b>	0.2% $\pm$ 0.0%	2.9 $\pm$ 2.1%	20.7 $\pm$ 0.2%	35.5 $\pm$ 4.8%

The comparison of the amount of cells among the different populations from the diverse stained and treated NRK cells in Table 6.2, shows that the staining with C-dots roughly gave the same information as the one with PI. Both stainings indicate that most of the untreated control cells can be assigned as healthy, with only a small number of dead cells. The treatment with tBuOOH drastically changed the amounts among the different populations, leaving only a few cells alive and inducing cell death among most of them. Thereby, the particles left a comparable number of low volume NRK cells, which are supposed to be apoptotic, unaffected similar to PI.

In summary, it could be shown that C-dots may be used for the distinguishing between living and dead cells, utilizing the particles green fluorescence upon excitation at 488 nm. Although the particular experiment did not allow the staining of all dead cells, the C-dots did behave exactly as the dead cell specific organic dye PI. Both stained parts of the apoptotic NRK cells, which may be referred to intact plasma membranes among those affected cells. However, the study proved the independence of the C-dot staining of living and dead mammalian cells from CLSM.

Imaging of Living and Dead NRK Cells with N-doped C-dots from Citric Acid

The studies on the C-dots utilized in this work have proven that these particles exhibit unique properties. In order to classify the mammalian cell imaging possibilities of the C-dots from starch and Trp, they were compared with the performance of another C-dot preparation from literature. Therefore, comparable N-doped C-dots from citric acid and ethylene diamine with the highest QY known up to know were prepared (Zhu *et al.* 2013b). These were used for staining of NRK cells which were subsequently treated with saponin as toxicant in increasing concentrations. After incubation with the particles, the cells were examined via CLSM. The corresponding micrographs are shown in Fig. 6.13.

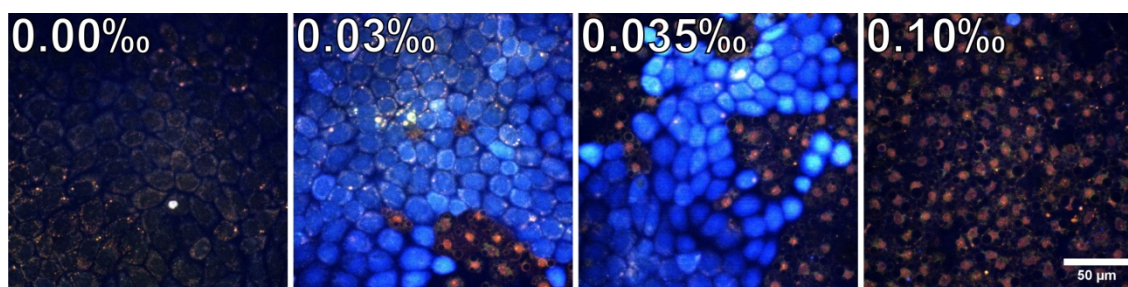


**Fig. 6.13:** Optical sections via CLSM through NRK cells incubated with saponin in increasing concentrations (0.00 - 0.10‰) in PBS<sup>++</sup> for 30 min at 37 °C prior to staining. Carbon dot staining was performed with 0.5 mg/mL C-dots (derived from citric acid and EDA) in PBS<sup>++</sup> for 30 min at 37 °C. Exc.: 405/488 nm simultaneously. The magnification and the RGB detector settings kept constant for all micrographs.

The micrographs in Fig. 6.13 show that the incubation of untreated NRK cells (0.00‰) with C-dots from citric acid results in insufficient staining. Those cells exhibit only marginal fluorescence. As such, it may be suggested that living cells with intact plasma membrane integrity barely incorporate these particles. At higher saponin concentrations (0.03 and 0.035‰) NRK cells exhibit bright blue photoluminescence throughout the whole cells. This has also been attributed to partial losses of plasma membrane integrity due to saponin enabling the diffusion of the particles in small amounts into the cell. This may also be observed for partly damaged cells stained with C-dots from starch and Trp. However, the latter exhibit a more differentiated staining of cytoplasm and nucleus. Completely dead NRK cells (mostly 0.10‰) exhibit bright red nuclei. Accordingly, the selective DNA staining and the subsequent color shift seems to also exist for these C-dots. Thus, it may be possible that a red-emissive species favors binding to DNA or that the accumulation of those particles results in even stronger emission red-shifts. In summary, it has to be said that the staining abilities of the C-dots from starch and Trp are superior to the other preparation, as they allow a staining of living cells and a more thorough staining of the cell compartments (cytoplasm and nucleus).

### 6.3 Imaging of MCF-7 Spheroids as Tissue Models using Carbon Dots

In the previous chapter it was shown that the C-dots, investigated in this work, exhibit unique properties for the multicolor imaging of cell monolayers via CLSM. However, since diagnostic and therapeutic applications *in vivo* are implemented on three dimensional (3D) cell structures, the C-dots were investigated for the staining of 3D tissue models. Therefore, multicellular spheroids (MCS) of MCF-7 cells were chosen as 3D tissue model for tumors. These were stained with C-dots and subsequently underwent multicolor imaging via CLSM. An example of such an MCS is shown in Fig. 6.14 together with a CaAM/EthD-1 stained one.

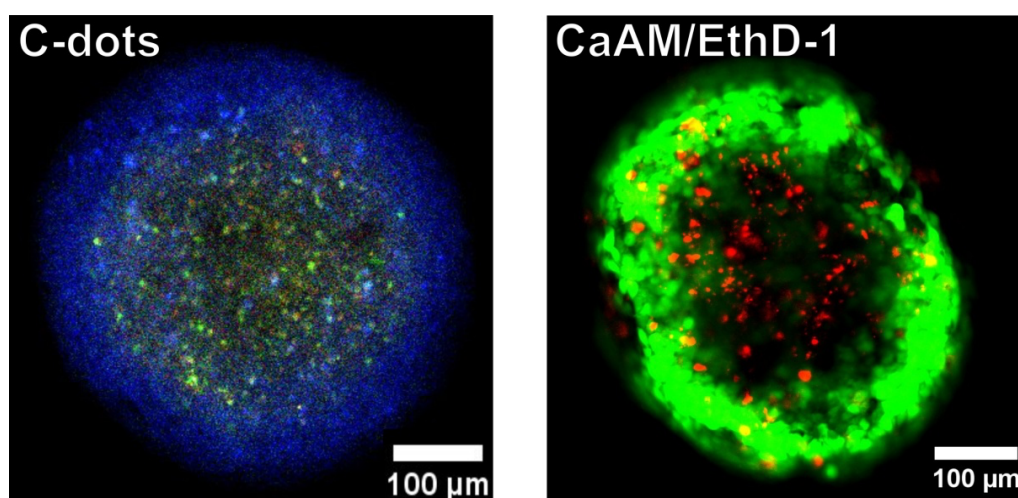


**Fig. 6.14:** Optical sections via CLSM through MCS of MCF-7 cells grown for 7 d. Carbon dot staining was performed with 1.0 mg/mL C-dots in PBS<sup>++</sup> for 2 h at 37 °C. Exc.: 405/488 nm simultaneously. Control staining was performed with 2 μM CaAM/ 4 μM EthD-1 in PBS<sup>++</sup> for 2 h at room temperature. Exc.: 488/543 nm simultaneously.

The optical section of the C-dot stained MCS in Fig. 6.14 exhibits bright blue luminescence in the cells in the periphery of the spheroid. Cells located in the inner of the spheroid appear greenish. Furthermore, distinct bright green spots, especially deeper inside the spheroid were observed. These can be most likely assigned to C-dot stained nuclei of dead cells, similar to the monolayer studies. From the staining with the particles it may be suggested that the MCS consists of living cells in the outer layers of the MCS together with a vast amount of dead cells inside the spheroid. This would be in accordance with the observation of necrotic cores inside MCF-7 MCS, as described in literature (Faute *et al.* 2002). These are about 200 μm in size inside the spheroid with only the outermost cell layers actively proliferating (Zhang *et al.* 2005). These dimensions are in accordance with the diameter of the green luminescent area in the optical section of the MCS. Furthermore, the control staining with CaAM/EthD-1 shows similar results with mostly living cells (green) in the spheroid periphery with several dead cells (red) inside. However, it may not be excluded that the blue coloration throughout the spheroid and the green coloration of the core is due

to optic effects. Thereby, long wavelength light, in this case the green emission, is only detected for the region of the spheroid core since it is not as strongly reabsorbed by the surrounding tissue as the shorter wavelength emission. This effect may also be observed for the CaAM/EthD-1 stained MCS, since only red emission of several dead cells is detected from the core.

A more thorough investigation on the staining of MCS with C-dots was performed through the recording of z-stacks via CLSM. Thereby, optical sections of C-dot stained and non-stained MCF-7 spheroids were recorded by moving the position of the focal plane through the specimen. This enables 3D multicolor imaging of the MCS in a whole. Individual optical sections of these z-stacks are shown in Fig. 6.15.

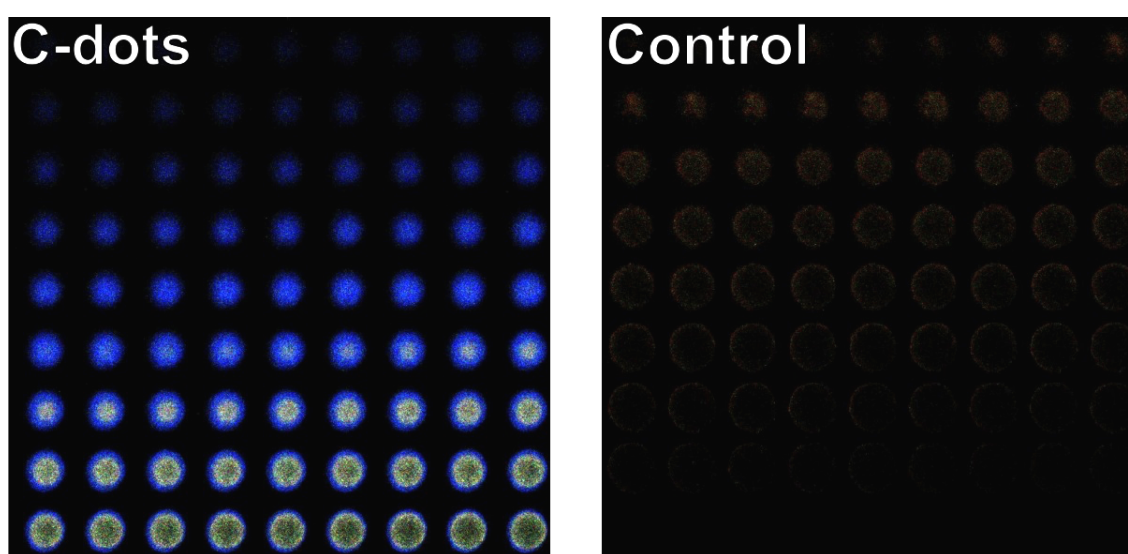


**Fig. 6.15:** Optical sections via CLSM through MCS of MCF-7 cells grown for 7 d (diameter  $\sim 450 \mu\text{m}$ ) in  $2.5 \mu\text{m}$  steps between focal planes. Carbon dot staining was performed with  $1.0 \text{ mg/mL}$  C-dots in  $\text{PBS}^{++}$  for 4 h at  $37^\circ\text{C}$ . Exc.:  $405/488 \text{ nm}$  simultaneously. The control MCS was not stained. The RGB detector settings were kept constant for both z-stacks.

The optical sections of the C-dot stained MCS in Fig. 6.15 shows that the spheroid exhibits a complete shell of bright blue luminescent cells. Furthermore, the inner core of the spheroid shows green fluorescence, as described before. In order to exclude autofluorescence as reason for the green core, control MCSs not stained with C-dots were examined under similar conditions and detector settings, as control. The marginal green fluorescence was observed, possibly deriving from cell residues in the inside of the spheroid. This partly contributes to the observed green fluorescence of the stained MCS. However, the intensity of fluorescence in control spheroids is fairly weak. As such, it may be suggested that most of the green fluorescence from the inner core of the C-dot stained MCS results from green fluorescent dead cells. The data suggests that the C-dots penetrated the whole MCS, since fluorescence emission is also detected from the inner core of the stained MCS, while the control MCS shows only marginal intensities. This would correspond to a very good tissue penetration of C-dots.

In summary, the studies on the MCS showed that multicolor imaging and distinguishing between living and dead cells with C-dots is also possible in 3D cell structures. The staining of the spheroids, resulting in a distinct blue shell and a green core may be attributed to the different staining of living and dead cells on the one hand. On the other hand, the better tissue penetration of long wavelength light emitted from the inside of the spheroid upon laser excitation may further be involved in this phenomenon.



## 7 Carbon Dots as “Theranostic” Particles in Photodynamic Treatment

The following chapter describes studies on the generation of reactive oxygen species (ROS) upon photoexcitation of C-dots. Related to this, studies on the phototoxicity of C-dots in contact NRK cells were performed under different conditions. The occurring phototoxicity of the particles was utilized for the development of a “theranostic” approach, combining the C-dots unique multicolor imaging properties together with their application as photosensitizer.

### 7.1 Photogeneration of Reactive Oxygen Species through Irradiation of Carbon Dots

Generation of ROS through photoexcitation of nanoparticles and organic dyes are well known processes and thoroughly described in literature (DeRosa *et al.* 2002; Chatterjee *et al.* 2008). The ability of the in-situ generation of highly oxidizing molecules through these photosensitizers is used to locally damage target tumor cells and to induce cell death in photodynamic therapy (Dolmans *et al.* 2003). Carbon dots are a novel nanomaterial and combine the morphology of nanoparticles together with the organic nature of typical photosensitizers, such as organic dyes or aromatic hydrocarbons. Accordingly, the possible photogeneration of ROS via C-dots is highly probable. In this direction several reports in literature were recently made for graphene oxide (Chang *et al.* 2011), GQDs (Markovic *et al.* 2012) and other C-dot preparations (Hsu *et al.* 2013; Ge *et al.* 2014).

Interestingly, descriptions in literature of ROS generation by C-dots are not consistent. On the one hand, several preparations are described as highly efficient ROS generators upon photo-excitation, using these C-dots unmodified for photodynamic therapy (Juzenas *et al.* 2013; Ge *et al.* 2014). On the other hand, several C-dot preparations are explicitly described as non-generating these species, making the modification of these particles with photosensitizers reasonable for photodynamic therapy approaches (Huang *et al.* 2012; Choi *et al.* 2014; Wang *et al.* 2014). This emphasizes the variance of chemical species among C-dots as a class of carbon nanomaterials and that comparisons between those particles have to be seen critical.

For the investigation of possible ROS generation through photoexcitation of the C-dots prepared from starch and Trp in this work, the ROS sensitive dye Dihydrorhodamine 123 (DHR) was used. This is non-fluorescent until oxidation with any type of ROS (e.g. superoxide, hydroxyl and hydroperoxyl radicals or singlet oxygen) to form the fluorescent Rhodamine 123. A schematic of the reaction is shown in Fig. 7.1a.

The initial studies were performed through irradiation of DHR, C-dots and the mixture of both in solution with a UV lamp applied for varying times. All three samples were analyzed for their fluorescence at excitation/emission 500/530 nm, in order to detect the formation of Rhodamine 123 or any side-effects through the long-term irradiation of C-dots and DHR, respectively. The fluorescence intensities plotted against irradiation times are shown in Fig. 7.1b.

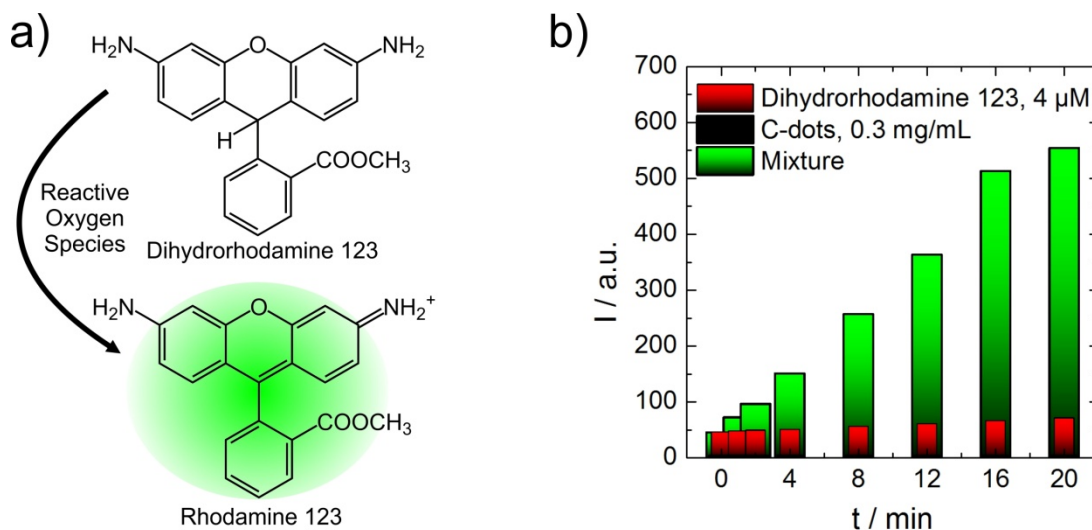


**Fig. 7.1:** Investigation of ROS photogeneration by C-dots. a) Reaction of the ROS selective oxidation of the non-fluorescent DHR to the green fluorescent Rhodamine 123. b) Fluorescence intensities of 0.3 mg/mL C-dots, 4 μM DHR and their mixture, all in EBSS<sup>++</sup>, plotted as a function of irradiation time with a UV lamp (366 nm, 2x6 W). Exc./Em.: 500/530 nm. Detector settings were kept constant for all measurements. The data was obtained from a single experiment which was repeated three times under slightly conditions, always resulting in particularly increasing fluorescence intensities of the “mixture”.

From the intensities in Fig. 7.1b, it may be seen that UV irradiation of pure DHR over 20 min induces no significant fluorescence intensity increases under the chosen conditions. The same applies to the pure C-dot suspension, which exhibits only marginal fluorescence for all irradiation times. Therefore, the plotted intensities of the C-dots in Fig. 7.1 are not visible. In contrast to this, the mixture of both shows drastic increases of the fluorescence intensities after irradiation. The non-irradiated mixture and DHR solution exhibit similar fluorescence intensities. As such, it may be suggested that the addition of C-dots itself is not responsible for the intensity increase. Through the UV irradiation the fluorescence intensity of the mixture increases linearly with the irradiation time up to a maximum, which may be attributed to the full transformation of DHR to Rhodamine 123. In conclusion, only the combination of C-dots together with UV irradiation induces the formation of Rhodamine 123. Accordingly, C-dots from starch and Trp may be suggested as efficient sensitizers, generating ROS upon photoexcitation.

However, this assay does not allow for the investigation on the mechanistic pathway of the ROS generation. As indicated in Fig. 7.2, ROS may be generated via photoexcitation of sensitizers, in this case C-dots, on two different pathways from excited triplet states.



Thereby, type I results in the generation of radical and anion oxygen species, such as superoxide, hydroxyl radicals and hydroperoxide, via electron transfer from the particles. The type II mechanism by contrast, represents the direct energy transfer from the photosensitizer onto molecular oxygen, transforming triplet oxygen into singlet oxygen (Foote 1991).

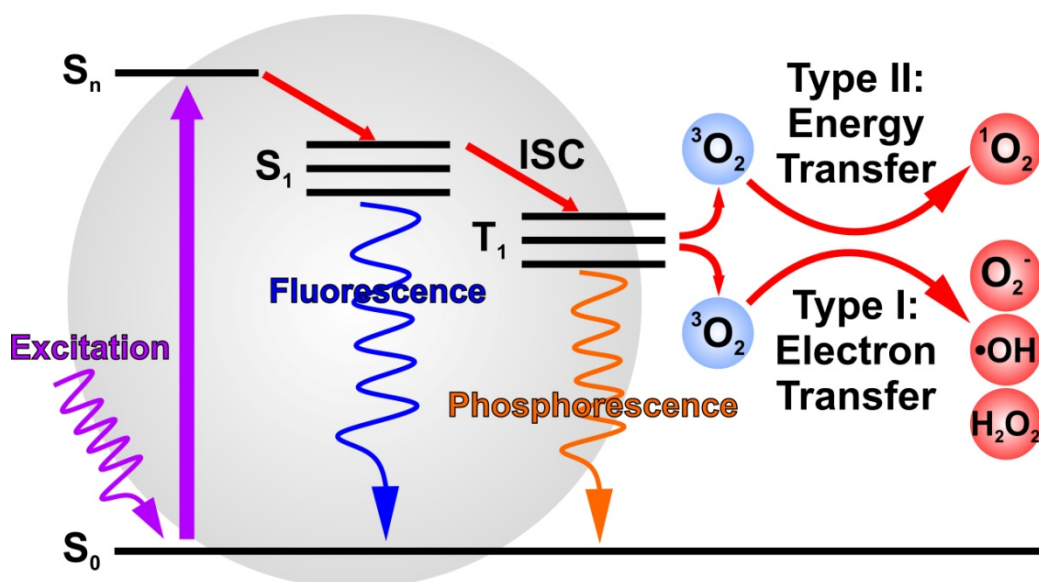


**Fig. 7.2:** Schematic for the photogeneration of ROS via C-dots on two possible pathways from excited triplet states. Type I induces the generation of ROS, such as superoxide, hydroxyl radicals and hydroperoxide via electron transfer onto molecular oxygen. Type II results in the formation of singlet oxygen ( $^1O_2$ ) via energy transfer onto triplet oxygen.

In order to investigate the mechanistic ROS generation pathway via photoexcitation of C-dots, 9,10-Anthracenediyl-bis(methylene)dimalonic acid (ADBDA) was utilized as singlet oxygen specific dye. This dye specifically reacts with singlet oxygen, forming an endoperoxide, as shown in Fig. 7.3a. While ADBDA is fluorescent in the VIS, the corresponding endoperoxide formation results in the loss of this feature. As such, the presence or generation of singlet oxygen may be investigated monitoring the dyes absorption at 380 nm and its fluorescence at 410 nm. Among the emission peaks of ADBDA, the one at 410 nm was chosen, since the C-dot emission contributes the least at this wavelength. For the study, 2  $\mu M$  ADBDA was mixed with 0.3 mg/mL C-dots in EBSS<sup>++</sup> and the suspension was irradiated with a UV lamp (366 nm, 2x6 W). The absorption or fluorescence was measured as a function of irradiation time, respectively. For control, pure C-dot and ADBDA solutions were studied under similar conditions. The results of this study are shown in Fig. 7.3.

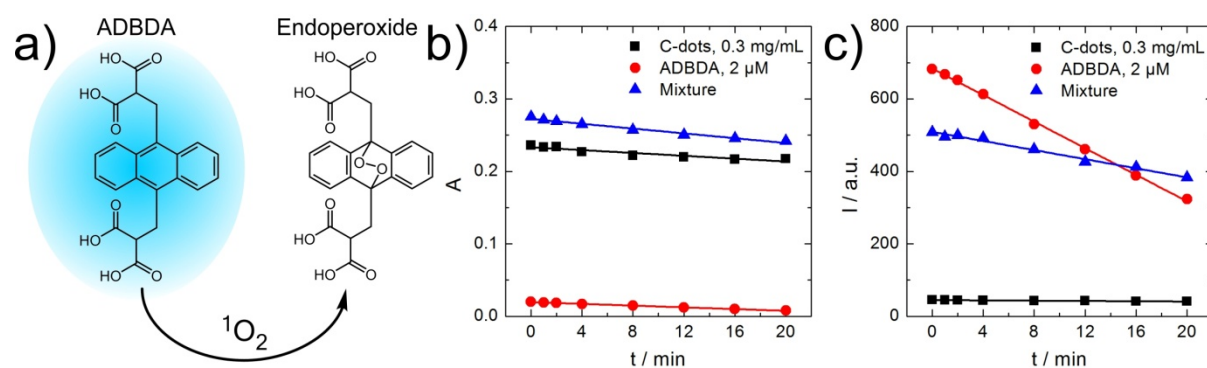


**Fig. 7.3:** Detection of singlet oxygen ( $^1O_2$ ) generation via ADBDA. a) Specific molecular reaction of the fluorescent ADBDA with singlet oxygen to its corresponding endoperoxide. b) Absorption at 380 nm and c) fluorescence intensities at 410 nm of 0.3 mg/mL C-dots, 2 μM ADBDA and their mixture, all in EBSS<sup>++</sup>, plotted against irradiation times with a UV lamp (366 nm, 2x6 W). Exc./Em.: 380/410 nm. Detector settings were kept constant for all measurements. The data was obtained from two independent single experiments.

As shown in Fig. 7.3b, the absorbance of ADBDA at 380 nm shows a linear decrease of about 60% during 20 min of UV irradiation. This may be suggested as photobleaching through the irradiation with UV lamp. Since the excitation maximum of the C-dots is almost the same as for ADBDA, photobleaching may not be excluded for this experimental set-up used here. According to this, decreases through the endoperoxide formation via singlet oxygen should distinguish themselves by more negative slopes or exponential decreases, in contrast to the irradiation of the pure ADBDA. The absorbance of the bare C-dots remains at high absorbance values with a slight decrease of about 10% during the experiment. Similarly, the mixture of both, ADBDA and C-dots, also shows this linear absorbance decrease with a slope that may be seen as the sum of the slopes from the pure samples. Thus, no significant amounts of singlet oxygen are generated through the UV irradiation of the C-dots.

For verification of this result, the fluorescence at 410 nm of all three samples was measured in a second experiment, as indicated in Fig. 7.3c. There, the pure ADBDA shows a fluorescence decrease of 55% over time due to photobleaching, which agrees in qualitative terms with the absorption measurements. The pure C-dot fluorescence remains at low levels with a slight decrease of 10%. Interestingly, the mixture of both shows lower fluorescence intensities at the beginning of the experiment, compared to the pure ADBDA solution. This might be explained by the reabsorption of the light emitted from ADBDA through the various C-dot species. The subsequent irradiation of the mixture results in less photobleaching of the ADBDA, indicated through the lower fluorescence decrease and the higher intensity after 20 min of irradiation, compared to pure ADBDA. On the one hand, the high absorption of C-dots at the irradiation wavelength of 366 nm could have protected ADBDA from photobleaching. Moreover C-dots may have reabsorbed photons emitted by C-dots. On the other hand, C-dots were reported in literature as antioxidant and therefore could have acted protective towards the photobleaching of ADBDA (Christensen *et al.* 2011). Das *et al.*, for example, described C-dots as *in-vitro* scavengers of ROS due to

surface active hydroxyl, aldehyde, and ketone groups. These work as proton donor, able to transfer electrons to the C-dot bulk structure. This in turn, could degrade the particles, upon release of carbonates and bicarbonates (Das *et al.* 2014). However, this study was performed with hydrogen peroxide and stays in contrast to the ROS generation of C-dots. As such, these reports have to be seen critical and could be attributed to unique materials.

Taken together, experimental evidence indicates that the C-dots from starch and Trp tend to act as type I photosensitizers and transfer electrons onto molecular oxygen forming ROS in form of anions and radicals. In this behavior C-dots from starch and Trp are similar to C-dots prepared via arc discharge of graphite rods and subsequent passivation with PPEI-EI (Juzenas *et al.* 2013). The authors assign the ROS production to the generation of electron hole pairs upon photoexcitation of the C-dots (Hoffmann *et al.* 1995). These enable the formation of radical oxygen species and hydrogen peroxide via redox processes. These ROS represent toxicants, inducing apoptosis in cells through DNA strand breaks for example, which may be generated locally using C-dots (Oleinick *et al.* 1998). This and the ultrafast penetration of C-dots into mammalian cells and tissues should make them highly suitable for the application as photodynamic therapy agent, as it is described for the application of Q-dots as photosensitizers (Bakalova *et al.* 2004).

## 7.2 Phototoxicity of Carbon Dots under Long-term Irradiation

### Irradiation

The results of the previous chapter showed that C-dots may act as photosensitizer, generating ROS. In the following chapter this issue was further investigated through the investigation of phototoxic effects on NRK cells exposed to long-term irradiation in presence of C-dots in suspension and in the cytoplasm after incorporation. Furthermore, studies on the mechanism of cell death were performed.

#### Phototoxicity of Carbon Dot Suspensions in Contact to NRK Cells

First studies on the phototoxicity of C-dots were performed in commercially available 8W10E ECIS arrays. Therefore, confluent NRK cells grown on the arrays were incubated with 0.3 mg/mL C-dots in EBSS<sup>++</sup>/G and the whole wells were irradiated using a UV lamp (366 nm, 2x6 W). Thereby, irradiated NRK cells without C-dots and non-irradiated NRK cells with/without C-dots served as controls. Details on the experimental set-up are described in chapter 3.6.1. Studying the effect of different irradiation time points with respect to the start of C-dot exposure, excitation of the particles was performed 10 min and 6 h after the incubation start, respectively. The time courses of the normalized magnitude of the impedance at 4 kHz for both experiments are shown in Fig. 7.4.

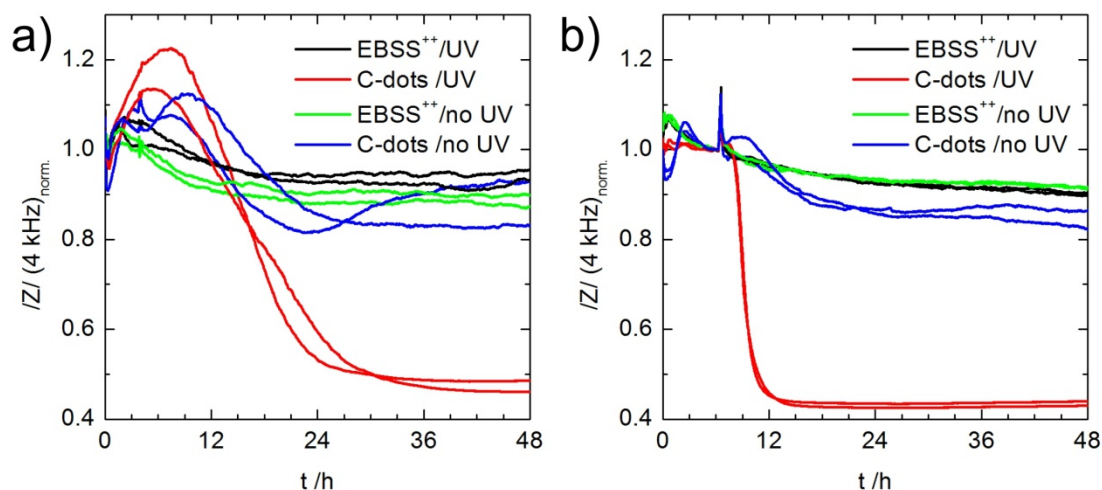


**Fig. 7.4:** Studies on the phototoxicity of C-dots in suspension with confluent NRK cells on 8W10E ECIS arrays. Time courses of the normalized magnitude of the impedance at 4 kHz for NRK cells in EBSS<sup>++</sup>/G with/without UV irradiation (360 nm, 2x6 W) and in presence of 0.3 mg/mL C-dots in EBSS<sup>++</sup>/G with/without UV irradiation. a) Irradiation started after 10 min of incubation with C-dots for 10 min at t = 0. b) Irradiation for 10 min started at t = 6 h. The data was obtained from single independent experiments.

Comparing the time courses of the impedance for both experiments in Fig. 7.4 shows that healthiness of the NRK cells incubated in EBSS<sup>++</sup> is unaffected by UV lamp irradiation only, since both control populations show similar impedance profiles over time. The cells incubated with the C-dot suspensions without irradiation show aberrations from these controls, indicated by increasing impedance values shortly after the incubation start and

fluctuating impedance time courses afterwards. This may be caused by cell reactions to the C-dots in the bulk phase which induce cell morphology changes. However, for both experiments the NRK cells did not undergo cell death but are considered as healthy since comparable impedance values as for the other control cell groups were monitored throughout the studies. In contrast to this, the irradiation of the C-dot suspension on top of NRK cells induced cell death in both cases, as indicated in Fig. 7.4a and b. While the NRK cells irradiated 10 min after incubation, shown in Fig. 7.4a, underwent cell death in about 24 h, those irradiated 6 h after the incubation showed the same behavior in only 6 h, demonstrated in Fig. 7.4b. This is expressed by the decreasing impedance values of the electrodes in both studies. The reasons of this phenomenon are not fully understood. However, two effects may play a role for the two different time courses of cell death. On the one hand, the prolonged incubation with the C-dots might have induced preimpairment of the NRK cells. This together with the ROS generation may lead to immediate cell death. On the other hand, and most likely, those NRK cells incubated for 6 h with C-dots are fully packed with the particles. As such, ROS would be generated in much higher concentrations inside the cells, inducing cell death much faster. However, it has to be mentioned that the irradiation with a UV lamp represents a non-focused excitation of the particles in- and outside of the cells. Accordingly, there is no information whether cell death is induced because of the ROS generation in the bulk phase or through accumulated C-dots in the cytoplasm of the cells. In order to get more insight on the ROS induced cell death of NRK cells, a different set-up was used, as described below.

#### Phototoxicity of Internalized Carbon Dots using Microscope Irradiation

For the investigation of C-dot phototoxicity, explicitly induced through ROS generation of internalized particles, custom made ECIS electrode arrays using ITO as electrode material were utilized. These allow the focused irradiation of the cell layer with an inverse microscope since ITO represents an optically transparent and conducting material at the same time. Further details on the experimental set-up and the preparation of these arrays are described in chapter 3.6.3. NRK cells grown on these electrodes were *loaded* with C-dots through the incubation with 1.0 mg/mL of the particles for 1 h in EBSS<sup>++</sup>/G. Subsequently, twofold washing of the cells with EBSS<sup>++</sup>/G was performed to ensure that only internalized C-dots remain in the NRK cells. Those cells grown on the electrode areas were focused and irradiated as described before. Subsequently, the time courses of the magnitude of the impedance of these electrodes were recorded. Furthermore, the treated NRK cells were stained with CaAM/EthD-1 after the measurement. The results of this study are shown in Fig. 7.5

The time courses of the impedance at 16 kHz in Fig. 7.5a shows that the short-term incubation (*loading*) of the NRK cells with C-dots without subsequent irradiation did not induce cell death or harm the cells, as the impedance stays constant over time. The

irradiated NRK cells with internalized particles by contrast underwent cell death in about 8 h for both, 3 and 5 min irradiation. This becomes apparent by the fast decreasing impedance values for the electrodes of these cell groups.

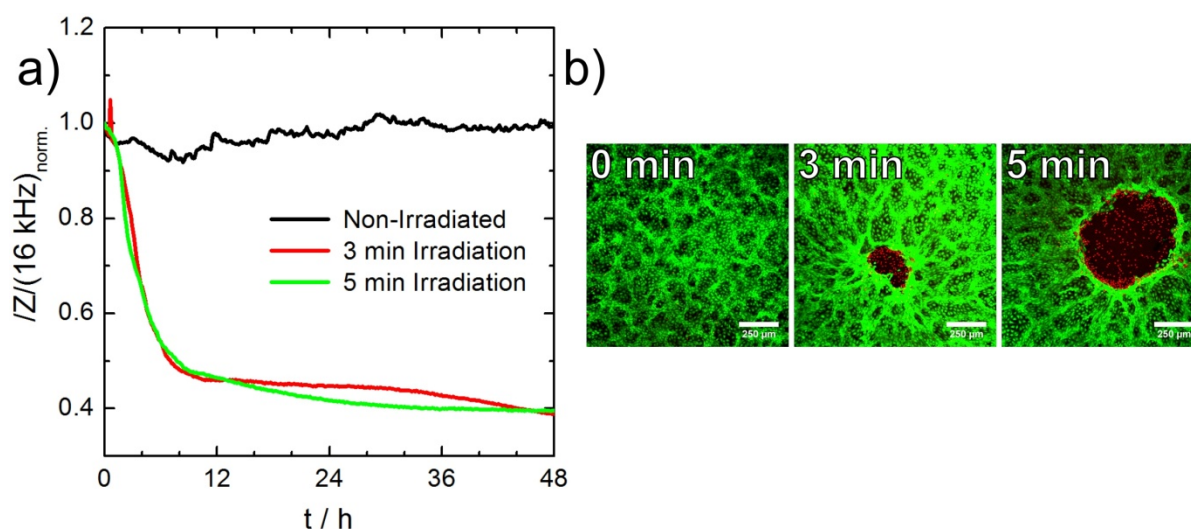


**Fig. 7.5:** Studies on the phototoxicity of C-dots which were incorporated in NRK cells with irradiation on custom-made ECIS electrodes made from ITO. a) Time courses of the normalized magnitude of the impedance at 16 kHz for NRK cells loaded with 1.0 mg/mL C-dots in EBSS<sup>++</sup>/G for 1 h. Impedance was measured for non-irradiated cells and cells irradiated on the electrode area for 3 and 5 min, respectively. Irradiation was performed using an inverse microscope with a 10-fold objective and an UV-2A filter (330 – 380 nm) with a mercury vapor lamp as light source. b) Optical sections via CLSM through CaAM/EthD-1 stained NRK cells after the measurement. Exc.: 488/543 nm. The experiment was performed twice with similar results.

The micrographs in Fig. 7.5b confirm the conclusions from the ECIS measurements. For the C-dot-loaded and non-irradiated NRK cells (0 min) only green stained cells are observed, indicating living cells. The NRK cell layer irradiated for 3 min exhibits dead cells in a circular area of about 200 μm in diameter, while the layer irradiated for 5 min shows an even larger area of dead cells with about 600 μm in diameter. Interestingly, the wound of the longer irradiated cell layer is bigger than the one for the shorter irradiation. This may be assigned to reduced photon density in the outer region of the focus point of the microscope. As such, ROS generation may be more efficient in the center of the focus and short irradiation times only induce cell death in its center. Longer irradiation times such as 5 minutes, as used in other experiments in this work, compensate for this effect, inducing cell death in the whole field of view of the cell layer. The fact that living NRK cells from the periphery of the wound did not migrate into the area of the damaged cells after the treatment may be due to elevated cell residues around the layer wound. This is indicated by particularly brighter green fluorescing cells around the wound. These living NRK cells are more in focus of the microscope, since they are in elevated position, in comparison to the other cells. As shown in chapter 5.3, the short-term incubation or loading of NRK cells with C-dots should not inhibit migration of NRK cells into an area with dead cells.

#### Investigations Regarding the Photo-Induced Cell Death Mechanism

According to the previously described studies, it has been demonstrated that NRK cells can be damaged in precisely defined areas through generation of ROS by internalized C-dots. For a better understanding of the cellular processes involved in this photodynamic treatment, the exact mechanism of the induced cell death was investigated. Therefore, NRK cells were *loaded* with C-dots and irradiated for 5 min, as described before. After irradiation the cells were incubated with Annexin V FITC/PI for 2.5 h (see chapter 3.4.3) and subsequently analyzed via CLSM. The resulting multicolor micrographs of the treated NRK cells are shown in Fig. 7.6 in different magnifications.

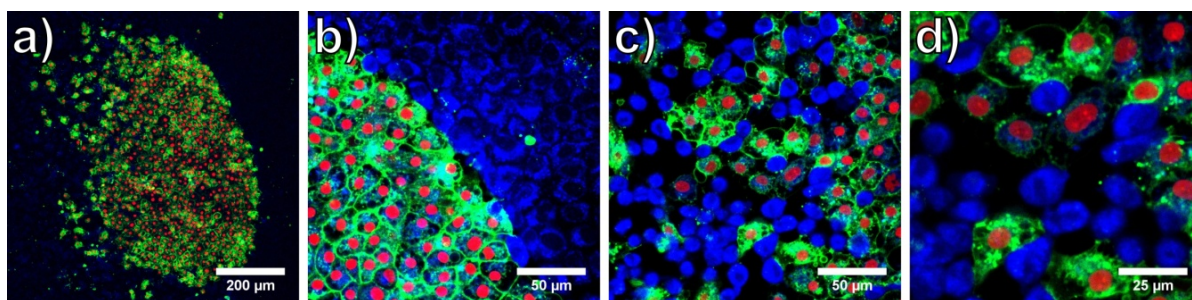


**Fig. 7.6:** Optical sections via CLSM through Annexin V FITC/PI stained NRK cells after loading with C-dots (1.0 mg/mL, 1 h in EBSS<sup>++</sup>/G) and 5 min UV light irradiation. Irradiation was performed using an inverse microscope with a 20-fold objective and an UV-2A filter block with a mercury vapor lamp as light source. Washing and examination of the cell layer was performed after 2.5 h incubation with the dyes at 37 °C, 5% CO<sub>2</sub>. Blue channel: C-dots (exc.: 405 nm), green channel: Annexin V FITC (exc.: 488 nm), red channel PI (exc.: 488 nm). a) Overview with a 10-fold objective. b-d) High resolution micrographs were recorded with a 60-fold objective. The experiment was performed twice with identical results.

The photo-wound resulting from ROS generation of the internalized C-dots, shown in Fig. 7.6a exhibits a well defined fluorescing area within the field of view. Thereby, the fluorescing area exhibits a sharp edge on the right side, while the other side is more heterogeneous. This is due to a not exactly planar placement of the sample with a more efficiently induced cell death for the right side of the sample. The higher magnification of the edge on the right side in Fig. 7.6b, shows a precise separation in the fluorescence staining between irradiated and non-irradiated cells. While the non-irradiated living NRK cells exhibit the typical blue luminescent cytoplasm of the C-dot staining, the irradiated dead cells show green luminescent cell membranes with red stained nuclei. This may be assigned to the labeling with Annexin V FITC/PI. As such, these cells are assigned as late apoptotic cells. This would be in accordance to the observation of NRK cells undergoing apoptosis through internally generated ROS (Guo *et al.* 2012). Interestingly, shorter incubation times (0.5 and 1 h) after the photodynamic treatment did not show early apoptotic cells, solely labeled with Annexin V FITC, but always the dual staining together with PI, just in smaller areas of dead cells. As such, it may be possible that the photogeneration of ROS induces loss of plasma membrane integrity, even before the cells undergo controlled apoptosis. This enables the staining of the nuclei with PI directly and the labeled Annexin V may bind to phosphatidylserine even from the inside of the cell due to free diffusion into the cytoplasm.

The magnification of the left side of the photo-wound in Fig. 7.6c, shows that several cells in the irradiated region do not show Annexin V FITC/PI labeling. These exhibit drastically different morphologies in comparison to healthy cells with the blue luminescence of the C-dots at the same time. For a closer examination of these cells, further magnified optical sections were recorded, as shown in Fig. 7.6d. Therein several blue stained nuclei are visible without the Annexin V FITC/PI staining. Furthermore, some of these cells exhibit all three colors (C-dots and the apoptosis detection kit) but with only weak intensity. These observations might be explained by the generation of ROS by C-dots trapped in endosomes of the NRK cells which may induce the degradation of their phospholipid cage through photooxidation of the lipids, as described in literature (Shum *et al.* 2001). A schematic for the photo-induced oxidation of a phospholipid is shown in Fig. 7.7a. The subsequent release of C-dots from endosomes due to structural changes of the phospholipids, influencing membrane fluidity and integrity is shown in Fig. 7.7b.

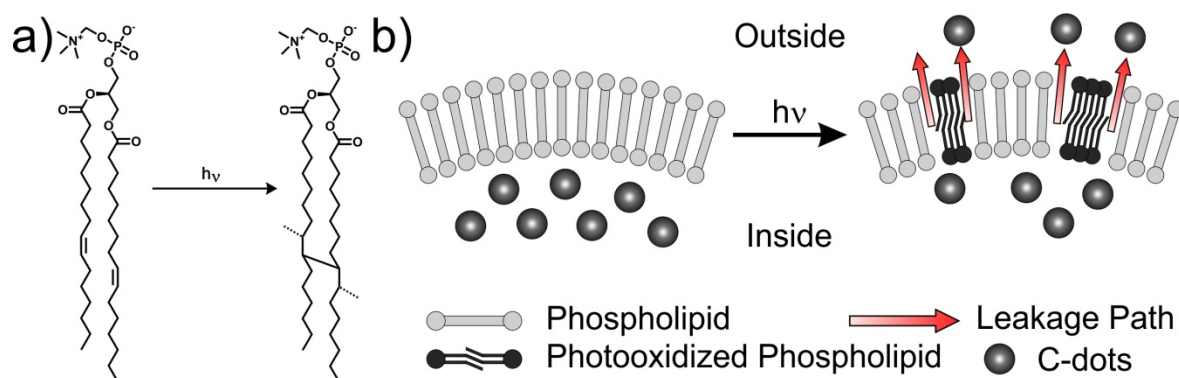


**Fig. 7.7:** Suggested photo-induced release of C-dots from endosomes via oxidation processes. a) Photo-oxidation of 1,2-dipalmitoleyl-sn-glycero-3-phosphocholine, as example, inducing structural changes and crosslinking of the fatty acids. b) Schematic for the release of C-dots from endosomes after photo-oxidation of membrane phospholipids. Structural changes of the phospholipids enable leakage of the C-dots to the outside of endosomes. (Shum *et al.* 2001)

Thereupon, the C-dots could freely enter the cell nuclei and bind to their DNA, before the cells are completely permeabilized by ROS generation throughout the cells. As such, the cells are stained from the inside by the internalized particles in very early stages of programmed cell death, even before the Annexin V FITC labeling. This of course only applies for cells, which were not exactly in focus of the irradiation as it is the case in this study. The photo-induced release of C-dots from endosomes was studied on liposomes for further verification of this theory as described later.

Asides from the not entirely completed photo-induced cell death, the ability of the selective staining of dying NRK cell nuclei by internalized C-dots, serves as basis for the theranostic approach with the particles, described in chapter 7.3.

#### Photo-Induced Release of C-dots from Liposomes



For a better understanding of the processes upon irradiation of incorporated C-dots in mammalian cells, liposomes with encapsulated C-dots (see chapter 3.2.3, high conc.) were used as models for endosomes. These were irradiated in suspension with a UV lamp (366 nm, 2x6 W) for increasing times and the fluorescence of the suspension was analyzed with exc./em. at 360/465 nm. The outcome of this experiment was compared to non-irradiated liposomes and SDS (20 mM) lysed versions, analog to the studies in Fig. 4.24b. The low intensities of the non-irradiated liposomes were assigned as 0% lysed, while the high intensities for the SDS treated ones were assigned as 100% lysed. Due to a reversal of the self-quenching of the particles, the lysis of liposomes results in higher fluorescence intensities. According to this calculation basis, the irradiation of the liposomes resulted in the following lysis rates: 5 min: 2.1%, 10 min: 6.9% and 20 min: 5.4%. As such, the UV lamp irradiation induced the lysis of liposomes or a partial loss of the liposome membrane integrity. In the case of these liposomes, most likely the photo-oxidation of the cholesterol in the artificial membrane could have induced the release of C-dots (Suwa *et al.* 1978). This is in accordance with speculations about the photo-release of the C-dots inside living cells from endosomes. Furthermore, the focused irradiation with a microscope, as applied in the cell experiments, much more efficient for the ROS generation and the subsequent photo-oxidation of the endosome phospholipids. As such, the release of the particles should be even more likely.

### 7.3 “Theranostic” Approach Based on the Photodynamic Treatment and Imaging of Mammalian Cells

In earlier experiments it was shown that the nuclei of NRK cells undergoing cell death through ROS generation by internalized C-dots are selectively stained by the particles from the inside. This ability was used for the development of a “theranostic” approach, combining photodynamic treatment of target cells and imaging of cell viability via CLSM as a diagnostic control.

The principle relies on *loading* of the NRK cells via short-term incubation and washing for the removal of external particles. Focused excitation of the internalized C-dots enables photo-generation of ROS inside the cells, inducing apoptosis in target cells. The simultaneous release of C-dots, most likely through photo-oxidation of endosomes, enables the particles to enter the cell nuclei. Thereby, the internalized C-dots undergo an emission red-shift upon binding to the DNA, as described before for particles in the bulk phase, and therefore give evidence on the physical condition of the cells. Cell death may be controlled via imaging of the sample by CLSM, distinguishing between living and dead cells by the characteristic C-dot emission. A schematic for the principle of the approach is shown in Fig. 7.8.

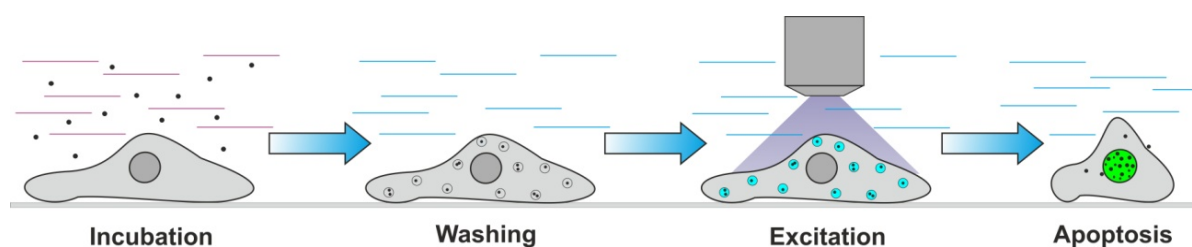


**Fig. 7.8:** Schematic for the principle of a “theranostic” approach for the targeted photodynamic treatment of living cells and a subsequent diagnostic control using C-dots.

The theranostic approach was carried out on confluent NRK cells. These were loaded with C-dots and irradiated as described in chapter 3.8. Non-incubated NRK cells served as control to exclude the possibility of cell damage caused by irradiation itself. After 1 h at 37 °C, 5% CO<sub>2</sub>, the NRK cells were analyzed in the irradiated field of view via phase contrast microscopy and CLSM. The resulting micrographs are shown in Fig. 7.9.

The phase contrast micrographs in Fig. 7.9a show that the irradiation of non-*loaded* NRK cells leaves the cells unharmed after the treatment. In contrast to this, a sharply delimited region of dead cells with significant morphology changes is observed for the *C-dot-loaded* NRK cells. As such, the irradiation under the chosen conditions is considered as non-invasive, while only the photogeneration of ROS through internalized C-dots induces cell death in target cell regions.

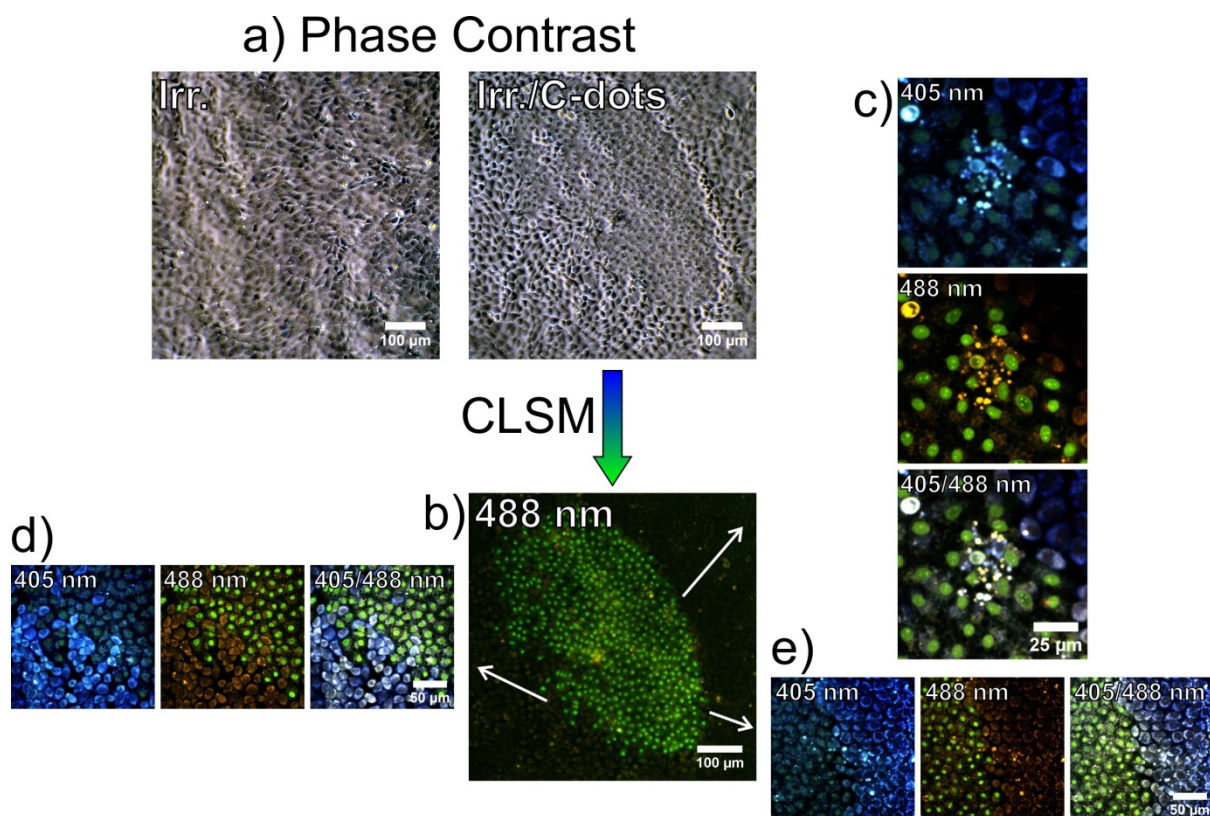


**Fig. 7.9:** Large area theranostic approach on NRK cells loaded with C-dots after epiluminescence microscope irradiation. a) Phase contrast micrographs of C-dot-loaded (1.0 mg/mL, 1 h, in EBSS<sup>++</sup>/G) and non-loaded NRK cells after 5 min UV light irradiation. Irradiation was performed using an inverse microscope with a 20 fold objective and an UV-2A filter block with a mercury vapor lamp as light source. b-e) Optical sections through the treated NRK cells 1 h after irradiation while cells were kept at 37 °C, 5% CO<sub>2</sub>. b) Overview of the treated cells with a 10-fold objective. c-e) High resolution micrographs of sections of the treated cells with a 60-fold objective. Excitation wavelengths are denoted in the micrographs. RGB detector settings were kept constant.

The photo-induced wound of the cell layer was analyzed via CLSM upon excitation with 488 nm, as shown in Fig. 7.9b. Exactly those cells show green luminescence that were irradiated and underwent cell death. As such, the internalized C-dots did not only allow the photodynamic treatment of target cell areas, but they also indicate apoptosis of the NRK cells. Higher magnified optical sections were recorded on different sites of the cell wound with excitation at 405 and 488 nm, as well as the simultaneous excitation with both lasers. These allow a detailed examination of the cells after the treatment and are shown in Fig. 7.9c-e. In the micrographs of Fig. 7.9c, most interestingly, small luminescent structures in a size between 1 and 3 μm are observed besides several green stained nuclei of dead cells. These are present at several sites of the wound and appear bright blue upon excitation at 405 nm, orange at 488 nm and brightly white for the simultaneous excitation. Since the ROS induced cell death mechanism is suggested to be apoptosis, these small structures are assumed to be apoptotic bodies, resulting from the photodynamic treatment. The different coloration and particular brightness of the apoptotic bodies may be explained by a relatively high C-dot concentration pinched off into these vesicles and not being bound to DNA. Magnifications of the left and right side of the photo-generated wound of the cell

layer, respectively are shown in Fig. 7.9d and e. The right side exhibits a sharp delimitation with different coloration for non-irradiated and irradiated NRK cells. While the photodynamic treated and dead cells show the typically green stained nuclei with excitation upon 488 nm, non-irradiated and living cells exhibit a blue luminescent cytoplasm upon excitation at 405 nm. The simultaneous use of both lasers allows the determination between the treated and non-treated area. On the left side of the wound, the transition between living and dead cells appears more fluent. This may be assigned to several cells which were not in the focal plane undergoing the photodynamic treatment due to an uneven illumination of the sample.

In summary, the “theranostic” approach combining photodynamic treatment of target cell areas and subsequent diagnostic control via CLSM may be performed using epiluminescence microscope irradiation. The principle only relies on internalized C-dots, as shown in the schematic of Fig. 7.8. Thereby, the effect of photodynamic treatment could clearly be assigned to the irradiation of internalized C-dots generating ROS. Side effects through the solely irradiation (Fig. 7.9a) or the incorporation of the particles (Fig. 5.3 and Fig. 7.5b) could be excluded. The usage of bare C-dots for photodynamic treatments is a big advantage in comparison to established techniques utilizing nanoparticles, since these afford modifications or complex conjugates. The nanoparticles are often only delivery vehicles for organic photosensitizers into the cells (Bechet *et al.* 2008). C-dots by contrast may be easily prepared and combine water-dispersibility, cellular uptake, ROS generation and the ability for fluorescence imaging in diagnostics.

### Photodynamic Treatment using Carbon Dots on Single Cell Level

Since ROS generation and photo-induced cell death is dependent on local irradiation of internalized C-dots, high-resolution techniques for the photodynamic treatment on single cell level were investigated. Therefore, NRK cells were *loaded* with C-dots as described in chapter 3.8. These were heated with a thermostat maintaining 37 °C during CLSM imaging and treatment of the cells. After analysis, a small region of interest with a delimited number of cells was chosen with digital zoom and irradiated for 5 min by continuously scanning this region with a 405 nm laser. Subsequently, the cells were kept at 37 °C for 1 h without changing the imaging position of the sample. Thereupon, the NRK cells were analyzed again with similar settings as before the continuous laser scanning of the target cells. The corresponding optical sections of this study are shown in Fig. 7.10.

The micrograph in Fig. 7.10a shows C-dot-*loaded* NRK cells in unharmed morphology with blue cytoplasmic luminescence prior to the photodynamic treatment. The white marked region was irradiated by continuous laser scanning and the corresponding micrograph is shown in Fig. 7.10b. In this region six NRK cells loaded with C-dots are located with their full cell body and further cells by parts in the periphery. After 1 h at 37 °C, morphology changes and a differing fluorescence emission can be observed for NRK cells in the irradiated

region, as indicated in Fig. 7.10c. Thereby, the cells disintegrated junctions with surrounding non-irradiated and living cells. Furthermore, the cells show the typical morphology of apoptotic cells together with green luminescent nuclei. As such, the photo-generation of ROS through internalized C-dots did not only induce apoptosis but also led to binding of the particles to cellular DNA as a result of the continuous scanning with the 405 nm CLSM laser. This observation is in accordance with the studies upon irradiation with the epiluminescence microscope described before.

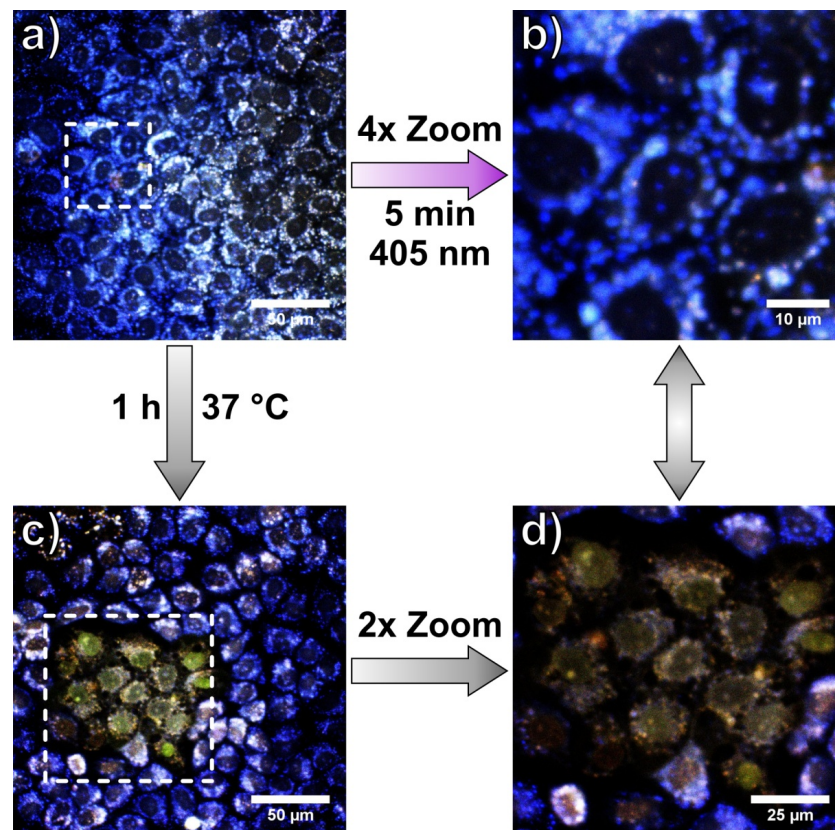


**Fig. 7.10:** Optical sections through NRK cells that had undergone the theranostic approach on single cell level via CLSM using incorporated C-dots. The cells were loaded with C-dots (1.0 mg/mL, 1 h, in EBSS<sup>++</sup>/G) prior to irradiation. a) NRK cells before irradiation. The marked cells were focused using a 4 fold digital zoom. b) Selected NRK cells irradiated for 5 min using the 405 nm laser with 256x256 pixel resolution. c) NRK cells 1 h after irradiation during which cells were kept at 37 °C using a thermostat. The marked area is magnified in (d). d) Selected NRK cells 1 h after irradiation. Exc. 405/488 nm and RGB detector settings are constant for all micrographs. The experiment was performed three times with different irradiation areas, obtaining similar results for the irradiated area.

The two-fold digital zoom in Fig. 7.10d allows for a better comparison of the NRK cells before and after the irradiation. Conclusions from preceding chapters are confirmed. Following the fate of single cells is possible as the cells, before and after the treatment, still are in similar position relative to each other. Additionally to the six NRK cells completely irradiated, several cells at the left and right underwent apoptosis, since ROS were generated in parts of these. Those cells exhibit the same morphology changes and green stained nuclei as completely irradiated ones.

## Carbon Dots as “Theranostic” Particles in Photodynamic Treatment

In conclusion, it was shown that the irradiation by the 405 nm laser during scanning via CLSM also enables the theranostic approach with C-dots on single cell level. Thereby, selected cells may be exposed to the photodynamic treatment and the successfully induced apoptosis may be controlled via imaging without addition of reagents or changes of the set-up. Thereby, the smallest possible treatment area is only delimited by the field of view during irradiation. As such, even fewer numbers of neighboring NRK cells may be treated with C-dots in the combined theranostic approach, as shown in Fig. 7.11.

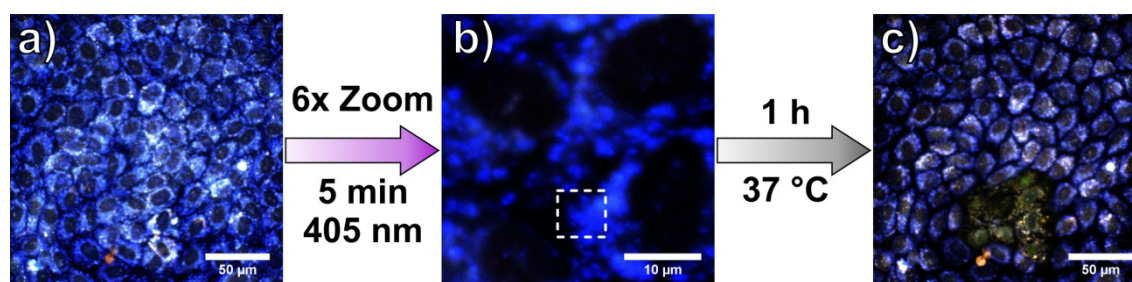


**Fig. 7.11:** Optical sections through NRK cells that had undergone a highly selective theranostic approach on single cell level via CLSM using incorporated C-dots. The cells were loaded with C-dots (1.0 mg/mL, 1 h, in EBSS<sup>++</sup>/G) prior to irradiation. a) NRK cells before irradiation. The marked cells were focused using a 6 fold digital zoom. b) Selected NRK cells irradiated for 5 min using the 405 nm laser with 256x256 pixel resolution. c) NRK cells 1 h after irradiation during which cells were kept at 37 °C using a thermostat. Exc. 405/488 nm and RGB detector settings are constant for all micrographs. The experiment was performed three times with different irradiation areas, obtaining similar results for the irradiated area.

Hereby, NRK cells were treated similarly as described before, just with the application of a higher digital zoom. Among the blue luminescent, healthy and C-dot-loaded NRK cells in Fig. 7.11a, four cells were chosen via six-fold digital zoom, as indicated by the white marked area. These are shown in Fig. 7.11b, and they were irradiated by continuous scanning with the 405 nm laser for 5 min. The analysis of the cell layer after 1 h at 37 °C, in Fig. 7.11c, shows that exactly those NRK cells underwent cell death, indicated by the green fluorescence of their nuclei, which were irradiated. Again neighboring cells on the right periphery did also undergo cell death, possibly due to partial irradiation of the cell body. As such, the technique utilizing CLSM for irradiation may be delimited in this respect, since the cell death of neighboring cells may not be excluded with the chosen set-up. In further experiments, it was not possible to induce cell death in just one single cell through higher digital zoom factors, as other cells around the target. Besides the irradiation area, diffusion of ROS out of the field of view could induce apoptosis of surrounding cells.

In summary, it was shown that the unique optical properties as well as the photogeneration of ROS by C-dots from starch and Trp enable a “theranostic” approach in the treatment of adherent cells. Thereby, living cells with internalized C-dots may selectively undergo photoinduced apoptosis through local ROS generation. The irradiation may be performed via epifluorescence microscopy or CLSM depending on the intended resolution.

Additionally CLSM imaging allows the diagnostic control of cell death through the emission shift from a blue cytoplasm to green nuclei.

#### Photodynamic Treatment of MCF-7 Multicellular Spheroids using Carbon Dots

The theranostic approach with C-dots, combining selective photodynamic treatment and imaging of mammalian cells grown in monolayer was demonstrated in the previous chapter. However, photodynamic therapy approaches are developed for the application on tumors in living organisms in order to cure cancer. Those tumors are three-dimensional cell clusters and tissues, which should be specifically targeted in therapy approaches. In order to investigate the applicability of C-dots as “theranostic” agent for tumors, photodynamic therapy and subsequent imaging was performed on MCF-7 MCS, grown for 7 days, as breast cancer tumor model. Therefore, MCS were incubated with 1.5 mg/mL C-dots in EBSS<sup>++</sup>/G for 2 h at 37 °C, 5% CO<sub>2</sub>. Subsequently, the MCS were washed twice with EBSS<sup>++</sup>/G and irradiated for 10 min using an inverse microscope with a 10 fold objective and an UV-2A filter block with a mercury vapor lamp as light source. Afterwards, the MCS were kept at 37 °C with 5% CO<sub>2</sub> atmosphere for 4 h, before microscopic analysis. Untreated MCS in EBSS<sup>++</sup>/G served as control, as well as non-irradiated MCS *loaded* with C-dots and UV irradiated MCS without C-dots. Phase contrast micrographs before the treatments and 4 h afterwards are shown in Fig. 7.12.

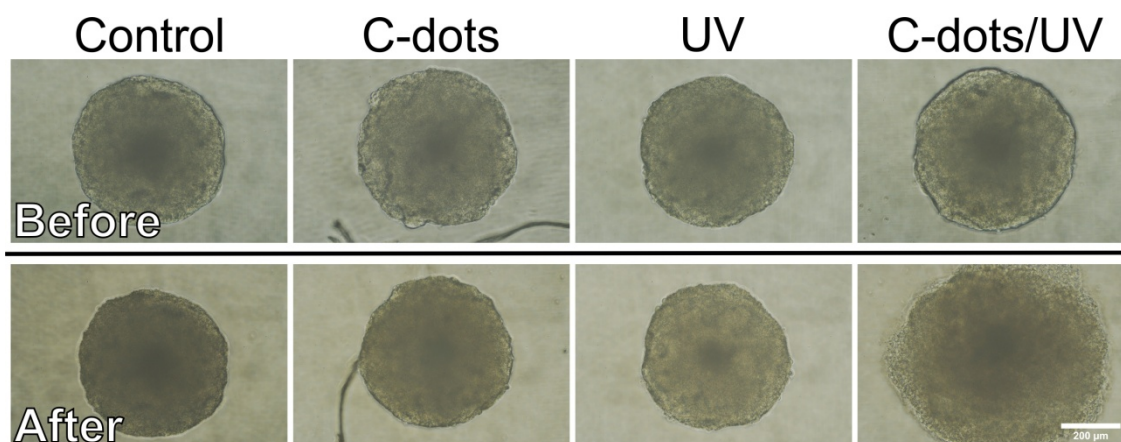


**Fig. 7.12:** Phase contrast micrographs of MCF-7 MCS (grown for 7 d) before and 4 h after the photodynamic treatment with C-dots “C-dots/UV”. Untreated MCS denoted as “Control”, C-dot loaded MCS without UV irradiation are denoted as “C-dots”, irradiated MCS without C-dots are denoted as “UV”. This experiment was performed twice with at least two samples per group, yielding identical results.

Phase contrast micrographs in Fig. 7.12, show that the morphology of the untreated MCS does not change over time. Similarly, the *loading* with C-dots and the application of UV irradiation to particle-free MCS did not induce morphology changes, comparing the micrographs before and afterwards. Thus, the loading with C-dots and the long-term irradiation of the MCS does not induce significant toxic effects. In contrast to this, the long-term UV irradiation of C-dot *loaded* MCS induced drastic morphology changes. Before the

treatment the MCS had a size of about 450  $\mu\text{m}$  with sharply defined borders, indicating smooth and healthy MCF-7 cells on the periphery of the MCS. After the treatment, the MCS expands laterally with fuzzy borders. A vast number of round-shaped cells detach from the MCS and the density of the MCS is reduced. This indicates that the MCF-7 cells undergo cell death, degrade cell-cell junctions and round off from the cell network. Accordingly, the selective photodynamic treatment with C-dots proven in cell monolayer is also applicable to 3D cell formations. As such, the C-dots from starch and Trp could be promising photodynamic therapy agents for the application on tumor tissues in cancer therapy, as recently shown in literature for a different C-dot preparation (Ge *et al.* 2014).

In further investigations, the diagnostic part of the “theranostic” approach with C-dots was performed via CLSM analysis of the MCF-7 MCS. Therefore, the photodynamically treated MCS, as well as three different control groups were imaged via CLSM with laser excitation at 405 nm, 488 nm and simultaneously 405/488 nm. The resulting optical sections of the MCF-7 MCS are shown in Fig. 7.13.

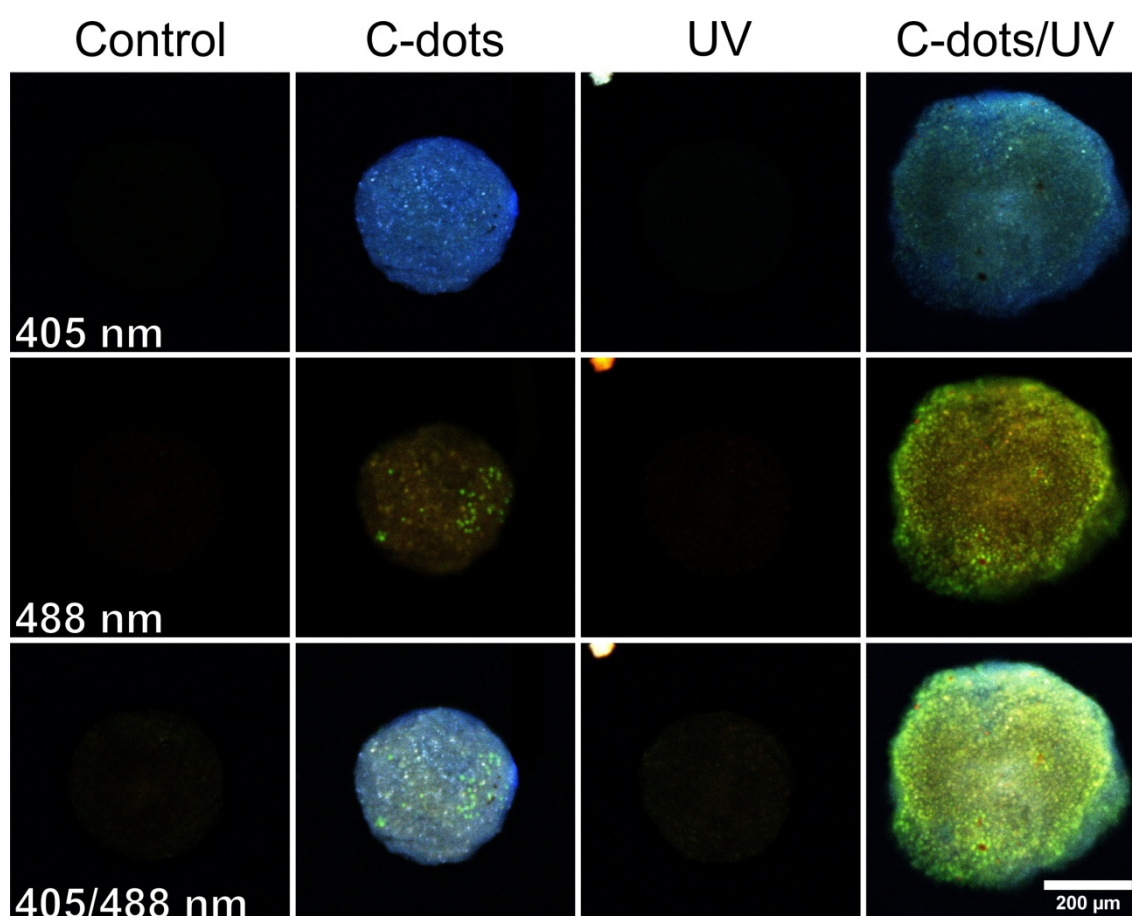


**Fig. 7.13:** Optical sections through MCF-7 MCS via CLSM, 4 h after the photodynamic treatment with C-dots “C-dots/UV”. Untreated MCS are denoted as “Control”, C-dot loaded MCS without UV irradiation are denoted as “C-dots”, and irradiated MCS without C-dots are denoted as “UV”. Exc. wavelengths are denoted in the micrographs. RGB detector settings were kept constant.

The CLSM imaging of the untreated MCS (“Control”) and the irradiated ones without C-dot loading (“UV”), in Fig. 7.13, do not show fluorescence with excitation at 405 and 488 nm.



Only the simultaneous excitation with both lasers shows marginal auto-fluorescence from the MCS under these optimized conditions. As such, fluorescence detected from the MCS loaded with C-dots, can only arise from the particles. The non-irradiated MCS loaded with C-dots (“C-dots”) exhibit bright blue luminescence upon excitation at 405 nm, indicating mostly living MCF-7 cells with low concentrations of incorporated C-dots. Furthermore, the excitation at 488 nm shows a few green luminescence spots, resulting from the staining of dead cells nuclei inside the MCS. This phenomenon was already observed for intact MCF-7 MCS and described in chapter 6.3. Thus, the non-irradiated MCS loaded with C-dots, undergo the procedure largely unharmed. The observation of a limited number of dead cells inside the MCS is common for MCS or cell monolayers *in vitro*.

In contrast to the controls, the photodynamically treated MCS shows a very different fluorescence emission upon laser excitation, apart from their drastically changed morphology. As such, upon 405 nm laser excitation light green emission is detected from the inside of the MCS, resulting from a red-shifted emission in dead cells’ nuclei. Furthermore, blue luminescence is detected throughout the whole MCS. However, this has lower intensities than from the non-irradiated MCS and may be assigned to entrapped remnants of C-dots inside the MCS. The excitation at 488 nm clearly reveals the physiological status of the spheroids’ MCF-7 cells. As such, green luminescent nuclei are observed throughout the whole MCS. Interestingly, highest intensities occur on the periphery of the spheroid, which can be assigned to less reabsorption of light from surrounding tissues on the one hand. On the other hand, dead cells round off from the spheroid, detach from its border and therefore are particularly well detectable. The excitation with both lasers combines the collected information and emphasizes the suggestion of cell death induction throughout the MCS, with highest green intensities from dead MCF-7 cell nuclei.

According to the results of this study, C-dots are capable of mediating cell death throughout a three dimensional MCF-7 breast cancer tumor model. Furthermore, the success of the treatment can be observed via a changed emission behavior from the MCS dead cells via CLSM imaging. Multifunctional nanoparticles for the treatment and imaging of tumors are highly relevant for clinical applications (Cheng *et al.* 2012). The “theranostic” approach using C-dots represents a novel application of nanoparticles for the combined photodynamic treatment of whole MCS and diagnosis of the treatment success. Photodynamic therapy of spheroids with TiO<sub>2</sub> nanoparticles, for example, affords passivation with hydrophilic polymers in order to induce water-dispersibility. Furthermore, analysis of success of the treatment relies on the subsequent application of organic dyes, such as Annexin V and Propidium iodide (Yamaguchi *et al.* 2010). Q-dots also lack water-dispersibility. For their application in diagnosis and therapy of tumors or spheroids, delivery vehicles (often in large dimensions) such as liposomes are necessary (Azzazy *et al.* 2007).

## *Carbon Dots as “Theranostic” Particles in Photodynamic Treatment*

The fact that C-dots do not afford such modifications for therapy and diagnosis applications represents a promising advantage.

Although the studies of the photodynamic treatment of MCS using C-dots are on the level of fundamental research, C-dots are expected to be promising theranostic agents for the treatment of tumors tissues in the cancer therapy of living organisms.

## 8 Summary and Outlook

### 8.1 Summary

The hydrothermal preparation of N-doped C-dots from starch and L-tryptophan which was developed and optimized represents a simple and sustainable synthetic method to obtain a highly interesting carbon nanomaterial for bioanalytical applications. These particles exhibit a size distribution between 0.5 and 4.5 nm with an average size of  $(1.6 \pm 0.8)$  nm. They furthermore show a high functionalization with oxygen containing-groups, remnants from the precursor molecules, which renders them highly water-dispersible. This is in accordance to the elemental composition of 44.9% C, 6.1% H, 1.1% N and 47.9% O. The experimental evidence suggests that mainly hydroxyl and carboxyl groups cover the C-dots surface, resulting in a slightly negative charged surface with a zeta potential of  $(-9.3 \pm 3.5)$  mV at physiological pH.

Based on the functionalization with different chemical groups on the surface, the C-dots are incorporated into mammalian cells in a time range of minutes via endocytosis. Probably, the particles are internalized via unspecific pinocytosis due to their ultra-small size, inducing vesicle-mediated incorporation. Receptor-mediated endocytosis cannot be excluded, but is not suggested due to the high selectivity of the receptors. In addition to this, hints indicating further uptake mechanisms such as simple diffusion across the membrane have been gathered. The ultra-small dimensions of these nanoparticles, together with their unique surface may be responsible for the high translocation rates through cell layers observed for several mammalian cell lines. The high penetration rates and the ultra-fast uptake into cells outline the applicability of these C-dots as probes or contrast agents for imaging studies.

Biocompatibility is a necessary criterion for the utilization of this novel nanomaterial in cell imaging. The verification of this quality presented a mixed picture for the C-dots. Thereby, cytotoxicity evaluations clearly showed a “critical concentration” of about 1.1 mg/mL for the long-term incubation of NRK cells over days. Higher particle concentrations induced apoptosis among the cells, while lower concentrations left the NRK cells mostly unaffected. Furthermore, cell adhesion, proliferation and migration were dose-dependently delayed in permanent presence of the particles. However, the staining and *loading* of NRK cells as necessary for the developed applications requires only shortest incubation times in the range of minutes. Thus C-dot stained NRK cells did not show any sign of cytotoxicity. Additionally, migration, as example among impairments of cell behavior, showed only marginal affection for such loaded NRK cells. Accordingly, C-dots may be considered as biocompatible, based on the right choice of concentration and incubation time (typically 1.0 mg/mL for 30 – 60 min) for the respective application.

## Summary and Outlook

A thorough investigation of the C-dots optical properties revealed unique features of this novel material. Aqueous C-dot suspensions typically exhibit quantum yields of  $(25.1 \pm 2)\%$ . This is about thirty-fold higher than quantum yields of undoped C-dots from starch and may be attributed to the N-doping through the addition of Trp. Since the addition of Trp inducing the formation of larger particles, the amino acid most likely also enables the formation of highly emissive species. Low concentrated suspensions of the N-doped C-dots have their excitation maximum at about 370 nm and exhibit bright blue luminescence with an emission maximum at about 450 nm. Fluorescence is heavily concentration dependent and the excitation wavelength can be varied presumably leading to emission from different C-dot species. Increasing particle concentration in aqueous suspension is suggested to induce reabsorption of emitted light and/or self-quenching among the emitting species. This results in red-shifted fluorescence emission for higher C-dot concentration. The studies of the particles fluorescence at the excitation wavelengths of the CLSM laser wavelengths 405, 488 and 543 nm showed that this phenomenon might be used for the tracking of local concentrations of C-dots via imaging. Bright blue emission is observed for low concentrations at 405 nm excitation. High particle concentrations result in an emission-shift from blue to green with excitation at 405 nm. Furthermore, the green emission upon excitation at 488 nm becomes most prominent.

These spectral characteristics can be documented nicely by, utilizing C-dots as fluorescence contrast agent for the imaging of mammalian cells via CLSM. Thereby, local accumulation of C-dots was concluded from the red-shifted fluorescence emission of the particles in suspension at higher concentrations. Similarly to the studies in suspension, the emission shifts from blue to green upon particle accumulations for excitation at 405 nm. Furthermore, the emission intensities rise for higher particle amounts upon excitation at 488 and 543 nm. Living cells were shown to take up C-dots in low concentration mostly via endocytosis, resulting in a blue luminescent cytoplasm upon 405 nm laser excitation, with most of the particles entrapped in vesicles. Dead cells by contrast, exhibited green luminescent nuclei with highest intensities under excitation with the 488 nm laser. This may be attributed to the accumulation of C-dots in the cell nuclei through binding to DNA, resulting in the emission shift. Cells that have lost plasma membrane integrity and underwent cell death enable the direct contact between their nuclei and the bulk phase. As such, C-dots, being not entrapped in vesicles may freely diffuse through the nuclear pore complex and accumulate therein. Furthermore, the binding between C-dots and the DNA is suggested to change the emission properties of the particles, which also contributes to the different coloration.

Utilizing both lasers, the 405 nm laser for the blue luminescence of living cells cytoplasm and the 488 nm laser for the dead cells nuclei, allowed the application of C-dots within a Live-Dead-Assay. This gives the same information as commercial available staining kits to distinguish between living and dead cells via imaging. Having proven the independency

of the C-dot based readout from the cell death inducing toxicant, the C-dots can furthermore be utilized for the determination of  $EC_{50}$  values for a selected toxicant via CLSM imaging. Thereby, the ratio between the green and blue fluorescence intensities at the respective laser excitation could be used as measure for cytotoxicity. The method may be applied on cytotoxicity evaluations for several mammalian cell lines. For NRK cells treated with tBuOOH, for example, the green/blue intensity ratio changed from about 0.1 for healthy cells to about 1.5 for completely dead cells. Additionally, it could be shown that the utilization of the C-dot staining of living and dead cells is not limited on CLSM, but can also be analyzed via FACS. Besides cytotoxicity evaluations, C-dots might be used for the imaging of living and dead cells in MCS as tissue models. As such, also the application of the particles in tissues seems promising.

Besides luminescence, the C-dots were found to effectively generate reactive oxygen species (ROS) upon long-term photo-excitation. Thereby, the particles combine every necessary requirement for a photodynamic therapy agent: good water-dispersibility, fast internalization into cells and efficient ROS generation. This was used to selectively subject NRK cells to photodynamic treatment through the photo-excitation of both, C-dots in the bulk phase and internalized particles. It was demonstrated that besides near-UV, also the blue light irradiation may cause phototoxicity. As such, irradiation conditions of applications using C-dots as photodynamic agents are variable. The photogeneration of ROS by internalized C-dots is suggested to result in oxidation of the phospholipids of the vesicles surrounding the incorporated particles. As such, C-dots are suggested to be released from endosomes and generate ROS throughout the whole cell. This induces cell death via apoptosis, which was proven through Annexin V binding studies. Interestingly, released cell-internal C-dots were observed to stain the nuclei of dying cells from the inside even before Annexin V bound to those cells membranes.

In a theranostic approach with C-dots, the particles' ability to stain dead cells' nuclei from the inside together with cell death inducing ROS generation upon photo-excitation was combined. NRK cells were loaded with C-dots through short-term incubation. Target cells were subjected to controlled photodamage via photo-excitation of internalized C-dots for several minutes. This could be performed on large cell areas via epiluminescence microscopy with UV excitation (330 – 380 nm) and on single cell level via CLSM laser excitation at 405 nm. The subsequent analysis of the cells via CLSM allows the explicit control of the treatment through the changed optical properties of the internalized C-dots for dead cells. Thereby, the internalized C-dots undergo the same red-shift through binding and accumulation in the cells' nuclei DNA as described for the C-dot staining from the bulk phase. Non-treated NRK cells exhibit a blue luminescent cytoplasm, upon 405 nm excitation, while the nuclei of those cells subjected to the photodynamic therapy appear green with 488 nm excitation. Accordingly, the C-dots do not only allow the active *therapy* of target cells, but also *diagnosis* on the effort of the treatment – *theranostic*. Studies on

## Summary and Outlook

MCF-7 MCS as breastcancer tumor models showed that this approach may also be applied on such large cell aggregates. Therefore, C-dots have to be considered as promising theranostic agents in cancer therapy of living organisms.

In side projects of this work, the C-dots were embedded into other nano-sized structures and chemically modified in order to demonstrate possible applications of the particles. Among these, the embedding into agarose nanoparticles was utilized for the optical observation of osmolarity changes based on fluorescence self-quenching in confined volumes. Thereby, fluorescence intensity increases of 15% were observed for the addition of 1 M osmolyte. Although this represents a poor sensitivity, the experiments show a fundamental possibility for future applications of the particles. Additionally, liposomes were investigated as transport vehicles for C-dots into NRK cells. Thereby, internalization of the particles was observed, most likely through a different uptake-mechanism, compared to free C-dots. These studies may be considered as first steps towards the incorporation into target cells. Also the chemical modification of the C-dots is meant to show principle application possibilities for the particles. The modification with oleic acid drastically changed the physicochemical and optical properties of the C-dots. As such, the binding to DNA, for example, is unlikely and not observed. Although, the applied thionyl chloride chemistry may be considered as harsh, this modification route may be utilized for promising surface modifications of the particles.

Concerning the inconsistencies in literature, several differences between the bottom-up prepared C-dots and the top-down prepared GQDs with respect to physicochemical and optical properties have been elaborated, to clearly differentiate between both materials. At first, morphology of both materials was found to be highly diverse. As such, C-dots are quasi-spherical in shape with only a few nanometers in diameter and suggested to be mostly amorphous. By contrast, GQDs exhibit flake-like structures with similar heights, but in lateral dimensions of 5 – 25 nm. Furthermore, GQDs are suggested to mostly consist of graphitic carbon, since the precursor material is graphite. Both materials have shown to exhibit fluorescence emission shifts with variation of the excitation wavelengths. However, C-dots seem to have only a few major emissive species dominating their optical properties. By contrast, GQDs exhibit a direct correlation between excitation and emission. As such, GQDs may contain an infinite variety of emissive sites. In conclusion, both materials are closely related to each other concerning composition and functionalities, but clearly have their differences. Accordingly, a differentiation between both materials, C-dots and GQDs, is advisable.

## 8.2 Zusammenfassung auf Deutsch

Die Entwicklung und Optimierung der hydrothermalen Präparation von N-dotierten C-dots aus Stärke und L-Tryptophan (Trp) stellt eine einfache und nachhaltige synthetische Methode dar, um ein für bioanalytische Anwendungen hochinteressantes, Kohlenstoffnanomaterial zu gewinnen. Diese Partikel besitzen eine Größenverteilung zwischen 0.5 und 4.5 nm mit einer Durchschnittsgröße von  $(1.6 \pm 0.8)$  nm. Desweiteren weisen sie eine hohe Dichte an sauerstoffhaltigen chemischen Gruppen auf, welche Rückstände der Vorläufermoleküle sind und die Partikel äußerst gut Wasser-dispergierbar machen. Dies ist in Übereinstimmung mit der elementaren Zusammensetzung von 44.9% C, 6.1% H, 1.1% N and 47.9% O. Die Experimente deuten darauf hin, dass hauptsächlich Hydroxyl- und Carboxyl-Gruppen die Oberfläche der C-dots bedecken, was sich in einer leicht negativ geladenen Oberfläche bei physiologischem pH mit einem Zeta-Potential von  $(-9.3 \pm 3.5)$  mV, niederschlägt.

Erklärbar durch die vermutete Funktionalisierung mit verschiedensten chemischen Gruppen auf der Oberfläche der C-dots, werden diese innerhalb von Minuten von tierischen Zellen durch Endozytose aufgenommen. Höchstwahrscheinlich werden die Partikel aufgrund ihrer geringen Größe, unspezifisch mittels Pinozytose über Vesikel in die Zellen aufgenommen. Eine Rezeptor-vermittelte Endozytose kann dabei nicht ausgeschlossen werden, erscheint aber unwahrscheinlich wegen der hohen Selektivität der Rezeptoren. Zusätzlich wurden Indizien auf weitere Aufnahmemechanismen, wie einfache Diffusion über die Zellmembran, beobachtet. Die äußerst geringe Dimension der Nanopartikel, gemeinsam mit ihrer einzigartigen Oberfläche, dürften für die schnelle Translokationsraten durch Zellschichten verantwortlich sein, welche für verschiedene tierische Zelllinien beobachtet wurde. Die hohen Durchdringungsraten und die ultraschnellen Aufnahme in Zellen unterstreichen die Anwendbarkeit der C-dots als Sonden oder Kontrastmittel für bildgebende Studien.

Biokompatibilität ist ein notwendiges Kriterium für die Anwendung jedes neuen Nanomaterials für bildgebende Zelldiagnostik. Die Verifizierung dieser Bedingung ergab ein gemischtes Resultat für die C-dots. Dabei zeigten Zytotoxizitätsmessungen eine eindeutig kritische Konzentration von ungefähr 1.1 mg/mL für die Langzeit-Inkubation von NRK Zellen über mehrere Tage. Höhere Partikel-Konzentrationen führten zu Apoptose unter den Zellen, während niedrigere Konzentrationen die NRK Zellen weitestgehend unbeeinflusst ließen. Desweiteren wurden Zell-Adhäsion, -Proliferation und -Migration proportional zur C-dot Konzentration verzögert, bei permanenter Aussetzung den Partikeln gegenüber. Jedoch benötigen die Färbung und die Beladung von NRK Zellen, wie sie für die entwickelten Anwendungen verwendet werden lediglich Inkubationszeiten von wenigen Minuten. Auf diese Weise behandelte NRK Zellen zeigten keine Anzeichen von Zytotoxizität. Desweiteren wurde die Migration, als Beispiel eine Beeinträchtigung des

## Summary and Outlook

Zellverhaltens, von auf diese Weise beladenen NRK Zellen nur marginal beeinflusst. Folglich können die in dieser Arbeit beschriebenen C-dots unter den gegebenen Expositionsbedingungen als biokompatibel bezeichnet werden. Dies basiert auf der richtigen Wahl von Konzentration und Inkubationszeit (i.d.R. 1.0 mg/mL für 30 – 60 min) für die jeweilige Anwendung.

Eine gründliche Untersuchung der optischen Eigenschaften der C-dots ergab einzigartige Eigenschaften dieses neuen Materials. Dabei weisen wässrige C-dot Suspensionen typischerweise eine Quantenausbeute von  $(25.1 \pm 2)\%$  auf. Dies ist ungefähr 30-mal höher als Quantenausbeuten von nicht-dotierten C-dots aus Stärke und dürfte auf die N-Dotierung durch das Hinzufügen von Trp zum Reaktionsansatz zurückzuführen sein. Da die Zugabe von Trp auch mit der Formation von größeren Partikeln zusammenhängt, dürfte die Aminosäure höchstwahrscheinlich auch die Bildung von stark emittierenden Spezies begünstigen. Niedrig konzentrierte Suspension von N-dotierten C-dots haben ihr Anregungsmaximum bei ungefähr 370 nm und weisen blaue Lumineszenz mit einem Emissionsmaximum bei etwa 450 nm auf. Die Fluoreszenz ist konzentrationsabhängig und die Anregungswellenlänge kann über einen weiten Wellenlängenbereich variiert werden, was zur Emission von unterschiedlichen C-dot Spezies führt. Eine Erhöhung der Partikel-Konzentration in wässriger Suspension führt vermutlich zu Reabsorption von emittiertem Licht und/oder zu Selbst-Löschung unter den verschiedenen emittierenden C-dot Spezies. Dies führt zu einer Rot-Verschiebung der Fluoreszenz-Emission für höhere C-dot Konzentrationen. Untersuchungen der Partikel-Fluoreszenz bei den Wellenlängen der Laser des verwendenden CLSMs von 405, 488 und 543 nm zeigten, dass dieses Phänomen dazu genutzt werden kann um C-dot Verteilungen durch Fluoreszenzmikroskopie nachzuweisen. Dabei kann intensiv-blaue Emission für niedrige Konzentrationen bei 405 nm beobachtet werden. Hohe Partikel-Konzentrationen führen zu einer Emissions-Verschiebung von Blau nach Grün bei Anregung mit 405 nm. Zusätzlich wird die grüne Emission bei Anregung mit 488 nm am intensivsten.

Die Verwendung der C-dots als Fluoreszenz-Kontrastmittel für die Abbildung tierischer Zellen, kann diese spektralen Eigenschaften nutzbar machen. Dabei wurde die lokale Akkumulation von C-dots erhöhter Konzentration der Rot-verschobenen Fluoreszenz-Emission der Partikel in Suspension zugeordnet. Ähnlich wie bei den Studien in Suspension verschiebt sich die Emission von Blau nach Grün für Partikel Ansammlungen in großer Menge bei Anregung mit 405 nm. Desweiteren steigen die Intensitäten der Emission bei Anregung mit 488 und 543 nm. Es hat sich gezeigt, dass lebende Zellen C-dots in niedrigen Konzentrationen mittels Endozytose aufnehmen, was bei Laser-Anregung mit 405 nm in blau lumineszierendem Zytoplasma resultiert. Dabei befinden sich die meisten Partikel in Vesikel. Tote Zellen hingegen weisen grün lumineszierende Zellkerne mit höchster Intensität bei 488 nm Anregung auf. Dies lässt sich auf die Ansammlung von C-dots in den Zellkernen durch Bindung an die darin enthaltene DNA



zurückführen, was die Emissionsverschiebung induziert. Bei Zellen, die die Plasmamembran-Integrität verloren haben und den Zelltod durchlaufen, besteht direkter diffusiver Kontakt zwischen Zellkernen und der Umgebung. Deshalb können C-dots, welche nicht in Vesikeln zurückgehalten werden, frei durch den Kernporen-Komplex diffundieren und sich dort ansammeln. Zusätzlich wird vermutet, dass die Bindung zwischen den C-dots und der DNA die Emissionseigenschaften der Partikel verändert, was zusätzlich für die Unterschiedliche Färbung verantwortlich sein kann.

Durch die Verwendung beider Laser ist es möglich die C-dots für einen Nachweis von lebenden und toten Zellen zu benutzen. Dabei wird der 405 nm Laser für den Nachweis der blauen Lumineszenz im Zytoplasma von lebenden Zellen benutzt, während der 488 nm Laser dazu dient, die grün gefärbten Zellkerne von toten Zellen zu visualisieren. Dieser Nachweis gibt dieselben Informationen wie es ein kommerziell erhältliches Färbe-Set zur Unterscheidungen von lebenden und toten Zellen mittels Mikroskopie tut. Da die Unabhängigkeit der Methode vom Toxin bewiesen wurde, können C-dots für die Bestimmung von  $EC_{50}$ -Werten für ausgewählte Giftstoffe mittels CLSM verwendet werden. Dabei kann das Verhältnis zwischen der grünen und blauen Fluoreszenz-Intensität bei der jeweiligen Laseranregung als Maß für die Zytotoxizität benutzt werden. Die Methode kann für Zytotoxizitäts-Bestimmungen für verschiedenste tierische Zelllinien benutzt werden. Für NRK-Zellen zum Beispiel, stieg das Grün/Blau Intensitäts-Verhältnis, durch die Behandlung mit tBuOOH, von ca. 0.1 für gesunde Zellen zu ca. 1.5 für tote Zellen. Zusätzlich konnte gezeigt werden, dass die Färbung von lebenden und toten Zellen mittels C-dots nicht nur mittels CLSM, sondern auch durch FACS analysiert werden kann. Abgesehen von Zytotoxizitäts-Bestimmungen konnten C-dots auch für die Mikroskopie von lebenden und toten Zellen in MCS als Gewebemodell verwendet werden. Deshalb erscheint die Anwendung der Partikel in Gewebe als vielversprechend.

Neben Lumineszenz hat es sich gezeigt, dass C-dots unter Langzeit-Bestrahlung effektiv reaktive Sauerstoff-Spezies (ROS) erzeugen können. Dabei kombinieren die Partikel mit ihren Eigenschaften alle nötigen Anforderungen eines *Photosensitizers* für die photodynamische Therapie: gute Wasser-Dispergierbarkeit, schnelle Internalisierung in Zellen und effektive ROS Erzeugung. Dies wurde dafür genutzt, NRK Zellen selektiv einem der photodynamischen Therapie nachempfundenen experimentellen Protokoll zu unterziehen. Dies wurde sowohl durch die Anregung von extrazellulären C-dots in Suspension, sowie mit internalisierten Partikeln durchgeführt. Dabei konnte gezeigt werden das neben der nah-UV, auch die Bestrahlung mit blauem Licht Phototoxizität hervorrufen kann. Demzufolge können die Bestrahlungsbedingungen in der Anwendung von C-dots als photodynamisches Agens variiert werden. Die Erzeugung von ROS durch die Bestrahlung internalisierter C-dots führt vermutlich zur Oxidation von Phospholipiden der Vesikel, welche die eingelagerten Partikel im Cytoplasma umgeben. Dies ermöglicht die Freisetzung der C-dots, welche ROS somit in der gesamten Zelle produzieren. Dies

## Summary and Outlook

führt zur Einleitung des Zelltods durch Apoptose, was durch Annexin V Bindungs-Studien bewiesen wurde. Interessanterweise hat es sich gezeigt, dass freigesetzte zellinterne C-dots den Kern von Zellen die den programmierten Zelltod durchlaufen von innen heraus anfärben bevor Annexin V an die Membran dieser Zellen bindet.

In einem „*theranostischem*“ Ansatz wurde diese Fähigkeit der C-dots, Kerne toter Zellen von innen zu färben, gemeinsam mit der zum Zelltod führenden ROS Erzeugung bei Langzeit-Anregung kombiniert. Dabei wurden NRK Zellen mit C-dots durch Kurzzeit-Inkubation beladen. Ausgewählte Zellen wurden daraufhin einer Art photodynamischen Therapie durch Photo-Anregung der internalisierten C-dots für einige Minuten unterzogen. Dies konnte auf großen Zellflächen durch Epilumineszenz-Mikroskopie mittels UV-Anregung (330 – 380 nm) angewandt werden. Derselbe Ansatz wurde auch erfolgreich auf Einzel-Zell-Ebene mittels CLSM 405 nm Laser Anregung durchgeführt. Die darauf folgende Analyse der Zellen mittels CLSM erlaubt eine eindeutige Erfolgskontrolle der Behandlung durch die sich veränderten optischen Eigenschaften der internalisierten C-dots für tote Zellen. Dabei zeigen die zellintern freigesetzten C-dots die selbe Rot-Verschiebung durch die Ansammlung im Kern, wie es für die Färbung von außen beschrieben wurde. Nicht-bestrahlte NRK Zellen weisen ein blau lumineszierendes Zytoplasma bei Anregung mit 405 nm auf, während die Kerne jener Zellen, die der photodynamischen Therapie ausgesetzt waren, grün erscheinen bei Anregung mit 488 nm. Dementsprechend erlauben C-dots nicht nur die aktive *Therapie* von Zielzellen, sondern auch die *Diagnostik* des Erfolgs der Behandlung – *Theranostik*. Studien an MCF-7 MCS als Brustkrebs Tumor-Model haben gezeigt, dass dieser Ansatz auch an solch großen Zellaggregaten durchgeführt werden kann. Aufgrund dessen können C-dots als vielversprechendes theranostisches Agens für die Behandlung von Tumorgewebe in der Krebstherapie in lebenden Organismen angesehen werden.

In Nebenprojekten dieser Arbeit wurden C-dots in andere Nanostrukturen eingebettet und chemisch modifiziert, um die möglichen Anwendungen dieser Partikel zu zeigen. Dabei konnte die Einbettung in Agarose Nanopartikel dazu benutzt werden, Änderungen der Osmolarität durch Aufhebung der Selbst-Löschung der Fluoreszenz optisch zu verfolgen. Dabei erhöhte sich die Fluoreszenzintensität um 15% bei der Zugabe von 1 M eines Osmolyts zum Puffer. Obwohl dies eine schlechte Sensitivität darstellt, soll dies grundsätzliche Anwendungsmöglichkeiten der Partikel zeigen. Zusätzlich wurden Liposome als Transportvehikel für C-dots in NRK Zellen untersucht. Hierbei konnte eine Internalisierung der Partikel durch einen, im Vergleich zu freien C-dots, höchstwahrscheinlich anderen Aufnahmemechanismus beobachtet werden. Diese Untersuchungen können als erste Schritte in Richtung der selektiven Einlagerung von C-dots in Zielzellen angesehen werden. Auch die chemische Modifikation der C-dots ist dazu gedacht prinzipielle Anwendungsmöglichkeiten der Partikel zu zeigen. Die Modifikation mit Ölsäure veränderte die physikochemischen und optischen Eigenschaften

der C-dots drastisch. Als solches konnte die Anlagerung an DNA, zum Beispiel, unterbunden werden. Obwohl die angewandte Thionylchlorid Chemie als harsch angesehen wird, kann diese genutzt werden um andere vielversprechende Modifikationen durchzuführen.

Bezüglich der Widersprüche in der Literatur konnten viele Unterschiede zwischen den physikochemischen und optischen Eigenschaften der bottom-up hergestellten C-dots und der top-down hergestellten QDs ausgearbeitet werden. Zunächst hat es sich gezeigt, dass die Morphologie beider Materialien äußerst unterschiedlich ist. Dabei können C-dots als quasi-sphärisch mit nur wenigen Nanometern im Durchmesser und als amorph angesehen werden. Im Gegensatz dazu weisen QDs eine Flocken-artige Struktur auf in vergleichbarer Höhe, aber in Ausdehnung von 5 - 25 nm. Desweiteren, ist davon auszugehen, dass QDs hauptsächlich aus Kohlenstoff in Graphit-Struktur bestehen, da es sich bei dem Ausgangsmaterial um Graphit handelt. Beide Materialien zeigen eine Verschiebung ihrer Fluoreszenz-Emission mit Variation der Anregungs-Wellenlänge. Jedoch scheint es, dass C-dots nur wenige emittierende Hauptspezies besitzen, welche deren optischen Eigenschaften dominieren. Im Gegensatz dazu weisen QDs eine direkte Korrelation zwischen Anregung und Emission auf. Dies könnte darauf zurückzuführen sein, dass diese eine beliebig hohe Anzahl verschiedener emittierender Spezies besitzen. Zusammenfassend sind beide Materialien eng verwandt betreffend der Zusammensetzung und Funktionalisierung, aber zeigen auch eindeutige Unterschiede. Als solches ist eine Unterscheidung zwischen beiden Materialien, C-dots und QDs, ratsam.

### 8.3 Conclusion and Outlook

Concluding, the studies on C-dots in this work have given insight on the unique properties and manifold potential applications of this material. Further utilizations of C-dots in bioanalysis are suggested to involve chemical modifications. These could be used to address target cells or cell structures. Together with the changing emission properties for locally accumulated C-dots, as described, targets could be easily identified via CLSM imaging. Thereby, the particles could be modified with ligands, even under harsh chemical conditions, addressing receptors on the cell membranes. Recently, first attempts were successful in this direction for other C-dot preparations. As such, folate-modified C-dots for example were used for the distinguishing of cancer cells via imaging (Liu *et al.* 2015). A similar approach with C-dots was used to mediate drug delivery and selectively target cancer cells for a selective treatment of these cells (Mewada *et al.* 2014).

For future applications *in vitro* and *in vivo*, several uncertainties have to be investigated: (i) possible cellular degradation and (ii) exclusion of C-dots from living organisms have to be studied. In this respect research is at the very beginning.

Especially promising seems the application of C-dots as photodynamic therapy agent. The studies on the selective treatment of mammalian cells in this work rely on the local photo-generation of ROS through the irradiation of C-dot loaded cells. Although the loading with C-dots has proven to be only marginal invasive for NRK cells, an even more specific therapeutic approach with C-dots is possible. Thereby, the accomplishment of ROS generation by C-dots may only apply for cells with internalized particles. As such, only specific individuals within a cell population should be loaded with C-dots and the whole population could be irradiated. Accordingly, ROS generation and subsequent cell death would only be induced for target cells, leaving the rest of the population completely unharmed. The selected loading of target cells with C-dots could be accomplished via ligand-tagged liposomes with encapsulated C-dots. In this work, it was already shown that liposomes are suitable as delivery vehicle for C-dots into mammalian cells. This could be utilized to induce incorporation of these C-dot loaded liposomes only in target (cancer) cells. Subsequent irradiation is suggested to release the particles into the whole cell body through photo-oxidation of the surrounding phospholipids. Further irradiation would induce cell death through oxidative stress via photo-generation of ROS in the whole cell. The effort of this treatment could be studied through the emission shift of the dead cells' nuclei, as described in this work's "theranostic" approach based on C-dots. The principle of the delivery path via tagged liposomes is well established and described manifold in literature (Lee *et al.* 1995; Park 2002). Furthermore, it has already been shown that Q-dots, which share several properties of C-dots, for example may be selectively transferred into cancer cells for imaging or therapy (Muthu *et al.* 2012).

Future (bio-)applications of C-dots in general, are surely going to take the decisive step from *in vitro* to *in vivo* studies to investigate the particles potential for diagnostics and therapy. Yet, several reports for the application of C-dots in living organisms were made in literature, but have to be considered as the very beginning. As such, the imaging *in vivo*, utilizing the C-dots unique optical properties will be one major application field. (Luo *et al.* 2013; Huang *et al.* 2014). However the greatest potential of C-dots may be seen in cancer therapy and theranostic applications, as indicated in this work. In this field, recently promising reports were made on the successful tumor treatment in living organisms, using C-dots within photodynamic therapies (Choi *et al.* 2014; Hola *et al.* 2014).

The applicability of C-dots for imaging in tissues was already proven on MCS as model. As such, also the “theranostic” approach in tissues and living organisms, based on the ROS generation ability of the particles is suggested to be promising for the utilization in cancer therapy.



## 9 References

- Alivisatos, A. P. (1996). "Semiconductor clusters, nanocrystals, and quantum dots." Science **271**(5251): 933-937.
- Alivisatos, A. P. *et al.* (2005). "Quantum dots as cellular probes." Annual Review of Biomedical Engineering **7**: 55-76.
- Allen, M. J. *et al.* (2010). "Honeycomb Carbon: A Review of Graphene." Chemical Reviews **110**(1): 132-145.
- Anderson, R. G. W. (1998). "The caveolae membrane system." Annual Review of Biochemistry **67**: 199-225.
- Azzazy, H. M. E. *et al.* (2007). "From diagnostics to therapy: Prospects of quantum dots." Clinical Biochemistry **40**(13-14): 917-927.
- Bacon, M. *et al.* (2014). "Graphene Quantum Dots." Particle & Particle Systems Characterization **31**(4): 415-428.
- Bakalova, R. *et al.* (2004). "Quantum dots as photosensitizers?" Nature Biotechnology **22**(11): 1360-1361.
- Baker, S. N. *et al.* (2010). "Luminescent Carbon Nanodots: Emergent Nanolights." Angewandte Chemie-International Edition **49**(38): 6726-6744.
- Bao, L. *et al.* (2011). "Electrochemical Tuning of Luminescent Carbon Nanodots: From Preparation to Luminescence Mechanism." Advanced Materials **23**(48): 5801-+.
- Barbosa, C. D. D. S. *et al.* (2015). "Carbon Dots (C-dots) from Cow Manure with Impressive Subcellular Selectivity Tuned by Simple Chemical Modification." Chemistry-a European Journal **21**(13): 5055-5060.
- Barker, G. *et al.* (1981). "Identification of two strains of cultured canine renal epithelial cells (MDCK cells) which display entirely different physiological properties." Q J Exp Physiol **66**(1): 61-72.
- Becerril, H. A. *et al.* (2008). "Evaluation of solution-processed reduced graphene oxide films as transparent conductors." Acs Nano **2**(3): 463-470.
- Bechet, D. *et al.* (2008). "Nanoparticles as vehicles for delivery of photodynamic therapy agents." Trends in Biotechnology **26**(11): 612-621.
- Bergius, F. (1913). "Die Anwendung hoher Drucke bei chemischen Vorgängen und eine Nachbildung des Entstehungsprozesses der Steinkohle." Verlag Wilhelm Knapp, Germany.
- Berne, B. J. *et al.* (2000). Dynamic Light Scattering, Courier Dover Publications.
- Bohmert, L. *et al.* (2012). "Cytotoxicity of peptide-coated silver nanoparticles on the human intestinal cell line Caco-2." Archives of Toxicology **86**(7): 1107-1115.
- Boukamp, P. *et al.* (1988). "Normal Keratinization in a Spontaneously Immortalized Aneuploid Human Keratinocyte Cell-Line." Journal of Cell Biology **106**(3): 761-771.

## References

- Bourlinos, A. B. *et al.* (2008a). "Photoluminescent carbogenic dots." Chemistry of Materials **20**(14): 4539-4541.
- Bourlinos, A. B. *et al.* (2008b). "Surface functionalized carbogenic quantum dots." Small **4**(4): 455-458.
- Bourlinos, A. B. *et al.* (2012). "Luminescent Surface Quaternized Carbon Dots." Chemistry of Materials **24**(1): 6-8.
- Brus, L. (1991). "Quantum Crystallites and Nonlinear Optics." Applied Physics a-Materials Science & Processing **53**(6): 465-474.
- Byrappa, K. *et al.* (2013). Handbook of hydrothermal technology Oxford; Waltham, Mass., William Andrew.
- Cao, L. *et al.* (2007). "Carbon dots for multiphoton bioimaging." Journal of the American Chemical Society **129**(37): 11318-+.
- Chang, Y. L. *et al.* (2011). "In vitro toxicity evaluation of graphene oxide on A549 cells." Toxicology Letters **200**(3): 201-210.
- Chatterjee, D. K. *et al.* (2008). "Nanoparticles in photodynamic therapy: an emerging paradigm." Adv Drug Deliv Rev **60**(15): 1627-1637.
- Chen, C. S. *et al.* (2006). "Liposome encapsulation of fluorescent nanoparticles: Quantum dots and silica nanoparticles." Journal of Nanoparticle Research **8**(6): 1033-1038.
- Chen, R. F. *et al.* (1988). "Mechanism of Fluorescence Concentration Quenching of Carboxyfluorescein in Liposomes - Energy-Transfer to Nonfluorescent Dimers." Analytical Biochemistry **172**(1): 61-77.
- Cheng, Z. L. *et al.* (2012). "Multifunctional Nanoparticles: Cost Versus Benefit of Adding Targeting and Imaging Capabilities." Science **338**(6109): 903-910.
- Chithrani, B. D. *et al.* (2006). "Determining the size and shape dependence of gold nanoparticle uptake into mammalian cells." Nano Letters **6**(4): 662-668.
- Cho, S. J. *et al.* (2007). "Long-term exposure to CdTe quantum dots causes functional impairments in live cells." Langmuir **23**(4): 1974-1980.
- Cho, W. S. *et al.* (2014). "Surface functionalization affects the zeta potential, coronal stability and membranolytic activity of polymeric nanoparticles." Nanotoxicology **8**(2): 202-211.
- Choi, Y. *et al.* (2014). "Highly Biocompatible Carbon Nanodots for Simultaneous Bioimaging and Targeted Photodynamic Therapy In Vitro and In Vivo." Advanced Functional Materials **24**(37): 5781-5789.
- Christensen, I. L. *et al.* (2011). "Carbon Dots as Antioxidants and Prooxidants." Journal of Biomedical Nanotechnology **7**(5): 667-676.
- Clarke, S. J. *et al.* (2006). "Photophysics of dopamine-modified quantumdots and effects on biological systems." Nature Materials **5**(5): 409-417.
- da Silva, J. C. G. E. *et al.* (2011). "Analytical and bioanalytical applications of carbon dots." Trac-Trends in Analytical Chemistry **30**(8): 1327-1336.
- Das, B. *et al.* (2014). "Carbon nanodots from date molasses: new nanolights for the in vitro scavenging of reactive oxygen species." Journal of Materials Chemistry B **2**(39): 6839-6847.



- De Jong, K. P. *et al.* (2000). "Carbon nanofibers: Catalytic synthesis and applications." Catalysis Reviews-Science and Engineering **42**(4): 481-510.
- Demchenko, A. P. *et al.* (2013). "Novel fluorescent carbonic nanomaterials for sensing and imaging." Methods and Applications in Fluorescence **1**(4).
- Deng, Y. H. *et al.* (2013). "Long lifetime pure organic phosphorescence based on water soluble carbon dots." Chemical Communications **49**(51): 5751-5753.
- Derfus, A. M. *et al.* (2004). "Probing the cytotoxicity of semiconductor quantum dots." Nano Letters **4**(1): 11-18.
- DeRosa, M. C. *et al.* (2002). "Photosensitized singlet oxygen and its applications." Coordination Chemistry Reviews **233**: 351-371.
- Dikin, D. A. *et al.* (2007). "Preparation and characterization of graphene oxide paper." Nature **448**(7152): 457-460.
- Ding, C. *et al.* (2013). "Functional Surface Engineering of C-Dots for Fluorescent Biosensing and in Vivo Bioimaging." Acc Chem Res.
- Dolmans, D. E. J. G. J. *et al.* (2003). "Photodynamic therapy for cancer." Nature Reviews Cancer **3**(5): 380-387.
- Dong, Y. *et al.* (2013a). "Carbon-Based Dots Co-doped with Nitrogen and Sulfur for High Quantum Yield and Excitation-Independent Emission." Angew Chem Int Ed Engl **52**(30): 7800-7804.
- Dong, Y. Q. *et al.* (2013b). "Carbon-Based Dots Co-doped with Nitrogen and Sulfur for High Quantum Yield and Excitation-Independent Emission." Angewandte Chemie-International Edition **52**(30): 7800-7804.
- Du, F. K. *et al.* (2013). "Carbon dots-based fluorescent probes for sensitive and selective detection of iodide." Microchimica Acta **180**(5-6): 453-460.
- Du, F. Y. *et al.* (2014). "Nitrogen-doped carbon dots with heterogeneous multi-layered structures." Rsc Advances **4**(71): 37536-37541.
- Edwards, K. A. *et al.* (2006). "Liposomes in analyses." Talanta **68**(5): 1421-1431.
- Fang, Y. X. *et al.* (2012). "Easy Synthesis and Imaging Applications of Cross-Linked Green Fluorescent Hollow Carbon Nanoparticles." Acs Nano **6**(1): 400-409.
- Faute, M. A. D. *et al.* (2002). "Distinctive alterations of invasiveness, drug resistance and cell-cell organization in 3D-cultures of MCF-7, a human breast cancer cell line, and its multidrug resistant variant." Clinical & Experimental Metastasis **19**(2): 161-168.
- Fischer, S. A. *et al.* (2011). "Excited states and optical absorption of small semiconducting clusters: Dopants, defects and charging." Chemical Science **2**(3): 400-406.
- Foote, C. S. (1991). "Definition of Type-I and Type-II Photosensitized Oxidation." Photochemistry and Photobiology **54**(5): 659-659.
- Fortina, P. *et al.* (2005). "Nanobiotechnology: the promise and reality of new approaches to molecular recognition." Trends in Biotechnology **23**(4): 168-173.
- Fu, M. *et al.* (2015). "Carbon Dots: A Unique Fluorescent Cocktail of Polycyclic Aromatic Hydrocarbons." Nano Lett.

## References

- Fujino, T. *et al.* (2002). "Phase and structural change of carbonized wood materials by hydrothermal treatment." Solid State Ionics **151**(1-4): 197-203.
- Gao, X. H. *et al.* (2005). "In vivo molecular and cellular imaging with quantum dots." Current Opinion in Biotechnology **16**(1): 63-72.
- Ge, J. C. *et al.* (2014). "A graphene quantum dot photodynamic therapy agent with high singlet oxygen generation." Nature Communications **5**.
- Geiser, M. *et al.* (2005). "Ultrafine particles cross cellular membranes by nonphagocytic mechanisms in lungs and in cultured cells." Environmental Health Perspectives **113**(11): 1555-1560.
- Gerion, D. *et al.* (2001). "Synthesis and properties of biocompatible water-soluble silica-coated CdSe/ZnS semiconductor quantum dots." Journal of Physical Chemistry B **105**(37): 8861-8871.
- Ghosh, S. *et al.* (2014). "Photoluminescence of Carbon Nanodots: Dipole Emission Centers and Electron-Phonon Coupling." Nano Letters **14**(10): 5656-5661.
- Giaever, I. *et al.* (1984). "Monitoring Fibroblast Behavior in Tissue-Culture with an Applied Electric-Field." Proceedings of the National Academy of Sciences of the United States of America-Biological Sciences **81**(12): 3761-3764.
- Gogotsi, Y. *et al.* (2000). "Hydrothermal synthesis of multiwall carbon nanotubes." Journal of Materials Research **15**(12): 2591-2594.
- Goldenthal, K. L. *et al.* (1984). "Initial Steps in Receptor-Mediated Endocytosis - the Influence of Temperature on the Shape and Distribution of Plasma-Membrane Clathrin-Coated Pits in Cultured Mammalian-Cells." Experimental Cell Research **152**(2): 558-564.
- Greiner, N. R. *et al.* (1988). "Diamonds in Detonation Soot." Nature **333**(6172): 440-442.
- Guo, C. Z. *et al.* (2012). "Melamine causes apoptosis of rat kidney epithelial cell line (NRK-52e cells) via excessive intracellular ROS (reactive oxygen species) and the activation of p38 MAPK pathway." Cell Biology International **36**(4): 383-389.
- Hanada, S. *et al.* (2014). "Cell- Based in Vitro Blood-Brain Barrier Model Can Rapidly Evaluate Nanoparticles' Brain Permeability in Association with Particle Size and Surface Modification." International Journal of Molecular Sciences **15**(2): 1812-1825.
- He, X. D. *et al.* (2011). "Water soluble carbon nanoparticles: Hydrothermal synthesis and excellent photoluminescence properties." Colloids and Surfaces B- Biointerfaces **87**(2): 326-332.
- Hodge, J. E. (1979). "Citation Classic - Dehydrated Foods - Chemistry of Browning Reactions in Model Systems." Current Contents/Agriculture Biology & Environmental Sciences(12): 10-10.
- Hoffmann, M. R. *et al.* (1995). "Environmental Applications of Semiconductor Photocatalysis." Chemical Reviews **95**(1): 69-96.
- Hola, K. *et al.* (2014). "Carbon dots-Emerging light emitters for bioimaging, cancer therapy and optoelectronics." Nano Today **9**(5): 590-603.

- Horobin, R. W. *et al.* (2002). Conn's Biological Stains: A Handbook of Dyes, Stains and Fluorochromes for Use in Biology and Medicine, BIOS Scientific Publ.
- Hsu, P. C. *et al.* (2012a). "Synthesis of high-quality carbon nanodots from hydrophilic compounds: role of functional groups." Chemical Communications **48**(33): 3984-3986.
- Hsu, P. C. *et al.* (2013). "Extremely high inhibition activity of photoluminescent carbon nanodots toward cancer cells." Journal of Materials Chemistry B **1**(13): 1774-1781.
- Hsu, P. C. *et al.* (2012b). "Synthesis and analytical applications of photoluminescent carbon nanodots." Green Chemistry **14**(4): 917-920.
- Hu, B. *et al.* (2010). "Engineering Carbon Materials from the Hydrothermal Carbonization Process of Biomass." Advanced Materials **22**(7): 813-828.
- Huang, P. *et al.* (2012). "Light-Triggered Theranostics Based on Photosensitizer-Conjugated Carbon Dots for Simultaneous Enhanced-Fluorescence Imaging and Photodynamic Therapy." Advanced Materials **24**(37): 5104-5110.
- Huang, X. L. *et al.* (2010). "The effect of the shape of mesoporous silica nanoparticles on cellular uptake and cell function." Biomaterials **31**(3): 438-448.
- Huang, Y. F. *et al.* (2014). "One- Pot Synthesis of Highly Luminescent Carbon Quantum Dots and Their Nontoxic Ingestion by Zebrafish for In Vivo Imaging." Chemistry-a European Journal **20**(19): 5640-5648.
- Hummers, W. S. O., R. E. (1958). "Preparation of graphitic oxide." Journal of the American Chemical Society **80**(6): 1339-1339.
- Iijima, S. (1991). "Helical Microtubules of Graphitic Carbon." Nature **354**(6348): 56-58.
- Jaiswal, J. K. *et al.* (2004). "Use of quantum dots for live cell imaging." Nature Methods **1**(1): 73-78.
- Jawad, H. *et al.* (2011). "Assessment of cellular toxicity of TiO<sub>2</sub> nanoparticles for cardiac tissue engineering applications." Nanotoxicology **5**(3): 372-380.
- Jiang, J. *et al.* (2012). "Amino acids as the source for producing carbon nanodots: microwave assisted one-step synthesis, intrinsic photoluminescence property and intense chemiluminescence enhancement." Chemical Communications **48**(77): 9634-9636.
- Jin, F. M. *et al.* (2011). "Rapid and highly selective conversion of biomass into value-added products in hydrothermal conditions: chemistry of acid/base-catalysed and oxidation reactions." Energy & Environmental Science **4**(2): 382-397.
- Juzenas, P. *et al.* (2013). "Photoactivatable carbon nanodots for cancer therapy." Applied Physics Letters **103**(6).
- Kabyemela, B. M. *et al.* (1999). "Glucose and fructose decomposition in subcritical and supercritical water: Detailed reaction pathway, mechanisms, and kinetics." Industrial & Engineering Chemistry Research **38**(8): 2888-2895.
- Kharin, A. *et al.* (2015). "Carbon fluoroxide nanoparticles as fluorescent labels and sonosensitizers for theranostic applications " Science and Technology of Advanced Materials **16**(4).

## References

- Kolossov, E. *et al.* (2006). "Engraftment of engineered ES cell-derived cardiomyocytes but not BM cells restores contractile function to the infarcted myocardium." Journal of Experimental Medicine **203**(10): 2315-2327.
- Kolossov, E. *et al.* (2005). "Identification and characterization of embryonic stem cell-derived pacemaker and atrial cardiomyocytes." Faseb Journal **19**(1): 577-+.
- Kong, W. Q. *et al.* (2014). "High-bright fluorescent carbon dots and their application in selective nucleoli staining." Journal of Materials Chemistry B **2**(31): 5077-5082.
- Kroto, H. W. *et al.* (1985). "C-60 - Buckminsterfullerene." Nature **318**(6042): 162-163.
- Kummrow, A. *et al.* (2013). "Quantitative assessment of cell viability based on flow cytometry and microscopy." Cytometry Part A **83A**(2): 197-204.
- Kwon, W. *et al.* (2012). "Formation of highly luminescent nearly monodisperse carbon quantum dots via emulsion-templated carbonization of carbohydrates." Rsc Advances **2**(30): 11223-11226.
- Lai, C. W. *et al.* (2012). "Facile synthesis of highly emissive carbon dots from pyrolysis of glycerol; gram scale production of carbon dots/mSiO(2) for cell imaging and drug release." Journal of Materials Chemistry **22**(29): 14403-14409.
- Lai, L. F. *et al.* (2011). "One-step synthesis of NH<sub>2</sub>-graphene from in situ graphene-oxide reduction and its improved electrochemical properties." Carbon **49**(10): 3250-3257.
- Lajoie, P. *et al.* (2007). "Regulation of raft-dependent endocytosis." Journal of Cellular and Molecular Medicine **11**(4): 644-653.
- Lakowicz, J. R. (2006). Principles of Fluorescence Spectroscopy, **Third Edition**. Springer.
- Lash, L. H. *et al.* (2002). "Protection of NRK-52E cells, a rat renal proximal tubular cell line, from chemical-induced apoptosis by overexpression of a mitochondrial glutathione transporter." Journal of Pharmacology and Experimental Therapeutics **303**(2): 476-486.
- Lee, R. J. *et al.* (1995). "Folate-Mediated Tumor-Cell Targeting of Liposome-Entrapped Doxorubicin in-Vitro." Biochimica Et Biophysica Acta-Biomembranes **1233**(2): 134-144.
- Li, C. L. *et al.* (2014a). "Carbon dots prepared from ginger exhibiting efficient inhibition of human hepatocellular carcinoma cells." Journal of Materials Chemistry B **2**(28): 4564-4571.
- Li, H. T. *et al.* (2010a). "Water-Soluble Fluorescent Carbon Quantum Dots and Photocatalyst Design." Angewandte Chemie-International Edition **49**(26): 4430-4434.
- Li, H. T. *et al.* (2011a). "One-step ultrasonic synthesis of water-soluble carbon nanoparticles with excellent photoluminescent properties." Carbon **49**(2): 605-609.
- Li, H. T. *et al.* (2012a). "Carbon nanodots: synthesis, properties and applications." Journal of Materials Chemistry **22**(46): 24230-24253.

- Li, L. L. *et al.* (2013). "Focusing on luminescent graphene quantum dots: current status and future perspectives." Nanoscale **5**(10): 4015-4039.
- Li, N. *et al.* (2012b). "Biodistribution study of carbogenic dots in cells and in vivo for optical imaging." Journal of Nanoparticle Research **14**(10).
- Li, Q. *et al.* (2010b). "Photoluminescent Carbon Dots as Biocompatible Nanoprobes for Targeting Cancer Cells in Vitro." Journal of Physical Chemistry C **114**(28): 12062-12068.
- Li, X. M. *et al.* (2014b). "Engineering surface states of carbon dots to achieve controllable luminescence for solid-luminescent composites and sensitive Be<sup>2+</sup> detection." Scientific Reports **4**.
- Li, X. Y. *et al.* (2011b). "Preparation of carbon quantum dots with tunable photoluminescence by rapid laser passivation in ordinary organic solvents." Chemical Communications **47**(3): 932-934.
- Li, Y. *et al.* (2012c). "Nitrogen-Doped Graphene Quantum Dots with Oxygen-Rich Functional Groups." Journal of the American Chemical Society **134**(1): 15-18.
- Liang, Q. H. *et al.* (2013). "Easy synthesis of highly fluorescent carbon quantum dots from gelatin and their luminescent properties and applications." Carbon **60**: 421-428.
- Limonciel, A. *et al.* (2012). "Oxidative stress induced by potassium bromate exposure results in altered tight junction protein expression in renal proximal tubule cells." Archives of Toxicology **86**(11): 1741-1751.
- Lin, Z. *et al.* (2012). "Classical oxidant induced chemiluminescence of fluorescent carbon dots." Chemical Communications **48**(7): 1051-1053.
- Liu, C. J. *et al.* (2011a). "One-step synthesis of surface passivated carbon nanodots by microwave assisted pyrolysis for enhanced multicolor photoluminescence and bioimaging." Journal of Materials Chemistry **21**(35): 13163-13167.
- Liu, C. J. *et al.* (2012a). "Nano-carrier for gene delivery and bioimaging based on carbon dots with PEI-passivation enhanced fluorescence." Biomaterials **33**(13): 3604-3613.
- Liu, H. P. *et al.* (2007). "Fluorescent carbon nanoparticles derived from candle soot." Angewandte Chemie-International Edition **46**(34): 6473-6475.
- Liu, J. M. *et al.* (2012b). "Highly selective and sensitive detection of Cu<sup>2+</sup> with lysine enhancing bovine serum albumin modified-carbon dots fluorescent probe." Analyst **137**(11): 2637-2642.
- Liu, Q. L. *et al.* (2015). "Distinguish cancer cells based on targeting turn-on fluorescence imaging by folate functionalized green emitting carbon dots." Biosensors & Bioelectronics **64**: 119-125.
- Liu, R. L. *et al.* (2011b). "Bottom-Up Fabrication of Photoluminescent Graphene Quantum Dots with Uniform Morphology." Journal of the American Chemical Society **133**(39): 15221-15223.
- Liu, R. L. *et al.* (2009). "An Aqueous Route to Multicolor Photoluminescent Carbon Dots Using Silica Spheres as Carriers." Angewandte Chemie-International Edition **48**(25): 4598-4601.

## References

- Liu, S. *et al.* (2012c). "Hydrothermal Treatment of Grass: A Low-Cost, Green Route to Nitrogen-Doped, Carbon-Rich, Photoluminescent Polymer Nanodots as an Effective Fluorescent Sensing Platform for Label-Free Detection of Cu(II) Ions." Advanced Materials **24**(15): 2037-2041.
- Liu, Y. S. *et al.* (2014a). "One-step green synthesized fluorescent carbon nanodots from bamboo leaves for copper(II) ion detection." Sensors and Actuators B-Chemical **196**: 647-652.
- Liu, Z. X. *et al.* (2014b). "Effects of Internalized Gold Nanoparticles with Respect to Cytotoxicity and Invasion Activity in Lung Cancer Cells." Plos One **9**(6).
- Long, Y. M. *et al.* (2012). "Shifting and non-shifting fluorescence emitted by carbon nanodots." Journal of Materials Chemistry **22**(13): 5917-5920.
- Lu, C. H. *et al.* (2002). "Effect of t-butyl hydroperoxide on Ca<sup>2+</sup> movement in PC12 pheochromocytoma cells." Chinese Journal of Physiology **45**(2): 51-56.
- Lu, J. *et al.* (2009). "One-Pot Synthesis of Fluorescent Carbon Nanoribbons, Nanoparticles, and Graphene by the Exfoliation of Graphite in Ionic Liquids." Acs Nano **3**(8): 2367-2375.
- Lu, W. B. *et al.* (2012). "Economical, Green Synthesis of Fluorescent Carbon Nanoparticles and Their Use as Probes for Sensitive and Selective Detection of Mercury(II) Ions." Analytical Chemistry **84**(12): 5351-5357.
- Luijckx, G. C. A. *et al.* (1995). "The Role of Deoxyhexonic Acids in the Hydrothermal Decarboxylation of Carbohydrates." Carbohydrate Research **272**(2): 191-202.
- Luo, P. J. G. *et al.* (2013). "Carbon "quantum" dots for optical bioimaging." Journal of Materials Chemistry B **1**(16): 2116-2127.
- Ma, Z. *et al.* (2012). "One-step ultrasonic synthesis of fluorescent N-doped carbon dots from glucose and their visible-light sensitive photocatalytic ability." New Journal of Chemistry **36**(4): 861-864.
- Markovic, Z. M. *et al.* (2012). "Graphene quantum dots as autophagy-inducing photodynamic agents." Biomaterials **33**(29): 7084-7092.
- Medintz, I. L. *et al.* (2005). "Quantum dot bioconjugates for imaging, labelling and sensing." Nature Materials **4**(6): 435-446.
- Mewada, A. *et al.* (2014). "Swarming carbon dots for folic acid mediated delivery of doxorubicin and biological imaging." Journal of Materials Chemistry B **2**(6): 698-705.
- Mitra, S. *et al.* (2012). "Rapid microwave synthesis of fluorescent hydrophobic carbon dots." Rsc Advances **2**(32): 12129-12131.
- Mosmann, T. (1983). "Rapid Colorimetric Assay for Cellular Growth and Survival - Application to Proliferation and Cyto-Toxicity Assays." Journal of Immunological Methods **65**(1-2): 55-63.
- Mou, Y. C. *et al.* (2015). "Effects of 2,3-dimercaptosuccinic acid modified Fe<sub>2</sub>O<sub>3</sub> nanoparticles on microstructure and biological activity of cardiomyocytes." Rsc Advances **5**(25): 19493-19501.
- Mueller-Klieser, W. (1997). "Three-dimensional cell cultures: from molecular mechanisms to clinical applications." Am J Physiol **273**(4 Pt 1): C1109-1123.

- Mui, B. L. S. *et al.* (1993). "Osmotic Properties of Large Unilamellar Vesicles Prepared by Extrusion." Biophysical Journal **64**(2): 443-453.
- Muthu, M. S. *et al.* (2012). "Theranostic liposomes of TPGS coating for targeted co-delivery of docetaxel and quantum dots." Biomaterials **33**(12): 3494-3501.
- Nandi, S. *et al.* (2014). "Membrane analysis with amphiphilic carbon dots." Chemical Communications **50**(71): 10299-10302.
- Nethi, S. K. *et al.* (2014). "Bioconjugated gold nanoparticles accelerate the growth of new blood vessels through redox signaling." Chemical Communications **50**(92): 14367-14370.
- Novoselov, K. S. *et al.* (2004). "Electric field effect in atomically thin carbon films." Science **306**(5696): 666-669.
- Ohta, T. *et al.* (2006). "Controlling the electronic structure of bilayer graphene." Science **313**(5789): 951-954.
- Oleinick, N. L. *et al.* (1998). "The photobiology of photodynamic therapy: Cellular targets and mechanisms." Radiation Research **150**(5): S146-S156.
- Opp, D. *et al.* (2009). "Use of electric cell-substrate impedance sensing to assess in vitro cytotoxicity." Biosensors & Bioelectronics **24**(8): 2625-2629.
- Pan, D. Y. *et al.* (2010a). "Observation of pH-, solvent-, spin-, and excitation-dependent blue photoluminescence from carbon nanoparticles." Chemical Communications **46**(21): 3681-3683.
- Pan, D. Y. *et al.* (2010b). "Hydrothermal Route for Cutting Graphene Sheets into Blue-Luminescent Graphene Quantum Dots." Advanced Materials **22**(6): 734-+.
- Park, J. W. (2002). "Liposome-based drug delivery in breast cancer treatment." Breast Cancer Research **4**(3): 93-97.
- Patzke, G. R. *et al.* (2002). "Oxidic nanotubes and nanorods - Anisotropic modules for a future nanotechnology." Angewandte Chemie-International Edition **41**(14): 2446-2461.
- Pawley, J. B. (2006). Handbook of Biological Confocal Microscopy, **3rd edition**. Springer.
- Peng, H. *et al.* (2009). "Simple Aqueous Solution Route to Luminescent Carbogenic Dots from Carbohydrates." Chemistry of Materials **21**(23): 5563-5565.
- Pernodet, N. *et al.* (2006). "Adverse effects of citrate/gold nanoparticles on human dermal fibroblasts." Small **2**(6): 766-773.
- Peters, M. F. *et al.* (2015). "Human Stem Cell-Derived Cardiomyocytes in Cellular Impedance Assays: Bringing Cardiotoxicity Screening to the Front Line." Cardiovascular Toxicology **15**(2): 127-139.
- Puvvada, N. *et al.* (2012). "Synthesis of biocompatible multicolor luminescent carbon dots for bioimaging applications." Science and Technology of Advanced Materials **13**(4).
- Qian, Z. M. *et al.* (2002). "Targeted drug delivery via the transferrin receptor-mediated endocytosis pathway." Pharmacological Reviews **54**(4): 561-587.

## References

- Qiao, Z. A. *et al.* (2010). "Commercially activated carbon as the source for producing multicolor photoluminescent carbon dots by chemical oxidation." Chemical Communications **46**(46): 8812-8814.
- Qu, K. G. *et al.* (2013). "Carbon Dots Prepared by Hydrothermal Treatment of Dopamine as an Effective Fluorescent Sensing Platform for the Label-Free Detection of Iron(III) Ions and Dopamine." Chemistry-a European Journal **19**(22): 7243-7249.
- Qu, S. N. *et al.* (2012). "A Biocompatible Fluorescent Ink Based on Water-Soluble Luminescent Carbon Nanodots." Angewandte Chemie-International Edition **51**(49): 12215-12218.
- Rabenau, A. (1985). "The Role of Hydrothermal Synthesis in Preparative Chemistry." Angewandte Chemie-International Edition in English **24**(12): 1026-1040.
- Ray, S. C. *et al.* (2009). "Fluorescent Carbon Nanoparticles: Synthesis, Characterization, and Bioimaging Application." Journal of Physical Chemistry C **113**(43): 18546-18551.
- Richardson, J. C. W. *et al.* (1981). "Identification of 2 Strains of Mdkc Cells Which Resemble Separate Nephron Tubule Segments." Biochimica Et Biophysica Acta **673**(1): 26-36.
- Ritter, D. *et al.* (1999). "Development of a cell culture model system for routine testing of substances inducing oxidative stress." Toxicology in Vitro **13**(4-5): 745-751.
- Robertson, J. (1996). "Recombination and photoluminescence mechanism in hydrogenated amorphous carbon." Physical Review B **53**(24): 16302-16305.
- Rosenthal, S. J. *et al.* (2011). "Biocompatible Quantum Dots for Biological Applications." Chemistry & Biology **18**(1): 10-24.
- Ryu, J. *et al.* (2010). "Hydrothermal preparation of carbon microspheres from mono-saccharides and phenolic compounds." Carbon **48**(7): 1990-1998.
- Sahu, S. *et al.* (2012). "Simple one-step synthesis of highly luminescent carbon dots from orange juice: application as excellent bio-imaging agents." Chemical Communications **48**(70): 8835-8837.
- Salinas-Castillo, A. *et al.* (2013). "Carbon dots for copper detection with down and upconversion fluorescent properties as excitation sources." Chemical Communications **49**(11): 1103-1105.
- Salvador, F. *et al.* (2007). "C/H<sub>2</sub>O reaction under Supercritical conditions and their repercussions in the preparation of activated carbon." Journal of Physical Chemistry C **111**(37): 14011-14020.
- Schmid, S. L. *et al.* (1990). "Atp Is Required for Receptor-Mediated Endocytosis in Intact-Cells." Journal of Cell Biology **111**(6): 2307-2318.
- Serdiuk, T. *et al.* (2012). "Charge-driven selective localization of fluorescent nanoparticles in live cells." Nanotechnology **23**(31).
- Sevilla, M. *et al.* (2009a). "Chemical and Structural Properties of Carbonaceous Products Obtained by Hydrothermal Carbonization of Saccharides." Chemistry-a European Journal **15**(16): 4195-4203.



- Sevilla, M. *et al.* (2009b). "The production of carbon materials by hydrothermal carbonization of cellulose." Carbon **47**(9): 2281-2289.
- Shen, J. H. *et al.* (2012a). "Graphene quantum dots: emergent nanolights for bioimaging, sensors, catalysis and photovoltaic devices." Chemical Communications **48**(31): 3686-3699.
- Shen, R. *et al.* (2012b). "Dramatic Fluorescence Enhancement of Bare Carbon Dots through Facile Reduction Chemistry." Chemphyschem **13**(15): 3549-3555.
- Shi, W. *et al.* (2012). "A Tunable Ratiometric pH Sensor Based on Carbon Nanodots for the Quantitative Measurement of the Intracellular pH of Whole Cells." Angewandte Chemie-International Edition **51**(26): 6432-6435.
- Shum, P. *et al.* (2001). "Phototriggering of liposomal drug delivery systems." Advanced Drug Delivery Reviews **53**(3): 273-284.
- Simoës, E. F. *et al.* (2014). "Carbon dots from tryptophan doped glucose for peroxynitrite sensing." Anal Chim Acta **852**: 174-180.
- Song, Y. B. *et al.* (2014). "Bioimaging based on fluorescent carbon dots." Rsc Advances **4**(52): 27184-27200.
- Song, Y. C. *et al.* (2012). "Fluorescent carbon nanodots conjugated with folic acid for distinguishing folate-receptor-positive cancer cells from normal cells." Journal of Materials Chemistry **22**(25): 12568-12573.
- Stankovich, S. *et al.* (2007). "Synthesis of graphene-based nanosheets via chemical reduction of exfoliated graphite oxide." Carbon **45**(7): 1558-1565.
- Stern, S. T. *et al.* (2008). "Induction of autophagy in porcine kidney cells by quantum dots: A common cellular response to nanomaterials?" Toxicological Sciences **106**(1): 140-152.
- Sun, Y. P. *et al.* (2006). "Quantum-sized carbon dots for bright and colorful photoluminescence." Journal of the American Chemical Society **128**(24): 7756-7757.
- Suwa, K. *et al.* (1978). "Reaction of Singlet Oxygen with Cholesterol in Liposomal Membranes - Effect of Membrane Fluidity on Photo-Oxidation of Cholesterol." Photochemistry and Photobiology **28**(4-5): 469-473.
- Tafari, M. *et al.* (2002). "Regulation of intracellular pH mediates Bax activation in HeLa cells treated with staurosporine or tumor necrosis factor- $\alpha$ ." Journal of Biological Chemistry **277**(51): 49569-49576.
- Tellis, J. C. *et al.* (2011). "Relative Humidity Sensors Based on an Environment-Sensitive Fluorophore in Hydrogel Films." Analytical Chemistry **83**(3): 928-932.
- Tetsuka, H. *et al.* (2012). "Optically Tunable Amino-Functionalized Graphene Quantum Dots." Advanced Materials **24**(39): 5333-5338.
- Thurn, K. T. *et al.* (2007). "Nanoparticles for applications in cellular Imaging." Nanoscale Research Letters **2**(9): 430-441.
- Tian, L. *et al.* (2009). "Nanosized Carbon Particles From Natural Gas Soot." Chemistry of Materials **21**(13): 2803-2809.
- Torchilin, V. P. (2005). "Recent advances with liposomes as pharmaceutical carriers." Nature Reviews Drug Discovery **4**(2): 145-160.

## References

- Verma, A. *et al.* (2008). "Surface-structure-regulated cell-membrane penetration by monolayer-protected nanoparticles." Nature Materials **7**(7): 588-595.
- Vermes, I. *et al.* (1995). "A Novel Assay for Apoptosis - Flow Cytometric Detection of Phosphatidylserine Expression on Early Apoptotic Cells Using Fluorescein-Labeled Annexin-V." Journal of Immunological Methods **184**(1): 39-51.
- Viallat, A. *et al.* (2004). "Giant lipid vesicles filled with a gel: Shape instability induced by osmotic shrinkage." Biophysical Journal **86**(4): 2179-2187.
- Vinci, J. C. *et al.* (2013). "Hidden Properties of Carbon Dots Revealed After HPLC Fractionation." Journal of Physical Chemistry Letters **4**(2): 239-243.
- Wang, J. *et al.* (2012a). "Amphiphilic Egg-Derived Carbon Dots: Rapid Plasma Fabrication, Pyrolysis Process, and Multicolor Printing Patterns." Angewandte Chemie-International Edition **51**(37): 9297-9301.
- Wang, J. *et al.* (2015a). "High Performance Photoluminescent Carbon Dots for In Vitro and In Vivo Bioimaging: Effect of Nitrogen Doping Ratios." Langmuir **31**(29): 8063-8073.
- Wang, J. *et al.* (2014). "Carbon nanodots featuring efficient FRET for two-photon photodynamic cancer therapy with a low fs laser power density." Biomaterials **35**(34): 9372-9381.
- Wang, N. *et al.* (1997). "Preparation and characterization of agarose hydrogel nanoparticles for protein and peptide drug delivery." Pharm Dev Technol **2**(2): 135-142.
- Wang, Q. *et al.* (2012b). "Microwave-assisted synthesis of carbon nanodots through an eggshell membrane and their fluorescent application." Analyst **137**(22): 5392-5397.
- Wang, X. H. *et al.* (2011). "Microwave assisted one-step green synthesis of cell-permeable multicolor photoluminescent carbon dots without surface passivation reagents." Journal of Materials Chemistry **21**(8): 2445-2450.
- Wang, X. Y. *et al.* (2015b). "The permeability and transport mechanism of graphene quantum dots (GQDs) across the biological barrier." Nanoscale **7**(5): 2034-2041.
- Warnement, M. R. *et al.* (2007). "Fluorescent imaging applications of Quantum Dot probes." Current Nanoscience **3**(4): 273-284.
- Wastl, D. S. *et al.* (2013). "Optimizing atomic resolution of force microscopy in ambient conditions." Physical Review B **87**(24).
- Watson, P. M. D. *et al.* (2013). "Modelling the endothelial blood-CNS barriers: a method for the production of robust in vitro models of the rat blood-brain barrier and blood-spinal cord barrier." Bmc Neuroscience **14**.
- Wegener, J. *et al.* (1996). "Impedance analysis of epithelial and endothelial cell monolayers cultured on gold surfaces." Journal of Biochemical and Biophysical Methods **32**(3): 151-170.
- Wei, J. M. *et al.* (2014a). "Simple one-step synthesis of water-soluble fluorescent carbon dots from waste paper." New Journal of Chemistry **38**(3): 906-909.

- Wei, W. L. *et al.* (2014b). "Non-Enzymatic-Browning-Reaction: A Versatile Route for Production of Nitrogen-Doped Carbon Dots with Tunable Multicolor Luminescent Display." Scientific Reports **4**.
- Wetzel, B. K. *et al.* (2004). "Chameleon labels for staining and quantifying proteins." Angewandte Chemie-International Edition **43**(40): 5400-5402.
- Whitesides, G. M. (2003). "The 'right' size in nanobiotechnology." Nature Biotechnology **21**(10): 1161-1165.
- Wilson, W. L. *et al.* (1993). "Quantum Confinement in Size-Selected, Surface-Oxidized Silicon Nanocrystals." Science **262**(5137): 1242-1244.
- Wurm, F. M. *et al.* (2011). "First CHO genome." Nature Biotechnology **29**(8): 718-720.
- Xu, X. Y. *et al.* (2004). "Electrophoretic analysis and purification of fluorescent single-walled carbon nanotube fragments." Journal of the American Chemical Society **126**(40): 12736-12737.
- Xu, Y. *et al.* (2013). "Nitrogen-Doped Carbon Dots: A Facile and General Preparation Method, Photoluminescence Investigation, and Imaging Applications." Chemistry-a European Journal **19**(7): 2276-2283.
- Yamaguchi, S. *et al.* (2010). "Novel Photodynamic Therapy Using Water-dispersed TiO<sub>2</sub>-Polyethylene Glycol Compound: Evaluation of Antitumor Effect on Glioma Cells and Spheroids In Vitro." Photochemistry and Photobiology **86**(4): 964-971.
- Yan, Z. *et al.* (2015). "Preparation of carbon quantum dots based on starch and their spectral properties." Luminescence **30**(4): 388-392.
- Yang, S. T. *et al.* (2009). "Carbon Dots as Nontoxic and High-Performance Fluorescence Imaging Agents." Journal of Physical Chemistry C **113**(42): 18110-18114.
- Yang, Y. H. *et al.* (2012). "One-step synthesis of amino-functionalized fluorescent carbon nanoparticles by hydrothermal carbonization of chitosan." Chemical Communications **48**(3): 380-382.
- Yang, Z. C. *et al.* (2011). "Intrinsically fluorescent carbon dots with tunable emission derived from hydrothermal treatment of glucose in the presence of monopotassium phosphate." Chemical Communications **47**(42): 11615-11617.
- Youdim, K. A. *et al.* (2003). "In vitro trans-monolayer permeability calculations: often forgotten assumptions." Drug Discovery Today **8**(21): 997-1003.
- Yu, C. M. *et al.* (2013). "Carbon-dot-based ratiometric fluorescent sensor for detecting hydrogen sulfide in aqueous media and inside live cells." Chemical Communications **49**(4): 403-405.
- Yu, P. *et al.* (2012). "Temperature-Dependent Fluorescence in Carbon Dots." Journal of Physical Chemistry C **116**(48): 25552-25557.
- Zhang, L. W. *et al.* (2009). "Mechanisms of Quantum Dot Nanoparticle Cellular Uptake." Toxicological Sciences **110**(1): 138-155.
- Zhang, L. W. *et al.* (2008). "Biological interactions of quantum dot nanoparticles in skin and in human epidermal keratinocytes." Toxicology and Applied Pharmacology **228**(2): 200-211.

## References

- Zhang, X. L. *et al.* (2005). "Development of an in vitro multicellular tumor spheroid model using microencapsulation and its application in anticancer drug screening and testing." Biotechnology Progress **21**(4): 1289-1296.
- Zhang, Y. Q. *et al.* (2012). "One-pot synthesis of N-doped carbon dots with tunable luminescence properties." Journal of Materials Chemistry **22**(33): 16714-16718.
- Zhao, Q. L. *et al.* (2008). "Facile preparation of low cytotoxicity fluorescent carbon nanocrystals by electrooxidation of graphite." Chemical Communications(41): 5116-5118.
- Zheng, H. Z. *et al.* (2011). "Enhancing the luminescence of carbon dots with a reduction pathway." Chemical Communications **47**(38): 10650-10652.
- Zheng, L. Y. *et al.* (2009). "Electrochemiluminescence of Water-Soluble Carbon Nanocrystals Released Electrochemically from Graphite." Journal of the American Chemical Society **131**(13): 4564-+.
- Zhou, J. J. *et al.* (2012a). "Facile synthesis of fluorescent carbon dots using watermelon peel as a carbon source." Materials Letters **66**(1): 222-224.
- Zhou, L. *et al.* (2012b). "Carbon nanodots as fluorescence probes for rapid, sensitive, and label-free detection of Hg<sup>2+</sup> and biothiols in complex matrices." Chemical Communications **48**(8): 1147-1149.
- Zhu, A. W. *et al.* (2012). "Carbon-Dot-Based Dual-Emission Nanohybrid Produces a Ratiometric Fluorescent Sensor for In Vivo Imaging of Cellular Copper Ions." Angewandte Chemie-International Edition **51**(29): 7185-7189.
- Zhu, B. C. *et al.* (2013a). "Preparation of carbon nanodots from single chain polymeric nanoparticles and theoretical investigation of the photoluminescence mechanism." Journal of Materials Chemistry C **1**(3): 580-586.
- Zhu, S. J. *et al.* (2013b). "Highly Photoluminescent Carbon Dots for Multicolor Patterning, Sensors, and Bioimaging." Angewandte Chemie-International Edition **52**(14): 3953-3957.
- Zhu, S. J. *et al.* (2011). "Strongly green-photoluminescent graphene quantum dots for bioimaging applications." Chemical Communications **47**(24): 6858-6860.



## *References*

## 10 Appendix

### 10.1 List of Abbreviations

A	Absorbance
ADBDA	9,10-Anthracenediyl-bis(methylene)dimalonic acid
AFM	Atomic Force Microscopy
a.u.	Arbitrary Units
$\beta$	Mass Concentration
bpm	Beats per Minute
C	Capacitance
C-dot	Carbon (Nano)dot
CHO	Chinese Hamster Ovary
CPS	Counts per Second
D	Defect
$d_H$	Hydrodynamic Diameter
DHR	Dihydrorhodamine 123
Dil	1,1'-dioctadecyl-3,3,3'3'-tetramethylindocarbocyanine perchlorate
DLS	Dynamic Light Scattering
DMEM	Dulbecco's Modified Eagle's Medium
DMF	Dimethylformamide
DMSO	Dimethyl Sulfoxide
DPPC	Dipalmitoylphosphatidylcholine
DPPG	Dipalmitoylphosphatidylglycerol
ds	Double Stranded
E	Energy
EBSS	Earle's Balanced Salt Solution
EBSS <sup>++</sup> /G	EBSS <sup>++</sup> with Glucose (1 g/L)
ECIS	Electric Cell-Substrate Impedance Sensing
EDTA	Ethylenediaminetetraacetic Acid
EDX	Energy-Dispersive X-Ray Spectroscopy

## Appendix

Em.	Emission
EthD-1	Ethidium Homodimer-1
Exc.	Excitation
FCS	Fetal Calf Serum
FITC	Fluorescein Isothiocyanate
G	Graphene
GO	Graphene Oxide
GQD	Graphene Quantum Dot
HaCaT	Cultured Human Keratinocyte
HEPES	4-(2-Hydroxyethyl)-1-Piperazineethanesulfonic Acid
HTC	Hydrothermal Carbonization
Hz	Hertz
IR	Infrared
I	Intensity
ITO	Indium Tin Oxide
$\lambda$	Wavelength
MCF-7	Michigan Cancer Foundation-7
MCS	Multicellular Spheroid
MDCK	Madin-Darby Canine Kidney
MEM	Minimal Essential Medium
$\nu$	Wavenumber
NRK	Normal Rat Kidney
OAM C-dots	Oleic Acid Modified Carbon Dots
$P_{app}$	Apparent Permeability Coefficient
PBS	Phosphate Buffered Saline
PdI	Polydispersity Index
PDMS	Polydimethylsiloxane
PEG	Polyethylene Glycol
PES	Polyether Sulfone
PFA	para-Formaldehyde
PL	Photoluminescence



PMMA	Poly (methyl methacrylate)
PI	Propidium Iodide
PTFE	Polytetrafluoroethylene
Q-dot	Quantum Dot
QY	Quantum Yield
rGO	Reduced Graphene Oxide
SDS	Sodium Dodecyl Sulfate
T	Transmittance
t	Time
tBuOOH	tert-Butyl hydroperoxide
TEER	Transepithelial Electrical Resistance
TRIS	Tris(hydroxymethyl)aminomethane
TLC	Thin Film Chromatography
Trp	L-Tryptophan
UV	Ultraviolet
(v/v)	Volume Ratio
VIS	Visible Spectrum
(w/w)	Weight Ratio
XPS	X-Ray Photoelectron Spectroscopy
Z	Impedance
$\zeta$	Zeta Potential
-- / ++	Without Ca <sup>2+</sup> and Mg <sup>2+</sup> / With Ca <sup>2+</sup> and Mg <sup>2+</sup>

## 10.2 Publications and Presentations

### Publications

“Cell-Nanomaterial Interaction: A Label-free, integrative and multiparametric Approach”

**Michael-M. Lemberger**, Thomas Hirsch, Joachim Wegener, Nanotoxicology 2015  
(in preparation)

“Monitoring the Impact of Nanomaterials on Animal Cells by Impedance Analysis: A Non-Invasive, Label-Free and Multi-Modal Approach”

Michaela Sperber, Christina Hupf, **Michael-M. Lemberger**, Barbara Gorcnik, Nadja Hinterreiter, Sonja Lukic, Maximilian Oberleitner, Judith A. Stolwijk, Joachim Wegener, Bioanalytical Reviews 2015 (submitted)

“Carbon Nanodots: Synthesis, Characterization, and Bioanalytical Applications”

**Michael-M. Lemberger**, Thomas Hirsch, Joachim Wegener, Bioanalytical Reviews 2014

“Reduced Graphene Oxide and Graphene Composite Materials for Improved Gas Sensing at Low Temperature”

Alexander Zöpfl, **Michael-M. Lemberger**, Matthias König, Guenther Ruhl, Frank-Michael Matysik, Thomas Hirsch, Faraday Discussions 2014

**Oral Presentations**

- Mar 2015 “Carbon Dots – Promising Luminescent Carbon Nanomaterial for Bioanalytical Applications”  
Pittcon 2015, New Orleans, **USA**
- May 2014 “Multicolor Imaging of Mammalian Cell Viability with a Live-Dead-Assay using Carbon Dots”  
24<sup>th</sup> World Congress on Biosensors, Melbourne, **Australia**
- Aug 2013 “Monitoring the Influence of Carbon Dots on Animal Cells via Impedance Analysis”  
2<sup>nd</sup> Conference on Impedance-Based Cellular Assays, Budapest, **Hungary**
- Feb 2013 “Carbon dots for Cellular Imaging Applications and Bioanalytical Sensing”  
7. Interdisziplinäres Doktorandenseminar, Berlin, **Germany**

**Poster Presentations**

- Mar 2015 “Carbon Dots – Promising Luminescent Carbon Nanomaterial for Bioanalytical Applications”  
ANAKON 2015, Graz, **Austria**
- Apr 2014 “Carbon dots for Cellular Imaging and Intracellular Sensing Applications”  
Europt(r)ode XII, Athens, **Greece**
- Aug 2013 “Monitoring the Influence of Carbon Dots on Animal Cells via Impedance Analysis”  
2<sup>nd</sup> Conference on Impedance-Based Cellular Assays, Budapest, **Hungary**
- Mar 2013 “Highly Fluorescent Carbon Dots from Starch and Tryptophan”  
8. Deutsches Biosensor Symposium, Wildau, **Germany**

## 10.3 Curriculum Vitae

### Personal data

Name: Michael-Maximilian Lemberger  
Date of birth: 04.06.1987  
Place of birth: Straubing  
Nationality: German

### Studies

- 2012-2015 PhD thesis, Institute of Analytical Chemistry, Chemo- and Biosensors (IACCB), University of Regensburg,  
“Carbon nanomaterials for bioanalytical sensing and multicolor cell imaging”  
Supervisor: Prof. Dr. Joachim Wegener
- 2010-2012 Master of Science in Chemistry, University of Regensburg,  
**Graduation with Honors, Grade of 1.0**  
Master thesis: IACCB  
“Carbon nanoparticles: synthesis, characterization and delivery into adherent cells”  
Supervisor: Prof. Dr. Joachim Wegener
- 2007-2010 Bachelor of Science in Chemistry, University of Regensburg,  
**Grade of 1.6**  
Bachelor thesis: Institute of Organic Chemistry  
“Synthesis of pyrene-modified nucleosides and examination of the interaction with carbon nanotubes”  
Supervisor: Prof. Hans-Achim Wagenknecht

### **Military Service**

2006-2007 PzPiBtl 4, Graf-Aswin Kaserne, Bogen

### **Education**

1997-2006 A levels, Gymnasium Landau a.d. Isar, **Grade of 1.9**

Majors: Chemistry and English

### **Awards**

Jun 2013 Graduation award of the Dr. Alfons Paulus Foundation, Regensburg

Mar 2013 Poster award at the 8. German BioSensor Symposium, Wildau

### **Additional Qualifications**

Jul 2015 Seminar Series "BWL für Entwickler",  
Strategische Partnerschaft Sensorik e.V.

Apr 2015 European Business Competence License (EBC\*L) – Level B

Aug 2014 European Business Competence License (EBC\*L) – Level A



## 10.4 Eidesstattliche Erklärung

Ich erkläre hiermit an Eides statt, dass ich die vorliegende Arbeit ohne unzulässige Hilfe Dritter und ohne Benutzung anderer als der angegebenen Hilfsmittel angefertigt habe; die aus anderen Quellen direkt oder indirekt übernommenen Daten und Konzepte sind unter Angabe des Literaturzitats gekennzeichnet.

Weitere Personen waren an der inhaltlich materiellen Herstellung der vorliegenden Arbeit nicht beteiligt. Insbesondere habe ich hierfür nicht die entgeltliche Hilfe eines Promotionsberaters oder anderer Personen in Anspruch genommen. Niemand hat von mir weder unmittelbar noch mittelbar geldwerte Leistungen für Arbeiten erhalten, die im Zusammenhang mit dem Inhalt der vorgelegten Dissertation stehen.

Diese Arbeit wurde bisher weder im In- noch im Ausland in gleicher oder ähnlicher Form einer anderen Prüfungsbehörde vorgelegt.

---

Ort, Datum

Unterschrift